

2

AD A101729
Final Technical Report
May 1981

LEVEL



DOPPLER SPECTRAL CHARACTERISTICS OF HIGH LATITUDE IONOSPHERIC IRREGULARITIES: EFFECT ON HF RADARS

The John Hopkins University

Raymond A. Greenwald

AD A101729

APPROVED FOR PUBLIC RELEASE; DISTRIBUTION UNLIMITED

DTIC
ELECTE
JUL 22 1981
S D

ROME AIR DEVELOPMENT CENTER
Air Force Systems Command
Griffiss Air Force Base, New York 13441

DTIC FILE COPY

81 7 22 0 11

This report has been reviewed by the RADC Public Affairs Office and is releasable to the National Technical Information Service (NTIS). It will be releasable to the general public, including foreign countries.

RADC-TR-81-93 has been reviewed and approved for publication.

APPROVED:

William F. Ring
WILLIAM F. RING
Project Engineer

APPROVED:

Allan C. Schell
ALLAN C. SCHELL
Chief, Electromagnetic Sciences Division

FOR THE COMMANDER:

John P. Huss
JOHN P. HUSS
Acting Chief, Plans Office

If your address has changed or if you wish to be removed from the mailing list, or if the addressee is no longer employed by your organization, please notify RADC (KFP) Hanscom AFB MA 01731. This will assist us in maintaining a current mailing list.

Do not return this copy. Retain or destroy.

UNCLASSIFIED

SECURITY CLASSIFICATION OF THIS PAGE (When Data Entered)

19 REPORT DOCUMENTATION PAGE		READ INSTRUCTIONS BEFORE COMPLETING FORM
1. REPORT NUMBER RADC-TR-81-93	2. GOVT ACCESSION NO. AD A101729	3. RECIPIENT'S CATALOG NUMBER 9
4. TITLE (and Subtitle) DOPPLER SPECTRAL CHARACTERISTICS OF HIGH LATITUDE IONOSPHERIC IRREGULARITIES: EFFECT ON HF RADARS.		5. TYPE OF REPORT & PERIOD COVERED Final Technical Report, 23 Apr - 30 Sep 80
7. AUTHOR(s) Raymond A. Greenwald		6. PERFORMING ORG. REPORT NUMBER N/A
9. PERFORMING ORGANIZATION NAME AND ADDRESS The John Hopkins University John Hopkins Road Laurel MD 20810		8. CONTRACT OR GRANT NUMBER(s) N00024-78-C-5384 ✓
10. PROGRAM ELEMENT, PROJECT, TASK AREA & WORK UNIT NUMBERS 61102F 2305J230		11. REPORT DATE May 81
11. CONTROLLING OFFICE NAME AND ADDRESS Deputy for Electronic Technology (RADC/EEP) Hanscom AFB MA 01731		12. NUMBER OF PAGES 148
14. MONITORING AGENCY NAME & ADDRESS (if different from Controlling Office) Same		13. SECURITY CLASS. (of this report) UNCLASSIFIED
16. DISTRIBUTION STATEMENT (of this Report) Approved for public release; distribution unlimited.		15. DECLASSIFICATION/DOWNGRADING SCHEDULE N/A
17. DISTRIBUTION STATEMENT (of the abstract entered in Block 20, if different from Report) Same		
18. SUPPLEMENTARY NOTES RADC Project Engineer: William Ring (EEP)		
19. KEY WORDS (Continue on reverse side if necessary and identify by block number) Ionospheric Irregularities Ionospheric Clutter Over-the-horizon Radars Doppler Spectra Cross Spectral Analysis		
20. ABSTRACT (Continue on reverse side if necessary and identify by block number) This report considers the Doppler spectral properties of radar signals scattered from high latitude E and F-region ionospheric irregularities. Although the exact mechanism for the production of F-region irregularities is not yet known, it appears that the Doppler shift from these as well as from E-region irregularities is determined by the ionospheric electric field via the $E \times B/B^2$ drift velocity. The width of the backscattered spectra is determined by the viewing angle of the radar.		

DD FORM 1473 EDITION OF 1 NOV 65 IS OBSOLETE

UNCLASSIFIED
SECURITY CLASSIFICATION OF THIS PAGE (When Data Entered)

031-50

B-50000000

UNCLASSIFIED

SECURITY CLASSIFICATION OF THIS PAGE(When Data Entered)

relative to the $E \times B/B^2$ drift direction as well as the drift magnitude. Assuming an electrical potential distribution over the Earth's high latitude regions, it has been possible to predict the diurnal variability of the Doppler velocity and width associated with high latitude irregularities. Although some of these predictions agree with previous observations, considerably more knowledge is required of the high latitude potential distribution and its temporal variability. Finally, a novel new technique is proposed whereby through cross spectral analysis the detrimental effects of clutter due to ionospheric irregularities may be eliminated.

Accession For	
NTIS GRA&I	<input checked="" type="checkbox"/>
DTIC TAB	<input type="checkbox"/>
Unannounced	<input type="checkbox"/>
Justification	
By	
Distribution/	
Availability Codes	
Dist	Avail and/or Special
A	

UNCLASSIFIED

SECURITY CLASSIFICATION OF THIS PAGE(When Data Entered)

TABLE OF CONTENTS

1.0	INTRODUCTION	1
2.0	E-REGION IRREGULARITIES	3
	2.1 Observations	3
	2.1.1 C. W. Measurements	5
	2.1.2 Pulsed Radar Measurements	6
	2.2 Theory	8
	2.2.1 Linear Theory	8
	2.2.2 Shortcomings of Linear Theory	11
	2.2.3 Nonlinear Theory (2-Dimensional Turbulence)	12
3.0	F-REGION IRREGULARITIES	13
	3.1 Observations	13
	3.2 Mechanisms for High Latitude F-Region Irregularity Formation	17
	3.2.1 Production by Precipitating Low Energy Electrons	17
	3.2.2 F-Region E x B Instability	18
	3.2.3 Current Convective Instability	18
	3.2.4 Ion Acoustic Instability	19
	3.2.5 Electrostatic Ion Cyclotron Waves	19
	3.2.6 Temperature Gradient Instability	20
	3.3 Expected Doppler Spectral Characteristics	20
4.0	DOPPLER SPECTRUM MODELING	21
	4.1 Theoretical Foundation	21
	4.2 Results	24
	4.3 Discussion	29
5.0	REMOVAL OF SPREAD SPECTRA	32
6.0	SUMMARY OF RESULTS	42
7.0	RECOMMENDATIONS	43
8.0	REFERENCES	45
	FIGURE CAPTIONS	49
	APPENDIX A. Doppler Velocity and Width Plots for Potential Distribution Shown in Figure 4.1.	
	APPENDIX B. Doppler Velocity and Width Plots for Potential Distribution Shown in Figure 4.6.	

One of the better methods of distinguishing different types of radar targets is spectral analysis of the backscattered signal. Generally, each type of target contributes a distinct, characteristic spectral component to the total spectrum. The nature of this spectral component is determined by the nature of the line-of-sight target velocity, \tilde{v} , through the expression

$$\Delta f = -2fk \cdot \tilde{v}/kc \quad (1.1)$$

where f is the frequency of the radar and $c = 3 \times 10^8$ m/s is the velocity of light.

For discrete targets, such as aircraft, the characteristic spectral component would be a line spectrum. If an aircraft were to fly at a constant velocity with respect to the radar beam, this spectrum would remain constant with time; whereas if it were to change speed or direction the spectral line would change according to (1.1).

A second category of targets is comprised of scattering centers that are distributed in space. It includes ground clutter, sea scatter, rain and ionospheric clutter. Each of these scatterers displays different spectral properties ranging from ground clutter which has line spectra at zero Doppler shift to ionospheric clutter which has spectral widths and displacements characteristic of the acoustic velocity. Although any individual element of a distributed target may scatter considerably less incident power than a discrete target, the composite scattered power from a distributed target may be appreciably greater than the power scattered from a discrete target. Under this circumstance, ways must be sought to reduce the detrimental effects of the distributed clutter.

Present Over-the-Horizon (OTH) radars represent one case where clutter signals from a variety of distributed sources severely affect radar operation. For these radars transmitted signals typically are emitted simultaneously over an extended range of elevation angles. Since the radars operate at frequencies for which the signals follow rather complex propagation

paths, signals returning to the receiving antenna at any particular instant may have been scattered from a number of different altitudes and ranges. Moreover, they may have been scattered by a variety of targets.

Spectral analysis will enable one to eliminate many of the undesired targets from the backscattered signal. For example, ground clutter and sea scatter will have low or zero Doppler frequencies, whereas aircraft signals will have Doppler shifts characteristic of the speed of sound. Unfortunately, clutter from ionospheric irregularities may also have Doppler properties characteristic of the acoustic speed. Hence, this type of clutter may seriously degrade the performance of an OTH radar.

In this report we examine the Doppler spectral properties associated with ionospheric irregularities in the high latitude E and F-regions. Although only limited information exists on the spectral properties of backscatter from F-region irregularities, it appears that one can assume both E and F region irregularities to have spectral properties characterized by a convective drift velocity. This velocity is given by

$$\underline{V}_d = \underline{E} \times \underline{B}/B^2 = -\underline{\nabla}\phi \times \underline{B}/B^2$$

where B is the Earth's magnetic field strength and ϕ is the electrostatic potential at any point in the high latitude ionosphere.

On the basis of the convective drift hypothesis and an assumed electrostatic potential distribution, we have modeled the probable Doppler shift and Doppler width that one would observe at any observing latitude and viewing direction as a function of local time. The results indicate that irregularity spectra may often mask discrete spectra associated with aircraft. For an OTH radar directed in a northwesterly direction from Maine, the disturbance effect of ionospheric irregularities would be particularly bothersome during the afternoon and evening hours.

Finally, we have sought ways in which the disturbance effect of irregularity spectra might be minimized or eliminated. We propose what we believe to be a novel approach that will eliminate the spread Doppler spectra associated with ionospheric irregularities while retaining discrete spectral components associated with aircraft.

2.0 E-REGION IRREGULARITIES

2.1 Observations

E-region irregularities produced in the currents-carrying regions of the Earth's ionosphere are perhaps the best understood of all ionospheric irregularity structures. Basically, they are produced in the altitude range from 90-120 km as a result of streaming between collisionless electrons drifting under the $\vec{E} \times \vec{B}/B^2$ force and ions that are collisionally bound to the neutral atmosphere. This relative motion leads to the equatorial and high latitude horizontal current systems and is an important factor in the generation of the irregularities.

Figure 2.1 shows the regions above the Earth where one might expect to observe these irregularities. One sees that they are observed in a latitudinal strip of 6°-8° width at the magnetic dip equator and over both polar caps north of 60° geomagnetic latitude. Thus they occur over 50% of the Earth's surface.

Doppler spectral measurements of E-region irregularities have been made for more than 20 years. In general the results have varied depending on whether the observations were made at the equator or at high latitudes and on the frequency of the radar. We will concentrate our attention on high latitude VHF measurements made during the last eleven years when more sophisticated spectral techniques were available. The measurements were made in two basic modes: (1) bistatic continuous wave (CW) measurements conducted in Canada and Scandinavia, and (2) pulsed monostatic measurements made in Alaska. CW measurements are the most amenable to spectral analysis; however, they suffer the disadvantage that the viewing area defined by the intersection of the transmitting and receiving antenna patterns can be quite large. Thus, the backscatter spectra may be comprised of simultaneous signals from several different regions with differing phase velocity characteristics.

Pulse radars largely avoid the spatial aliasing problem by utilizing the range resolution of the transmitted rf pulse as well as the antenna beamwidth to achieve superior spatial resolution. However, care must be taken to assure that the pulse repetition frequency is sufficiently high for the resulting spectra to be unaliased. Studies at high latitudes with VHF radars

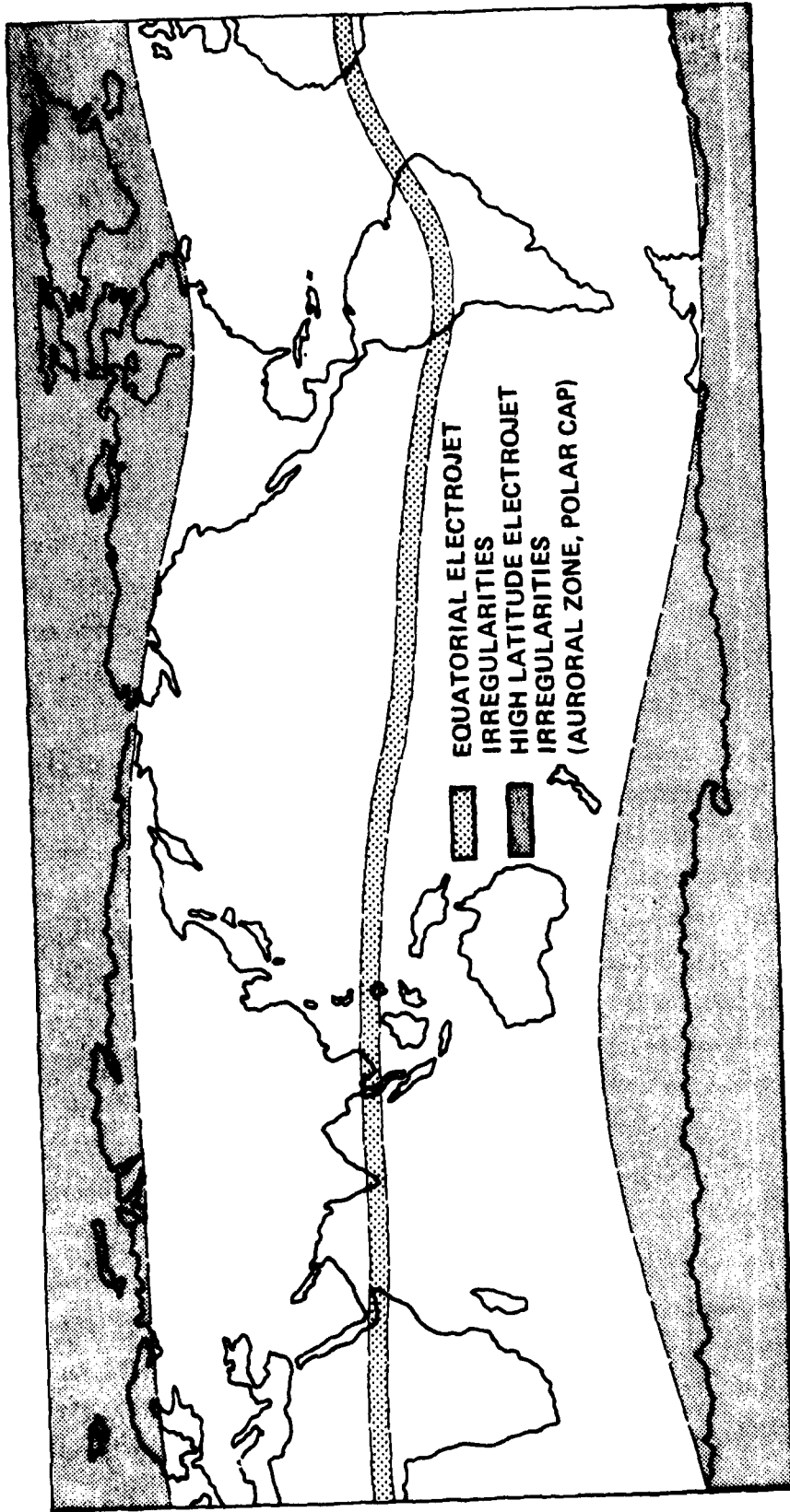


FIGURE 2.1

have indicated that the prerequisite pulse repetition frequency is often so high that one would still have to superimpose signals from two or more different spatial regions (see e.g., Balsley and Ecklund, 1972; Greenwald et al., 1975).

Since VHF radar studies have been made at many different frequencies, giving the observed Doppler characteristics in terms of frequency shift and spread may lead to a great deal of confusion. Therefore we interpret the observations in terms of velocity characteristics. In this way, one can recover the probable frequency characteristics at any wavelength simply by applying (1.1).

2.1.1 CW Measurements

CW measurements have been reported by Hofstee and Forsyth (1969, 1972), Czechowsky (1974), and Haldoupis and Sofko (1976). Hofstee and Forsyth (1969) conducted measurements near 40 MHz with a system that had an effective line-of-sight directed within 20° of magnetic north. They observed broad spectra with low Doppler shifts during the afternoon and evening hours and occasional line spectra near midnight. The broad spectra were typically shifted by less than 75 m/s and had a Doppler width of 200 m/s. The line spectra had shifts in the vicinity of 360 m/s and typical widths of 75 m/s.

Czechowsky (1974) also described measurements made within 20° of magnetic north. He reported two examples obtained near 146 MHz in which the Doppler shift maximized near local magnetic midnight with values of 300-400 m/s directed equatorward. During the post-midnight period, Czechowsky (1974) observed Doppler velocities of less than 100 m/s. Finally, Czechowsky (1974) presented several examples of multi-peaked Doppler spectra obtained near local magnetic midnight. He attributed the multiple peaks to the presence of different types of plasma instabilities; however, this result may also have been due to spatial structure within the large scattering volume that was associated with his bi-static system.

Haldoupis and Sofko (1976) presented spectral data from a 42 MHz radar system that was directed 4° west of geomagnetic north. Their observations were confined to the time frame extending from 3 hours before local magnetic midnight to 5 hours after local magnetic midnight. These authors

found that they could divide their observations into two basic categories which they referred to as diffuse and discrete spectra. This classification is similar to that used in pulsed radar spectral observations (e.g., Balsley and Ecklund, 1972).

Diffuse spectra constituted 75% of the observed cases reported by Haldoupis and Sofko (1976). These spectra exhibited a Doppler velocity that was dependent on local time and varied from 360 m/s equatorward to 180 m/s polewards. Typically the large equatorward Doppler velocities occurred prior to local magnetic midnight, while the smaller poleward velocities were observed later in the morning hours. The Doppler width of diffuse spectra generally ranged from 150-430 m/s. It appeared to vary inversely with the line-of-sight Doppler velocity with the smallest Doppler velocities corresponding to the largest Doppler widths. These were generally observed well into the morning period.

Discrete spectra were defined as spectra with a mean equatorward Doppler velocity varying from 210-460 m/s and a Doppler width of less than 150 m/s. This type of spectrum was observed before and up to one hour after local magnetic midnight and it constituted 25% of the observations of Haldoupis and Sofko (1976). Discrete spectra appeared to be associated with discrete radar aurora (Unwin, 1966) which are noted for their short-lived (1-10 minute) nature.

The maximum line-of-sight Doppler velocity reported by Haldoupis and Sofko (1976) was 1100 m/s.

2.1.2 Pulsed Radar Measurements

Modern VHF spectral studies with pulsed radars have been reported by Balsley and Ecklund (1972), Balsley et al., (1973), Greenwald et al. (1975), Ecklund et al. (1975), Greenwald and Ecklund (1975), and Ecklund et al. (1977).

Balsley and Ecklund (1972) reported observations at 50 MHz at angles of 38° west, 13° west, and 12° east of geomagnetic north. Seventy percent of their observations were of diffuse radar auroral while the remaining echoes (30%) were of the discrete type. They were generally unable to determine the line-of-sight Doppler velocity of the diffuse echoes because of spectral

aliasing; however, they were able to conclude that these echoes often had a Doppler width in excess of 800 m/s. The discrete spectra that they observed were divided into two sub-categories: 10% of the total observations exhibited narrow spectral widths and mean Doppler velocities ranging from 300-600 m/s and 20% exhibited Doppler velocities less than the ion acoustic velocity and Doppler widths in excess of the mean Doppler shift.

Using multiple antennas, Balsley and Ecklund (1972) were able to obtain some crude azimuth scans. They found that the observed echo Doppler variation was consistent with the expected electron drift motion in the morning sector.

Balsley et al. (1973) reported spectral observations of radar echoes located on the equatorward edge of an auroral form that was extended in longitude. The observations were consistent with the hypothesis that the irregularities were driven by westward drifting electrons on the equatorward edge of the form. When the radar beam was most aligned with the form, the line-of-sight Doppler velocity reached 360 m/s and the spectrum was appreciably narrower than at other times.

Greenwald et al. (1975) presented extensive spectral observations of diffuse radar aurora as determined with a 50 MHz radar located in Anchorage, Alaska. Their radar beam was directed 13° west of geomagnetic north. They found that these spectra could be divided into two categories: one having a Doppler width that was typically less than 450 m/s ("narrow" component) and the other having a Doppler width ranging from 600-1200 m/s ("broad" component). Both components exhibited line-of-sight velocities that were typically less than 180 m/s. In the period around local magnetic midnight, Greenwald et al. (1975) also observed spectra associated with discrete radar aurora. These spectra exhibited Doppler velocities in the vicinity of 400 m/s.

Other topics considered by Greenwald et al. (1975) were the dependence of the diffuse spectra on aspect angle and the angle between the radar wave vector and the electron drift velocity (θ). They found no evidence of any aspect angle dependence in the characteristics of diffuse spectra and

little evidence that the spectra changed other than in mean Doppler shift as the angle θ was varied from 60° to 103° . Ecklund et al. (1975) have presented a more in-depth study of the θ -dependence.

Recently, a number of studies have been conducted in which double-pulse mean Doppler techniques have been used (Greenwald and Ecklund, 1975; Greenwald et al. 1978; and Unwin and Cummack, 1979). Thus far, this approach has not been used to study Doppler widths; however, all of the above authors have observed Doppler velocities of the order of 2000 m/s.

Finally, measurements by Ecklund et al. (1977) and Cahill et al. (1978) have indicated that high latitude electrojet irregularities at VHF wavelengths convect with the E-region electron drift velocity. Since this velocity often ranges from 1000-2000 m/s, one should expect to observe equally large Doppler velocities with ground-based auroral radar systems.

2.2 THEORY

2.2.1 Linear Theory

The initial theoretical studies into the nature of E-region irregularities were conducted by Buneman (1963), Farley (1963) and Knox (1964). The former two studies predicted that the E-region plasma becomes unstable to ion acoustic waves when the streaming velocity exceeds the ion acoustic velocity. This instability has become known as the cross-field two-stream, or Farley-Buneman instability. The unstable modes or irregularities, as they are often called, propagate approximately perpendicular to the magnetic field with a phase velocity that is determined by the electron drift velocity.

Maeda et al. (1963) and Knox (1964) have shown that an ambient electron density gradient in the direction of the ambient ionospheric electric field will also lead to instability of the plasma. This instability also occurs in regions of relative electron-ion drift and it has become known as the gradient-drift instability. It may be excited when the relative drift velocity is significantly less than the ion acoustic velocity and it is most effective in exciting long wavelength irregularities of the order of 100m. As

in the case of the two-stream instability, the unstable modes are largely confined to the plane perpendicular to the ambient magnetic field and the irregularity phase velocity is determined by the electron drift velocity.

Both of these instability mechanisms were proposed to explain observations of field-aligned irregularities in the equatorial electrojet and later adapted to explain radar aurora in the high latitude ionosphere. In time it became apparent that both mechanisms were operative and that it was possible to combine their effects into a single set of dispersion relations. This was the approach adopted by Rogister and D'Angelo (1970) and later by Sudan et al. (1973). In this report, we follow closely the development of Sudan et al. (1973).

For simplicity, we will assume that the plasma can be treated adequately by fluid equations for both electrons and ions. This assumption is quite valid when considering irregularity wavelengths that would be probed with HF radars. We also assume:

- 1) $\Omega_i \ll \nu_i$ where Ω_i and ν_i are the ion gyrofrequency and collision frequency with neutrals, respectively,
- 2) electron gyroradius $\ll 2\pi/k$ where k is the unstable mode wave number,
- 3) the waves are electrostatic,
- 4) macroscopic charge neutrality,
- 5) isothermal distribution functions for the electrons and ions,
- 6) the unstable modes propagate perpendicular to the magnetic field (Farley (1963) has shown that the off-perpendicular modes are strongly damped. More recently, Ossakow et al. (1975) and Wang and Tsunoda (1975) have shown that, if the streaming velocity is much greater than the ion acoustic velocity, off-perpendicular modes may grow and be more unstable than $k \perp B$ modes) and,
- 7) electron inertia can be neglected.

Under these assumptions, the field equations are given by:

$$\frac{\partial N_e}{\partial t} + \nabla \cdot (N_e \mathbf{v}_e) = 0 \quad (2.1)$$

$$\frac{e}{m_e} (\tilde{E} + \tilde{V}_e \times \tilde{B} - \frac{\tilde{\nabla}}{m_e} \frac{\tilde{v}_e}{N_e}) = 0 \quad (2.2)$$

$$\frac{\partial N_1}{\partial t} + \tilde{\nabla} \cdot (N_1 \tilde{V}_1) = 0 \quad (2.3)$$

$$\left(\frac{\partial}{\partial t} + \tilde{V}_1 \cdot \tilde{\nabla} \right) \tilde{V}_1 = - \frac{T_1}{m_1} \frac{\tilde{\nabla} N_1}{N_1} + \frac{e}{m_1} \tilde{E} - \nu_1 \tilde{V}_1 \quad (2.4)$$

$$\tilde{E} = -\tilde{\nabla} \phi \quad (2.5)$$

where N_e , V_e , ν_e , m_e , T_e and N_1 , V_1 , ν_1 , m_1 , T_1 are respectively, the electron and ion density, velocity, collision frequency with neutrals, mass and temperature.

Linearizing (2.1)-(2.5) and assuming that the electron fluid is drifting through the ions with a velocity given by (1.2), one obtains the following linear dispersion relations for electrostatic waves propagating perpendicular to the magnetic field:

$$\omega = k \cdot \tilde{V}_d / (1 + \Psi) \quad (2.6)$$

$$\gamma = \frac{\Psi}{1 + \Psi} \frac{\Omega_e \omega}{\nu_e k L} + (\omega^2 - k^2 C_s^2) / \nu_1 \quad (2.7)$$

where $\Psi = \nu_e \nu_1 / \Omega_e \Omega_1$, $L = N_e / N'_e$ with N'_e the electron density gradient in the direction of E , and $C_s = ((T_e + T_1) / m_1)^{1/2}$ is the ion acoustic velocity.

Directing our attention to the high latitude ionosphere and assuming that the instabilities are excited at a mean altitude of 110 km, we would expect the ionospheric parameters to take on the following values: $\nu_e = 2 \times 10^4 \text{ s}^{-1}$, $\nu_1 = 10^3 \text{ s}^{-1}$, $\Omega_e = 10^7 \text{ s}^{-1}$ and $\Omega_1 = 1.8 \times 10^2 \text{ s}^{-1}$. Hence, $\Psi = 10^{-2}$ and, therefore, one sees from (2.6) that the phase velocity of the excited modes is determined solely by the electron drift velocity (in the equatorial electrojet $\Psi = 0.2$, causing the excited waves to propagate at less than the electron drift velocity).

If no density gradient is present in the plasma, (2.7) reduces to the two-stream growth condition in which instability occurs when the electron drift velocity is in excess of the ion acoustic velocity, whereas, if $V_d/C_s \ll 1, \omega^2$ can be neglected and (2.7) gives the gradient drift condition for growth. As a typical example of the behavior of (2.7) when both destabilizing terms are present, we will assume that $L = 5 \times 10^3 m$. Letting θ be the angle between \underline{k} and \underline{V}_d , we find that (2.7) reduces to

$$(V_d/C_s)^2 \cos^2 \theta + (0.25 V_d/k^2 C_s) \cos \theta^{-1} > 0 \quad (2.8)$$

for instability. If $V_d/C_s < 1$, waves will only grow because of the gradient drift term and then only for sufficiently small k . Defining k_m as the maximum unstable wavenumber and λ_m as the corresponding minimum unstable wavelength, if $V_d/C_s = 1/2$, $k_m(0^\circ) = 0.4 m^{-1}$ ($\lambda_m = 15m$) whereas $k_m(60^\circ) = 0.25 m^{-1}$ ($\lambda_m = 25m$). Thus over an arc extending $\pm 60^\circ$ about the electron drift direction, the minimum unstable wavelength changes by less than a factor of 2. Beyond $\theta = 60^\circ$, the wavelength of the marginally stable mode changes rapidly and at $\theta = 90^\circ$ the plasma should always be stable.

For the case $V_d/C_s > 1$, one finds similar behavior. Here the second term in (2.8) is generally negligible for $k > 1$. Unstable modes will propagate over the arc given by $\theta < \cos^{-1}(C_s/V_d)$ and, as in the previous case, unstable modes should never be excited at $\theta = 90^\circ$.

2.2.2 Shortcomings of Linear Theory

Radar studies of electrojet instabilities, particularly at the equator (Balsley, 1969; Farley and Balsley, 1973) have provided several observational features that cannot be explained by linear theory. Most notable is the presence of unstable modes at $\theta = 90^\circ$ even when $V_d \ll C_s$.

Another common observation that cannot be explained by linear theory is the presence of short wavelength irregularities when $V_d/C_s \ll 1$. At the equator, 3m wavelength irregularities are often observed where theory would predict the minimum unstable wavelength to be 15m.

Finally, the phase velocity dependence predicted by (2.6) does not appear to be valid in the equatorial electrojet when $V_d/C_s > 1$, although it is

valid when $V_d/C_s < 1$. Instead one obtains the classic "two-stream" spectrum in which the returned signal at all θ appears to be shifted by the ion acoustic speed. Similar behavior has been reported at UHF frequencies in the auroral zone (Tsunoda, 1976; Moorcroft and Tsunoda, 1978); however, high latitude measurements at VHF frequencies seem to indicate that (2.6) is valid (Ecklund et al., 1977; Cahill et al., 1978). Presumably the Doppler characteristics of high latitude HF backscatter would be similar to those of VHF backscatter.

2.2.3 Nonlinear Theory (2-Dimensional Turbulence)

Due to the discrepancies between observations and linear theory, much effort has been expended in extending the theoretical models to include effects such as particle kinetics, electromagnetic propagation, refraction of the unstable modes and non-linear saturation. Many of these mechanisms have been summarized by Lee et al. (1974) and Farley (1974). Of these, the concept of two-dimensional turbulence as proposed by Sudan et al. (1973) appears to be one of the most successful in explaining many of the observations.

Sudan et al. (1973) argue that the linearly unstable modes will grow to amplitudes of 5%-10% of the background density. At this level the electrostatic fields and density gradients of the unstable modes (these quantities are either parallel or antiparallel with the propagation vector of the linearly unstable wave and 90° out-of-phase with each other) are sufficient to produce large electron drifts in the $\pm \underline{V}_d \times \underline{B}$ directions. The magnitude of these secondary, wave-induced drift velocities may reach

$$V_s = V_d A v_i / \Omega_i \quad (2.9)$$

where A is the fractional amplitude of the primary wave. Sudan et al. (1973) then demonstrate that the expected secondary drift velocities will easily be of the same magnitude as V_d . Hence, once the instability begins to grow the electron drift in the electrojet will change rapidly from laminar flow to two-dimensional turbulence.

The theoretical construct of Sudan et al. (1973) readily explains unstable wave propagation at $\theta = 90^\circ$. Moreover, the turbulence leads to

cascading of the energy into shorter wavelengths thereby causing short wavelength irregularities to be excited where they would not be predicted by linear theory. This theory does not explain why equatorial two-stream irregularities always appear to propagate at the ion acoustic velocity; however, other theoretical work (Rogister, 1971) indicates that this attribute may have as much to do with the nature of the equatorial electrojet as with the instability mechanism.

A number of computer codes have been developed to simulate the 2-dimensional turbulence construct (e.g. McDonald et al., 1974). Although these codes have not been extended to $V_d/C_s > 1$, they have demonstrated the essential validity of the idea. Very recently, Keskinen et al. (1979) have calculated the Doppler velocity spectrum as a function of angle that would be observed from a fully turbulent simulation. They found these spectra to be in very good agreement with type II spectra observed in the equatorial electrojet.

Another recent study has been an attempt by Greenwald (1979) to develop an ad hoc model that might explain the discrepancy between high latitude VHF and UHF spectral observations. He found that the assumptions of two-dimensional turbulence and a scattering cross-section that is dependent on the angle between the radar viewing direction and the local electron drift direction are sufficient to explain many of the results. Specifically, the model showed that the Doppler width of the backscatter spectrum becomes much narrower as a radar is directed more parallel to the electron drift direction, whereas it broadens considerably when a radar is directed transverse to the drift.

3.0 F-REGION IRREGULARITIES

3.1 Observations

As in the case of E-region irregularities, F-region irregularities are commonly observed polewards of 60° geomagnetic latitude. Not only are they observed with ground-based HF radars, typically ionosondes, (see e.g., Baggaley, 1970; Bates and Albee, 1970; Basu et al., 1974; Oksman et al., 1979) but also from spacecraft carrying topside sounders (Hice and Frank, 1966),

Langmuir probes (Dyson, 1969), retarding potential analyzers (McClure and Hanson, 1973), and electrostatic analyzers (Sagalyn et al., 1974). Typical results from the satellite observations as reported by Dyson (1969) and Sagalyn et al. (1974) are shown in Figures 3.1 and 3.2, respectively. It is seen from these figures that the F-region irregularity zone, often called FLIZ, encompasses the auroral oval and is approximately coincident with the high latitude scintillation zone reported by Aarons et al. (1969).

Studies by Whalen and Pike (1973) and Dyson and Winningham (1974) have indicated that bottomside and topside FLIZ are coincident with F-region 6300 Å aurora and < 300 eV precipitating electrons, respectively. Both of these observations support the presently accepted idea that these irregularities are produced by structured precipitating electrons. Measurements by Dyson and Winningham (1974) have also shown that the FLIZ region extends poleward of the < 300 eV precipitation zone indicating that the irregularities, once formed, convect with the ionospheric plasma under the impressed magnetospheric electric field.

It should be stressed that the evidence supporting particle precipitation as the source of F-region irregularity structures is purely correlative. It is possible that some phenomena associated with the presence of < 300 eV electrons -- e.g., a field-aligned current or a temperature gradient -- may play a more significant role in producing the irregularities via a plasma instability. This point will be discussed in greater detail in the discussion of possible mechanisms.

There is some observational evidence that mechanisms other than low energy particle precipitation may be responsible for some types of auroral zone F-region irregularities. In a multi-radar study, Oksman et al. (1979) have observed that one commonly observed type of F-region irregularity lies on the same flux tube as diffuse radar aurora in the underlying E-region. Radar aurora is not characteristically associated with auroral precipitation. Moreover, this type of radar aurora lies in regions of downward field-aligned current (Tsunoda et al., 1976; Greenwald et al., 1980) and latitudinal density gradient (poleward edge of ionospheric trough). Thus certain conditions necessary for some types of F-region plasma instabilities are fulfilled.

Our present knowledge of the Doppler spectral properties of high latitude F-region irregularities is poor, indeed. This situation has arisen

FINE STRUCTURE
 BOUNDARY $Kp \geq 3^+$, $Kp > 3^+$
 EQUATORWARD ● ▲
 POLEWARD ○ ▲

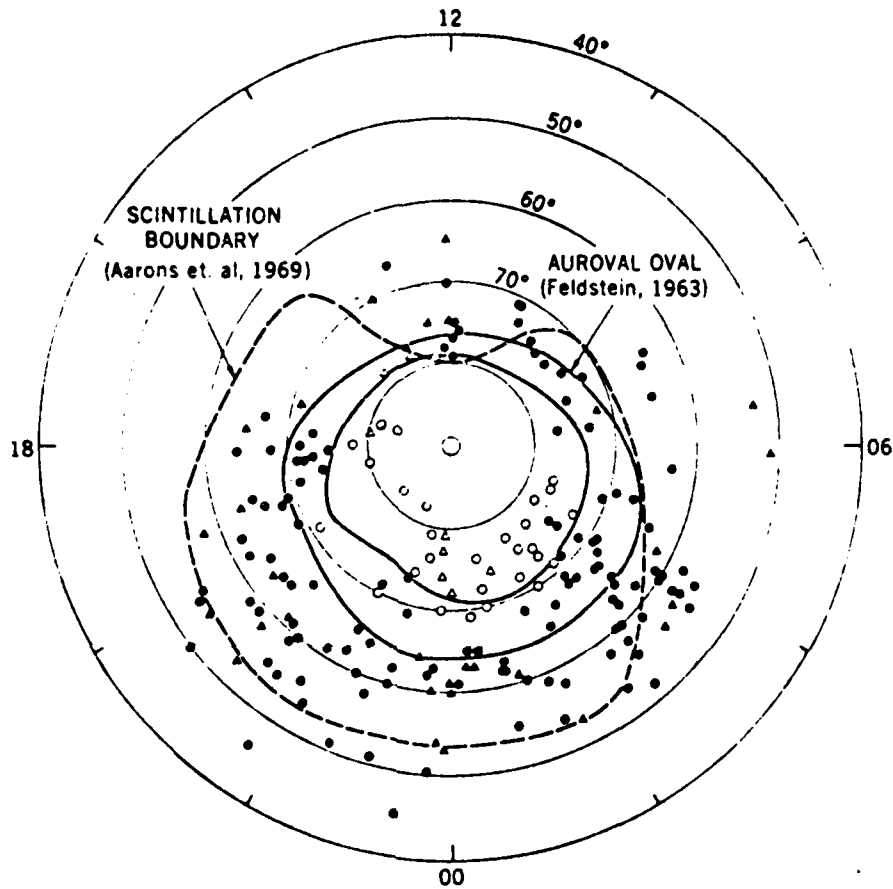
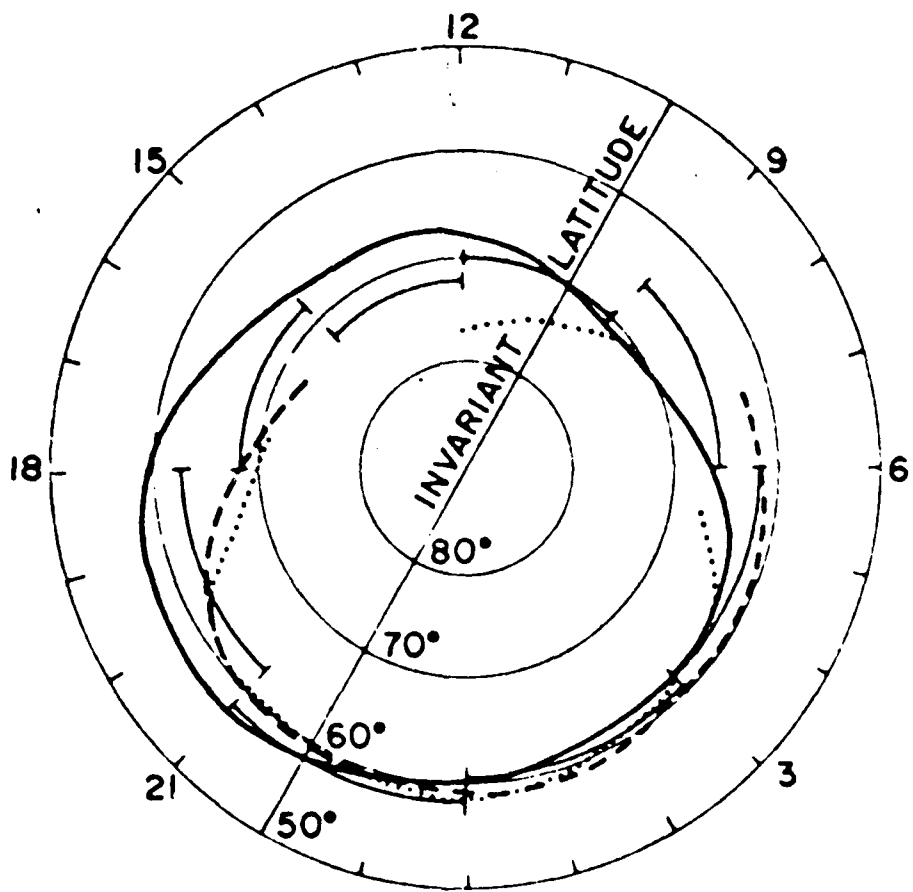


FIGURE 3.1



LOCAL TIME: 0 hrs

- IRREGULARITY BOUNDARY
- SCINTILLATION BOUNDARY
- - - ELECTRON TROUGH
- LANGMUIR PROBE

FIGURE 3.2

because VHF and UHF radars cannot achieve orthogonality to the magnetic field at high latitudes and altitudes, whereas HF radars, which achieve orthogonality through refraction, are typically operated as swept-frequency ionosondes without Doppler capability. Some attempts have been made to study the spectral characteristics of high latitude irregularities. Often these studies have resulted in highly aliased spectra and they have not been reported in the open scientific literature.

It is quite likely that our understanding of the Doppler spectral characteristics of F-region irregularities will improve greatly over the next few years. At the present time there is a need to know these spectral properties in order to improve the operational capabilities of OTH radars. Moreover, a number of new, highly capable, digital HF sounders have recently been developed and it is highly likely that they will be utilized, in part, for F-region irregularity studies.

3.2 Mechanisms for High Latitude F-Region Irregularity Formation

We now consider some of the mechanisms that might be responsible for the formation of high latitude irregularity formation. It will be noted whether the mechanism is more likely to be activated in the topside or bottomside ionosphere.

3.2.1 Production by Precipitating Low Energy Electrons

At wavelengths corresponding to the HF frequency band, direct formation of electron density irregularities would require structure in the precipitating electrons on the order of 10 m. It seems likely that these scale sizes occur in electron precipitation since structure on the order of 100 m or less is commonly seen in association with E-region aurora. Once the irregularities are formed they begin to decay through diffusion and recombination. The relatively high diffusion rate along the magnetic field as well as the field-alignment of the precipitating electrons would rapidly lead to field-aligned irregularities, whereas the very low F-region cross field diffusion rate and recombination rate would insure the existence of the irregularities for an extended period of time.

Irregularities formed in this manner are similar to density enhancements associated with barium releases. They, as the barium clouds, drift with the F-region plasma in an $E \times B$ fashion. A radar measuring the Doppler velocity of these irregularities would observe a component of this plasma drift as given by (1.1). Any spread in the Doppler spectrum would most likely result from structure in the magnetospheric electric field mapped into the field of view of the radar. These structures could be formed in both the bottomside and topside ionospheres. The decay rate would be greater on the bottomside due to the higher neutral densities.

3.2.2 F-Region $E \times B$ Instability (e.g., Reid, 1967)

This instability occurs where the ambient F-region plasma velocity is parallel to an electron density gradient. The ionospheric electric field causes a weak ion-Pederson drift parallel to an equidensity contour. Any perturbation of this contour will lead to the accumulation of polarization charges that will cause the perturbation to grow. The linearly unstable modes are directed transverse to the plasma flow direction and are virtually motionless. Backscatter from irregularities produced by the linear state of this instability would exhibit very low Doppler shifts. The instability would grow in both the bottomside and topside F-region.

3.2.3 Current Convective Instability (Ossakow and Chaturvedi, 1979)

The current convective instability is a more complicated form of the F-region $E \times B$ instability. In this case, a field-aligned current is also assumed. Normally, the $E \times B$ instability would be stable if the F-region plasma drift were directed antiparallel to any ambient density gradient. However, a field-aligned current will destabilize this configuration if $|\underline{k} \cdot \underline{V}_{\parallel}| > |\underline{k} \cdot (c\mathbf{E}_0/B_0)(v_1/\Omega_1)|$, where V_{\parallel} is the field-aligned, relative electron-ion drift velocity. Again, any perturbation of an equidensity contour will lead to the buildup of polarization charges and the onset of the instability. In the linear state, the current convective instability, as the $E \times B$ instability, will propagate with very low phase velocity. The

instability does not propagate exactly perpendicular to the magnetic field; however, the deviation from orthogonality is so small as to be virtually negligible.

Chaturvedi and Ossakow (1979) and Keskinen et al. (1980) have examined the non-linear state of the current convective instability. They found that when the linearly unstable modes reach amplitudes of several percent, the plasma becomes two-dimensionally unstable in the plane perpendicular to the magnetic field. These irregularities are embedded in the F-region plasma and, hence, have a net flow determined by (1.2).

Studies on the current convective instability have indicated that it can grow in both the bottomside and topside F-regions.

3.2.4 Ion Acoustic Instability (Kindel and Kennel, 1971)

Ion acoustic waves propagating parallel to the magnetic field are produced by one of two classes of instabilities described by Kindel and Kennel (1971). This instability is produced by the relative electron-ion drift velocity exceeding a value that is critically dependent on the ratio of T_e/T_i . For $T_e/T_i = 1$, the critical drift velocity is of the order of the electron thermal velocity, whereas for $T_e/T_i = 10$ the critical velocity is approximately four times the ion thermal velocity. In both cases, the marginally unstable waves have a phase velocity of the order of the ion thermal speed and a wavelength of the order of the Debye length. The latter quantity would be a few centimeters in the topside F-region. These waves have not been identified using ground-based radars.

3.2.5 Electrostatic Ion Cyclotron Waves (Kindel and Kennel, 1971)

Electrostatic ion cyclotron waves are relatively long wavelength waves that propagate nearly perpendicular to the magnetic field. They have characteristic frequencies at harmonics of the ion cyclotron frequency modified somewhat by the thermal speeds of the charge species. In a plasma where the electron and ion temperatures are approximately equal, these waves become unstable if the relative electron-ion drift velocity parallel to the magnetic field exceeds thirteen times the ion thermal speed. As for the ion

acoustic instability, these waves may only be unstable in the topside ionosphere, typically above 1000 km. The dispersion relations indicate that larger drift velocities are required to excite the harmonics of the ion gyrofrequency than are required for the fundamental. Also, heavier ion species are more susceptible to the instability than lighter ions.

The waves do not propagate exactly perpendicular to the magnetic field. For $T_e/T_i = 0$ the most unstable mode has $k_{\perp}/k \approx 10$, yielding an off-perpendicular angle of 6° . This mode would have a characteristic wavelength of approximately 3 m. Reed (1979) has reported the possible detection of these waves with a 50 MHz ground-based radar.

3.2.6 Temperature Gradient Instability (Hudson and Kelley, 1976)

Another proposed instability involving gradients is the temperature gradient instability. In this case, there must be a gradient in the electron temperature that is antiparallel to an ambient electron density gradient. Such a geometry might exist in the ionospheric projection of the plasmopause at altitudes above 400 km. Here the density gradient would correspond to the equatorward wall of the mid-latitude ionospheric trough and the thermal gradient would result from heating by plasma turbulence near the plasmopause. Hudson and Kelley (1976) have discussed the possible association of this phenomena with mid-latitude stable red (SAR) arcs. Although this instability will produce predominantly long wavelength irregularities (several hundred meters) of very low frequency, the irregular structures, once formed, may serve to destabilize other shorter wavelength, higher frequency modes.

3.3 Expected Doppler Spectral Characteristics

Due to the scarcity of Doppler spectral data from high latitude F-region irregularities we can only speculate as to its characteristics. Clearly there are many possible mechanisms for irregularity excitation. Moreover, many of these modes may feed on one another, i.e., the density gradients and electric fields produced by one unstable mode may help to excite another mechanism. This type of behavior has been observed to occur in the equatorial F-region (see, e.g., Fejer and Kelley, 1980). Given the presence

of multiple modes, the superposition of different characteristic frequencies will tend to produce broadened "turbulent" spectra. If any underlying characteristic velocity remains it will be that of the F-region plasma given by (1.2).

The width of the Doppler spectra will most likely be determined by the different characteristic velocities of the irregularities within the radar field-of-view and by structure in the ambient electric field. Measurements with OTH radars have shown that this Doppler spread is often greater than 400 m/s. As an upper bound one might assume that the Doppler spread approaches that of E-region irregularities (≈ 1200 m/s).

4.0 DOPPLER SPECTRUM MODELING

4.1 Theoretical Foundation

The previous two sections have presented theoretical and experimental evidence that high latitude E-region irregularities drift with the electron gas while F-region irregularities drift with the plasma. Both of these motions are collisionless convective drifts given by (1.2). Thus, knowledge of the electrostatic potential function over the high latitude ionosphere will enable one to determine the convective drift velocity at any point. Moreover, given the propagation direction of a radar signal located at any point, one can predict the Doppler velocity that would be observed.

The preceding discussion may be formalized as follows. Let \hat{n} be a unit vector in the direction of the radar propagation vector \underline{k} . Then, the Doppler velocity \underline{V} of irregularities moving with the plasma will be

$$\underline{V} = \hat{n} \cdot \underline{V}_d = \hat{n} \cdot \underline{E} \times \underline{B} / B^2 \quad (4.1)$$

$$= \hat{n} \times \underline{\nabla} \phi(\theta, \varphi) B / B^2 \quad (4.2)$$

$\phi(\theta, \varphi)$ is the electrostatic potential distribution assumed to be only a function of the co-latitude, θ , and the azimuth angle, φ . The azimuth angle increases in a positive sense toward the east.

Since \tilde{B} is well defined by accurate magnetic field models, the only unknown quantity in (4.2) is $\phi(\theta, \varphi)$. Unfortunately, present knowledge of the instantaneous global potential distribution north of 60° latitude is still quite limited. Two reasons for this condition are the difficulty and cost involved in developing a globally-distributed array of E-field monitors.

Theoretical studies of the high-latitude potential distribution were begun by Axford and Hines (1961) and have been extended by many others. Notable among these are the empirical models developed by Heppner (1977) on the basis of data from the Ogo 6 satellite and static and dynamic computer models developed by the Rice University Group under Wolf.

In this report, we consider the Doppler characteristics resulting from a potential function given by

$$\phi(\theta, \varphi) = -\phi_0 \sin\varphi / \theta_m, \quad \theta < \theta_m \quad (4.3)$$

$$\phi(\theta, \varphi) = -\phi_0 \exp\{-\alpha(\theta - \theta_m)^2\} \sin\varphi, \quad \theta > \theta_m \quad (4.4)$$

where $\theta_m(\varphi) = \theta_1 - \beta \cos \varphi$ and ϕ_0 is one-half of the cross-polar-cap potential drop. The assumed potential distribution is similar to distributions obtained by Axford and Hines (1961) and by Heppner (1977, Model A) among others. It yields a nearly uniform dawn-dusk electric field across the polar cap and predominantly northward and southward electric fields in the dusk and dawn sectors of the northern hemisphere auroral zone, respectively. The quantity $\theta_m(\varphi)$ is the co-latitude at which the magnitude of the electrostatic potential maximizes for each φ , $\alpha^{-1/2}$ is the arc over which the auroral zone potential decreases by e^{-1} , θ_1 is the average co-latitude of the potential maximum and β is the angle over which the entire pattern is shifted in an antisunward direction. The last quantity causes the convection pattern to move to higher latitudes on the dayside and lower latitudes at night in a manner similar to the displacement of the auroral oval. Figure 4.1 displays the potential contours associated with the assumed pattern.

The electric fields associated with the assumed $\phi(\theta, \varphi)$ are for $\theta < \theta_m$:

$$E_{\theta} = -\frac{1}{R_0} \frac{\partial \Phi(\theta, \varphi)}{\partial \theta} = \phi_0 \sin \varphi / R_0 \theta_m \quad (4.5)$$

$$E_{\varphi} = -\frac{1}{R_0 \sin \theta} \frac{\partial \Phi(\theta, \varphi)}{\partial \varphi} = \frac{\phi_0}{R_0 \sin \theta} (\theta \cos \varphi / \theta_m - \beta \theta \sin^2 \varphi / \theta_m^2) \quad (4.6)$$

and for $\theta > \theta_m$:

$$E_{\theta} = -2\alpha(\theta - \theta_m) \phi_0 \exp\{-\alpha(\theta - \theta_m)^2\} \sin \varphi / R_0 \quad (4.7)$$

$$E_{\varphi} = \phi_0 \exp\{-\alpha(\theta - \theta_m)^2\} \{\cos \varphi + 2\alpha\beta(\theta - \theta_m) \sin^2 \varphi\} / R_0 \sin \theta \quad (4.8)$$

where $R_0 = 6.377 \times 10^6 \text{ m}$ is the radius of the Earth.

Finally, the Doppler velocity as a function of local time that is observed at any given co-latitude (θ_0) and viewing direction (φ) relative to geomagnetic north is given by

$$V(t) = (\sin \gamma E_{\theta}(\theta_0, t) - \cos \gamma E_{\varphi}(\theta_0, t)) / B_0 \quad (4.9)$$

where the local time $t = (\varphi + 180)/15$. In (4.9), E_{θ} and E_{φ} are positive in the northward and eastward directions, respectively.

The Doppler width of signals scattered from ionospheric irregularities has been modeled from the work of Greenwald (1979). In that work, Greenwald presented curves of the Doppler width variation with viewing direction relative to the electron drift direction. Approximating these curves with the function

$$f(\delta) = \exp\{-\eta(V/V_d)^2\} \quad (4.10)$$

where $\delta = \cos^{-1}(V/V_d)$ and $\eta = 2$, one obtains an expected Doppler width given by

$$\Delta V = V_d f(\delta) \quad (4.11)$$

Although this result only applies to E-region irregularities, in the absence of knowledge to the contrary we will assume that it is also valid for F-region irregularities.

4.2 Results

Several typical examples of the Doppler characteristics associated with irregularities produced in the potential distribution given by Figure 4.1, are shown in Figures 4.2-4.4. For these results it has been assumed that the cross-polar-cap potential drop is 50 kV, $\alpha^{-1/2} = 5^\circ$, $\theta_1 = 20^\circ$, and $\beta = 50^\circ$. Higher cross-polar-cap potential drops would yield proportionately higher values for both the Doppler velocity and Doppler width.

In Figure 4.2, the measurement latitude is 60° and the viewing direction is also 60° . This configuration is similar to that which one might have from a facility in the northeastern U. S. Such a radar would observe receding Doppler velocities in excess of 250 m/s in the early morning hours (02-04 local time) and approaching Doppler velocities of the same magnitude in the late evening (20-22 local time). The associated Doppler widths are typically less than 100 m/s. Since the Doppler velocities and widths are both quite low, it is likely that instabilities such as the E-region streaming instabilities will only be excited near 0300 and 2100 local time.

Figure 4.3 represents a configuration in which the measurement latitude is 65° and the viewing angle is 30° . This is another example of parameters that might be utilized in the northeastern U. S. Here the morning Doppler velocity maximizes between 0400 and 0700 local time with a receding velocity approaching 500 m/s and the evening maximum occurs near 2000 local time with an approaching velocity of 250 m/s. The Doppler width in the morning reaches 300 m/s, whereas in the evening it is in excess of 600 m/s. Near midnight, if the instabilities are excited, they will exhibit narrow, approaching Doppler spectra. The only time that E-region instabilities definitely will not be excited is near local noon. It is to be noted that these Doppler characteristics compare favorably with observations.

Another example that compares favorably with observation is shown in Figure 4.4. Here the measurement latitude is 65° and the viewing angle is 0° . Except for a few hours about local noon, E-region irregularities might be

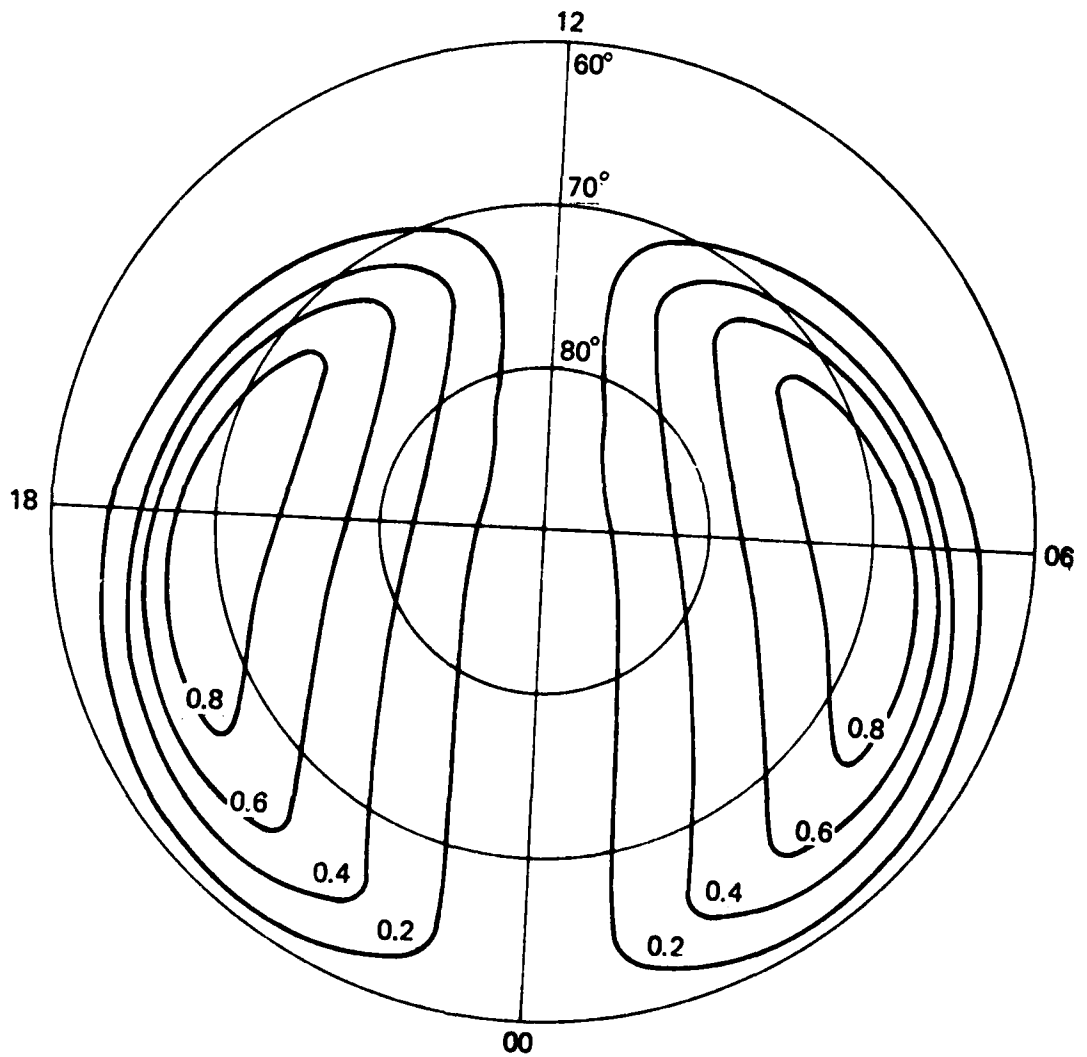
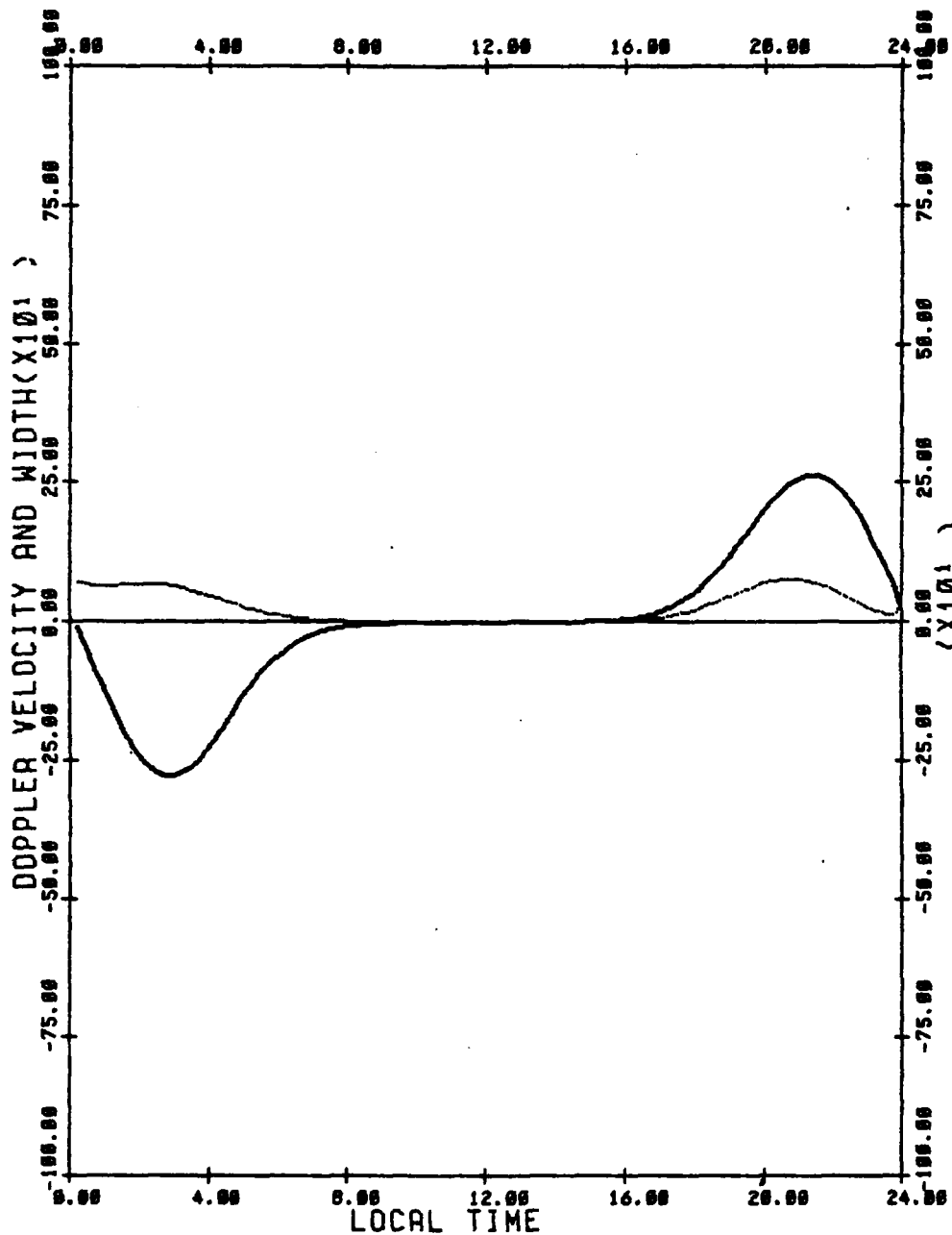
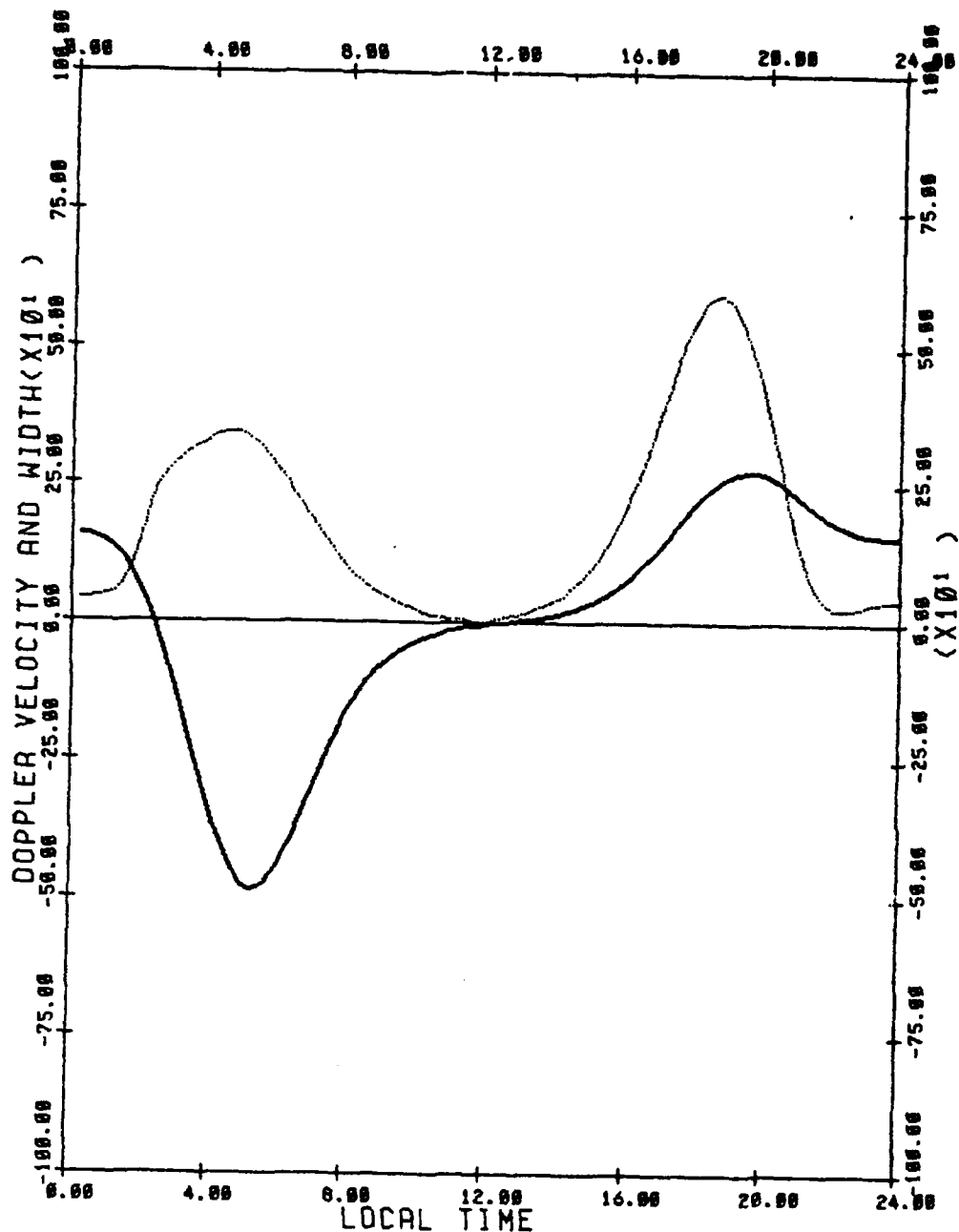


FIGURE 4.1



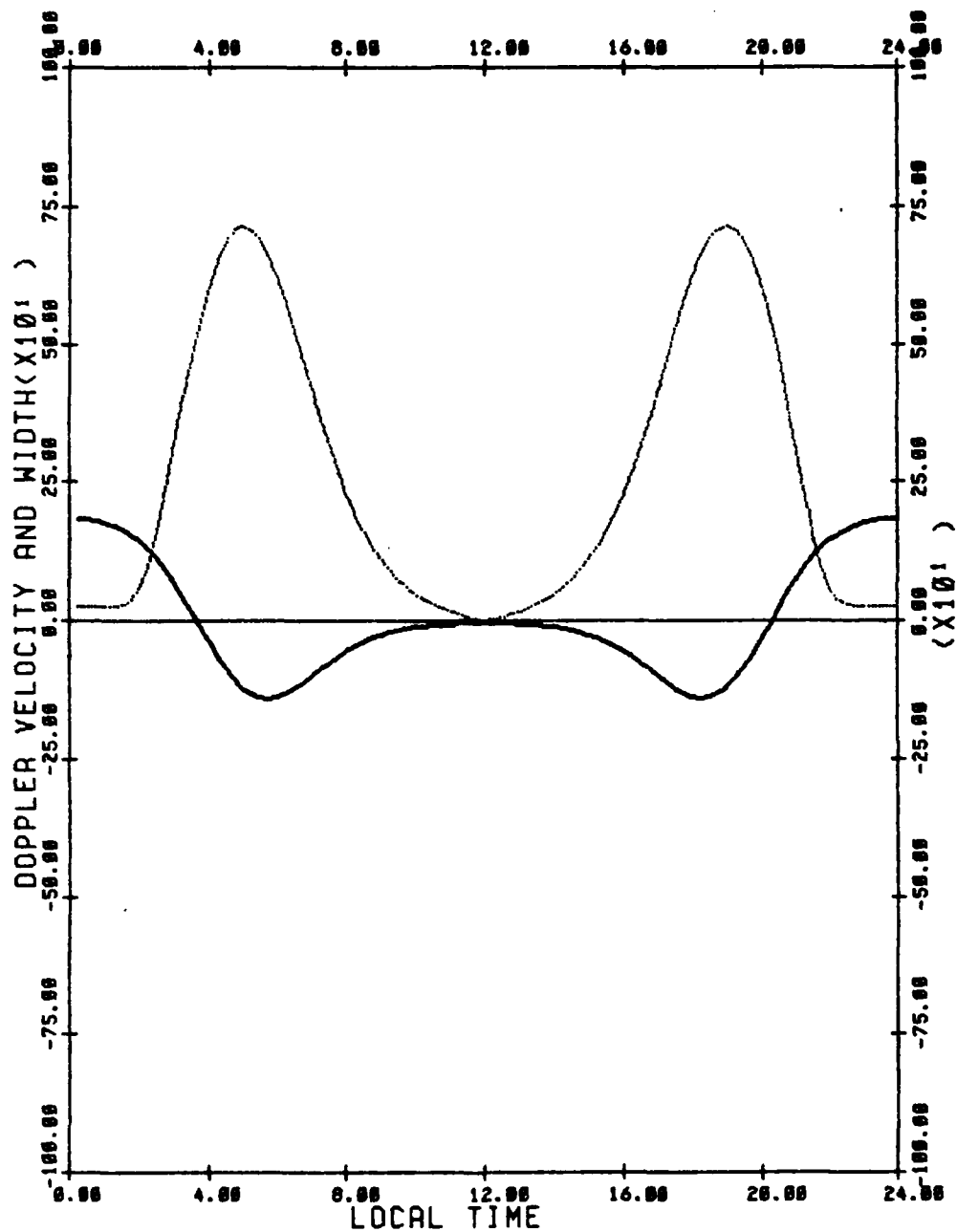
DOPPLER VELOCITY ———
 DOPPLER WIDTH - - - -
 CROSS POLAR CAP POTENTIAL DROP(V) = 50000
 E-FOLDING DISTANCE OF ARDAL E-FIELD(DEGREES) = 5
 LATITUDE OF POTENTIAL MAXIMUM(DEGREES) = 70
 OVAL OFFSET(DEGREES) = 5
 MEASUREMENT LATITUDE = 60
 VIEWING ANGLE = 60

FIGURE 4.2



DOPPLER VELOCITY —————
 DOPPLER WIDTH - - - - -
 CROSS POLAR CAP POTENTIAL DROP(V) = 50000
 E-FOLDING DISTANCE OF ARORAL E-FIELD(DEGREES) = 5
 LATITUDE OF POTENTIAL MAXIMUM(DEGREES) = 70
 OVAL OFFSET(DEGREES) = 5
 MEASUREMENT LATITUDE = 65
 VIEWING ANGLE = 30

FIGURE 4.3



DOPPLER VELOCITY ———
 DOPPLER WIDTH - - - - -
 CROSS POLAR CAP POTENTIAL DROP(V) = 50000
 E-FOLDING DISTANCE OF ARORAL E-FIELD(DEGREES) = 5
 LATITUDE OF POTENTIAL MAXIMUM(DEGREES) = 70
 OVAL OFFSET(DEGREES) = 5
 MEASUREMENT LATITUDE = 65
 VIEWING ANGLE = 0

FIGURE 4.4

observed over most of the day. At dawn and dusk, the Doppler width is significantly greater than the Doppler shift reaching values of nearly 750 m/s. Near midnight, if the instabilities are excited, they will exhibit narrow Doppler spectra with shifts in excess of 200 m/s.

Figure 4.4 may be compared directly with the observations of Haldoupis and Sofko (1976) shown in Figure 4.5. Their observations were made with a bistatic CW radar directed approximately 4° west of geomagnetic north. One can see that near midnight, they observed approaching irregularities for which the spectra were relatively narrow with mean Doppler shifts of 100 Hz (360 m/s). Several hours after midnight the irregularities were receding at approximately 100 m/s and had a Doppler velocity spread of several hundred meters per second. The observed behavior is in generally good agreement with the model. Although the magnitudes of the Doppler shifts and widths are not in precise agreement, the character and general time variability agree quite well.

Appendix A exhibits local time plots of the predicted Doppler velocity and Doppler width for three different latitudes of the average potential maximum (65° , 70° , 75°), three different viewing latitudes (55° , 60° , 65°) and five different viewing angles (-60° , -30° , 0° , 30° , 60°). The cases of the average potential maximum at 65° , 70° , and 75° may be associated with disturbed, normal, and quiet conditions, respectively. For quiet conditions, one would only expect to observe E-region backscatter at latitudes in excess of 65° , whereas for disturbed cases, one might observe irregularities to latitudes of 55° geomagnetic.

Appendix B exhibits local time plots of the Doppler velocity and width for the potential distribution shown in Figure 4.6. This distribution which concentrates the potential variation in the vicinity of the auroral oval leads to differing Doppler characteristics when the viewing latitude is in excess of the latitude at which the magnitude of the potential maximizes.

4.3 Discussion

The Doppler plots in Appendices A and B indicate the variety of spectral characteristics that one may observe in association with ionospheric irregularities in the course of a day. If these measurements were made with a

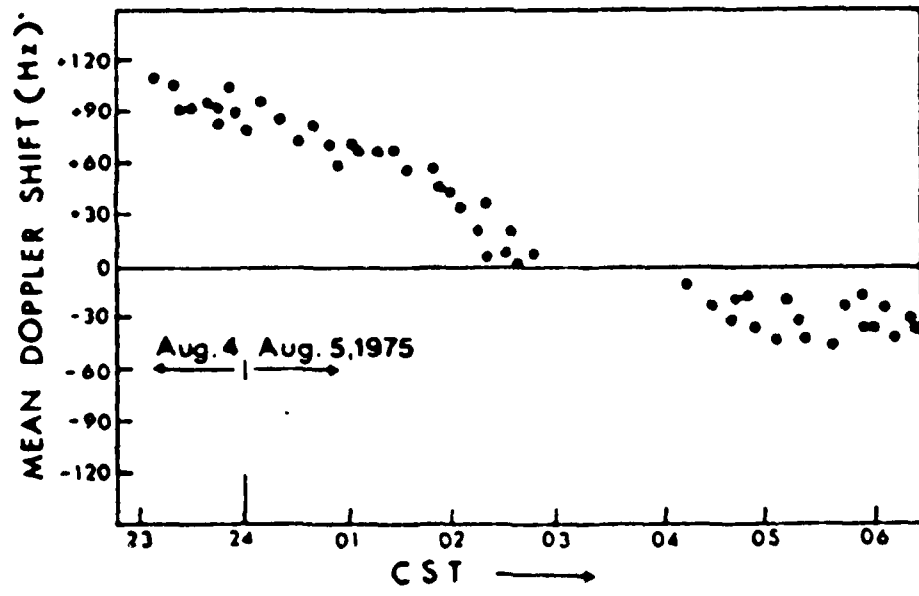
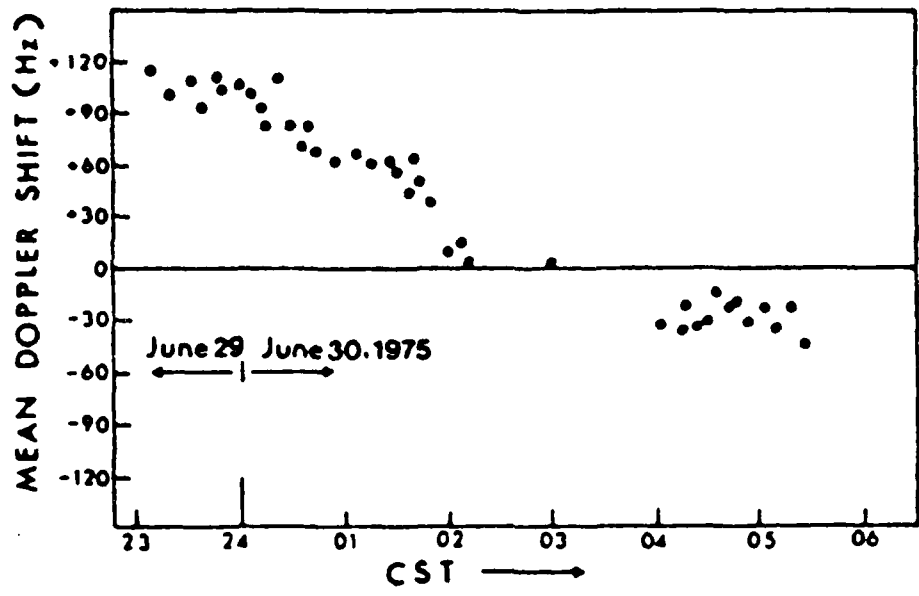


FIGURE 4.5

radar operating at 10 MHz, then, at times, the frequency shifts and widths of the backscatter spectra would exceed 50 Hz. Even larger values are to be expected if the cross-polar-cap potential exceeds 50,000 V, as is often the case, or if the gradients in the potential are steeper than those in the assumed model.

The Doppler plots are only estimates of Doppler characteristics that might be observed at any given time. Not only is it likely that the instantaneous potential distribution is more complicated than either Figures 4.1 or 4.6, but this pattern may change on an hourly time scale. In addition, the cross-polar-cap potential may change by factors approaching two on hourly time scales. In order to improve the predictability of the model, research is necessary that will yield additional information on 1) the instantaneous structure of the high latitude potential distribution, 2) the variability of this pattern during periods of magnetic disturbance, and 3) the variability of the cross-polar-cap potential and techniques to monitor this quantity.

Knowledge of the probable Doppler characteristics is of some aid in determining periods when an OTH radar might be severely disturbed by clutter from ionospheric irregularities. For example, given that the radar is utilized for the detection of incoming aircraft, it would be most affected by irregularity spectra with positive Doppler displacements. A radar directed toward the northeast would observe such irregularity spectra during the afternoon and evening hours. During the post-midnight hours the irregularities would be receding and, hence, less of a source of clutter.

Fortunately, separation of the dominant frequency components in target and irregularity spectra is only one method to reduce or eliminate the problem of irregularity clutter. An alternative approach involves the utilization of the different decorrelation times of backscattered signals from targets (aircraft) and clutter. To our knowledge this approach has not been utilized in OTH radars. It will be discussed in the next section.

5.0 REMOVAL OF SPREAD SPECTRA

If one compares the Doppler spread of spectra from ionospheric irregularities and aircraft, one notes an important difference. The Doppler widths of irregularity spectra typically range from 50-750 m/s in the regions

where instabilities are excited. A typical width is likely to be 300 m/s which, at a radar frequency of 10 MHz, corresponds to a frequency spread of 20 Hz. In contrast, backscatter spectra from aircraft are much narrower. The dominant contribution to their broadening is most likely the fluctuations in the propagation path of the radar signal. Measurements with ionosondes indicate that the broadening due to these fluctuations is typically less than 1 Hz.

Let us now consider the complex demodulated signal at the output of a radar receiver. The transmitted signal may have been pulsed, phase-encoded, or frequency encoded and the backscattered signal is assumed to have been treated with the appropriate matched filter. Thus the decoded signal corresponding to range R will be assumed to have a frequency spectrum given by

$$S(R, \omega) = A_1 \exp\{-(\omega - \omega_1)^2 / 2\sigma_1^2\} + A_2 \exp\{-(\omega - \omega_2)^2 / 2\sigma_2^2\} \quad (5.1)$$

Here, the noise is assumed to be white and has zero decorrelation time. A_1 and A_2 represent the fractional amplitudes of the signals due to ionospheric clutter and target backscatter respectively. The quantities ω_1 and ω_2 are the Doppler shifts of these signals and σ_1 and σ_2 are their respective spectral half widths. In general, we will assume $A_1 \gtrsim A_2$, $\sigma_1 \gg \sigma_2$, and allow ω_1 and ω_2 to be arbitrary. The Doppler shifts may even have the same value.

The autocorrelation function associated with $S(R, \omega)$ is given by

$$\rho(R, \tau) = \frac{1}{2\pi} \int_{-\infty}^{\infty} S(R, \omega) e^{i\omega\tau} d\omega \quad (5.2)$$

$$= \frac{1}{2\pi} (A_1 e^{i\omega_1\tau} e^{-\sigma_1^2 \tau^2 / 2} + A_2 e^{i\omega_2\tau} e^{-\sigma_2^2 \tau^2 / 2}) \quad (5.3)$$

$\rho(R, \tau)$ may also be written as

$$\rho(R, \tau) = \int_{-\infty}^{\infty} x(t) x^*(t + \tau) dt$$

where $X(t)$ is the complex demodulated signal associated with range R at the output of the receiver.

In order to illustrate a typical case we present in Figures 5.1-5.3 the spectrum and autocorrelation functions for the parameters $\sigma_1/\pi = 10 \text{ Hz}$, $\sigma_2/\pi = 1 \text{ Hz}$, $\omega_1/2\pi = 10 \text{ Hz}$, $\omega_2/2\pi = 5 \text{ Hz}$, $A_1 = 0.99$ and $A_2 = 0.01$. In this example, the integrated spectral power due to the irregularities is approximately 20 dB greater than that due to the target. Nevertheless for $\tau \gtrsim \pi/\sigma_1$, the autocorrelation function is due predominantly to the target signal even though it originally was the minor spectral component.

Given $\rho(R, \tau)$, one can recover the spectrum (R, ω) via the inverse Fourier transform,

$$S(R, \omega) = \int_{-\infty}^{\infty} \rho(R, \tau) e^{-i\omega\tau} d\tau \quad (5.4)$$

Now let us consider the spectrum $S'(R, \omega)$ due to a limited portion of the autocorrelation function

$$S'(R, \omega) = \int_{T-\Delta T}^{T+\Delta T} \rho(R, \tau) e^{-i\omega\tau} d\tau \quad (5.5)$$

Using (5.3) and reversing the order of integration, $S'(R, \omega)$ may be rewritten as

$$S'(R, \omega) = \int_{-\infty}^{\infty} dt \int_{T-\Delta T}^{T+\Delta T} X(t) X^*(t+\tau) e^{-i\omega\tau} d\tau \quad (5.6)$$

If we define

$$X^*(t + \tau) = \frac{1}{2\pi} \int B^*(\omega'') e^{i\omega''(t+\tau)} d\omega'' \quad (5.7)$$

and substitute this expression into (5.6), we can perform the integration over τ yielding

$$\begin{aligned} \frac{1}{2\pi} \int_{T-\Delta T}^{T+\Delta T} e^{i(\omega''-\omega)\tau} d\tau &= \frac{1}{\pi} \frac{e^{i(\omega''-\omega)T} \sin(\omega''-\omega)\Delta T}{(\omega''-\omega)} \\ &= \frac{1}{\Delta T} \int_{-\infty}^{\infty} e^{i(\omega''-\omega)T} \delta(\omega''-\omega) \end{aligned} \quad (5.8)$$

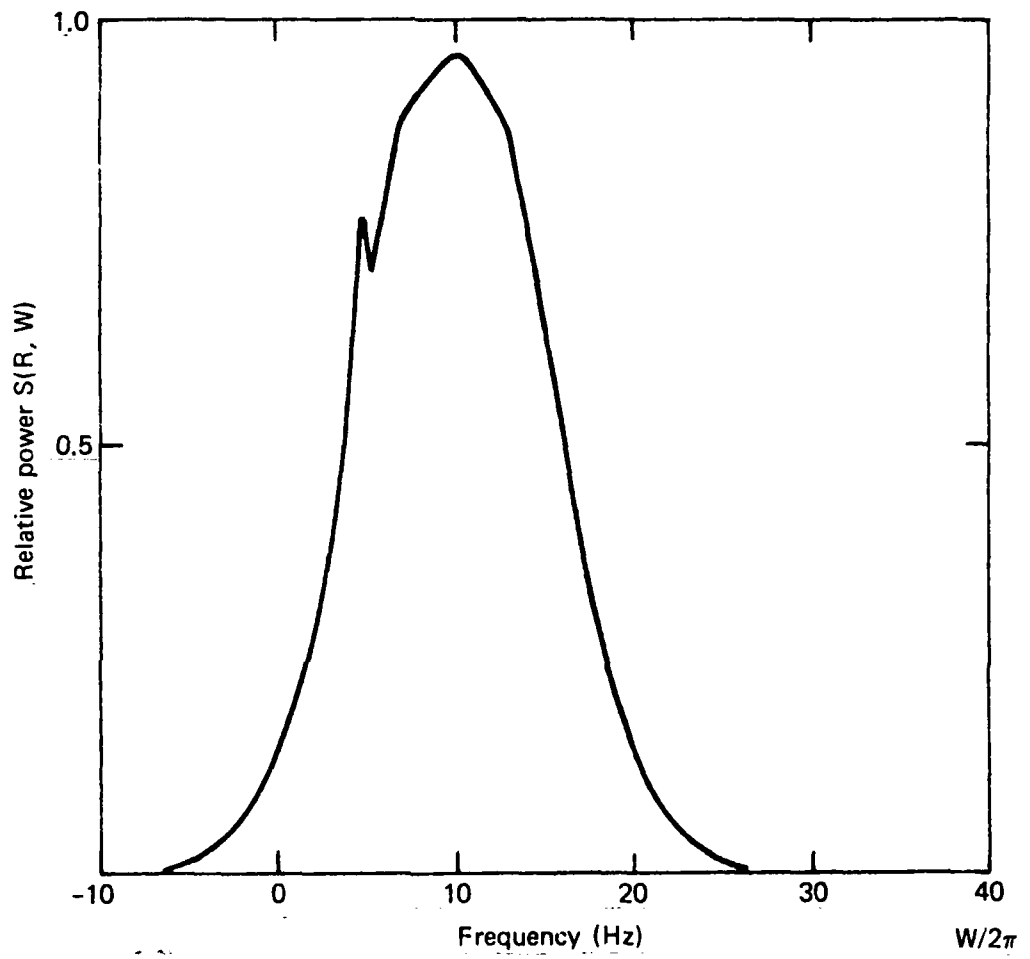


FIGURE 5.1

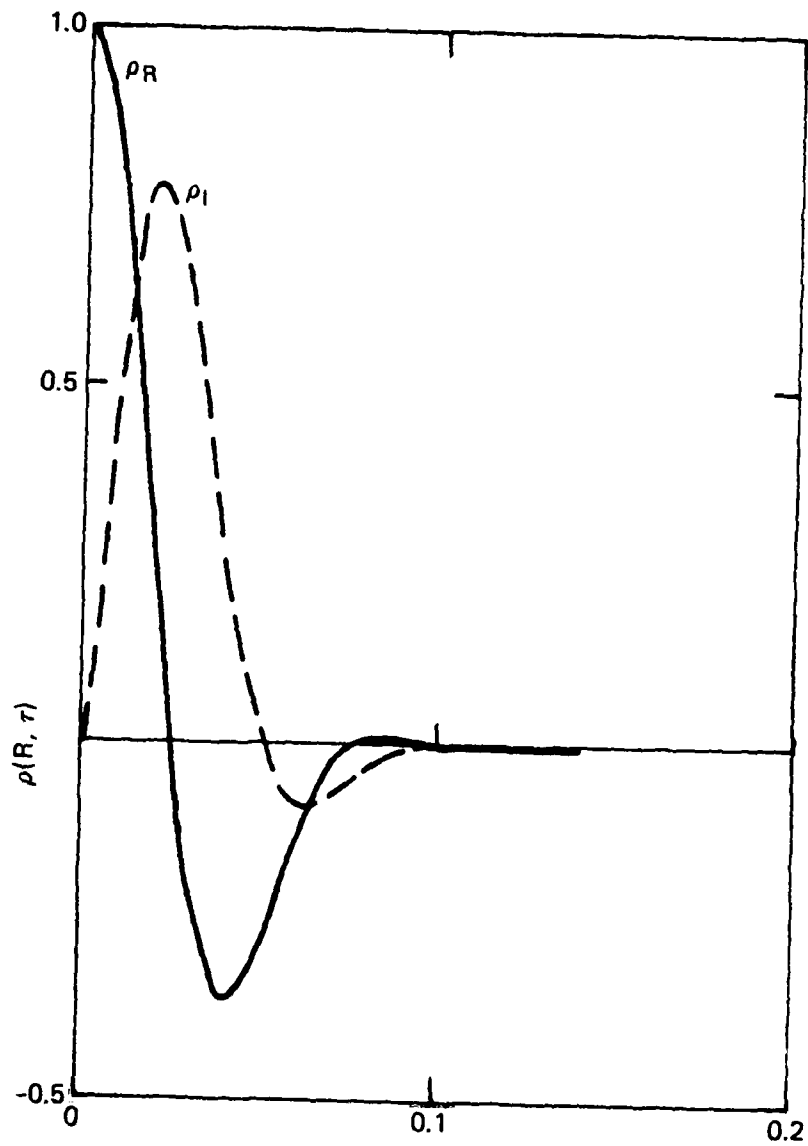


FIGURE 5.2

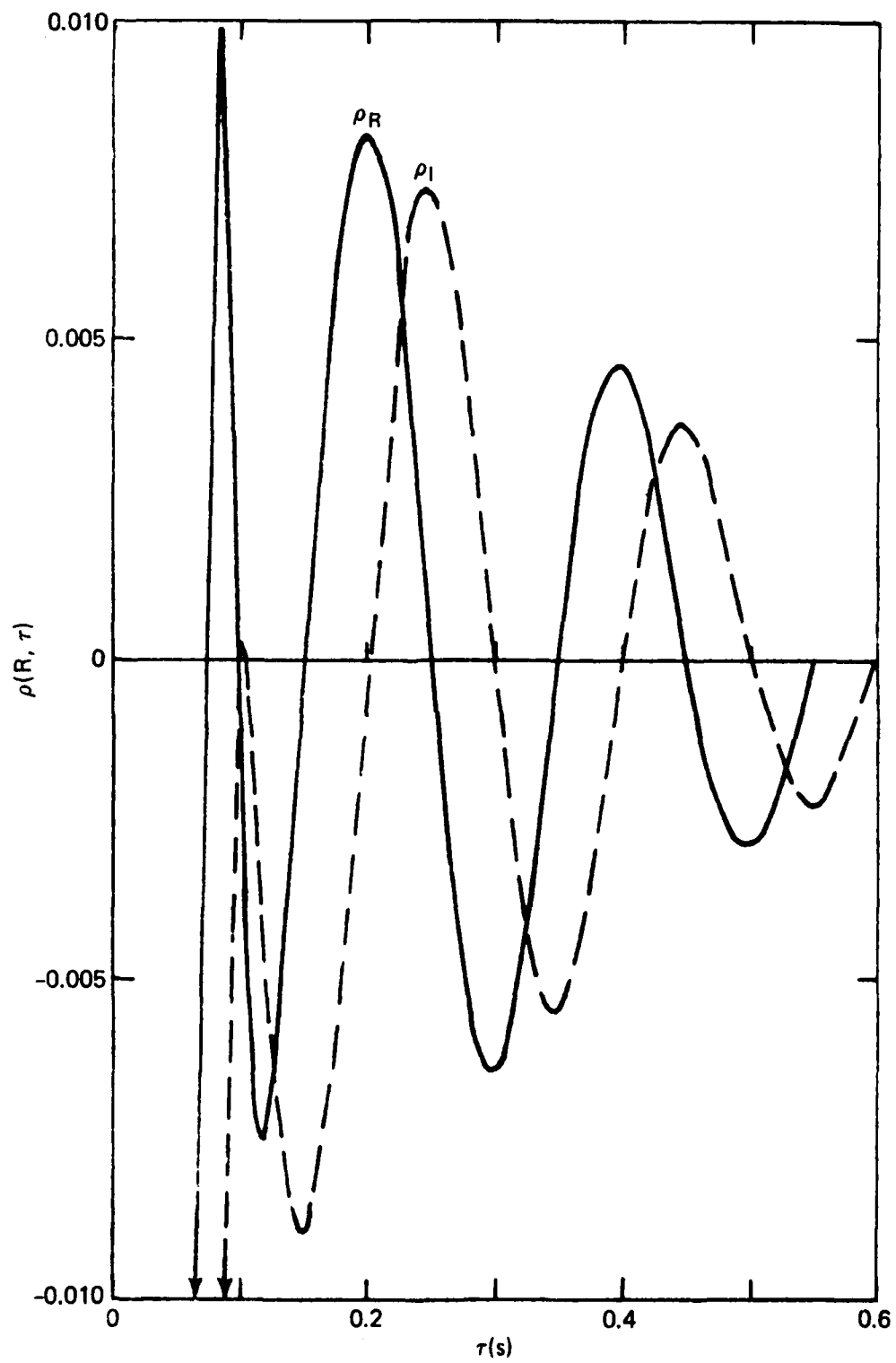


FIGURE 5.3

Performing the remaining integrations, one obtains

$$\begin{aligned} S'(R, \omega) &= \int dt e^{-i\omega T} X(t) \int d\omega'' B^*(\omega'') e^{i\omega''(t+T)} \delta(\omega'' - \omega) \\ &= B^*(\omega) \int dt e^{i\omega t} X(t) \\ &= A(\omega) B^*(\omega) \end{aligned} \quad (5.9)$$

Thus the power spectrum associated with a limited portion of the autocorrelation function may be viewed as the cross spectrum of the Fourier components associated with two time-lagged data sets.

The preceding result may be expressed explicitly in terms of discretely-sampled data. Let:

$$A(n, \mu) = \frac{1}{N} \sum_{j=0}^{N-1} X(j, \mu) W(j) \exp(-2\pi i j n / N) \quad (5.10)$$

$$B(n, \mu) = \frac{1}{N} \sum_{j=0}^{N-1} X(j+C, \mu) W(j) \exp(-2\pi i j n / N) \quad (5.11)$$

where $X(j, \mu)$ is the complex demodulated output of the receiver, $W(j)$ is a data window (Blackman and Tukey, 1959), and $A(n, \mu)$ and $B(n, \mu)$ are the Fourier coefficients associated with the μ th windowed data sets. Assuming that the receiver output is sampled at a rate equal to $1/f_s$, each data set to be transformed is obtained over a time

$$\Delta T = N/2f_s \quad (5.12)$$

and the lag between data sets used in the cross spectral determination is

$$T = C/f_s \quad (5.13)$$

The cross spectral estimator is then given by

$$\hat{P}_{xx_c}(n) = \sum_{\mu=1}^M A(n, \mu) B^*(n, \mu) \quad (5.14)$$

Note that this quantity is quite different from the power spectrum at the receiver output which would be given by

$$\hat{P}_{xx}(n) = \sum_{\mu=1}^M A(n,\mu)A^*(n,\mu) \quad (5.15)$$

and it can be easily shown (e.g. Calvert et al., 1971) that under relatively modest restrictions both of these quantities are unbiased estimators of $S'(R,\omega)$ and $S(R,\omega)$, respectively.

Since the receiver output may be thought of as a Gaussian random variable, the spectral estimators will be statistically scattered about $S'(R,\omega)$ and $S(R,\omega)$. The degree of scatter may be defined in terms of the standard deviation of an M spectra average. Calvert et al. (1971) have shown that this quantity may be approximated by

$$\sigma(n,M) \approx S(R,\omega_n)/\sqrt{M} \quad (5.16)$$

In cases where the ionospheric clutter signal within the desired frequency band is 10 dB stronger than the target signal, 100 spectra must be averaged in order to reduce the statistical uncertainty in the cross spectral estimator to a point where the target signal can be identified. If the clutter signal is also spread over 10-20 times the bandwidth of the target signal, the signal-to-noise improvement afforded by the proposed technique would be 20-23 dB.

Substitution of (5.2) into (5.5) yields a theoretically predicted cross spectrum given by

$$\begin{aligned}
 S'(R, \omega) = & \frac{1}{2\sqrt{2\pi}} [A_1 \exp\{-(\omega-\omega_1)^2/2\sigma_1^2\} \\
 & \{ \text{Erf}(\sigma_1(T+\Delta T)/\sqrt{2} - i(\omega-\omega_1)/\sqrt{2}\sigma_1) - \\
 & \text{Erf}(\sigma_1(T-\Delta T)/\sqrt{2} - i(\omega-\omega_1)/\sqrt{2}\sigma_1) \} \\
 & + A_2 \exp\{-(\omega-\omega_2)^2/2\sigma_2^2\}^2 \\
 & \{ \text{Erf}(\sigma_2(T+\Delta T)/\sqrt{2} - i(\omega-\omega_2)/\sqrt{2}\sigma_2) - \\
 & \text{Erf}(\sigma_2(T-\Delta T)/\sqrt{2} - i(\omega-\omega_2)/\sqrt{2}\sigma_2) \}] \quad (5.17)
 \end{aligned}$$

where Erf is the error function of complex argument.

Instead of evaluating (5.17) we have chosen to obtain $S'(R, \omega)$ by transforming (5.5) with the Fast Fourier Transform. To accomplish this we have selected times τ_0 in Figures 5.2 and 5.3 which have the following property. Namely, at these times the autocorrelation function for $\tau > \tau_0$ may be translated to $\tau = 0$ and, if $\rho(R, \tau)$ were folded about $\tau = 0$, then $\rho(R, \tau) = \rho^*(R, -\tau)$. This is a standard property of autocorrelation functions and it is valid for $\rho(R, 0)$ without translation. The translation is equivalent to setting $T = 0$ in (5.5). The folded autocorrelation function was sampled from $-\Delta T$ to ΔT and transformed with a 128-point transform. Figure 5.4 shows the resulting relative spectral power profiles for $\tau_0 = 0, 0.2, \text{ and } 0.8$ seconds. The spectrum labelled $\tau_0 = 0$ is a Fourier transform of the full autocorrelation function out to 0.5 s. One can see that it is quite similar to the spectrum given in (5.1). The middle spectrum in the figure corresponds to a lag of 0.2 s. By this time the wide spectral component has decorrelated and one has only a readily-definable narrow spectral component remaining. Finally, the bottom spectrum is associated with a lag of 0.8 s. In this case the narrow spectral component is also beginning to decorrelate.

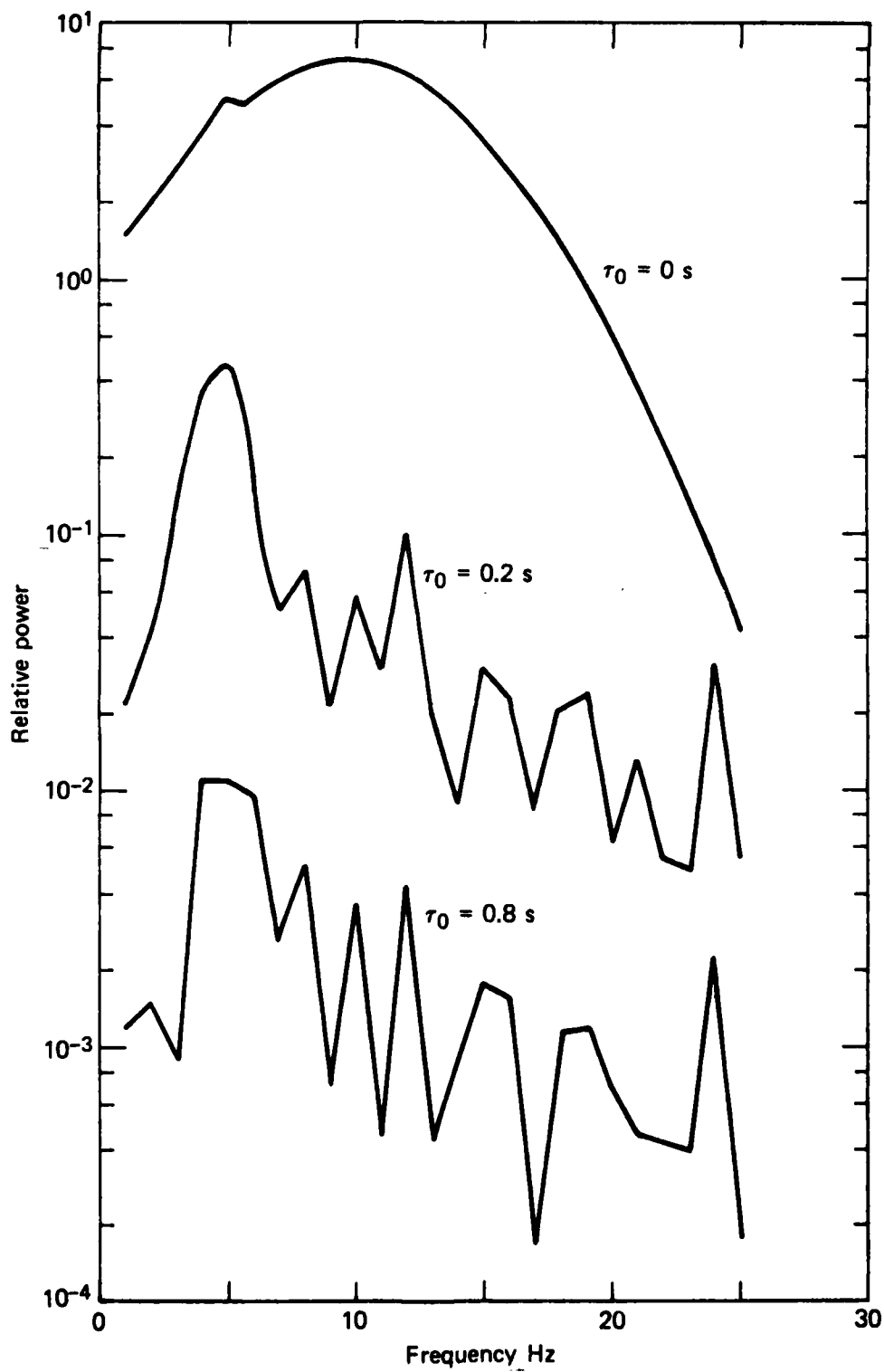


FIGURE 5.4

The previous example illustrates the usefulness of cross spectral analysis in the elimination of undesired broad bandwidth clutter spectra. If this approach is not already used in OTH radar systems, it is one that should be examined on a high priority basis. Quite possibly the procedures described in this report may be tested on existing data tapes from experimental Ava/Verona radar.

6.0 SUMMARY OF RESULTS

The principal results and conclusions obtained in this report may be summarized as follows.

E-Region Irregularities: E-Region irregularities result from the combined effects of the two-stream and gradient-drift plasma instabilities. They are two-dimensionally turbulent and, hence, may be observed in any direction in the plane perpendicular to the Earth's magnetic field. At wavelengths observed with HF and VHF radars, their Doppler velocity is determined by the electron drift velocity ($\underline{E} \times \underline{B}/B^2$) along the radar line-of-sight. The width of the Doppler spectrum is determined by the width of the velocity turbulence and may be in excess of 75 Hz for a 10 MHz radar.

F-Region Irregularities: At the present time neither the mechanism of formation nor the Doppler characteristics of F-region irregularities are well understood. This situation may improve in the coming years due to the recent development of a large number of HF Doppler sounders. The weight of current opinion supports irregularity formation by precipitating low energy electrons. Some evidence indicates that the irregularities move at the F-region plasma velocity ($\underline{E} \times \underline{B}/B^2$). Previous studies have also yielded many unresolved spectra indicating that the Doppler width of F-region spectra may be as broad as those from the E-Region.

Doppler Spectrum Modeling: By assuming a reasonable model for the high latitude potential distribution and a relation for spectral width as a function of viewing direction and Doppler velocity, it has been possible to predict the diurnal behavior of the Doppler shift and width of backscatter spectra. The model indicates that for modest cross-polar-cap potential drops of 50,000 V, the Doppler shift for a 10 MHz radar may lie anywhere in the band

± 50 Hz and the Doppler width may exceed 50 Hz. The model is particularly sensitive to the latitude at which the magnitude of the polar cap potential maximizes. Should the convection oval expand so that the potential maximum moves equatorward of the viewing region, the sign of the Doppler velocity would reverse. At the present time our knowledge of the instantaneous structure of the high latitude convection pattern and its dynamics are far from complete. Improvements are necessary to refine the predictability of the Doppler model presented.

Removal of Spread Spectra: Since undesirable clutter signals are typically spread over an appreciable bandwidth, whereas aircraft spectra are reasonably discrete, it is theoretically possible to remove the former without disturbing the latter. This may be accomplished by taking the cross spectrum of two lagged time series sampled at the complex demodulated outputs of the radar receivers. If the lag time is greater than the inverse spectral width of the clutter spectrum, only the desired aircraft spectrum will remain coherent. Calculations indicate that improvements of 20-23 dB in the signal-to-clutter ratio may be achieved in reasonable integration times.

7.0 RECOMMENDATIONS

On the basis of the preceding review of sources of ionospheric clutter and the associated effects on backscatter radar spectra, several recommendations can be made. Most importantly, additional research should be directed toward studying the usefulness of time-lagged cross spectra as a clutter reduction technique. This research may be initiated in a rather modest fashion through cross spectral analysis of data tapes from the experimental Ava/Verona radar. We propose performing the appropriate analysis during the coming year of this contract.

A more ambitious program should include the design and development of an on-line hardware cross-spectral analyzer that would filter out wide-bandwidth clutter spectra in an optimal fashion. The development of a prototype, operational analyzer could be performed by JHU/APL; however, it is not within the present funding level. Additional funding would be necessary for engineering and technical services.

The applicability of the cross spectral approach is limited by two sources or errors: 1) ionospheric clutter echoes with discrete spectra, and 2) rapid changes in the phase paths of signals scattered from aircraft. Both of these sources of error may be better understood through additional scientific research. In particular, more study is necessary into the spectral characteristics of ionospheric echoes, particularly those associated with the F-region. Also investigations are needed to determine whether disturbed ionospheric conditions lead to broadening of aircraft spectra.

Finally, in order to improve the quality of the Doppler models presented in this report, studies leading to a better understanding of the global structure of the high latitude potential distribution and its dynamics should be supported.

- Aarons, J., J. P. Mullen and H. E. Whitney, The scintillation boundary, J. Geophys. Res., 74, 884, 1969.
- Axford, W. I. and C. O. Hines, A unifying theory of high latitude geophysical phenomena and geomagnetic storms, Can. J. Phys., 39, 1433, 1961.
- Baggaley, W. J., Backscatter observations of F-region field-aligned irregularities during the IQSY, J. Geophys. Res., 75, 152, 1970.
- Balsley, B. B., Some characteristics of non-two-stream irregularities in the equatorial electrojet, J. Geophys. Res., 74, 2333, 1969.
- Balsley, B. B. and W. L. Ecklund, VHF power spectra of the radar aurora, J. Geophys. Res., 77, 4746, 1972.
- Balsley, B. B., W. L. Ecklund and R. A. Greenwald, VHF Doppler spectra of radar echoes associated with a visual auroral form: Observations and implications, J. Geophys. Res., 78, 1681, 1973.
- Basu, S., R. L. Vesprini and J. Aarons, F-layer irregularities as determined by backscatter studies at 19 MHz over half of a solar cycle, Radio Sci., 9, 355, 1974.
- Bates, H. F. and P. R. Albee, Aspect-sensitivity of F-layer HF backscatter echoes, J. Geophys. Res., 75, 165, 1970.
- Blackman, R. B. and T. W. Tukey, The Measurement of Power Spectra, (Dover, New York) 1959.
- Buneman, O., Excitation of field-aligned sound waves by electron streams, Phys. Rev. Letts., 10, 285, 1963.
- Cahill, L. J., Jr., R. A. Greenwald and E. Nielsen, Auroral radar and rocket double probe observations of the electric field across the Harang discontinuity, Geophys. Res. Letts., 5, 687, 1978.
- Calvert, W., R. A. Greenwald and K. H. Geissler, On-line spectral analysis, Review of Sci. Instru., 42, 1657, 1971.
- Chaturvedi, P. K. and S. L. Ossakow, Nonlinear stabilization of the current convective instability in the diffuse aurora, Geophys. Res. Letts., 6, 957, 1979.
- Czechowsky, P., Doppler shift of auroral backscatter signals, J. Geophys., 40, 229, 1974.
- Dyson, P. L., Direct measurement of the size and amplitude of irregularities in the topside ionosphere, J. Geophys. Res., 74, 6291, 1969.

- Dyson, P. L. and J. D. Winningham, Top side ionospheric spread-F and particle precipitation in the day side magnetospheric clefts, J. Geophys. Res., 79, 5219, 1974.
- Ecklund, W. L., B. B. Balsley and R. A. Greenwald, Crossed beam measurements of the diffuse radar aurora, J. Geophys. Res., 80, 1805, 1975.
- Ecklund, W. L., B. B. Balsley and D. A. Carter, A preliminary comparison of F region plasma drifts and E region irregularity drifts in the auroral zone, J. Geophys. Res., 82, 195, 1977.
- Farley, D. T., A plasma instability resulting in field-aligned irregularities in the ionosphere, J. Geophys. Res., 68, 6083, 1963.
- Farley, D. T., Irregularities in the equatorial ionosphere: The Berkner Symposium, Rev. Geophys. Space Phys., 12, 285, 1974.
- Farley, D. T. and B. B. Balsley, Instabilities in the equatorial electrojet, J. Geophys. Res., 78, 227, 1973.
- Fejer, B. G. and M. C. Kelley, Ionospheric irregularities, Rev. Geophys. Space Phys., 18, 401, 1980.
- Greenwald, R. A., An alternative explanation of the Doppler spectra of current-driven plasma instabilities, J. Geophys. Res., 84, 433, 1979.
- Greenwald, R. A. and W. L. Ecklund, A new look at radar auroral motions, J. Geophys. Res., 80, 3642, 1975.
- Greenwald, R. A., W. L. Ecklund and B. B. Balsley, Diffuse radar aurora: Spectral observations of non-two-stream irregularities, J. Geophys. Res., 80, 3642, 1975.
- Greenwald, R. A., W. Weiss, E. Nielsen and N. R. Thomson, STARE: A new radar auroral backscatter experiment in northern Scandinavia, Radio Sci., 13, 1021, 1978.
- Greenwald, R. A., T. A. Potemra and N. A. Saflekos, STARE and TRIAD observations of field-aligned current closure and Joule heating in the vicinity of the Harang discontinuity, J. Geophys. Res., 85, 563, 1980.
- Haldoupis, C. and G. Sofko, Doppler spectrum of 42 MHz CW auroral backscatter, Can. J. Phys., 54, 1571, 1976.
- Heppner, J., Empirical models of high-latitude electric fields, J. Geophys. Res., 82, 1115, 1977.
- Hice, J. D. and B. Frank, Occurrence patterns of topside spread-F on Alouette ionograms, J. Geophys. Res., 71, 3653, 1966.

- Hofstee, J. and P. A. Forsyth, Ion acoustic waves in the auroral plasma, Can. J. Physics, 47, 2797, 1969.
- Hofstee, J. and P. A. Forsyth, Ion acoustic waves and aspect sensitivity in radio aurora, J. Atmos. Terr. Phys., 34, 893, 1972.
- Hudson, M. K. and M. C. Kelley, The temperature gradient drift instability at the equatorward edge of the ionospheric plasma trough, J. Geophys. Res., 80, 4581, 1975.
- Keskinen, M. J., R. N. Sudan and R. L. Ferch, Temporal and spatial power spectrum studies of numerical simulations of type II gradient drift irregularities in the equatorial electrojet, J. Geophys. Res., 84, 1419, 1979.
- Keskinen, M. J., S. L. Ossakow and B. E. McDonald, Nonlinear evolution of diffuse auroral F-region ionospheric irregularities, Geophys. Res. Letts., 7, 573, 1980.
- Kindel, J. M. and C. F. Kennel, Topside current instabilities, J. Geophys. Res., 76, 3055, 1971.
- Knox, F. B., A contribution to the theory of the production of field-aligned ionization irregularities in the equatorial electrojet, J. Atmos. Terr. Phys., 26, 239, 1964.
- Lee, K., C. F. Kennel and F. V. Coroniti, On the marginally stable saturation spectrum of unstable type I equatorial electrojet irregularities, J. Geophys. Res., 79, 249, 1974.
- Maeda, K., T. Tsuda and H. Maeda, Theoretical interpretation of the equatorial sporadic E layers, Rpt. Ionosph. Space Res. Japan, 17, 147, 1963.
- McClure, J. P. and W. B. Hanson, A catalog of ionospheric F-region irregularity behavior based on Ogo 6 retarding potential analyzer data, J. Geophys. Res., 78, 7431, 1973.
- McDonald, B. E., T. P. Coffey, S. Ossakow and R. N. Sudan, Preliminary report of numerical simulation of type 2 irregularities in the equatorial electrojet, J. Geophys. Res., 79, 2551, 1974.
- Moorcroft, D. R. and R. T. Tsunoda, Rapid scan Doppler velocity maps of the diffuse radar aurora, J. Geophys. Res., 83, 1482, 1978.
- Oksman, J., H. J. Moller and R. A. Greenwald, Comparisons between strong HF backscatter and VHF radar aurora, Radio Sci., 14, 1121, 1979.
- Ossakow, S. L. and P. K. Chaturvedi, Current convective instability in the diffuse aurora, Geophys. Res. Letts., 6, 332, 1979.

- Reed, R. W., Spectra from 50 MHz auroral radar echoes, Ph.D Thesis, Cornell University, Ithaca, New York, 1979.
- Reid, G. C., The formation of small scale irregularities in the ionosphere, J. Geophys. Res., 73, 1627, 1968.
- Rogister, A., Nonlinear theory of type 1 irregularities in the equatorial electrojet, J. Geophys. Res., 76, 7754, 1971.
- Rogister, A. and N. D'Angelo, Type 2 irregularities in the equatorial electrojet, J. Geophys. Res., 75, 3879, 1970.
- Sagalyn, R. C., M. Smiddy and M. Ahmed, High latitude irregularities in the topside ionosphere based on ISIS-1 thermal ion probe data, J. Geophys. Res., 79, 4252, 1974.
- Sudan, R. N., J. Akinrimisi and D. T. Farley, Generation of small-scale irregularities in the equatorial electrojet, J. Geophys. Res., 78, 240, 1973.
- Tsunoda, R. T., Doppler velocity maps of diffuse radar aurora, J. Geophys. Res., 81, 425, 1976.
- Tsunoda, R. T., R. I. Presnell and T. A. Potemra, The spatial relationship between the evening radar aurora and field-aligned currents, J. Geophys. Res., 81, 3791, 1976.
- Unwin, R. S., The morphology of the radio aurora at sunspot maximum II, The behavior of different echo types, J. Atmos. Terr. Phys., 28, 1183, 1966.
- Unwin, R. S. and C. H. Cummack, The ionospheric signature of large poleward directed electric fields at subauroral latitudes, Paper presented at the First International Symposium on IMS Results, Melbourne, Australia, December, 1979.
- Whalen, J. A. and C. P. Pike, F-layer and 6300-Å measurements in the day sector of the auroral oval, J. Geophys. Res., 78, 3848, 1973.

FIGURE CAPTIONS

- FIGURE 2.1 World map indicating regions where E-region irregularities are commonly observed.
- FIGURE 3.1 Polar plot indicating equatorward and poleward boundaries of F-region fine structures as measured with an in situ Langmuir probe (from Dyson, 1969).
- FIGURE 3.2 Polar plot indicating equatorward boundaries of the small scale irregularity zone as measured with an electrostatic analyzer on ISIS 1, the scintillation zone, the ionospheric electron trough, and the Langmuir probe irregularity zone (from Sagalyn et al., 1974).
- FIGURE 4.1 High latitude electrostatic potential distribution associated with Equations (4.3) and (4.4) ($\theta_1 = 20^\circ$).
- FIGURE 4.2 Predicted line-of-sight Doppler velocity and Doppler width of ionospheric irregularities observed at 60° geomagnetic latitude and 60° azimuth angle.
- FIGURE 4.3 Predicted line-of-sight Doppler velocity and Doppler width of ionospheric irregularities observed at 65° geomagnetic latitude and 30° azimuth angle.
- FIGURE 4.4 Predicted line-of-sight Doppler velocity and Doppler width of ionospheric irregularities observed at 65° geomagnetic latitude and 0° azimuth angle.
- FIGURE 4.5 Diurnal variation of the line-of-sight Doppler velocity observed with a 42 MHz radar directed approximately northward from Saskatoon, Saskatchewan (120 Hz shift is approximately 430 M/S).
- FIGURE 4.6 High latitude electrostatic potential distribution for which most of the potential variation is confined to the auroral region.

FIGURE 5.1 Hypothetical backscatter spectrum comprised of irregularity backscatter (major peak) and a target (small spike).

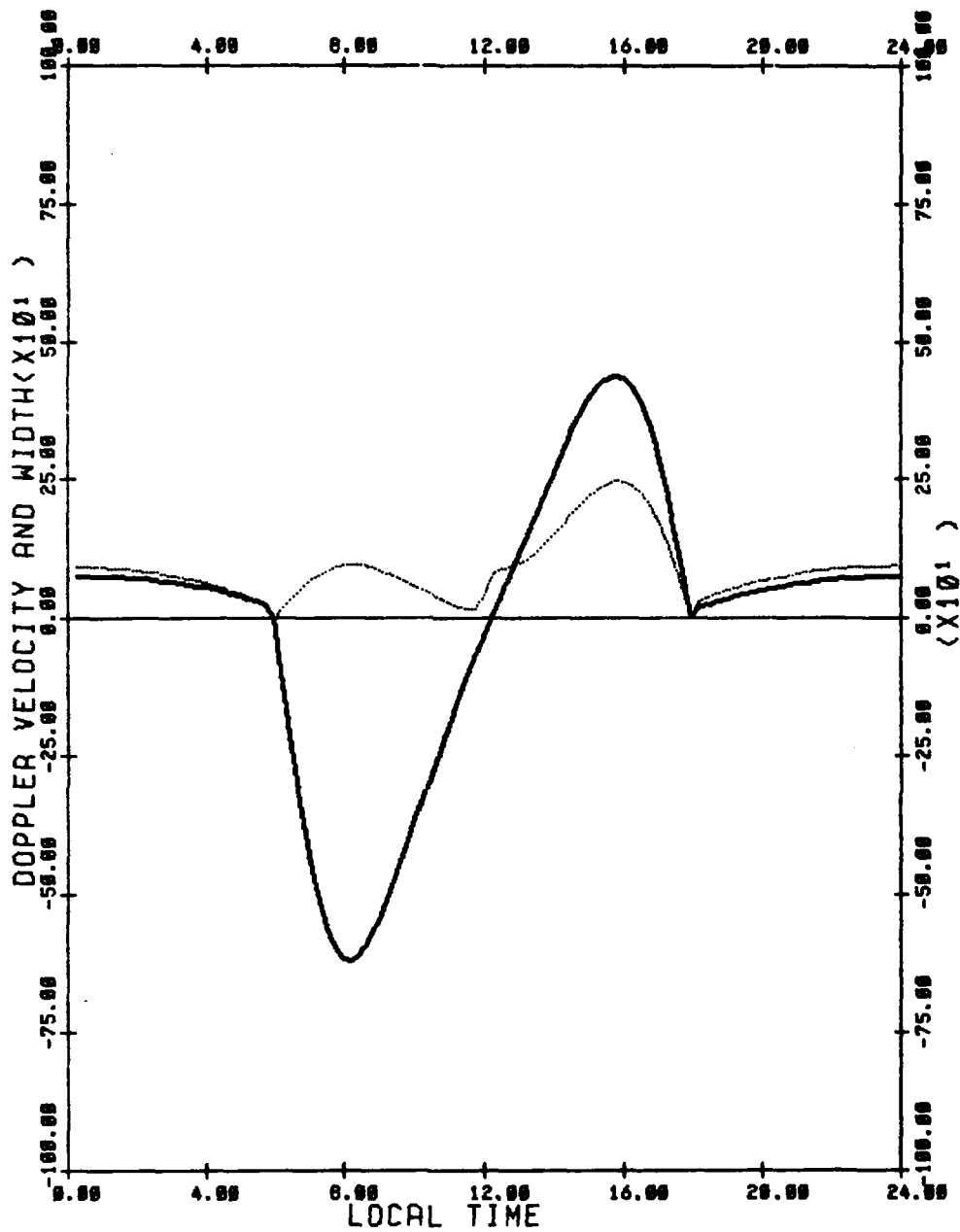
FIGURE 5.2 Autocorrelation function of the spectrum in Figure 10 out to a lag of 0.1 seconds.

FIGURE 5.3 Autocorrelation function of the spectrum in Figure 10 for lags ranging from 0.1 to 0.6 seconds.

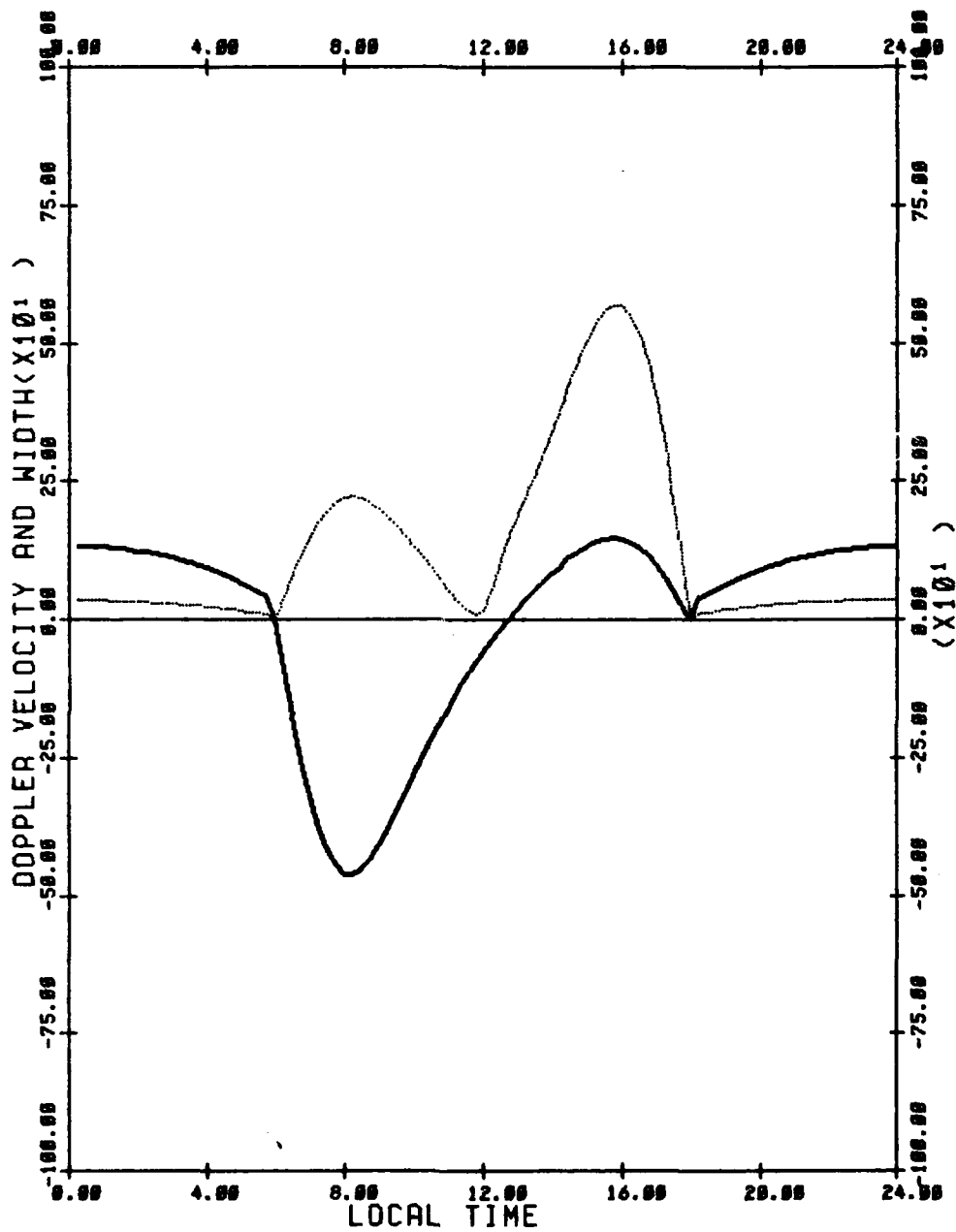
FIGURE 5.4 Cross-spectra obtained by eliminating the first τ_0 seconds from the autocorrelation functions in Figures 11 and 12 and Fourier transforming. The dominant peak in the middle cross spectrum ($\tau_0 = 0.2$ s) corresponds to the target signal; the irregularity backscatter has been virtually eliminated.

APPENDIX A

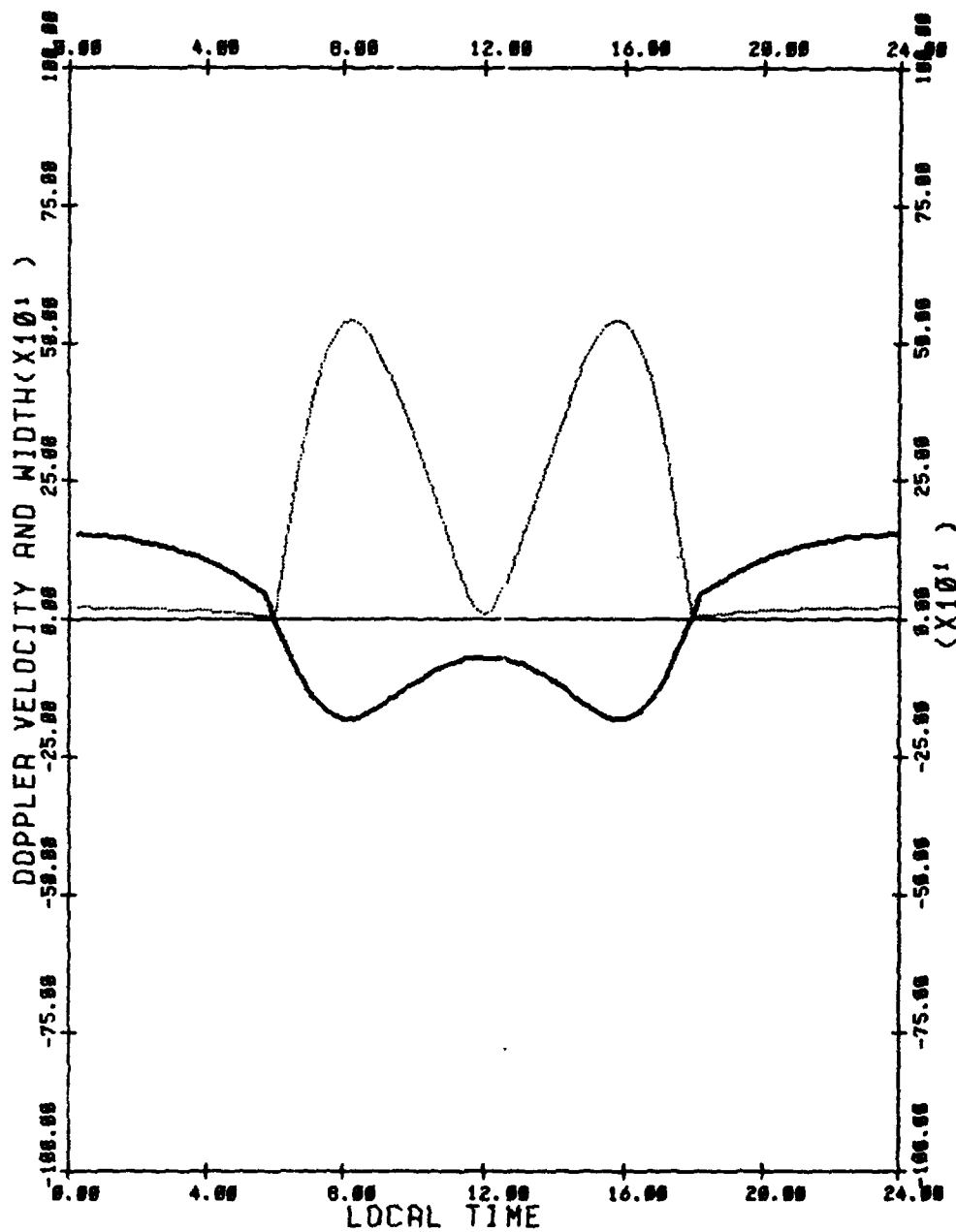
DOPPLER VELOCITY AND WIDTH PLOTS
FOR POTENTIAL DISTRIBUTION SHOWN IN FIGURE 4.1



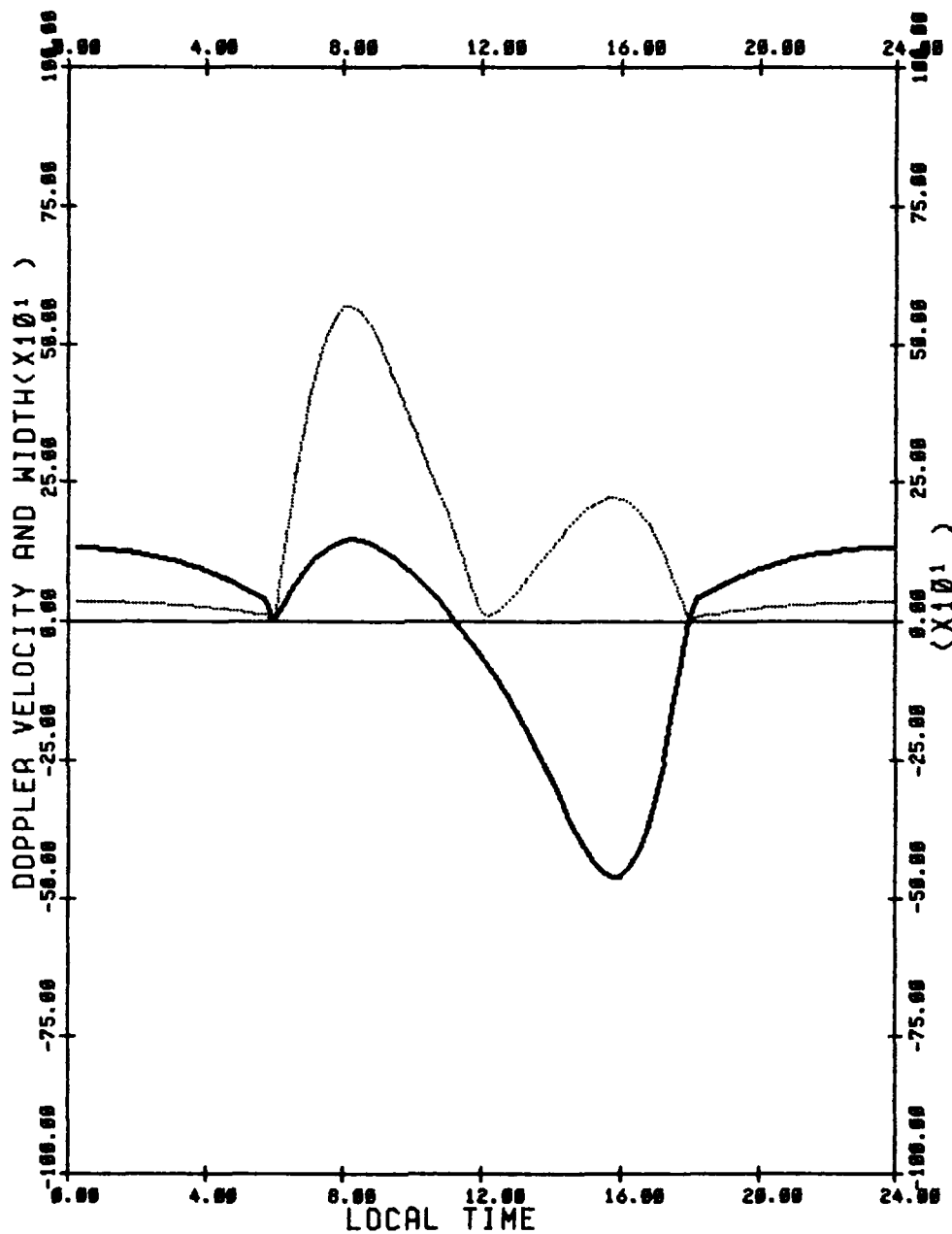
DOPPLER VELOCITY —————
 DOPPLER WIDTH - - - - -
 CROSS POLAR CAP POTENTIAL DROP(V) = 50000
 E-FOLDING DISTANCE OF ARORAL E-FIELD(DEGREES) = 5
 LATITUDE OF POTENTIAL MAXIMUM(DEGREES) = 65
 OVAL OFFSET(DEGREES) = 5
 MEASUREMENT LATITUDE = 65
 VIEWING ANGLE = 60



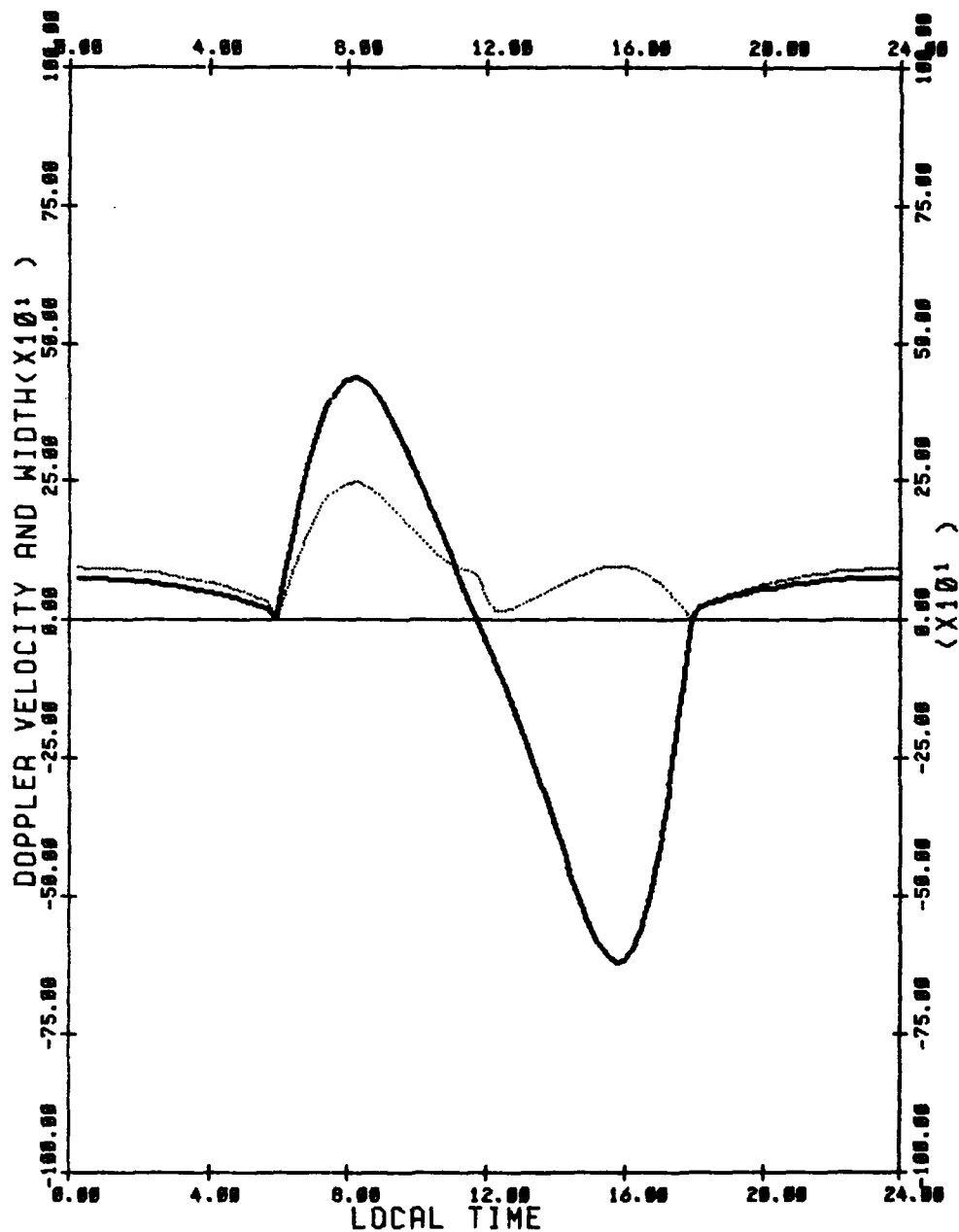
DOPPLER VELOCITY —————
 DOPPLER WIDTH -----
 CROSS POLAR CAP POTENTIAL DROP(V) = 50000
 E-FOLDING DISTANCE OF ARORAL E-FIELD(DEGREES) = 5
 LATITUDE OF POTENTIAL MAXIMUM(DEGREES) = 65
 OVAL OFFSET(DEGREES) = 5
 MEASUREMENT LATITUDE = 65
 VIEWING ANGLE = 30



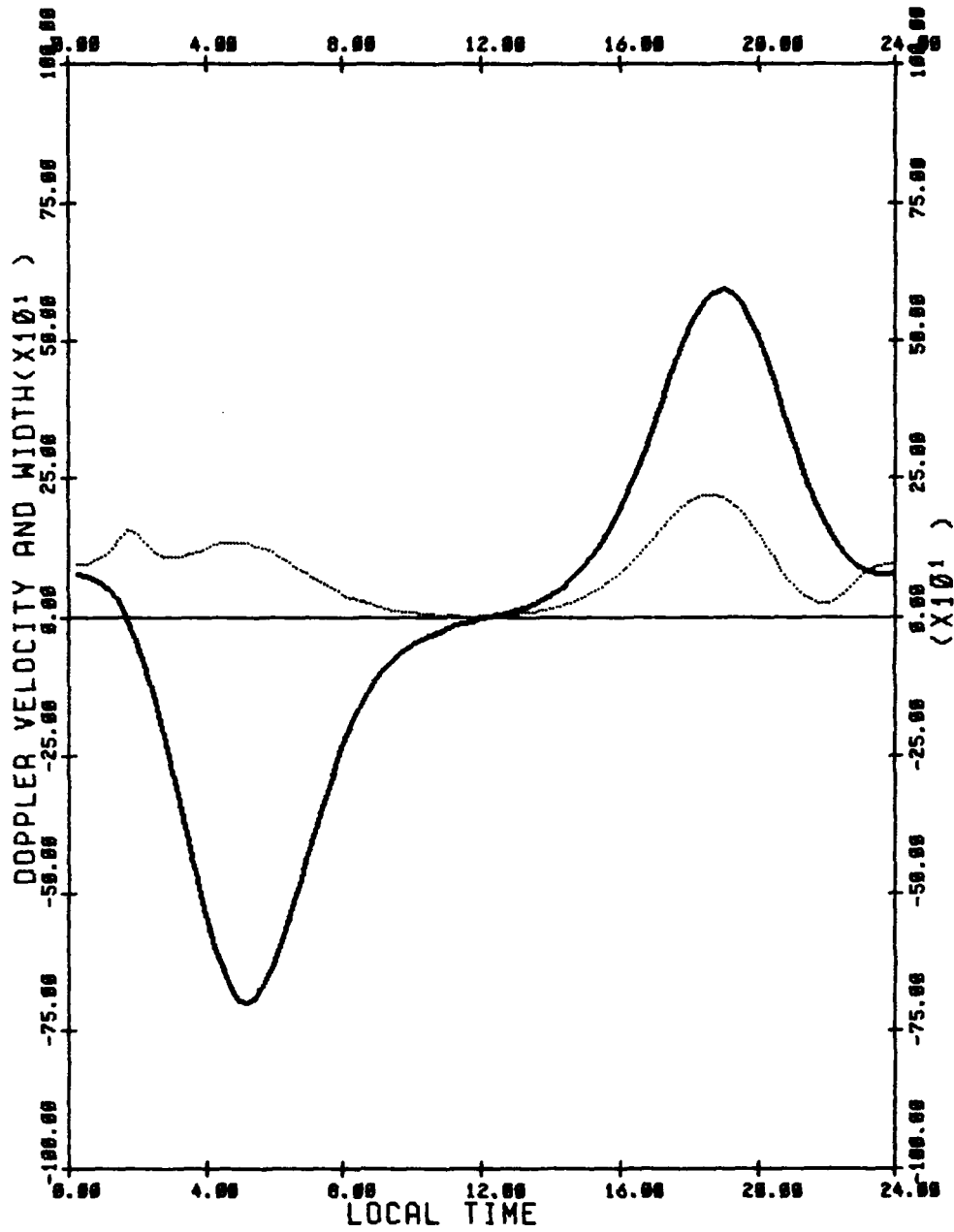
DOPPLER VELOCITY —————
 DOPPLER WIDTH - - - - -
 CROSS POLAR CAP POTENTIAL DROP(V) = 50000
 E-FOLDING DISTANCE OF ARDIAL E-FIELD(DEGREES) = 5
 LATITUDE OF POTENTIAL MAXIMUM(DEGREES) = 65
 OVAL OFFSET(DEGREES) = 5
 MEASUREMENT LATITUDE = 65
 VIEWING ANGLE = 0



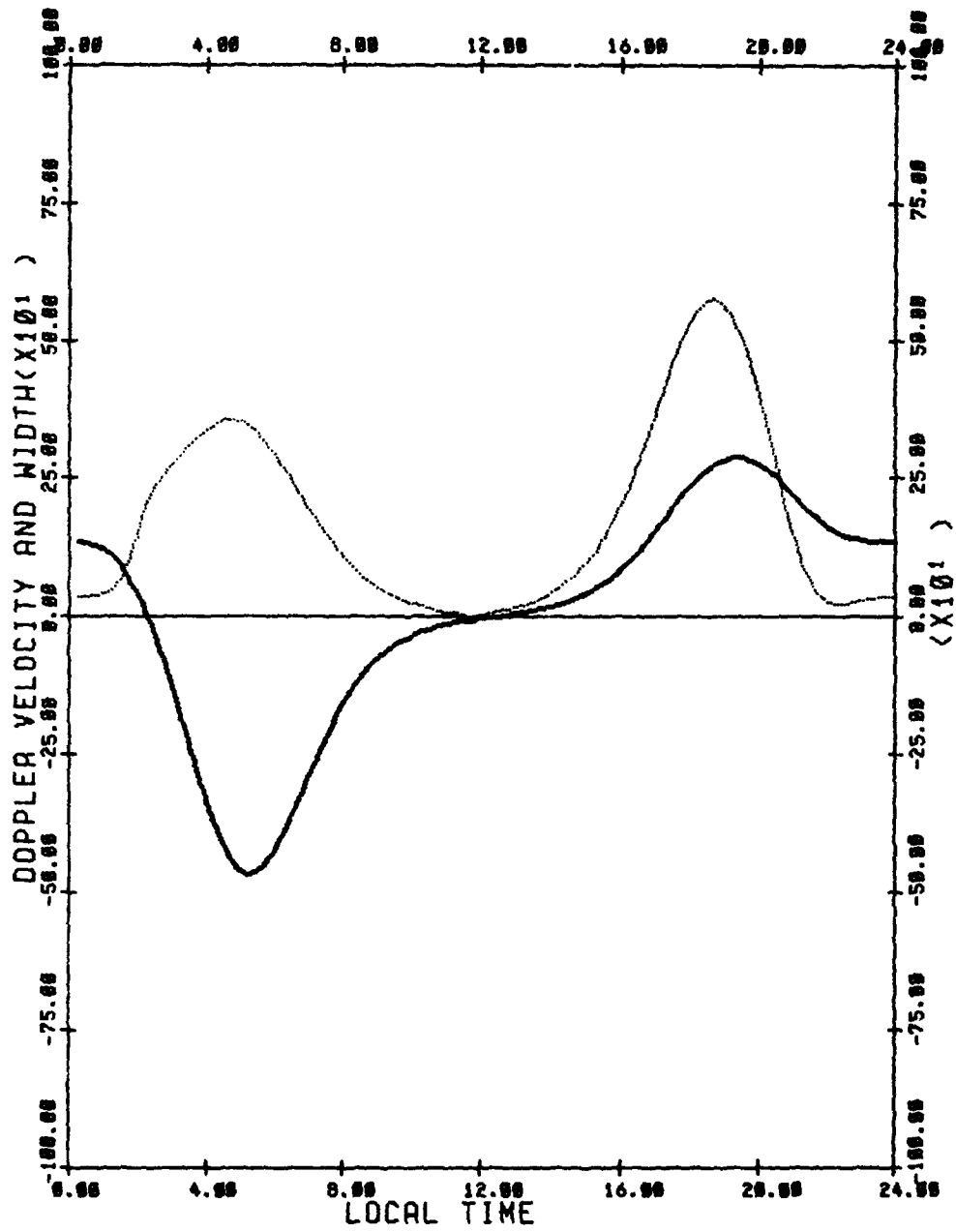
DOPPLER VELOCITY
 DOPPLER WIDTH
 CROSS POLAR CAP POTENTIAL DROP(V) = 50000
 E-FOLDING DISTANCE OF ARDAL E-FIELD(DEGREES) = 5
 LATITUDE OF POTENTIAL MAXIMUM(DEGREES) = 65
 OVAL OFFSET(DEGREES) = 5
 MEASUREMENT LATITUDE = 65
 VIEWING ANGLE = -30



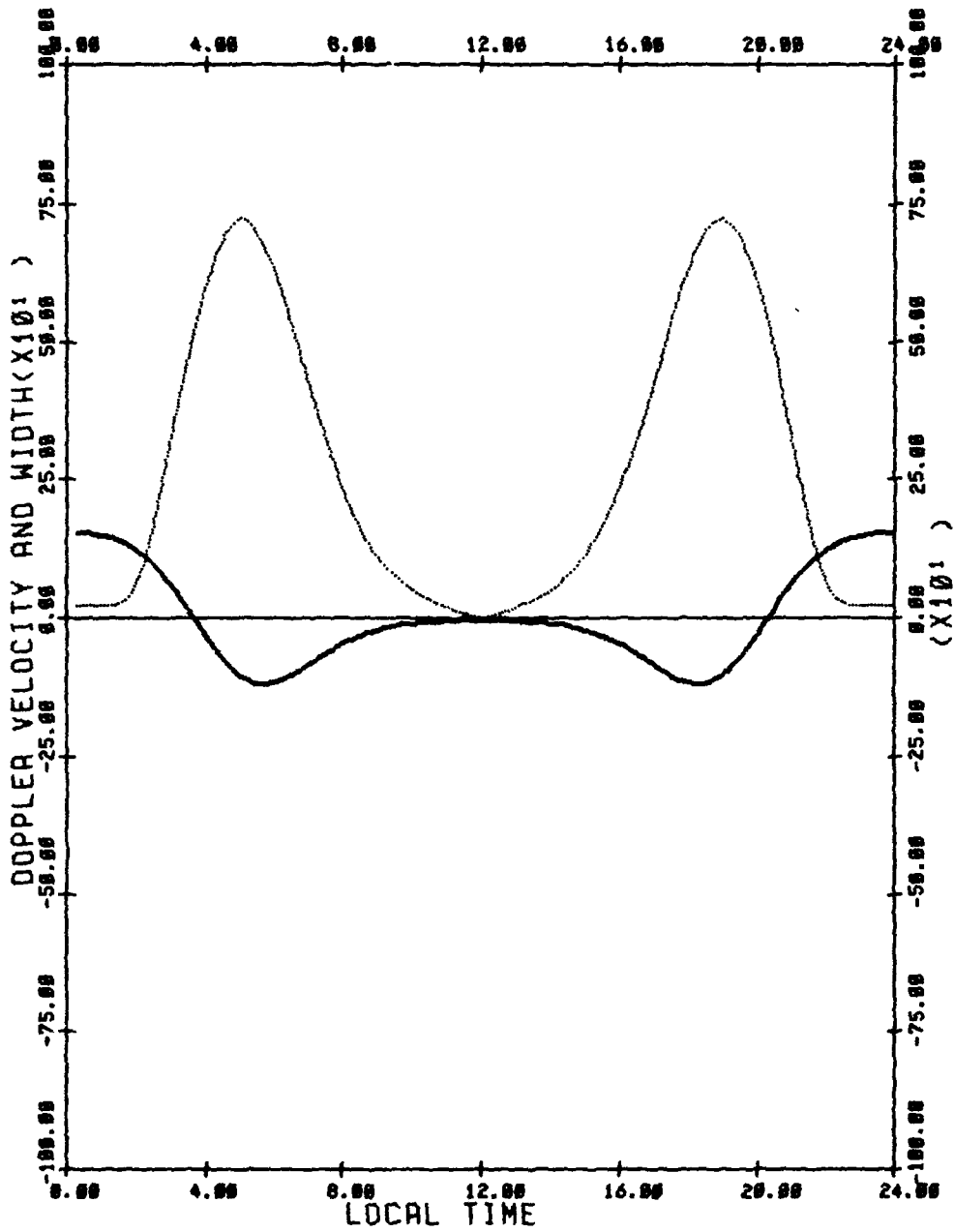
DOPPLER VELOCITY ———
 DOPPLER WIDTH - - - - -
 CROSS POLAR CAP POTENTIAL DROP(V) = 50000
 E-FOLDING DISTANCE OF ARORAL E-FIELD(DEGREES) = 5
 LATITUDE OF POTENTIAL MAXIMUM(DEGREES) = 65
 OVAL OFFSET(DEGREES) = 5
 MEASUREMENT LATITUDE = 65
 VIEWING ANGLE = -60



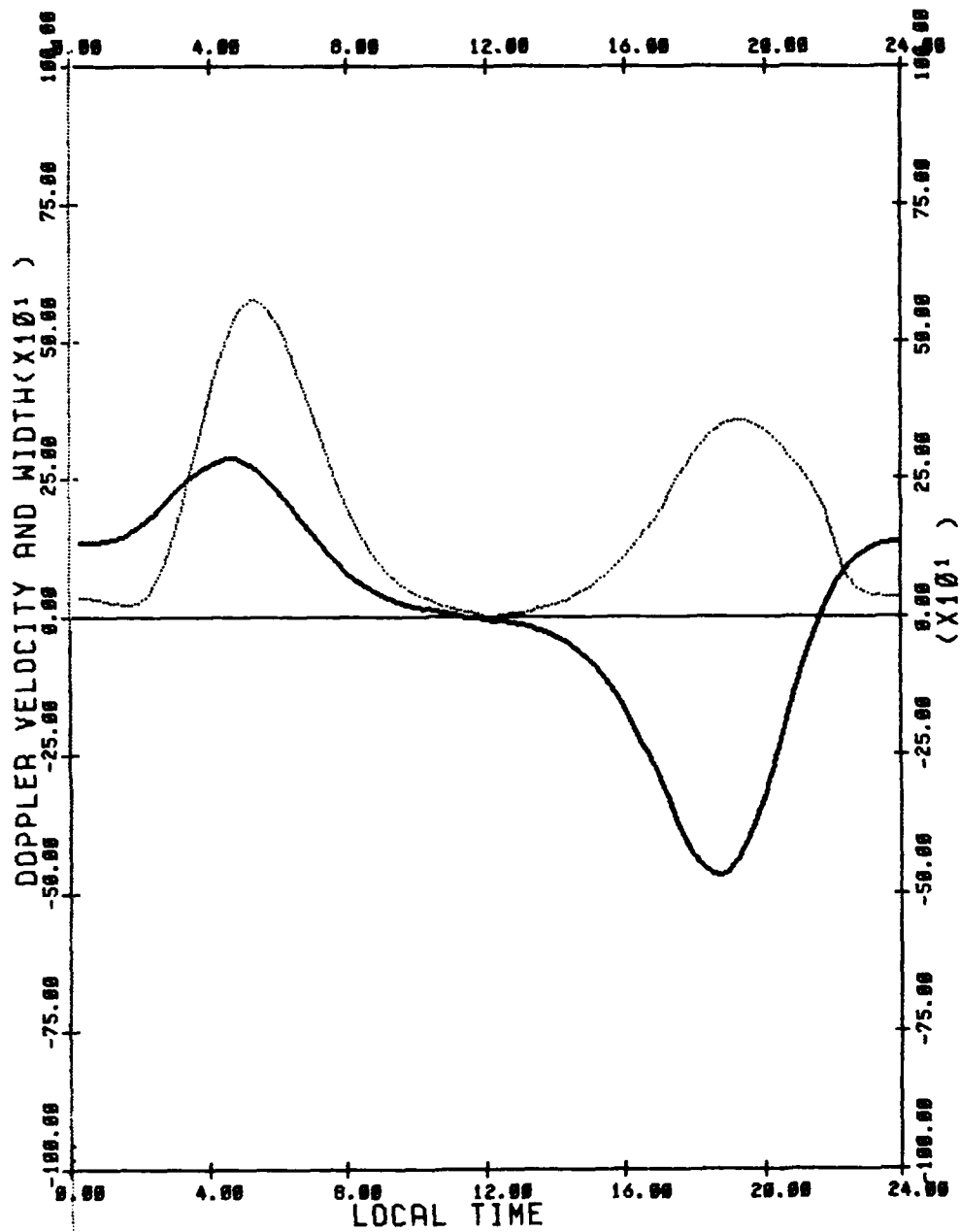
DOPPLER VELOCITY —————
 DOPPLER WIDTH - - - - -
 CROSS POLAR CAP POTENTIAL DROP(V) = 50000
 E-FOLDING DISTANCE OF ARORAL E-FIELD(DEGREES) = 5
 LATITUDE OF POTENTIAL MAXIMUM(DEGREES) = 65
 OVAL OFFSET(DEGREES) = 5
 MEASUREMENT LATITUDE = 60
 VIEWING ANGLE = 60



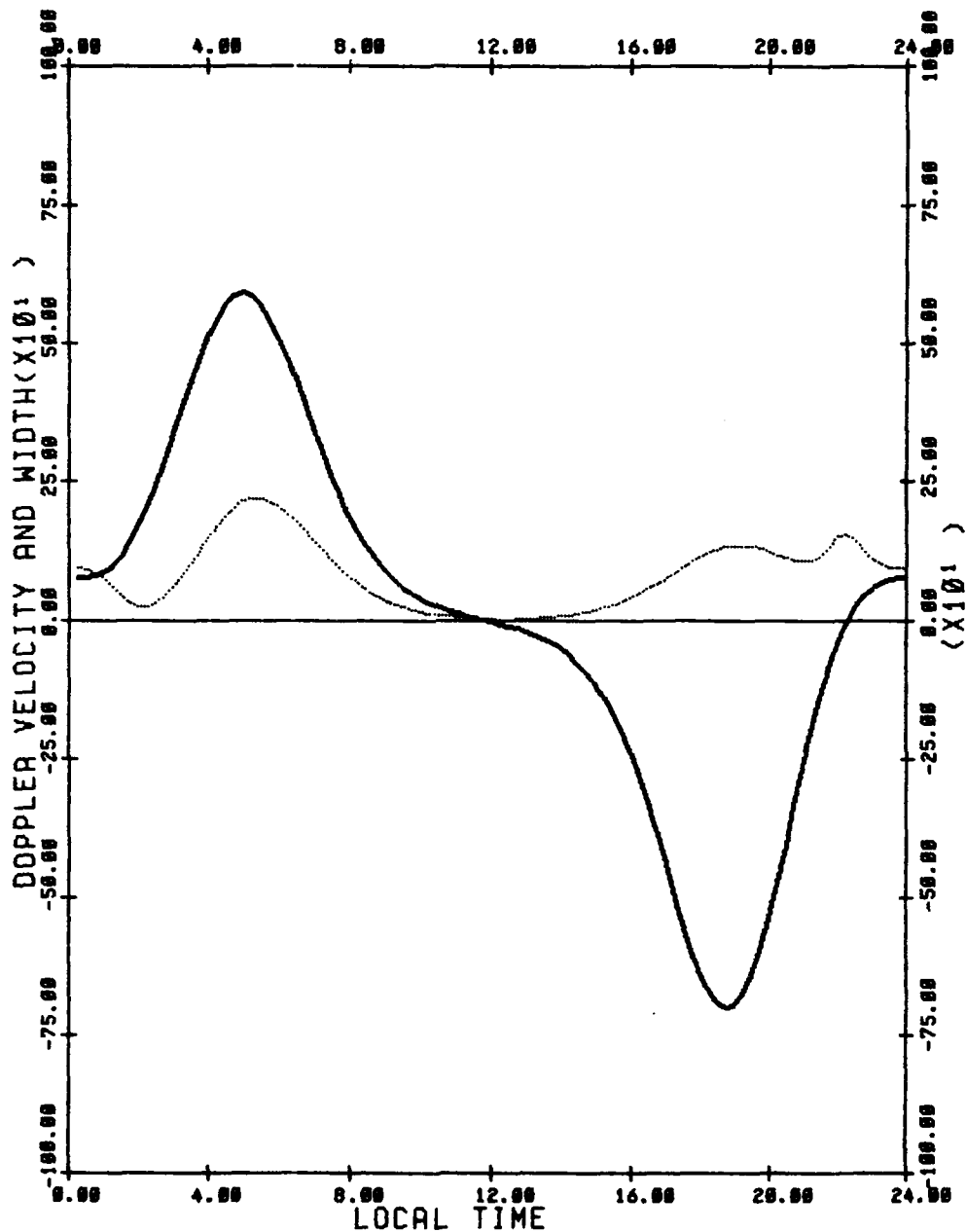
DOPPLER VELOCITY —————
 DOPPLER WIDTH - - - - -
 CROSS POLAR CAP POTENTIAL DROP(V) = 50000
 E-FOLDING DISTANCE OF RADIAL E-FIELD(DEGREES) = 5
 LATITUDE OF POTENTIAL MAXIMUM(DEGREES) = 65
 OVAL OFFSET(DEGREES) = 5
 MEASUREMENT LATITUDE = 60
 VIEWING ANGLE = 30



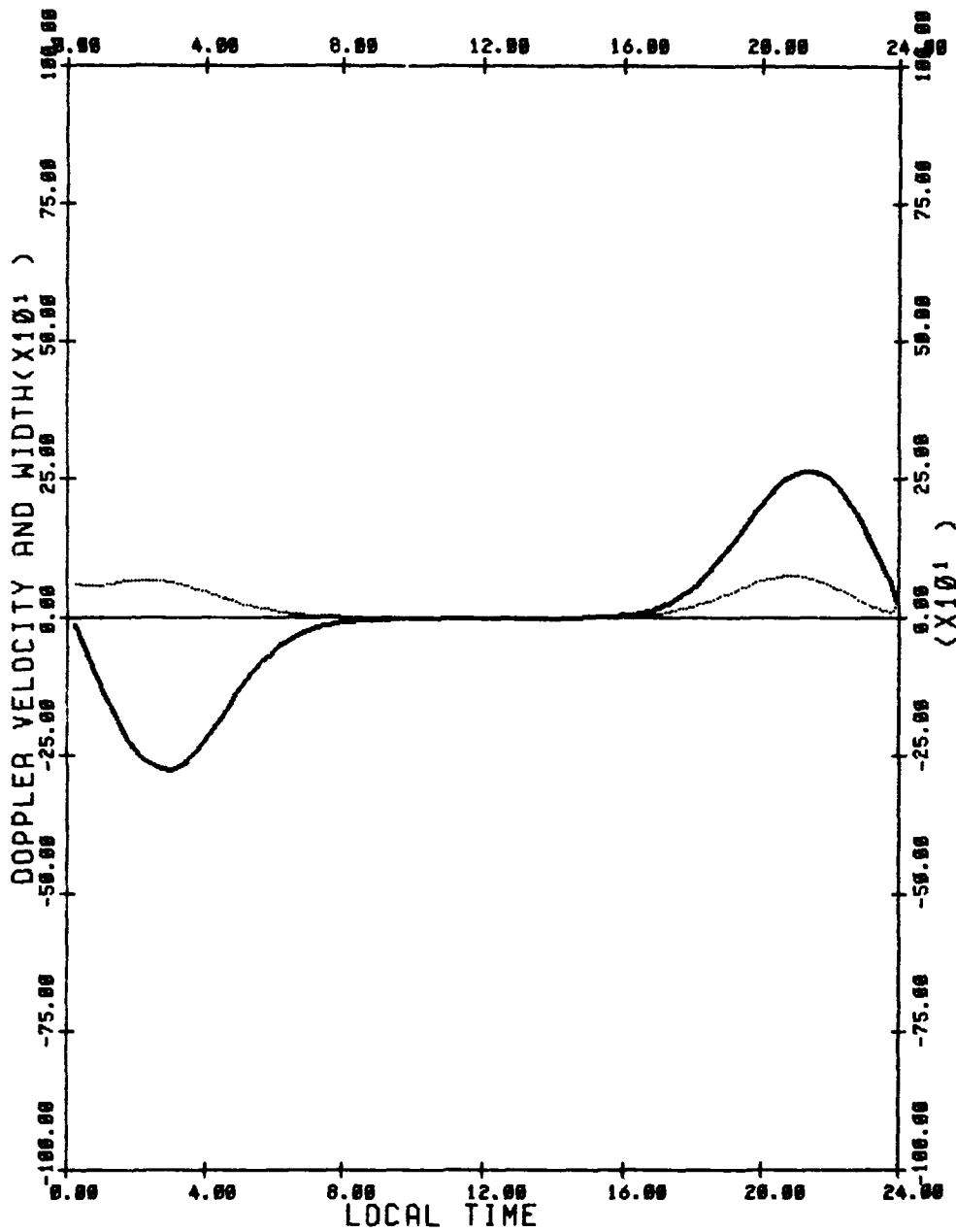
DOPPLER VELOCITY
 DOPPLER WIDTH
 CROSS POLAR CAP POTENTIAL DROP(V) = 50000
 E-FOLDING DISTANCE OF ARORAL E-FIELD(DEGREES) = 5
 LATITUDE OF POTENTIAL MAXIMUM(DEGREES) = 65
 OVAL OFFSET(DEGREES) = 5
 MEASUREMENT LATITUDE = 60
 VIEWING ANGLE = 0



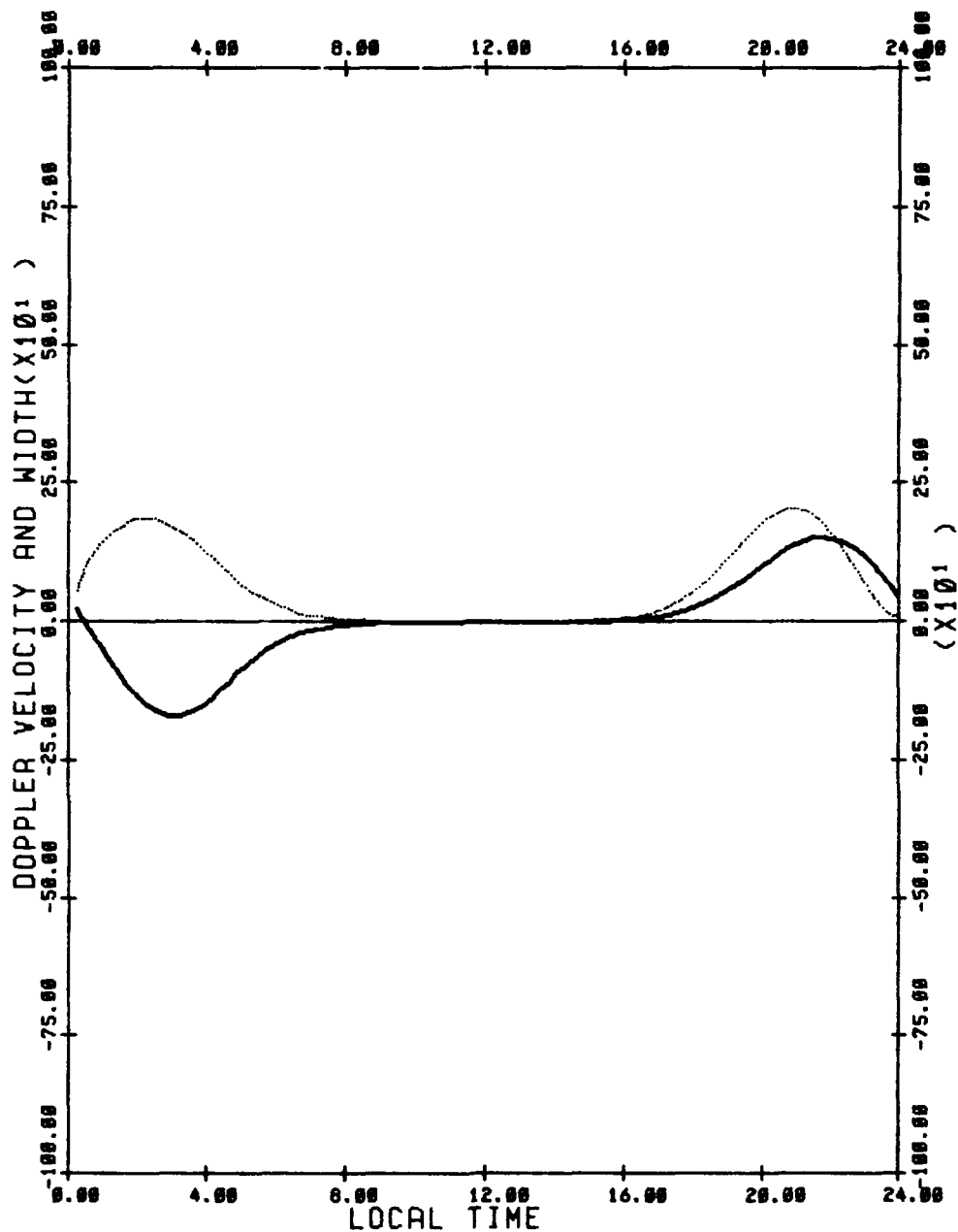
DOPPLER VELOCITY —————
 DOPPLER WIDTH - - - - -
 CROSS POLAR CAP POTENTIAL DROP(V) = 50000
 E-FOLDING DISTANCE OF ARDIAL E-FIELD(DEGREES) = 5
 LATITUDE OF POTENTIAL MAXIMUM(DEGREES) = 65
 OVAL OFFSET(DEGREES) = 5
 MEASUREMENT LATITUDE = 60
 VIEWING ANGLE = -30



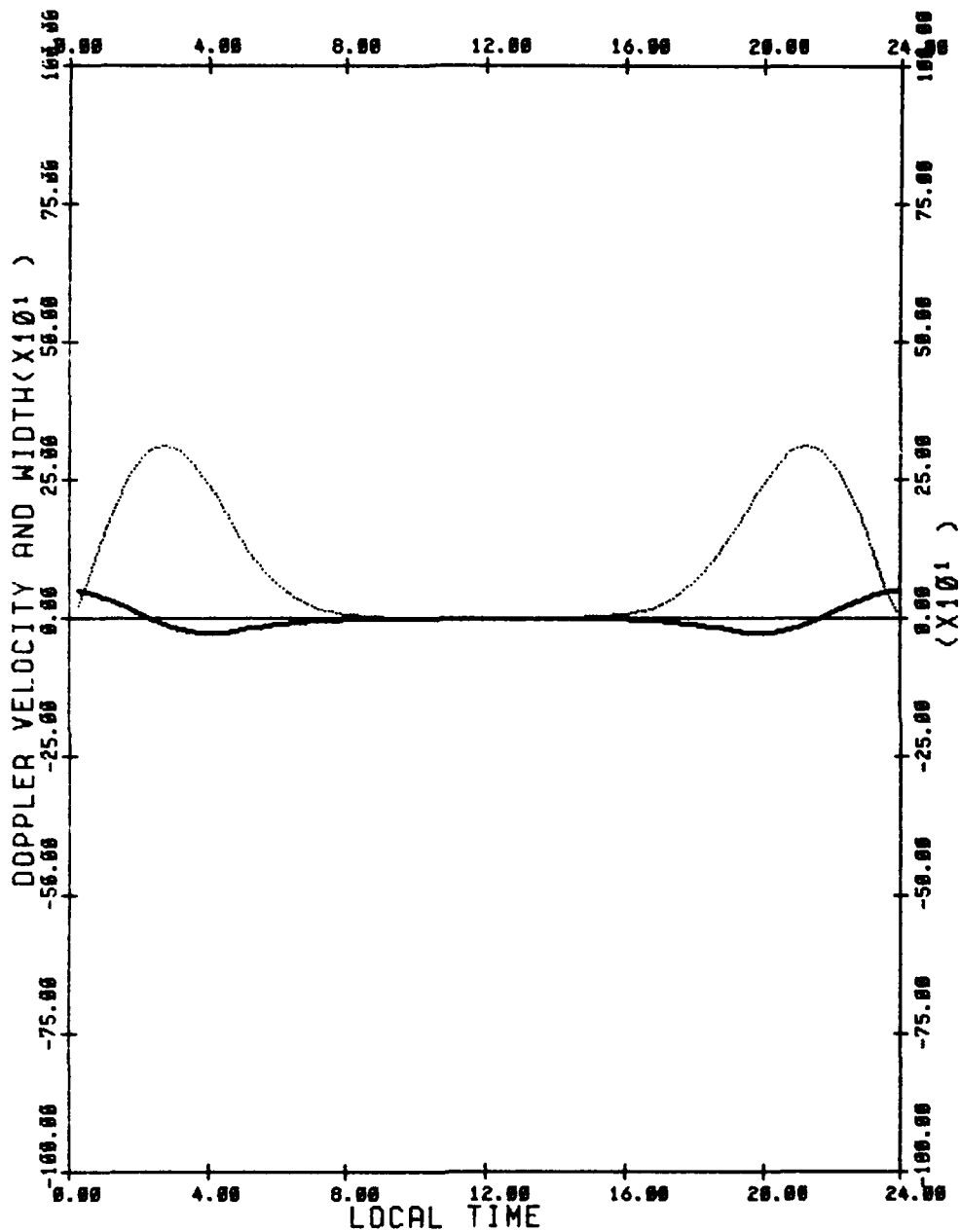
DOPPLER VELOCITY —————
 DOPPLER WIDTH - - - - -
 CROSS POLAR CAP POTENTIAL DROP(V) = 50000
 E-FOLDING DISTANCE OF ARDIAL E-FIELD(DEGREES) = 5
 LATITUDE OF POTENTIAL MAXIMUM(DEGREES) = 65
 OVAL OFFSET(DEGREES) = 5
 MEASUREMENT LATITUDE = 60
 VIEWING ANGLE = -60



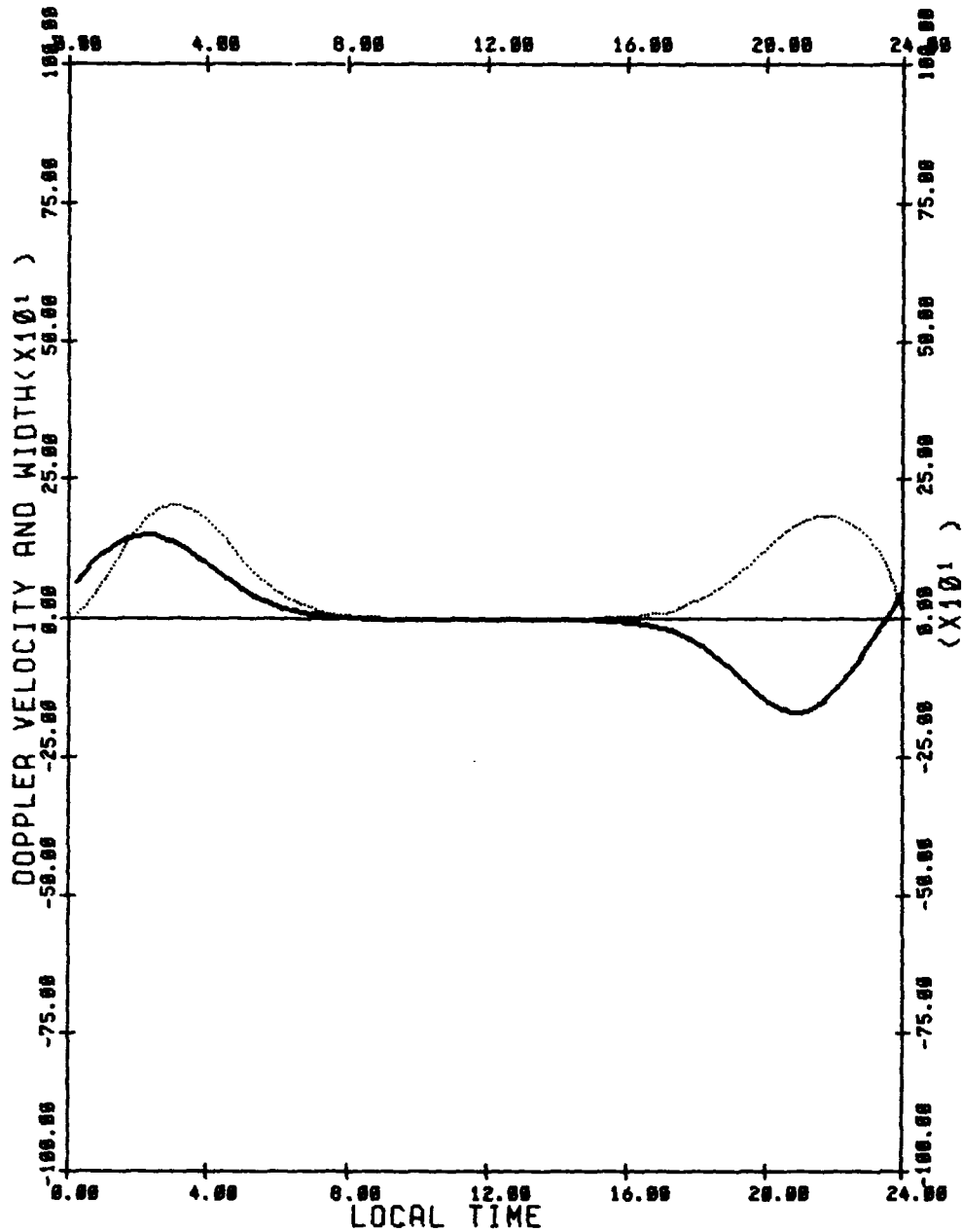
DOPPLER VELOCITY _____
 DOPPLER WIDTH _____
 CROSS POLAR CAP POTENTIAL DROP(V) = 50000
 E-FOLDING DISTANCE OF ARORAL E-FIELD(DEGREES) = 5
 LATITUDE OF POTENTIAL MAXIMUM(DEGREES) = 65
 OVAL OFFSET(DEGREES) = 5
 MEASUREMENT LATITUDE = 55
 VIEWING ANGLE = 60



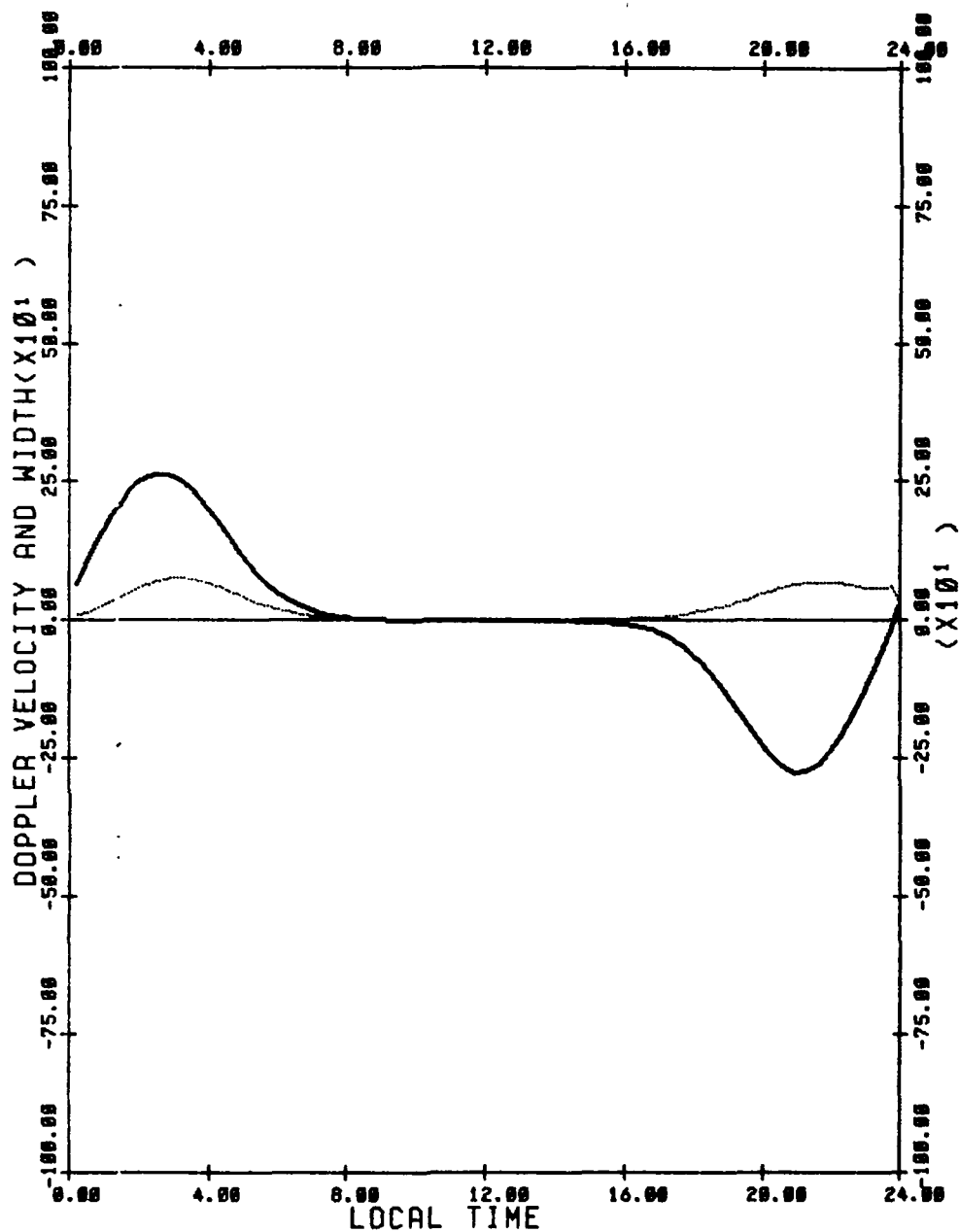
DOPPLER VELOCITY —————
 DOPPLER WIDTH - - - - -
 CROSS POLAR CAP POTENTIAL DROP(V) = 50000
 E-FOLDING DISTANCE OF ARORAL E-FIELD(DEGREES) = 5
 LATITUDE OF POTENTIAL MAXIMUM(DEGREES) = 65
 OVAL OFFSET(DEGREES) = 5
 MEASUREMENT LATITUDE = 55
 VIEWING ANGLE = 30



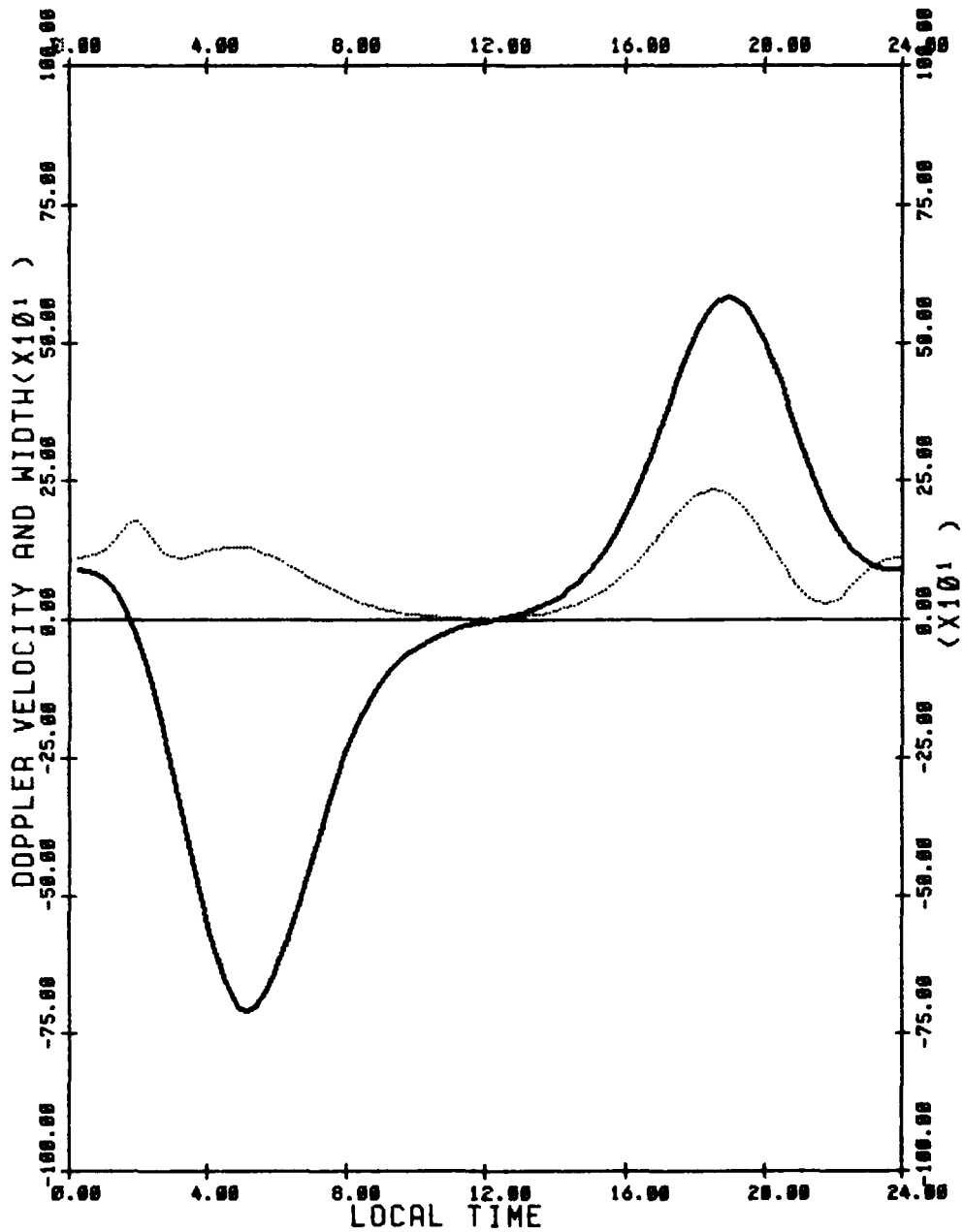
DOPPLER VELOCITY —————
 DOPPLER WIDTH —————
 CROSS POLAR CAP POTENTIAL DROP(V) = 50000
 E-FOLDING DISTANCE OF ARDRAL E-FIELD(DEGREES) = 5
 LATITUDE OF POTENTIAL MAXIMUM(DEGREES) = 65
 OVAL OFFSET(DEGREES) = 5
 MEASUREMENT LATITUDE = 55
 VIEWING ANGLE = 0



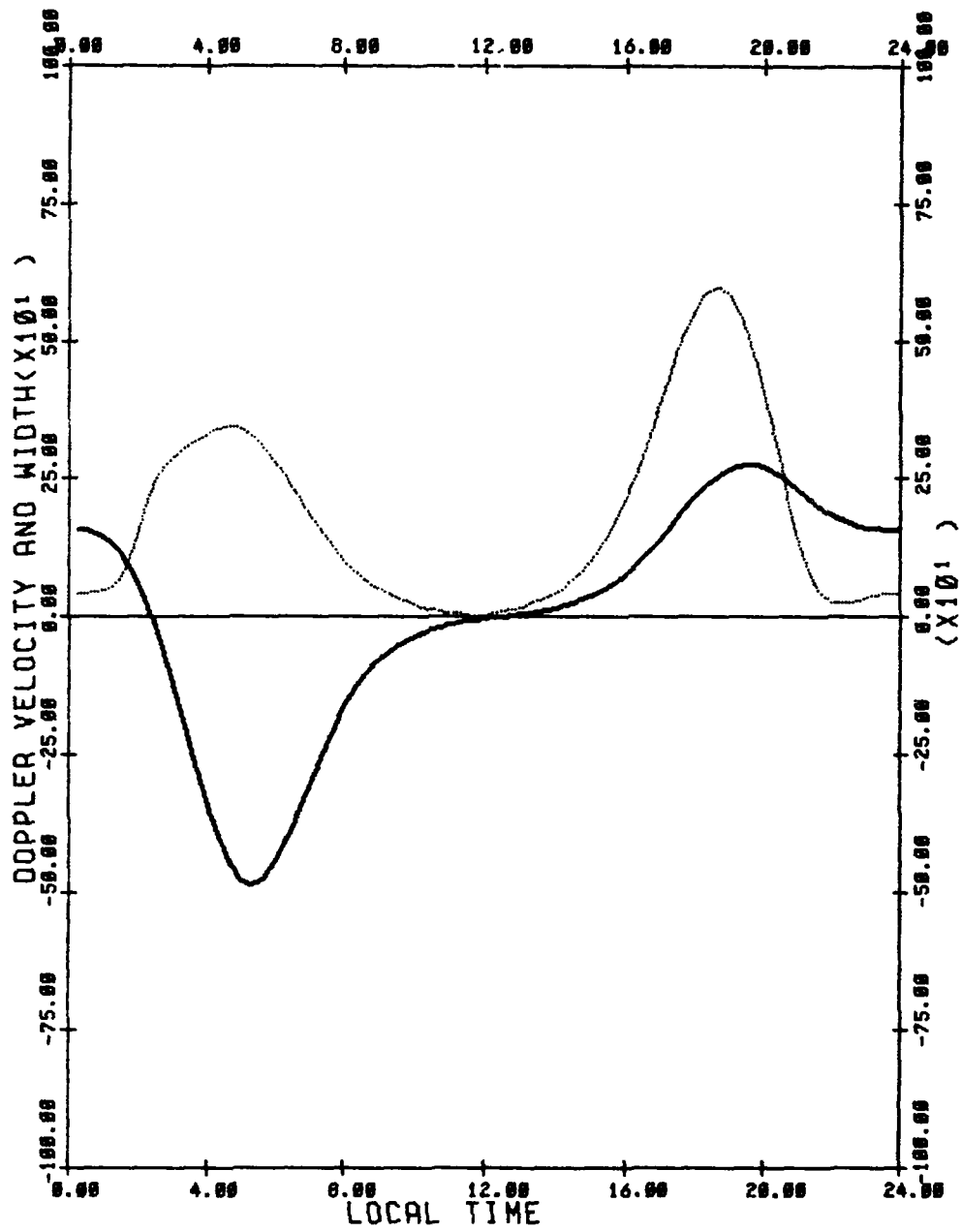
DOPPLER VELOCITY ———
 DOPPLER WIDTH - - - - -
 CROSS POLAR CAP POTENTIAL DROP(V) = 50000
 E-FOLDING DISTANCE OF ARORAL E-FIELD(DEGREES) = 5
 LATITUDE OF POTENTIAL MAXIMUM(DEGREES) = 65
 OVAL OFFSET(DEGREES) = 5
 MEASUREMENT LATITUDE = 55
 VIEWING ANGLE = -30



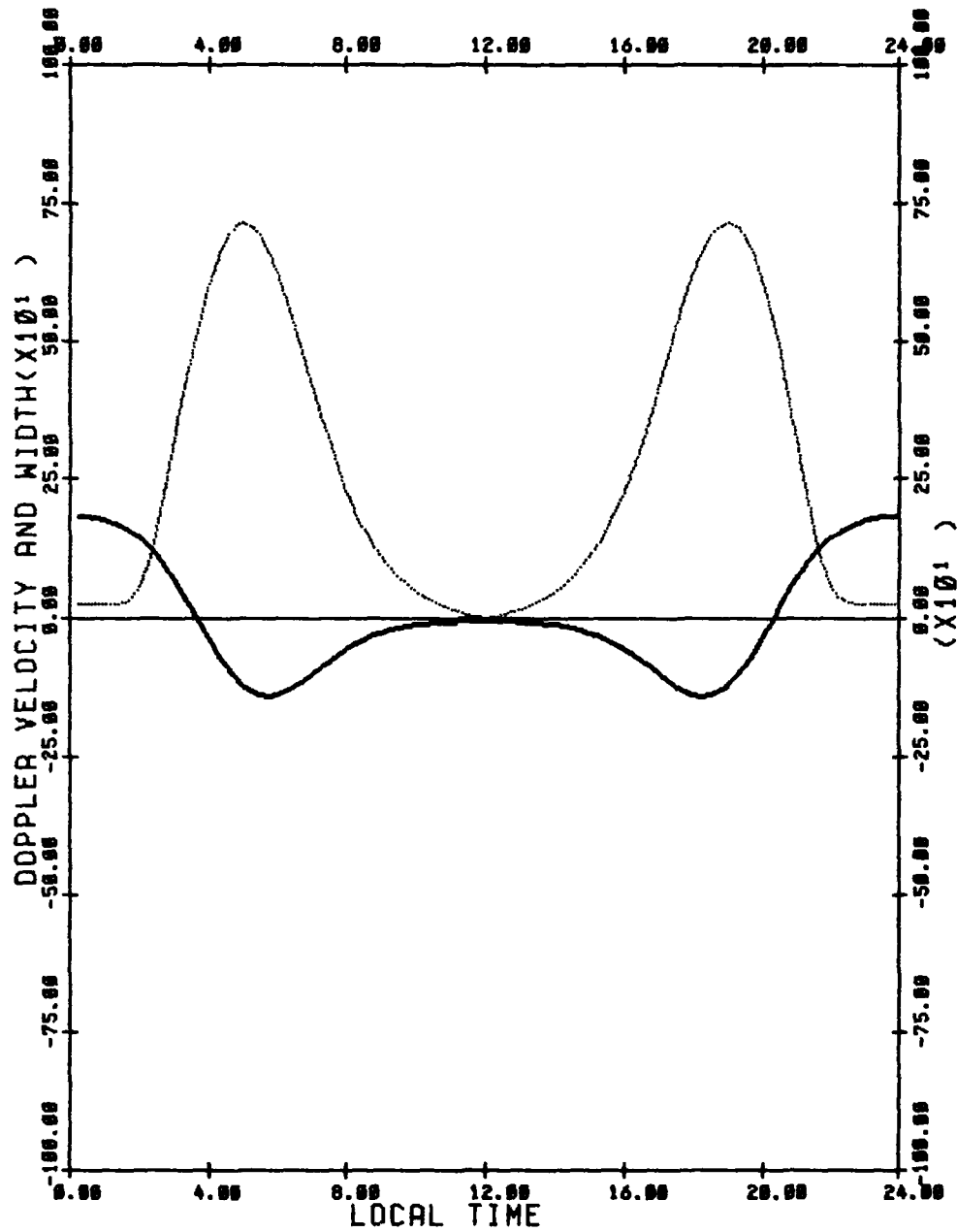
DOPPLER VELOCITY —————
 DOPPLER WIDTH - - - - -
 CROSS POLAR CAP POTENTIAL DROP(V) = 50000
 E-FOLDING DISTANCE OF ARORAL E-FIELD(DEGREES) = 5
 LATITUDE OF POTENTIAL MAXIMUM(DEGREES) = 65
 OVAL OFFSET(DEGREES) = 5
 MEASUREMENT LATITUDE = 55
 VIEWING ANGLE = -60



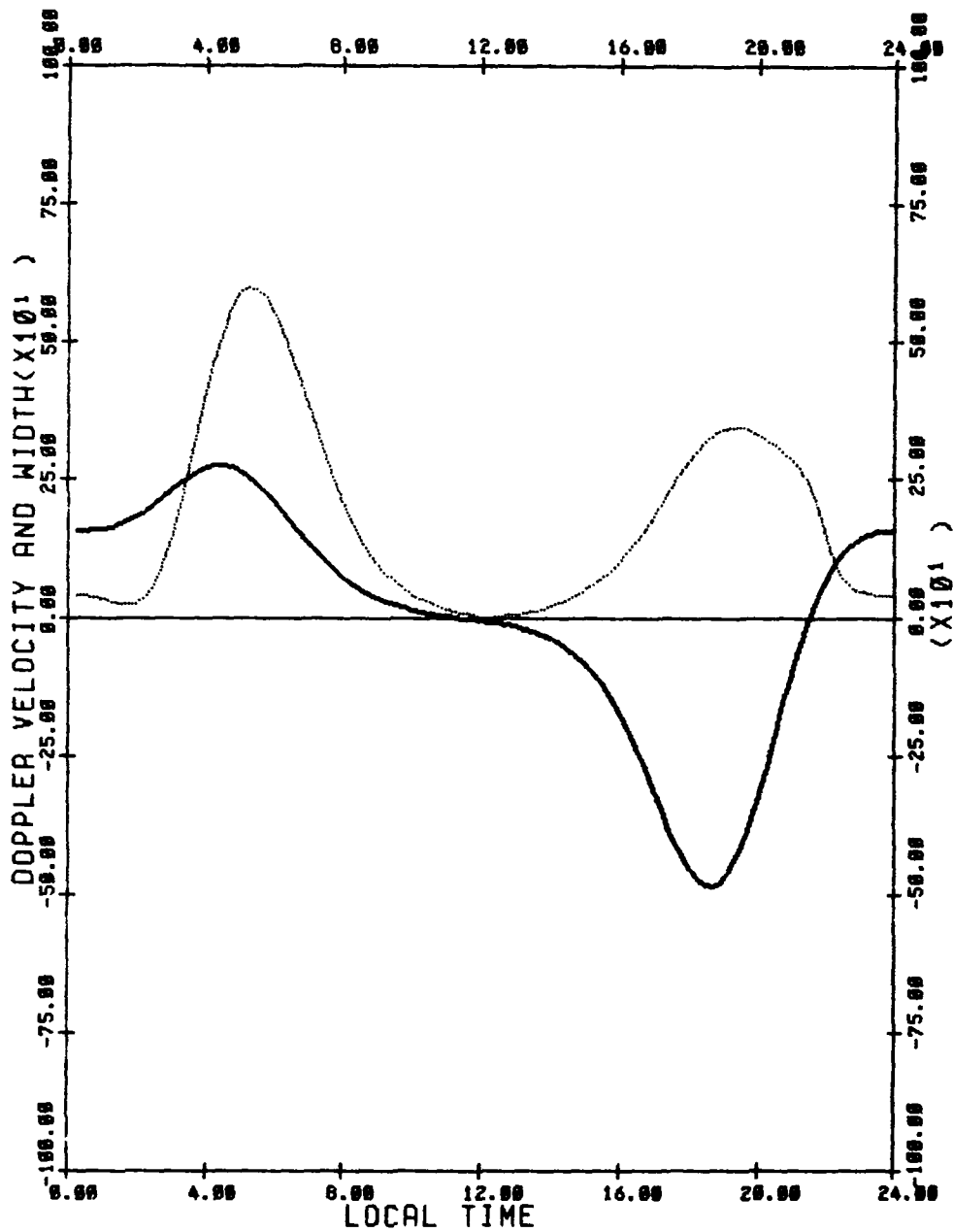
DOPPLER VELOCITY —————
 DOPPLER WIDTH - - - - -
 CROSS POLAR CAP POTENTIAL DROP(V) = 50000
 E-FOLDING DISTANCE OF ARORAL E-FIELD(DEGREES) = 5
 LATITUDE OF POTENTIAL MAXIMUM(DEGREES) = 70
 OVAL OFFSET(DEGREES) = 5
 MEASUREMENT LATITUDE = 65
 VIEWING ANGLE = 60



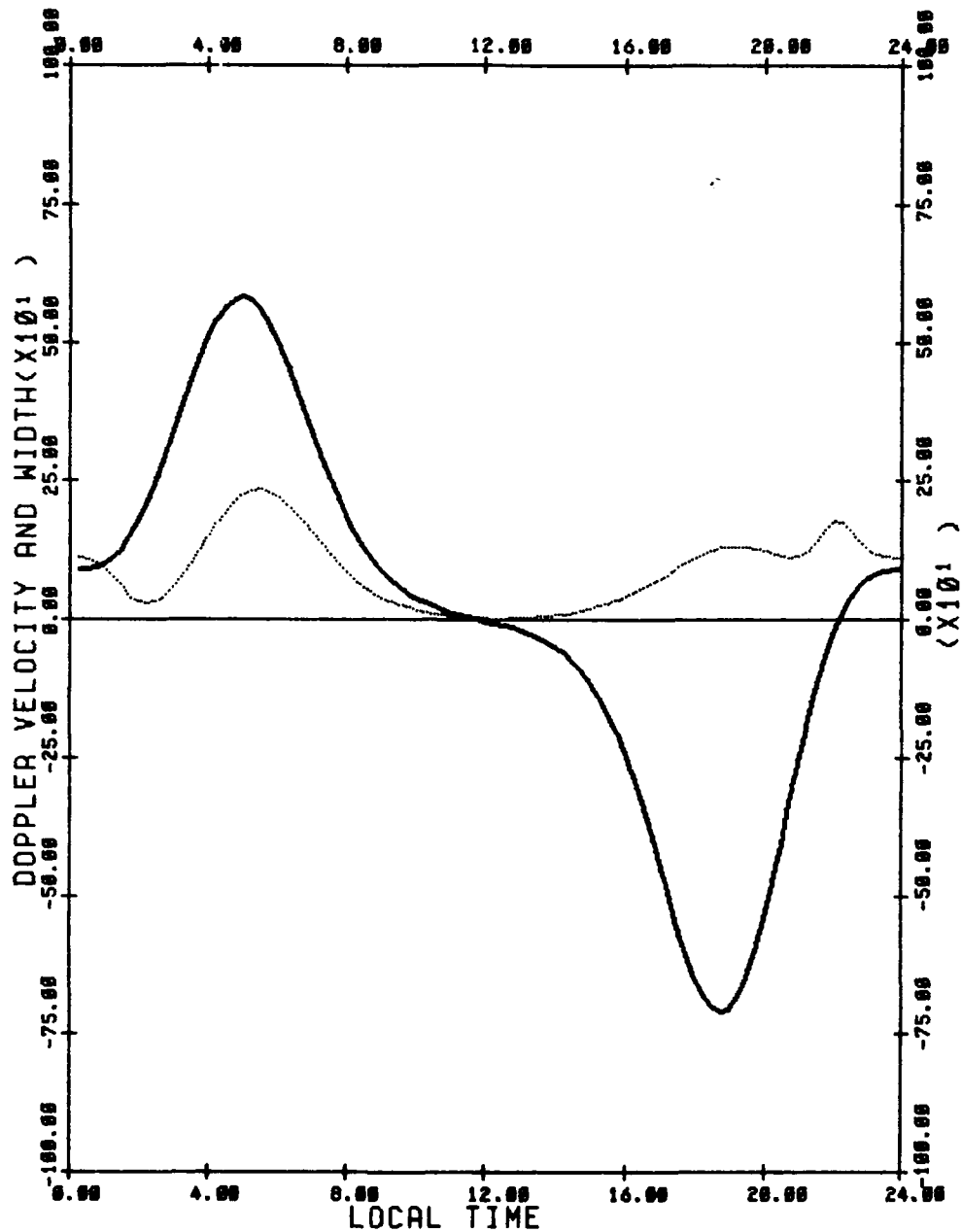
DOPPLER VELOCITY —————
 DOPPLER WIDTH - - - - -
 CROSS POLAR CAP POTENTIAL DROP(V) = 50000
 E-FOLDING DISTANCE OF ARORAL E-FIELD(DEGREES) = 5
 LATITUDE OF POTENTIAL MAXIMUM(DEGREES) = 70
 OVAL OFFSET(DEGREES) = 5
 MEASUREMENT LATITUDE = 65
 VIEWING ANGLE = 30



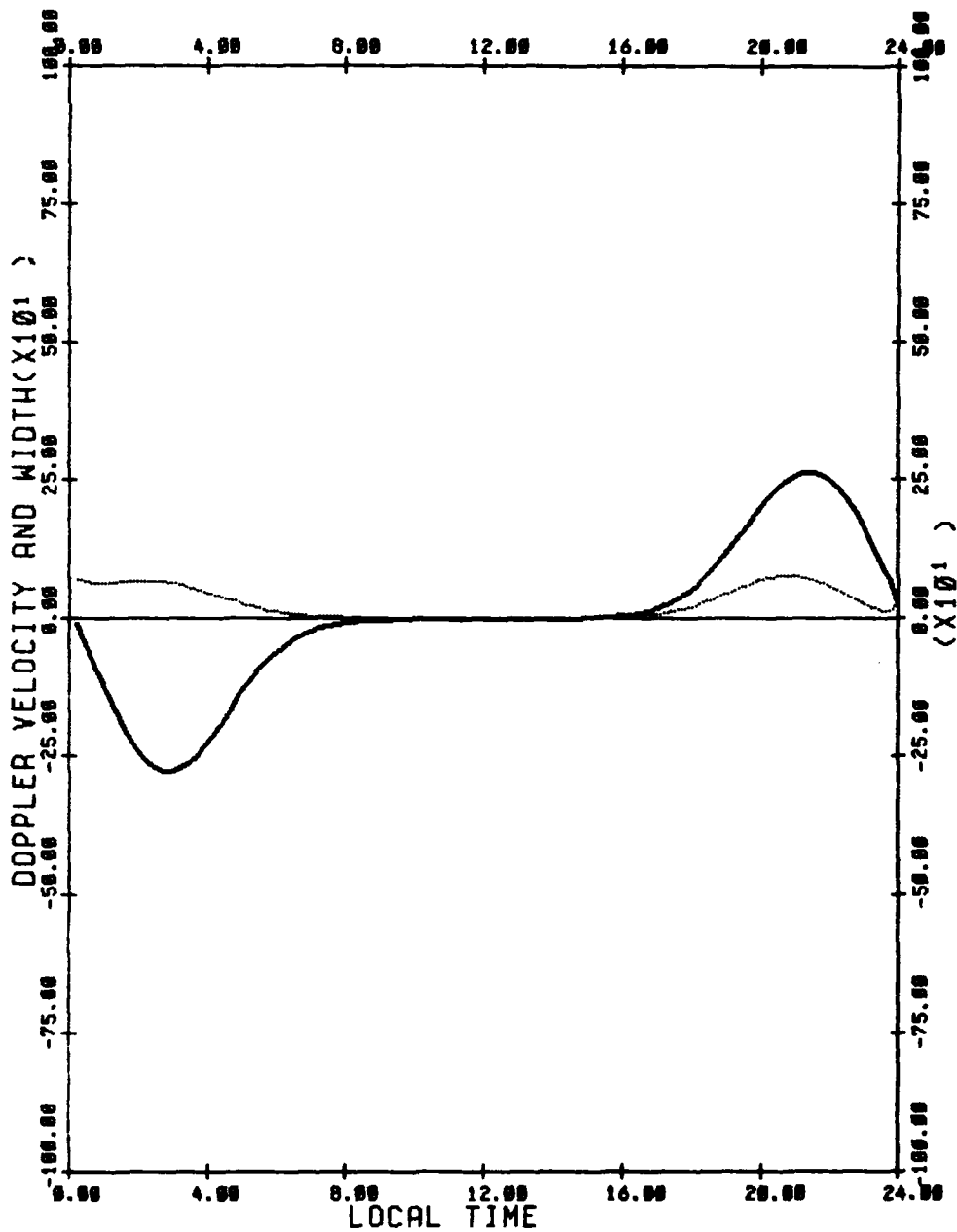
DOPPLER VELOCITY —————
 DOPPLER WIDTH - - - - -
 CROSS POLAR CAP POTENTIAL DROP(V) = 50000
 E-FOLDING DISTANCE OF ARORAL E-FIELD(DEGREES) = 5
 LATITUDE OF POTENTIAL MAXIMUM(DEGREES) = 70
 OVAL OFFSET(DEGREES) = 5
 MEASUREMENT LATITUDE = 65
 VIEWING ANGLE = 0



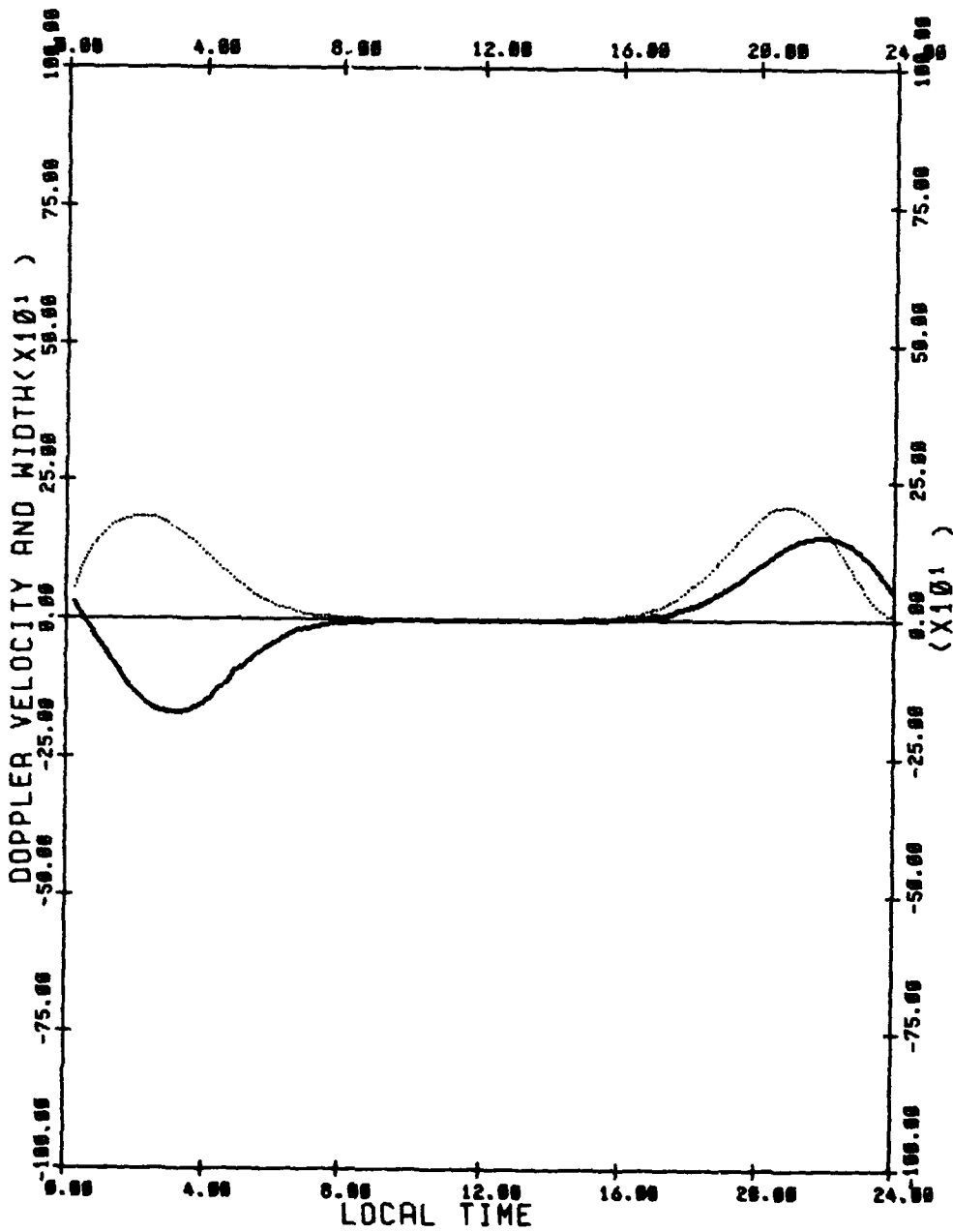
DOPPLER VELOCITY —————
 DOPPLER WIDTH - - - - -
 CROSS POLAR CAP POTENTIAL DROP(V) = 50000
 E-FOLDING DISTANCE OF ARORAL E-FIELD(DEGREES) = 5
 LATITUDE OF POTENTIAL MAXIMUM(DEGREES) = 70
 OVAL OFFSET(DEGREES) = 5
 MEASUREMENT LATITUDE = 65
 VIEWING ANGLE = -30



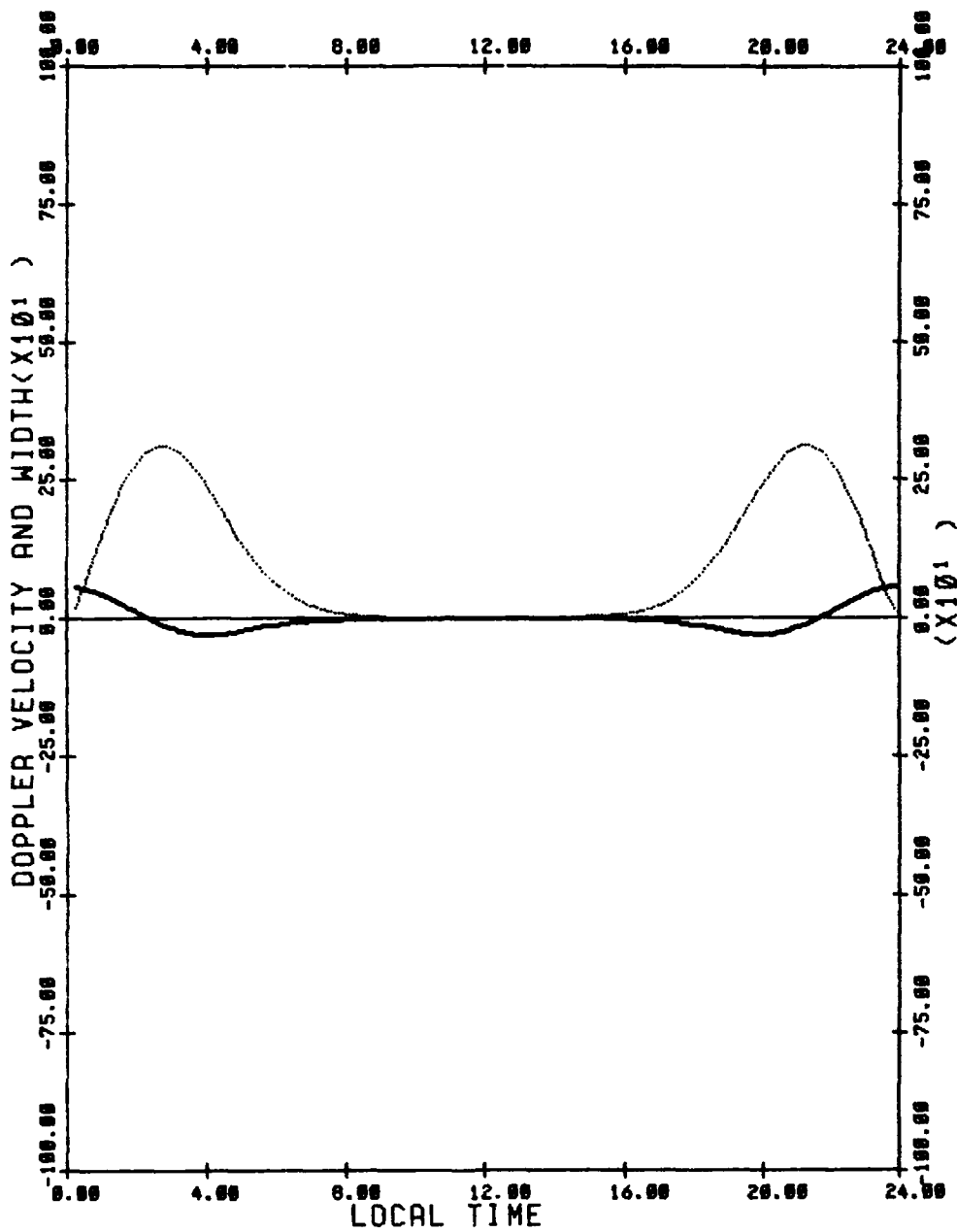
DOPPLER VELOCITY
 DOPPLER WIDTH
 CROSS POLAR CAP POTENTIAL DROP(V) = 50000
 E-FOLDING DISTANCE OF ARORAL E-FIELD(DEGREES) = 5
 LATITUDE OF POTENTIAL MAXIMUM(DEGREES) = 70
 OVAL OFFSET(DEGREES) = 5
 MEASUREMENT LATITUDE = 65
 VIEWING ANGLE = -60



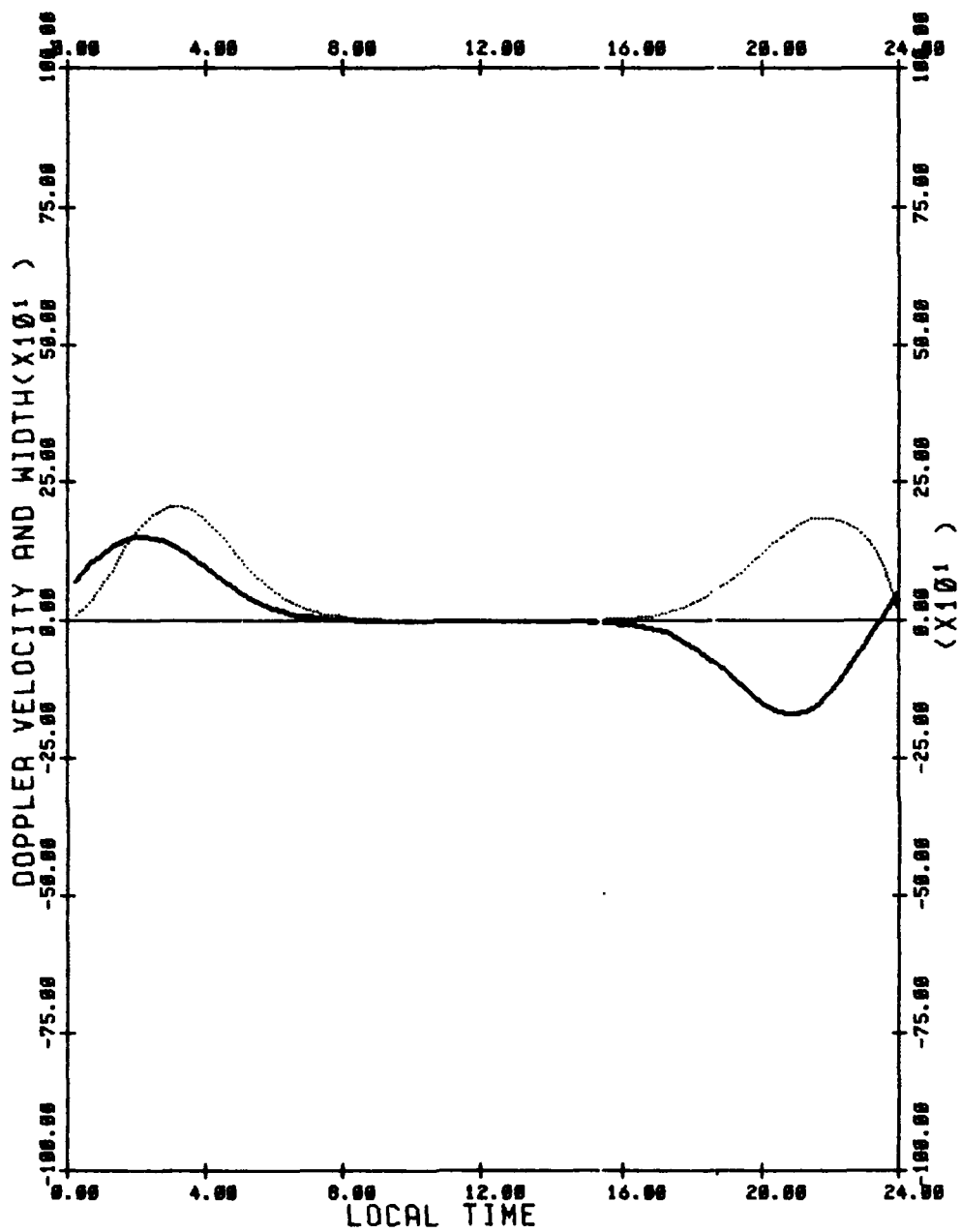
DOPPLER VELOCITY ———
 DOPPLER WIDTH - - - - -
 CROSS POLAR CAP POTENTIAL DROP(V) = 50000
 E-FOLDING DISTANCE OF ARORAL E-FIELD(DEGREES) = 5
 LATITUDE OF POTENTIAL MAXIMUM(DEGREES) = 70
 OVAL OFFSET(DEGREES) = 5
 MEASUREMENT LATITUDE = 60
 VIEWING ANGLE = 60



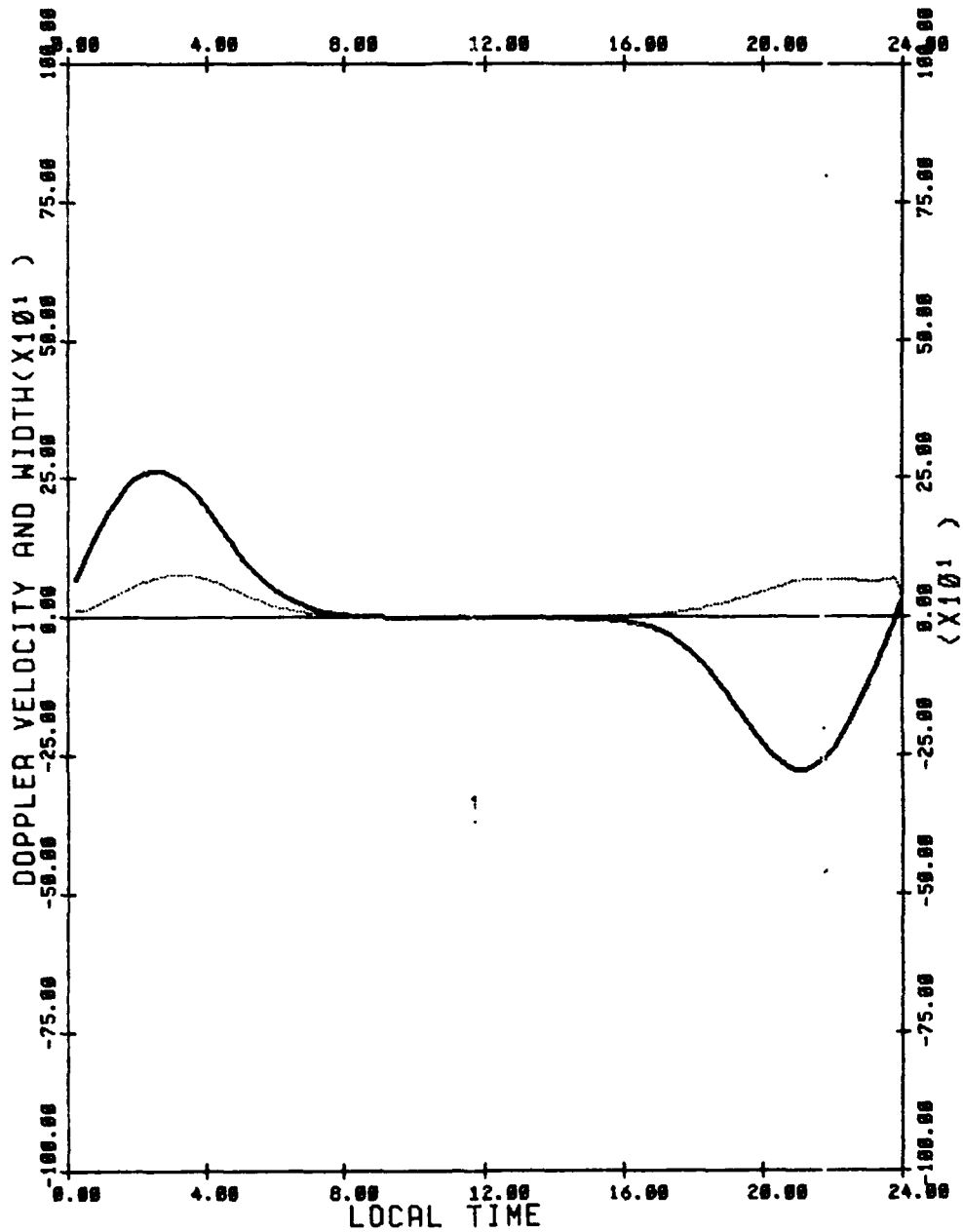
DOPPLER VELOCITY —————
 DOPPLER WIDTH : —————
 CROSS POLAR CAP POTENTIAL DROP(V) = 50000
 E-FOLDING DISTANCE OF ARORAL E-FIELD(DEGREES) = 5
 LATITUDE OF POTENTIAL MAXIMUM(DEGREES) = 70
 OVAL OFFSET(DEGREES) = 5
 MEASUREMENT LATITUDE = 60
 VIEWING ANGLE = 30



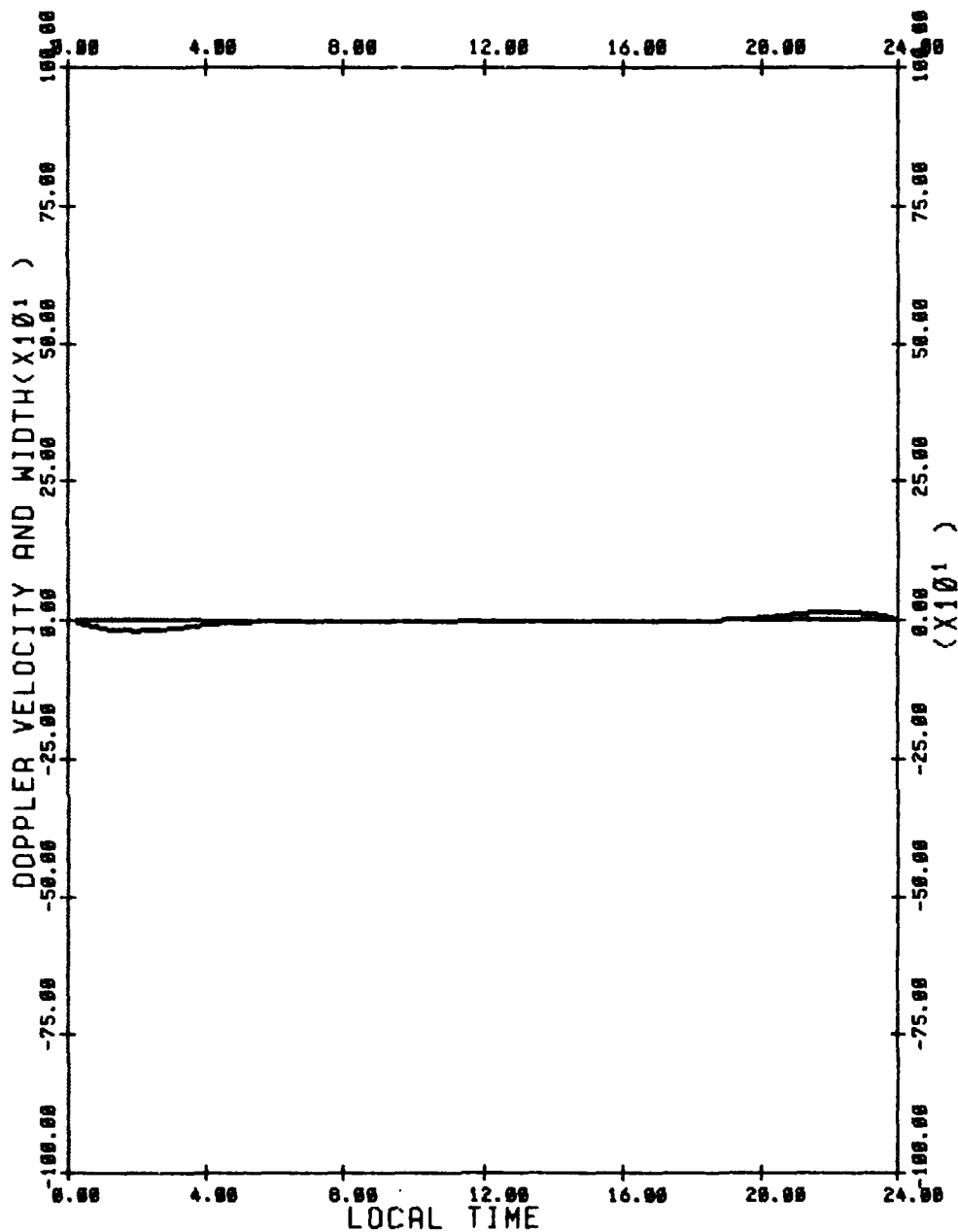
DOPPLER VELOCITY —————
 DOPPLER WIDTH - - - - -
 CROSS POLAR CAP POTENTIAL DROP(V) = 50000
 E-FOLDING DISTANCE OF ARDIAL E-FIELD(DEGREES) = 5
 LATITUDE OF POTENTIAL MAXIMUM(DEGREES) = 70
 OVAL OFFSET(DEGREES) = 5
 MEASUREMENT LATITUDE = 60
 VIEWING ANGLE = 0



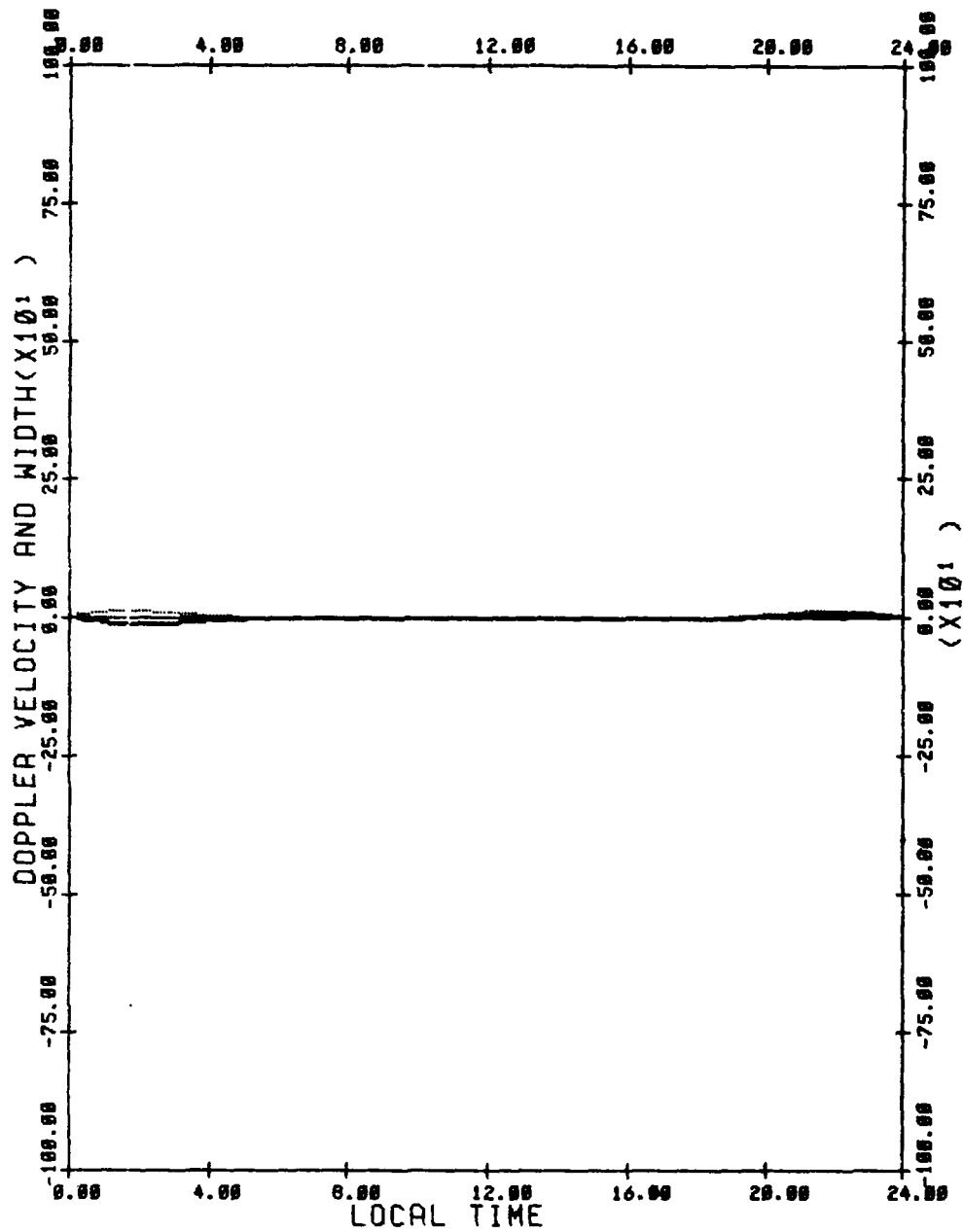
DOPPLER VELOCITY —————
 DOPPLER WIDTH - - - - -
 CROSS POLAR CAP POTENTIAL DROP(V) = 50000
 E-FOLDING DISTANCE OF ARDRAL E-FIELD(DEGREES) = 5
 LATITUDE OF POTENTIAL MAXIMUM(DEGREES) = 70
 OVAL OFFSET(DEGREES) = 5
 MEASUREMENT LATITUDE = 60
 VIEWING ANGLE = -30



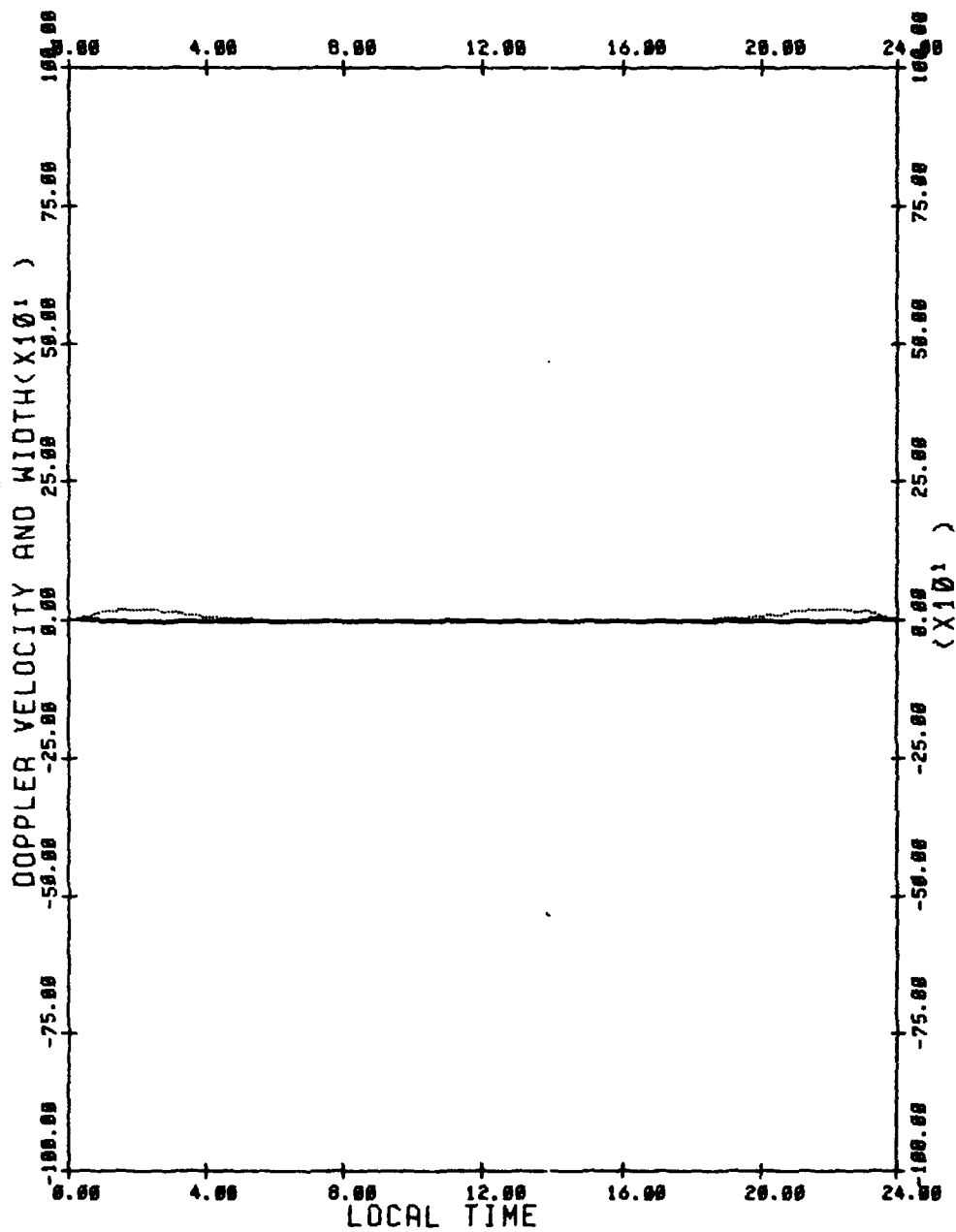
DOPPLER VELOCITY —————
 DOPPLER WIDTH - - - - -
 CROSS POLAR CAP POTENTIAL DROP(V) = 50000
 E-FOLDING DISTANCE OF ARORAL E-FIELD(DEGREES) = 5
 LATITUDE OF POTENTIAL MAXIMUM(DEGREES) = 70
 OVAL OFFSET(DEGREES) = 5
 MEASUREMENT LATITUDE = 60
 VIEWING ANGLE = -60



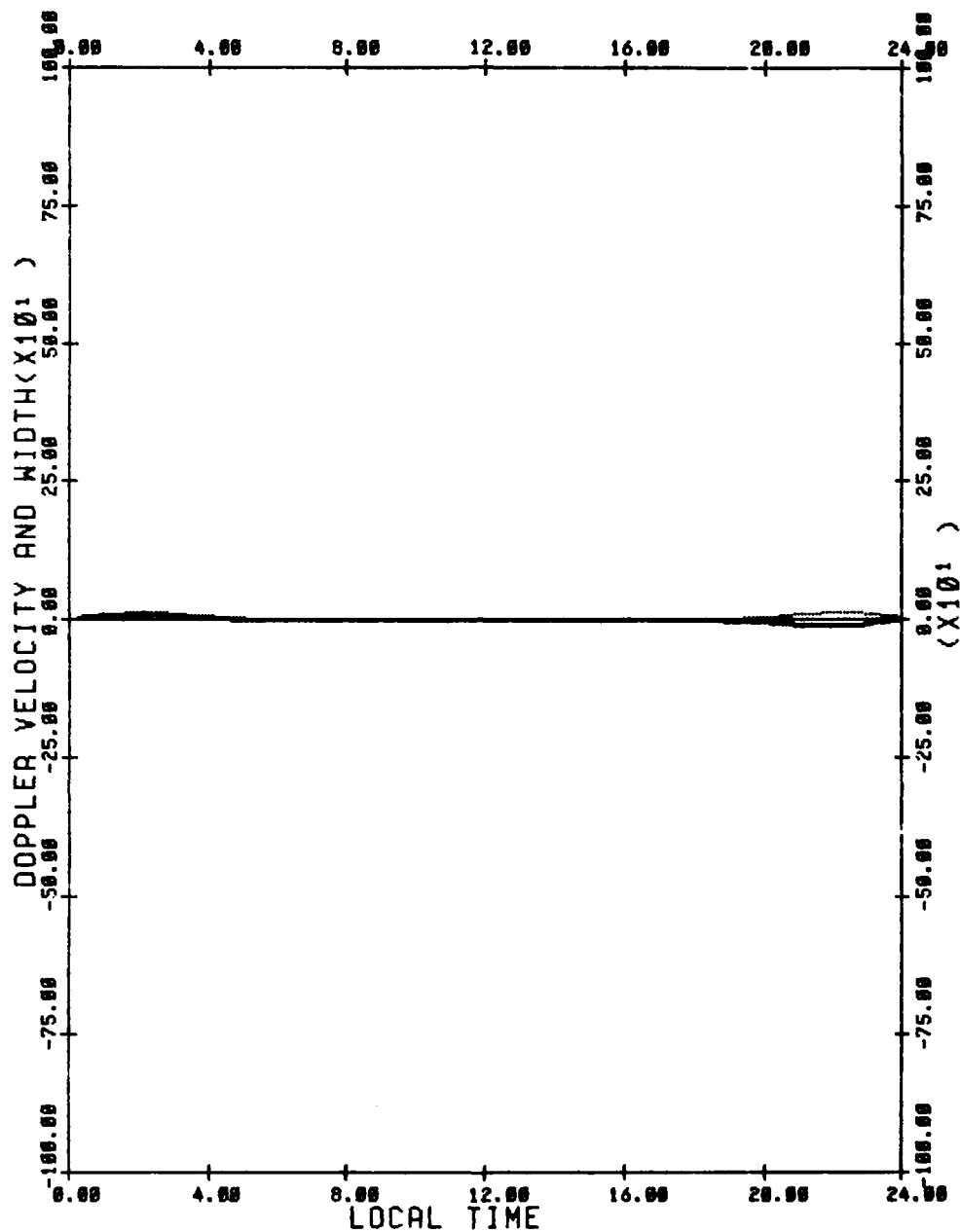
DOPPLER VELOCITY —————
 DOPPLER WIDTH -----
 CROSS POLAR CAP POTENTIAL DROP(V) = 50000
 E-FOLDING DISTANCE OF ARORAL E-FIELD(DEGREES) = 5
 LATITUDE OF POTENTIAL MAXIMUM(DEGREES) = 70
 OVAL OFFSET(DEGREES) = 5
 MEASUREMENT LATITUDE = 55
 VIEWING ANGLE = 60



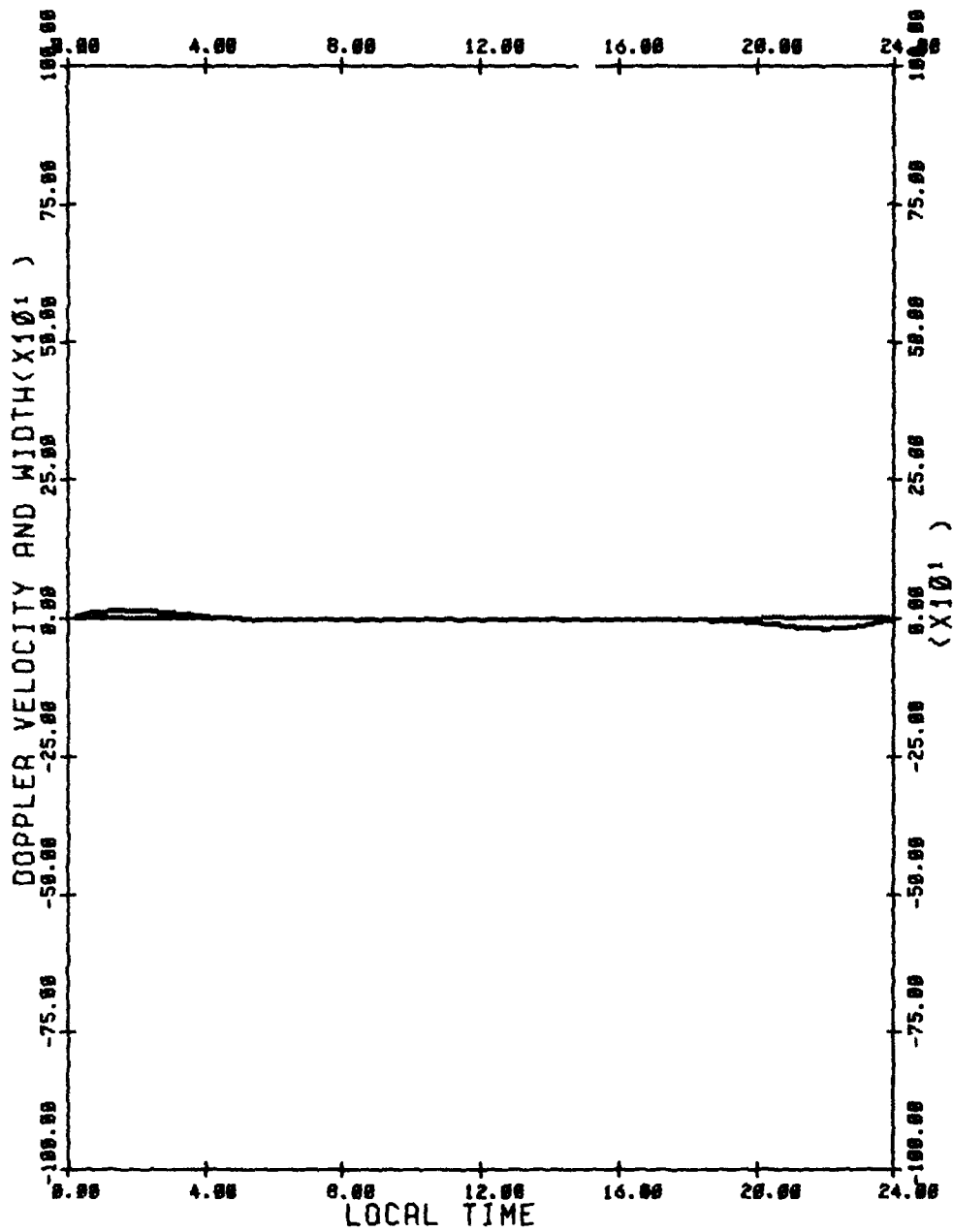
DOPPLER VELOCITY —————
 DOPPLER WIDTH —————
 CROSS POLAR CAP POTENTIAL DROP(V) = 50000
 E-FOLDING DISTANCE OF RADIAL E-FIELD(DEGREES) = 5
 LATITUDE OF POTENTIAL MAXIMUM(DEGREES) = 70
 OVAL OFFSET(DEGREES) = 5
 MEASUREMENT LATITUDE = 55
 VIEWING ANGLE = 30



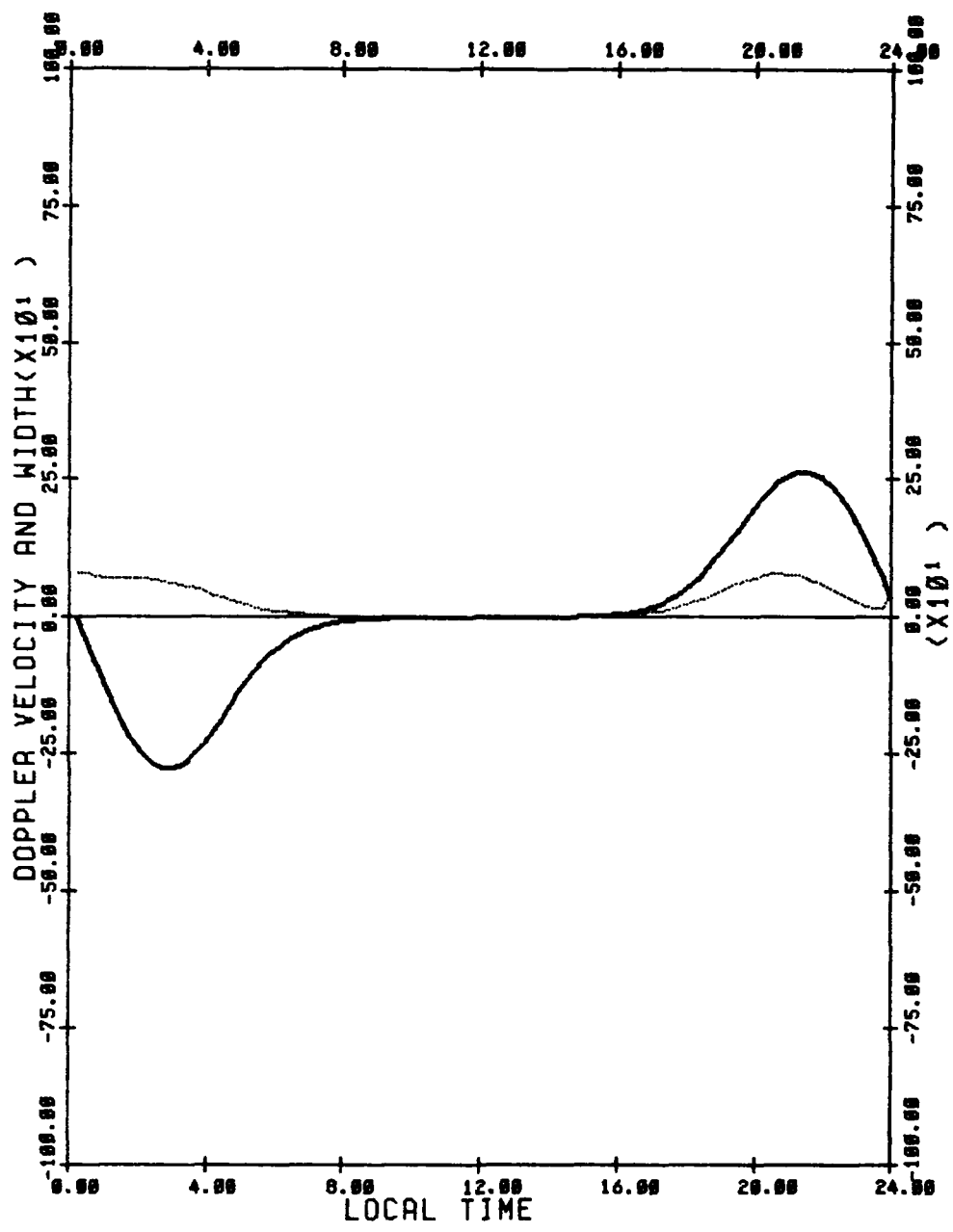
DOPPLER VELOCITY —————
 DOPPLER WIDTH - - - - -
 CROSS POLAR CAP POTENTIAL DROP(V) = 50000
 E-FOLDING DISTANCE OF ARORAL E-FIELD(DEGREES) = 5
 LATITUDE OF POTENTIAL MAXIMUM(DEGREES) = 70
 OVAL OFFSET(DEGREES) = 5
 MEASUREMENT LATITUDE = 55
 VIEWING ANGLE = 0



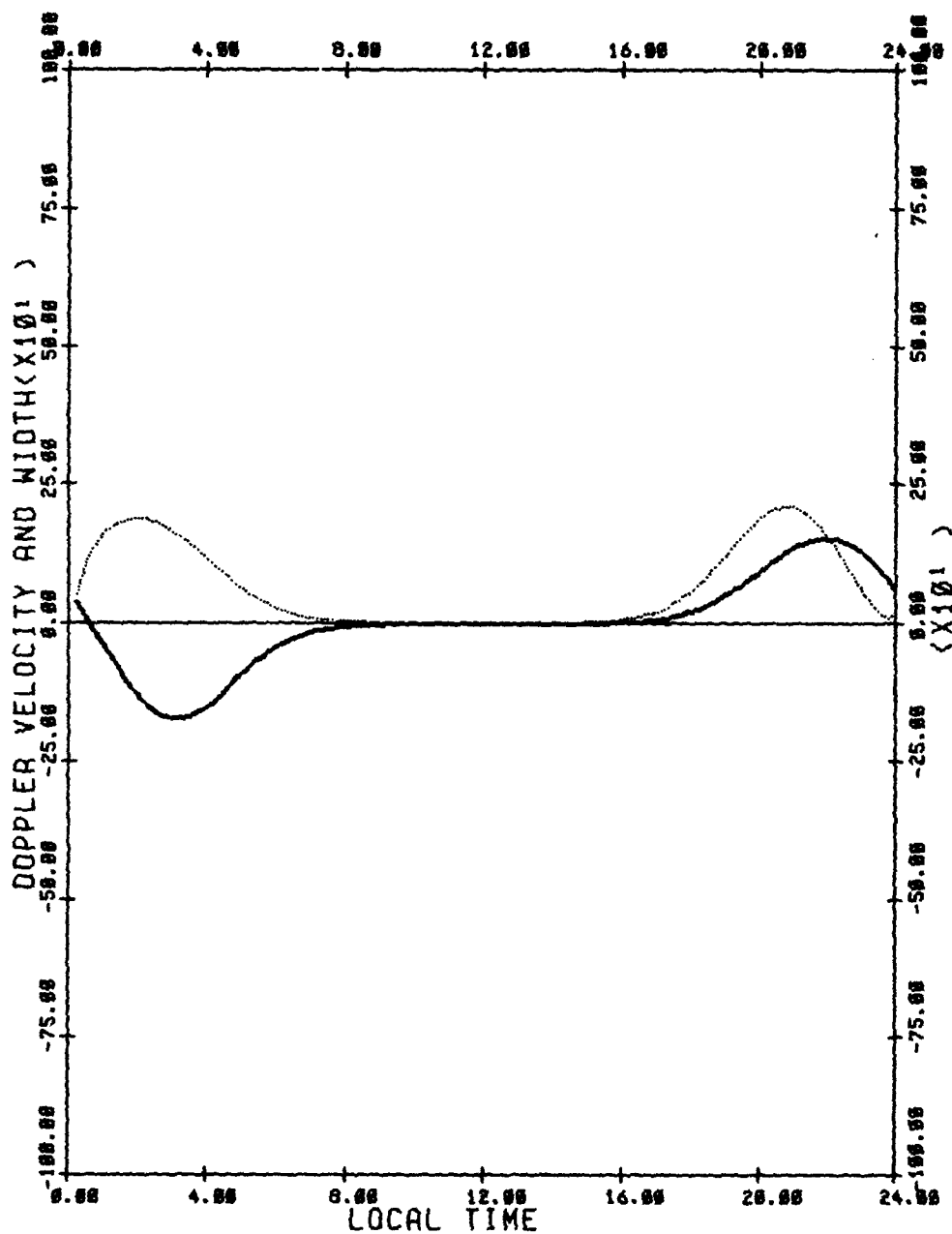
DOPPLER VELOCITY ———
 DOPPLER WIDTH - - - - -
 CROSS POLAR CAP POTENTIAL DROP(V) = 50000
 E-FOLDING DISTANCE OF ARDAL E-FIELD(DEGREES) = 5
 LATITUDE OF POTENTIAL MAXIMUM(DEGREES) = 70
 OVAL OFFSET(DEGREES) = 5
 MEASUREMENT LATITUDE = 55
 VIEWING ANGLE = -30



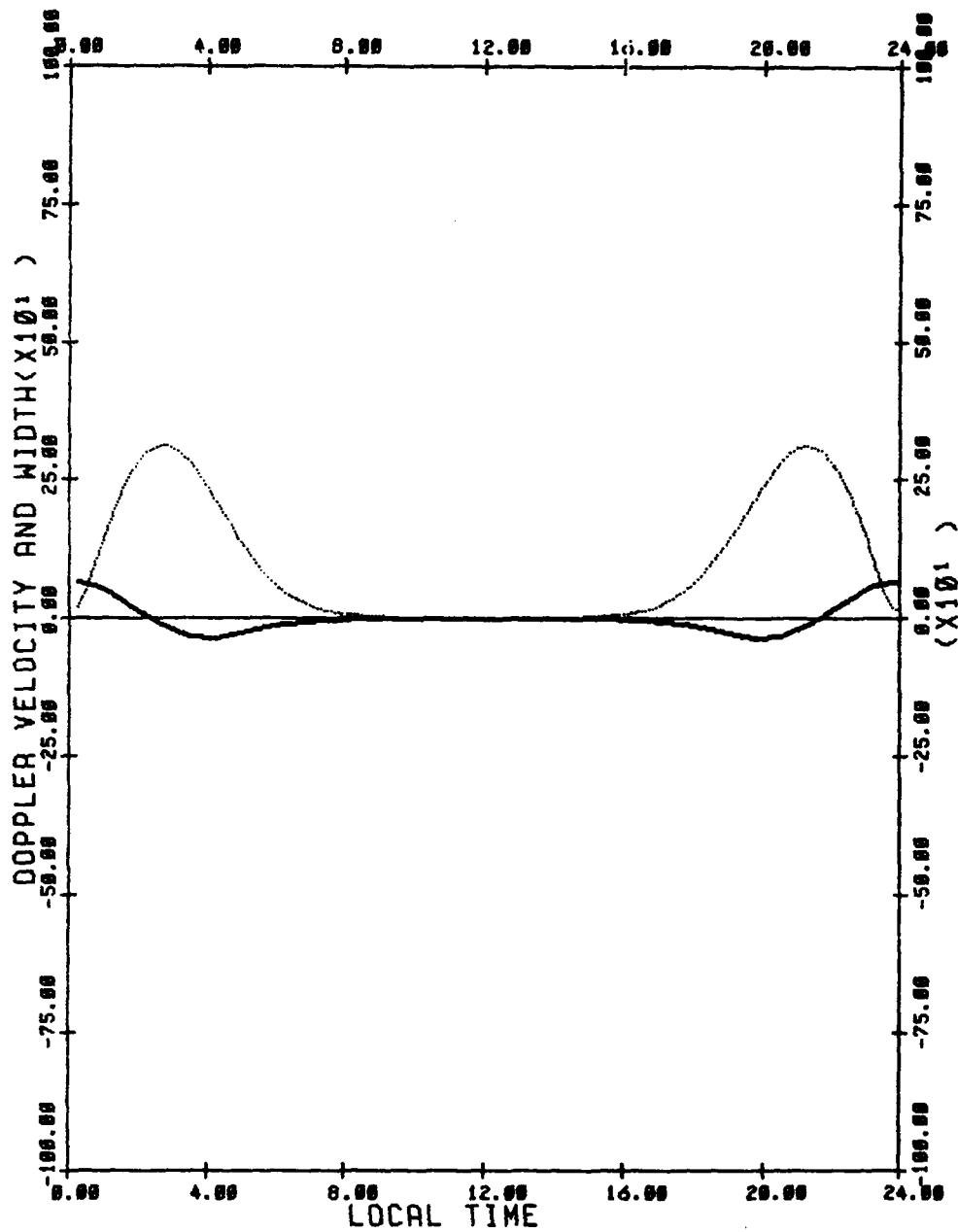
DOPPLER VELOCITY
 DOPPLER WIDTH
 CROSS POLAR CAP POTENTIAL DROP(V) = 50000
 E-FOLDING DISTANCE OF RADIAL E-FIELD(DEGREES) = 5
 LATITUDE OF POTENTIAL MAXIMUM(DEGREES) = 70
 OVAL OFFSET(DEGREES) = 5
 MEASUREMENT LATITUDE = 55
 VIEWING ANGLE = -60



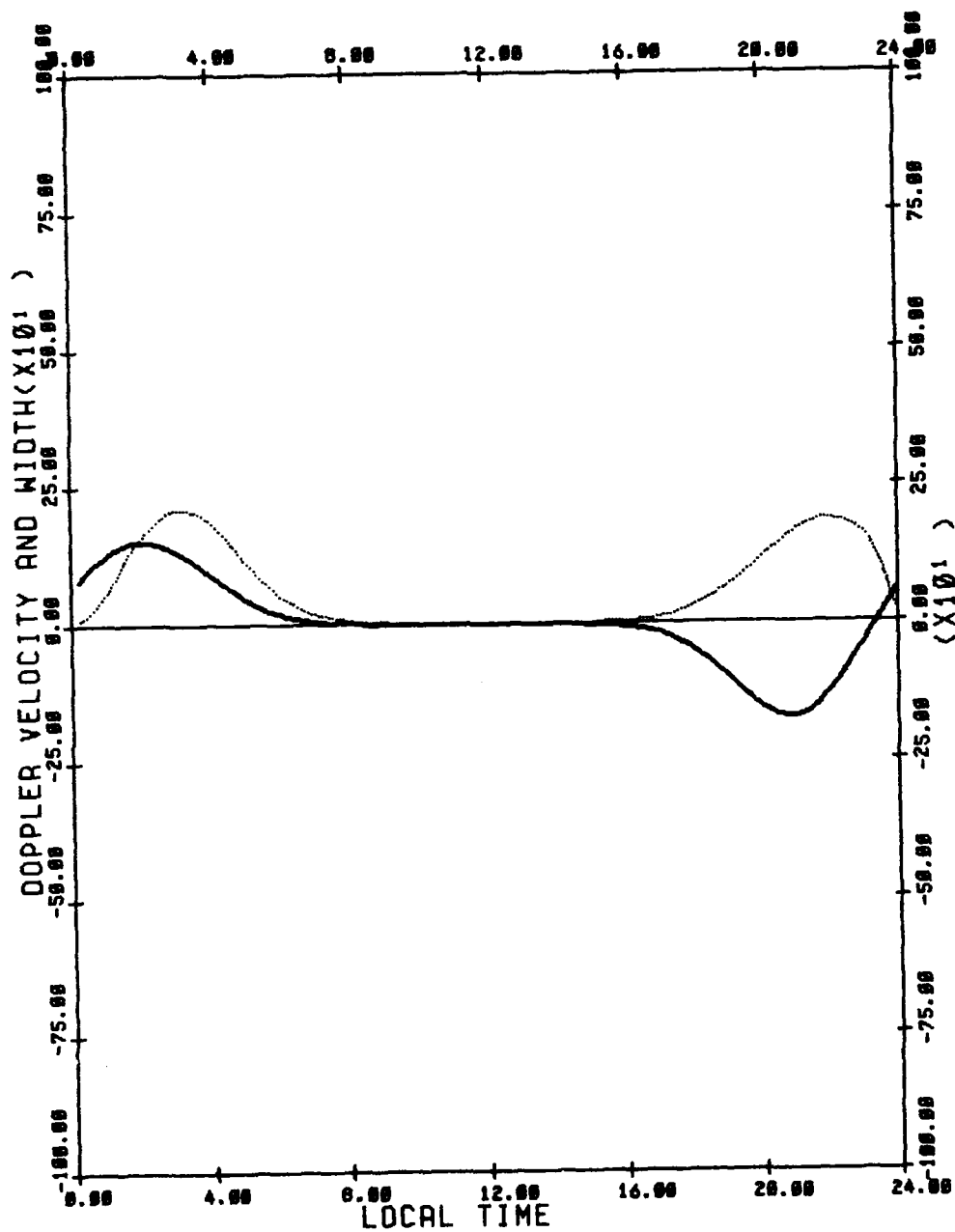
DOPPLER VELOCITY
 DOPPLER WIDTH
 CROSS POLAR CAP POTENTIAL DROP(V) = 50000
 E-FOLDING DISTANCE OF ARORAL E-FIELD(DEGREES) = 5
 LATITUDE OF POTENTIAL MAXIMUM(DEGREES) = 75
 OVAL OFFSET(DEGREES) = 5
 MEASUREMENT LATITUDE = 65
 VIEWING ANGLE = 60



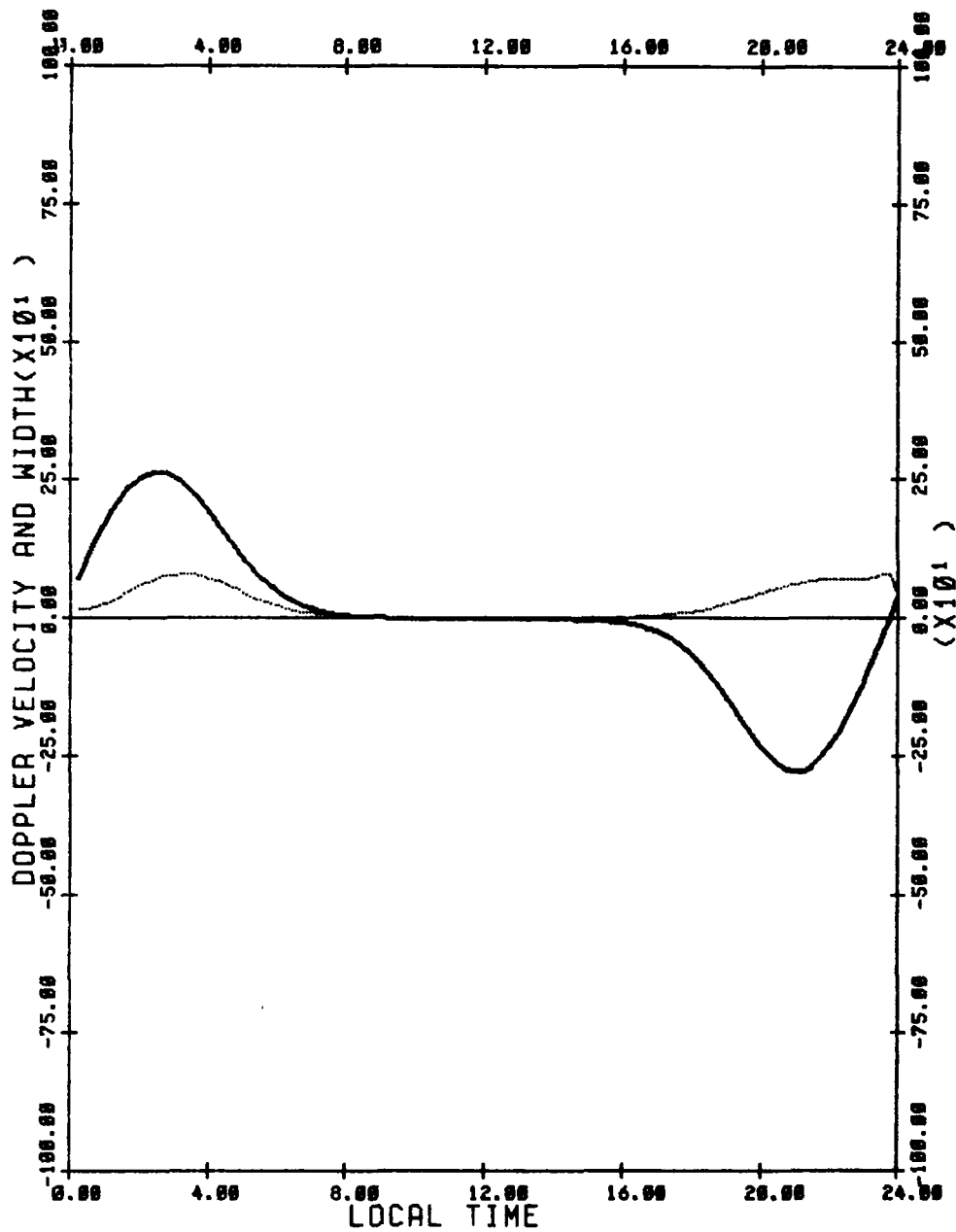
DOPPLER VELOCITY ———
 DOPPLER WIDTH - - - - -
 CROSS POLAR CAP POTENTIAL DROP(V) = 50000
 E-FOLDING DISTANCE OF RADIAL E-FIELD(DEGREES) = 5
 LATITUDE OF POTENTIAL MAXIMUM(DEGREES) = 75
 OVAL OFFSET(DEGREES) = 5
 MEASUREMENT LATITUDE = 65
 VIEWING ANGLE = 30



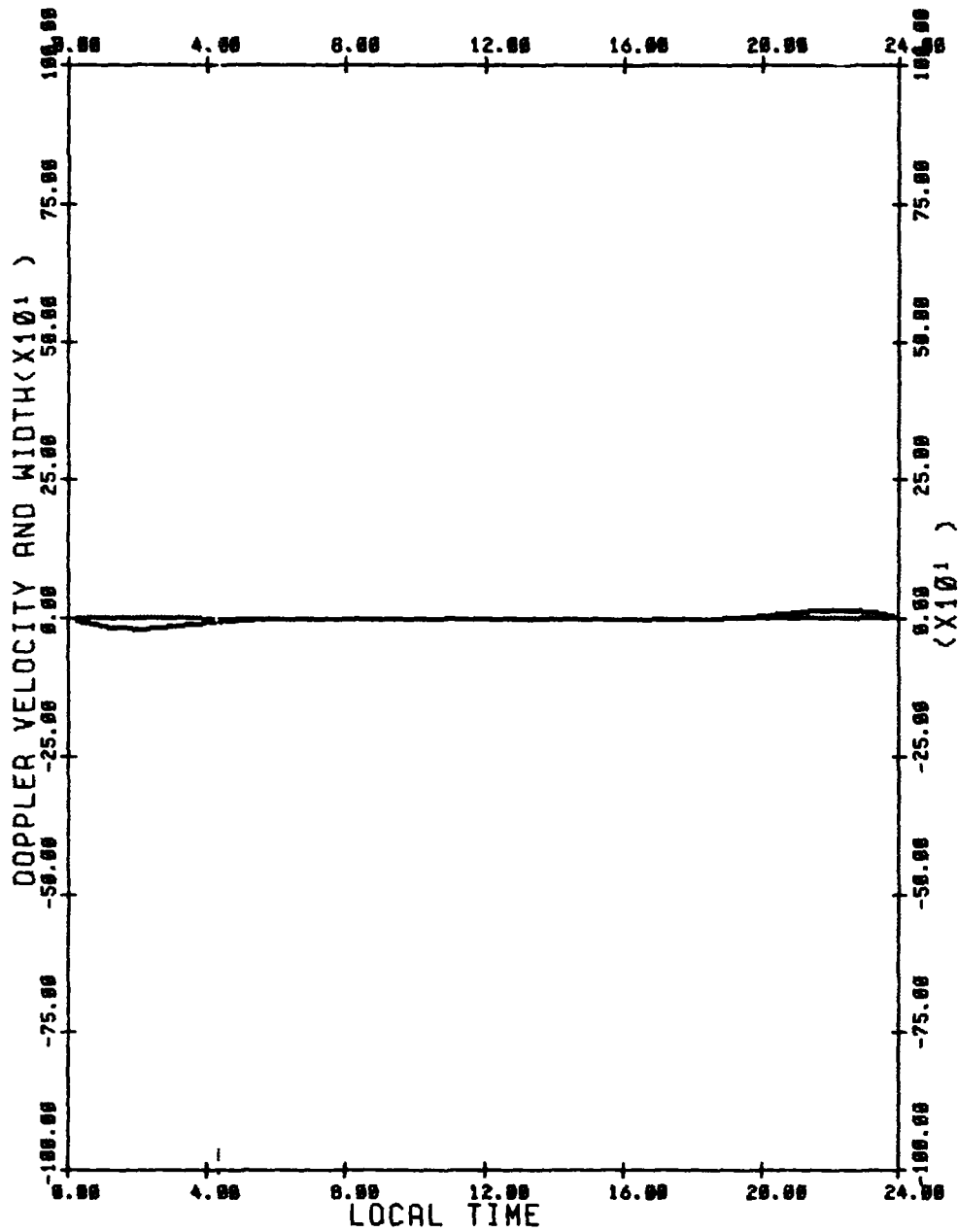
DOPPLER VELOCITY ———
 DOPPLER WIDTH ———
 CROSS POLAR CAP POTENTIAL DROP(V) = 50000
 E-FOLDING DISTANCE OF AURORAL E-FIELD(DEGREES) = 5
 LATITUDE OF POTENTIAL MAXIMUM(DEGREES) = 75
 OVAL OFFSET(DEGREES) = 5
 MEASUREMENT LATITUDE = 65
 VIEWING ANGLE = 0



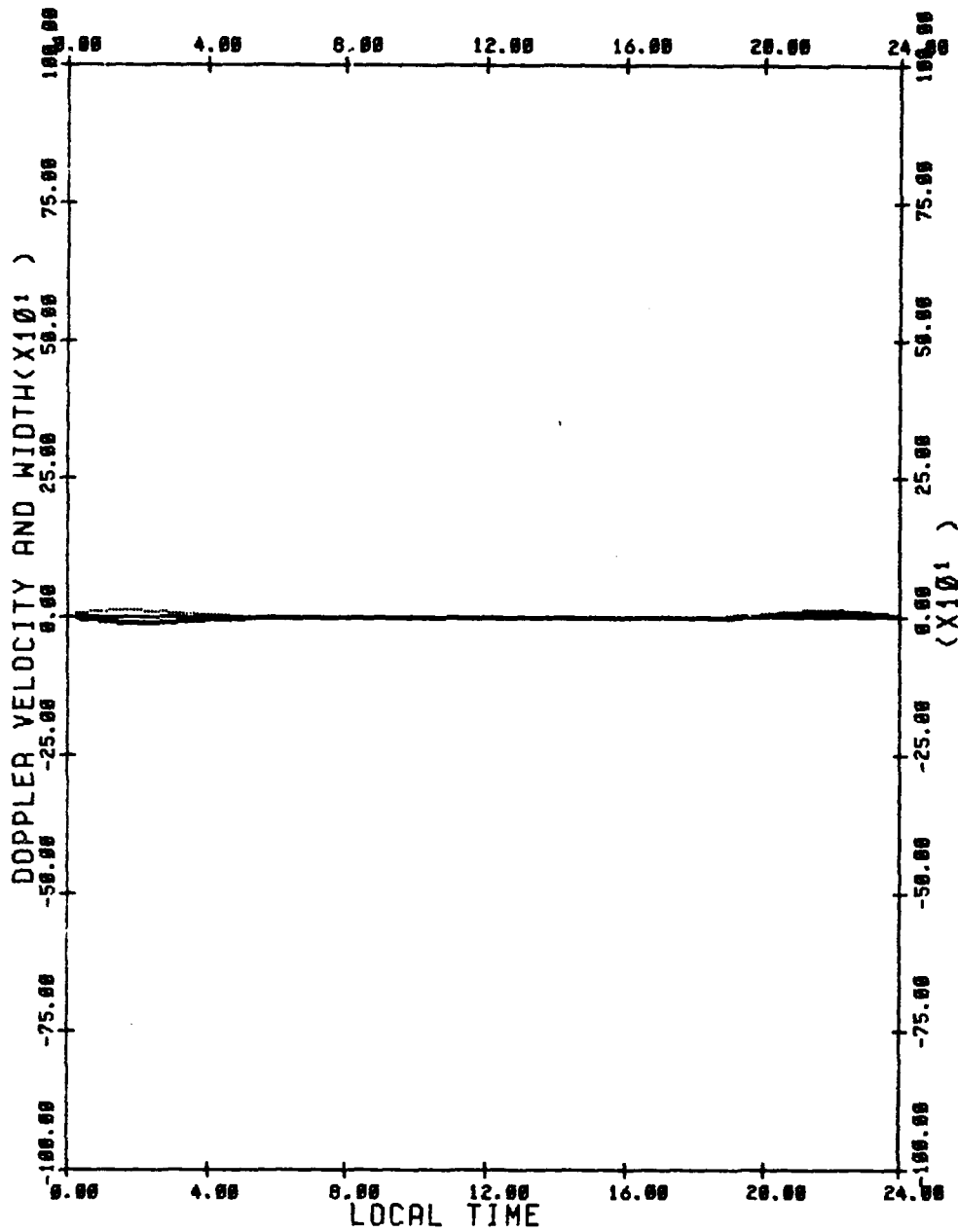
DOPPLER VELOCITY ———
 DOPPLER WIDTH - - - - -
 CROSS POLAR CAP POTENTIAL DROP(V) = 50000
 E-FOLDING DISTANCE OF ARORAL E-FIELD(DEGREES) = 5
 LATITUDE OF POTENTIAL MAXIMUM(DEGREES) = 75
 OVAL OFFSET(DEGREES) = 5
 MEASUREMENT LATITUDE = 65
 VIEWING ANGLE = -30



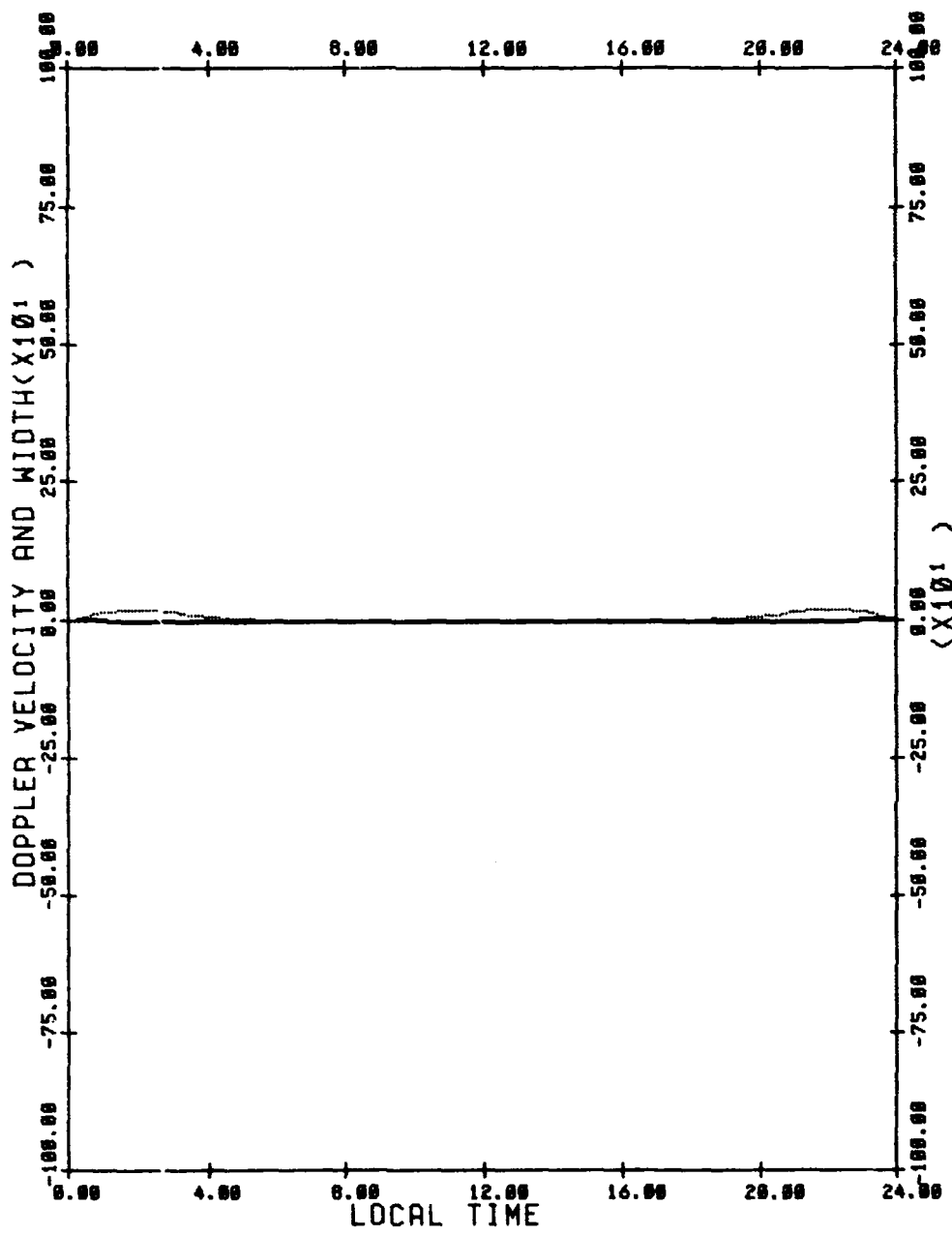
DOPPLER VELOCITY —————
 DOPPLER WIDTH - - - - -
 CROSS POLAR CAP POTENTIAL DROP(V) = 50000
 E-FOLDING DISTANCE OF ARDAL E-FIELD(DEGREES) = 5
 LATITUDE OF POTENTIAL MAXIMUM(DEGREES) = 75
 OVAL OFFSET(DEGREES) = 5
 MEASUREMENT LATITUDE = 65
 VIEWING ANGLE = -60



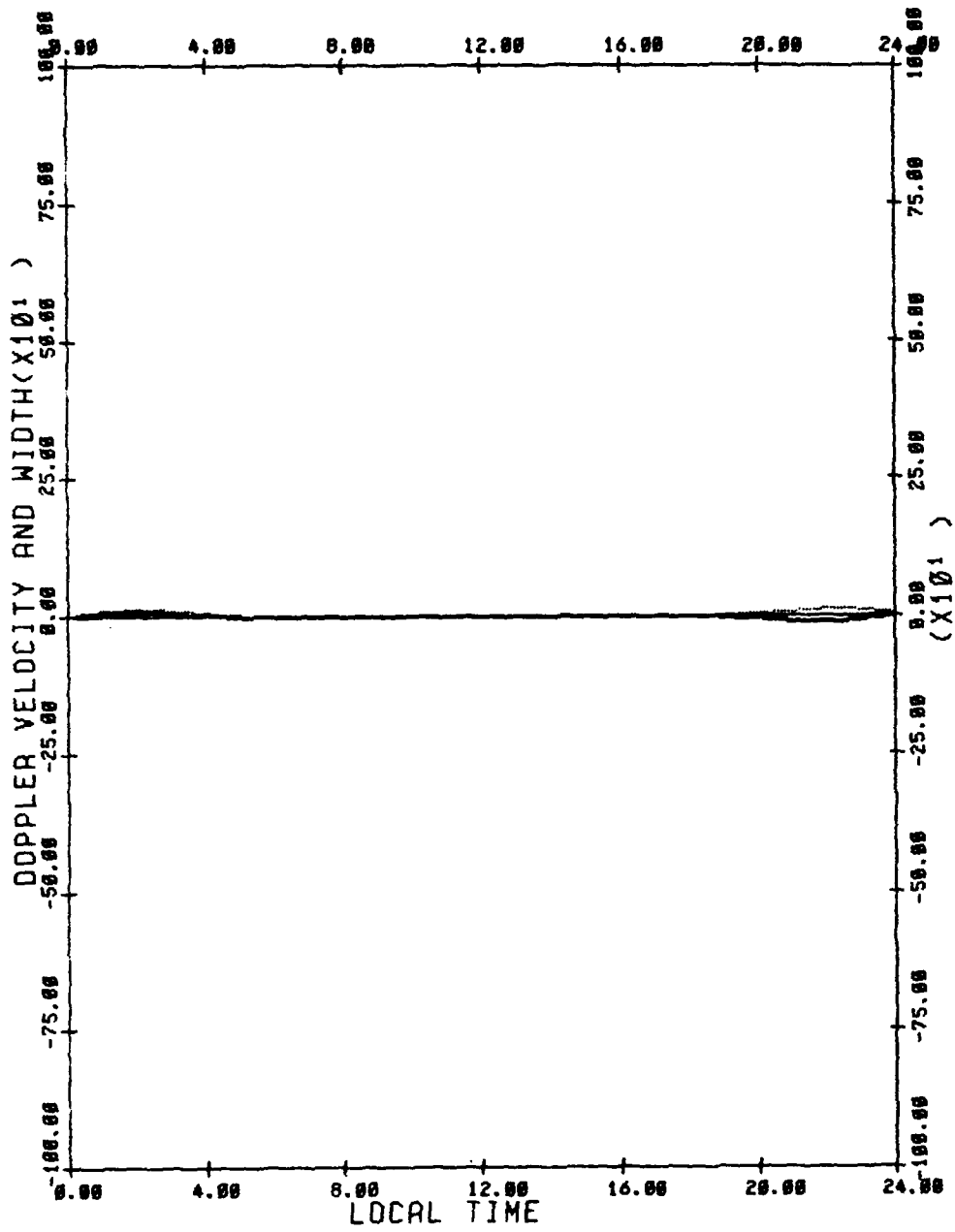
DOPPLER VELOCITY —————
 DOPPLER WIDTH - - - - -
 CROSS POLAR CAP POTENTIAL DROP(V) = 50000
 E-FOLDING DISTANCE OF ARORAL E-FIELD(DEGREES) = 5
 LATITUDE OF POTENTIAL MAXIMUM(DEGREES) = 75
 OVAL OFFSET(DEGREES) = 5
 MEASUREMENT LATITUDE = 60
 VIEWING ANGLE = 60



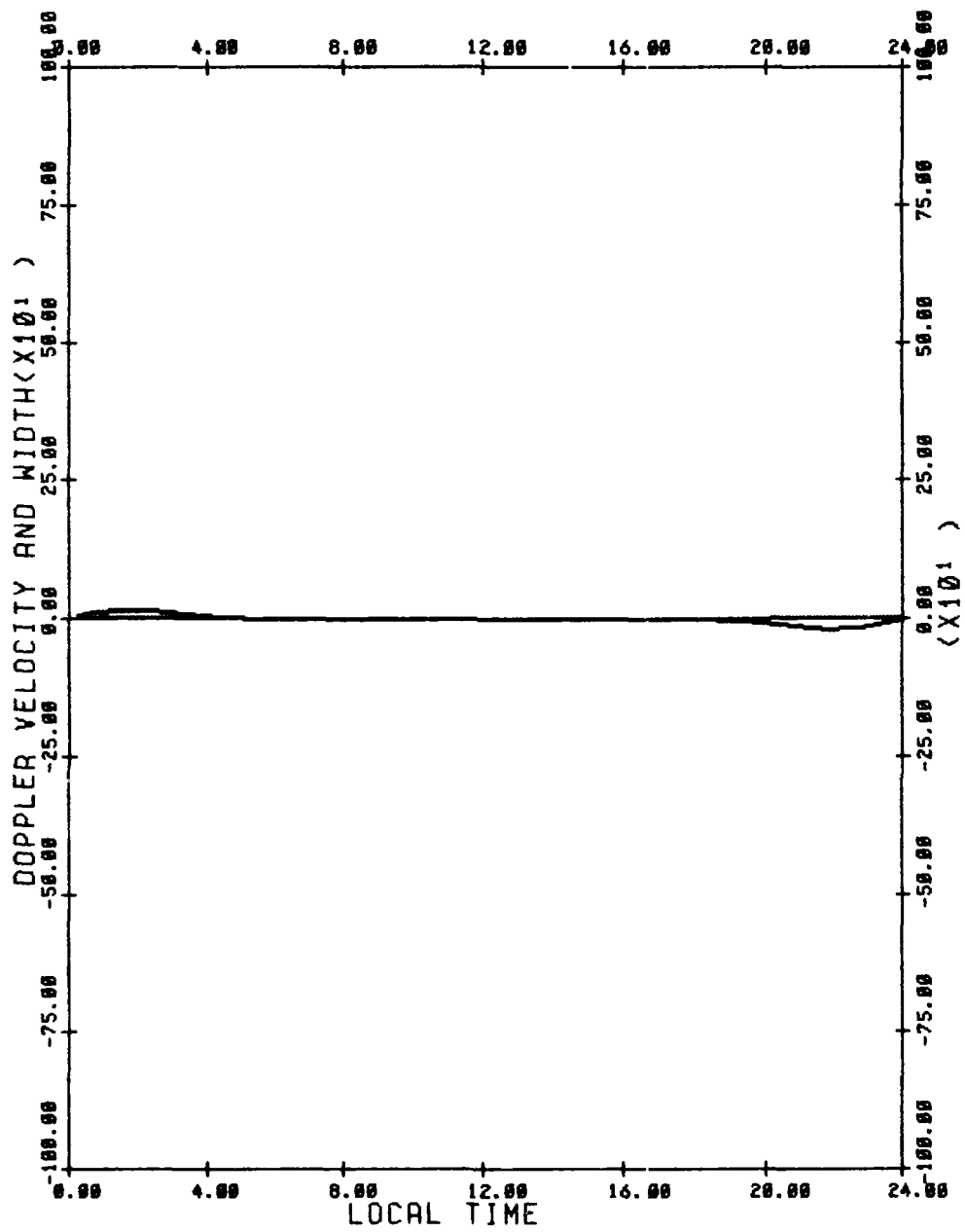
DOPPLER VELOCITY —————
 DOPPLER WIDTH —————
 CROSS POLAR CAP POTENTIAL DROP(V) = 50000
 E-FOLDING DISTANCE OF ARDIAL E-FIELD(DEGREES) = 5
 LATITUDE OF POTENTIAL MAXIMUM(DEGREES) = 75
 OVAL OFFSET(DEGREES) = 5
 MEASUREMENT LATITUDE = 60
 VIEWING ANGLE = 30



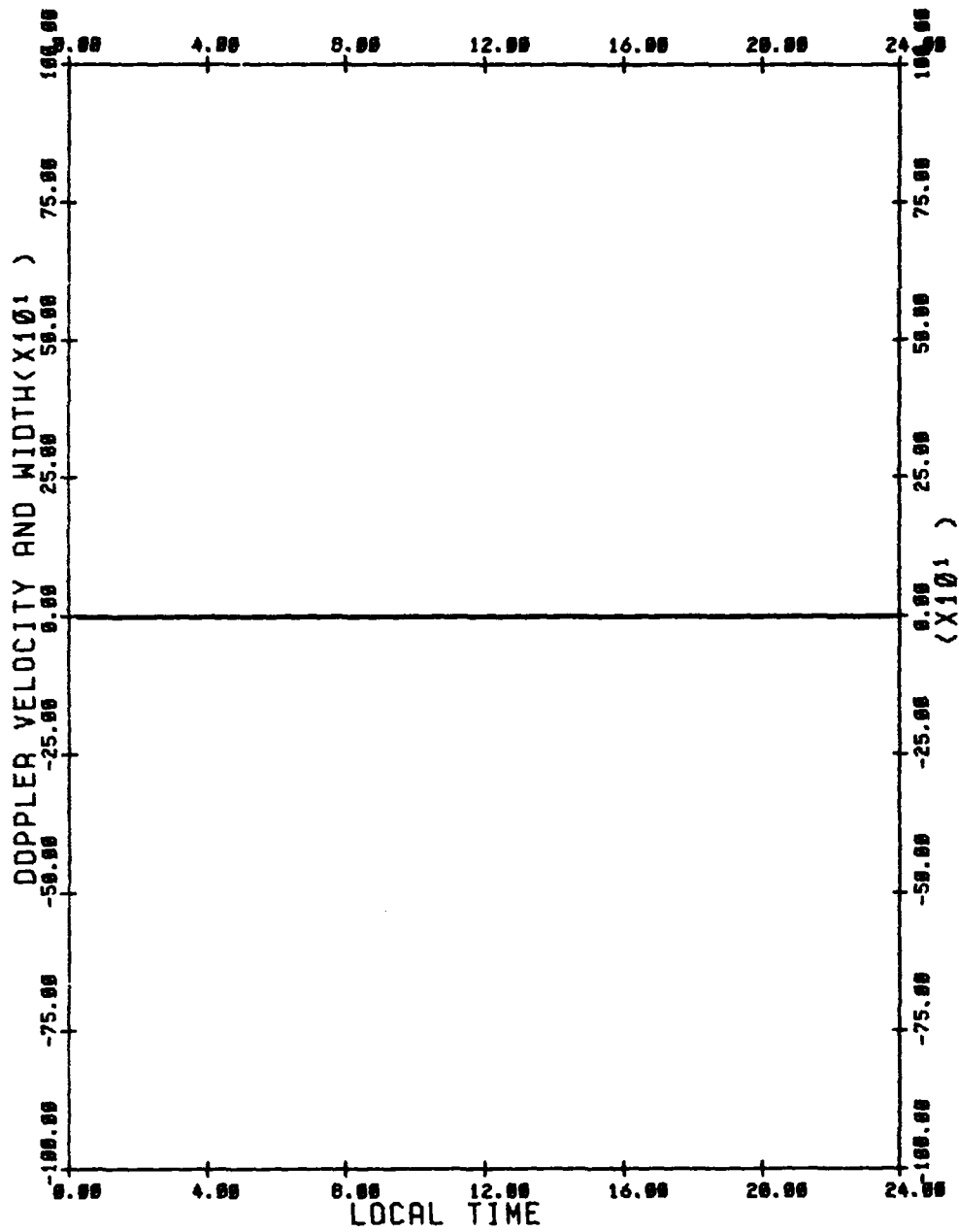
DOPPLER VELOCITY —————
 DOPPLER WIDTH - - - - -
 CROSS POLAR CAP POTENTIAL DROP(V) = 50000
 E-FOLDING DISTANCE OF ARDIAL E-FIELD(DEGREES) = 5
 LATITUDE OF POTENTIAL MAXIMUM(DEGREES) = 75
 OVAL OFFSET(DEGREES) = 5
 MEASUREMENT LATITUDE = 60
 VIEWING ANGLE = 0



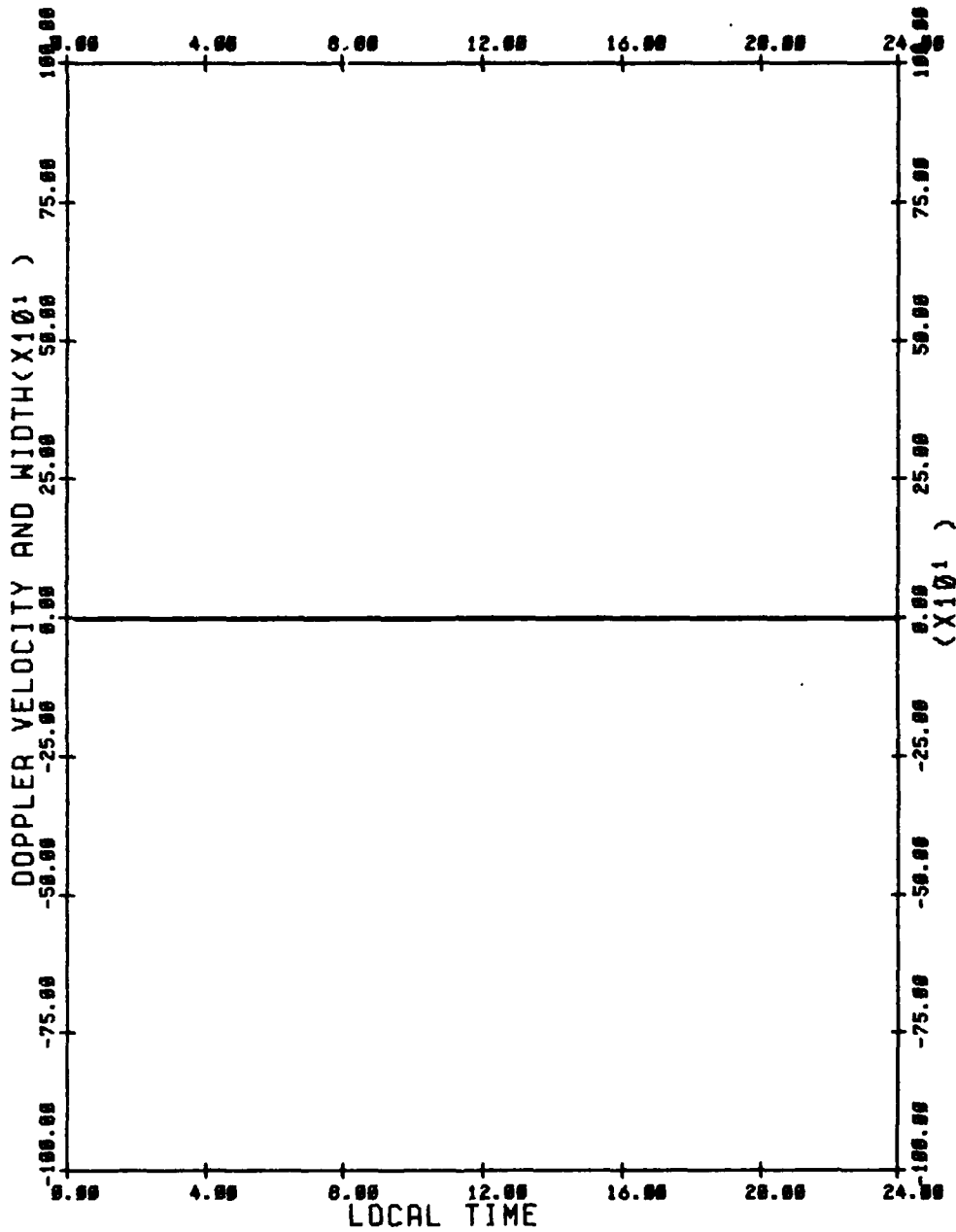
DOPPLER VELOCITY —————
 DOPPLER WIDTH -----
 CROSS POLAR CAP POTENTIAL DROP(V) = 50000
 E-FOLDING DISTANCE OF ARORAL E-FIELD(DEGREES) = 5
 LATITUDE OF POTENTIAL MAXIMUM(DEGREES) = 75
 OVAL OFFSET(DEGREES) = 5
 MEASUREMENT LATITUDE = 60
 VIEWING ANGLE = -30



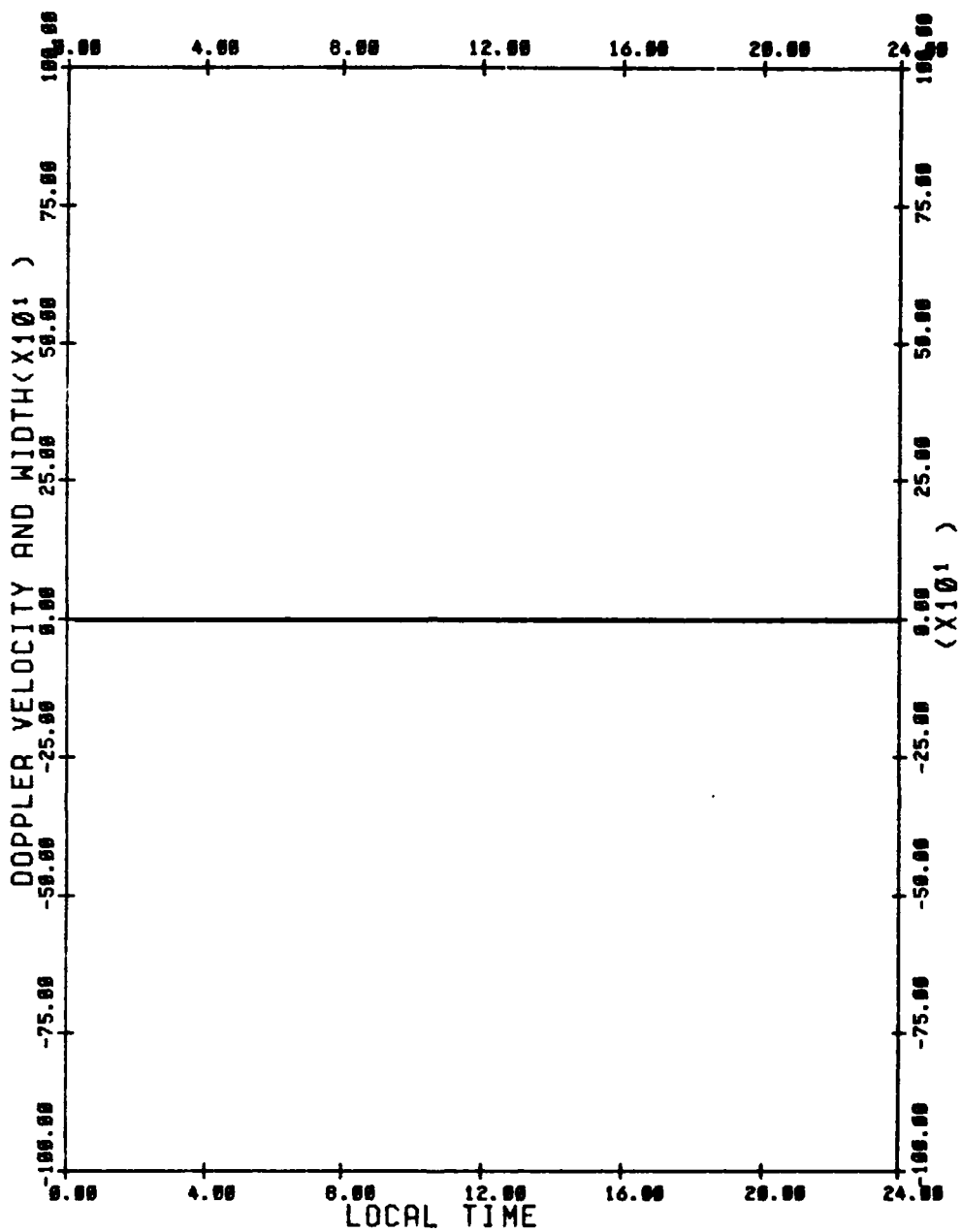
DOPPLER VELOCITY —————
 DOPPLER WIDTH - - - - -
 CROSS POLAR CAP POTENTIAL DROP(V) = 50000
 E-FOLDING DISTANCE OF ARORAL E-FIELD(DEGREES) = 5
 LATITUDE OF POTENTIAL MAXIMUM(DEGREES) = 75
 OVAL OFFSET(DEGREES) = 5
 MEASUREMENT LATITUDE = 60
 VIEWING ANGLE = -60



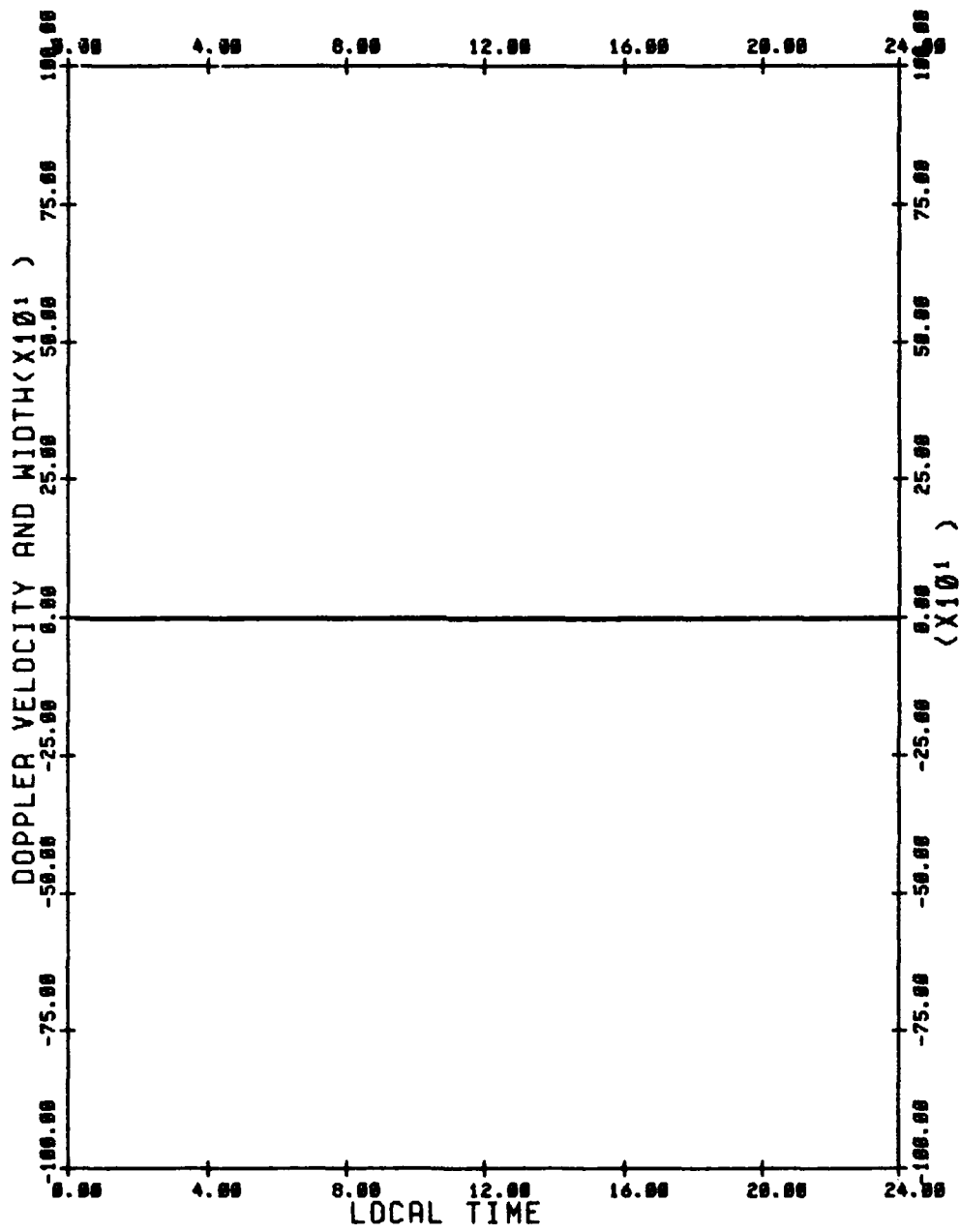
DOPPLER VELOCITY _____
 DOPPLER WIDTH _____
 CROSS POLAR CAP POTENTIAL DROP(V) = 50000
 E-FOLDING DISTANCE OF ARORAL E-FIELD(DEGREES) = 5
 LATITUDE OF POTENTIAL MAXIMUM(DEGREES) = 75
 OVAL OFFSET(DEGREES) = 5
 MEASUREMENT LATITUDE = 55
 VIEWING ANGLE = 60



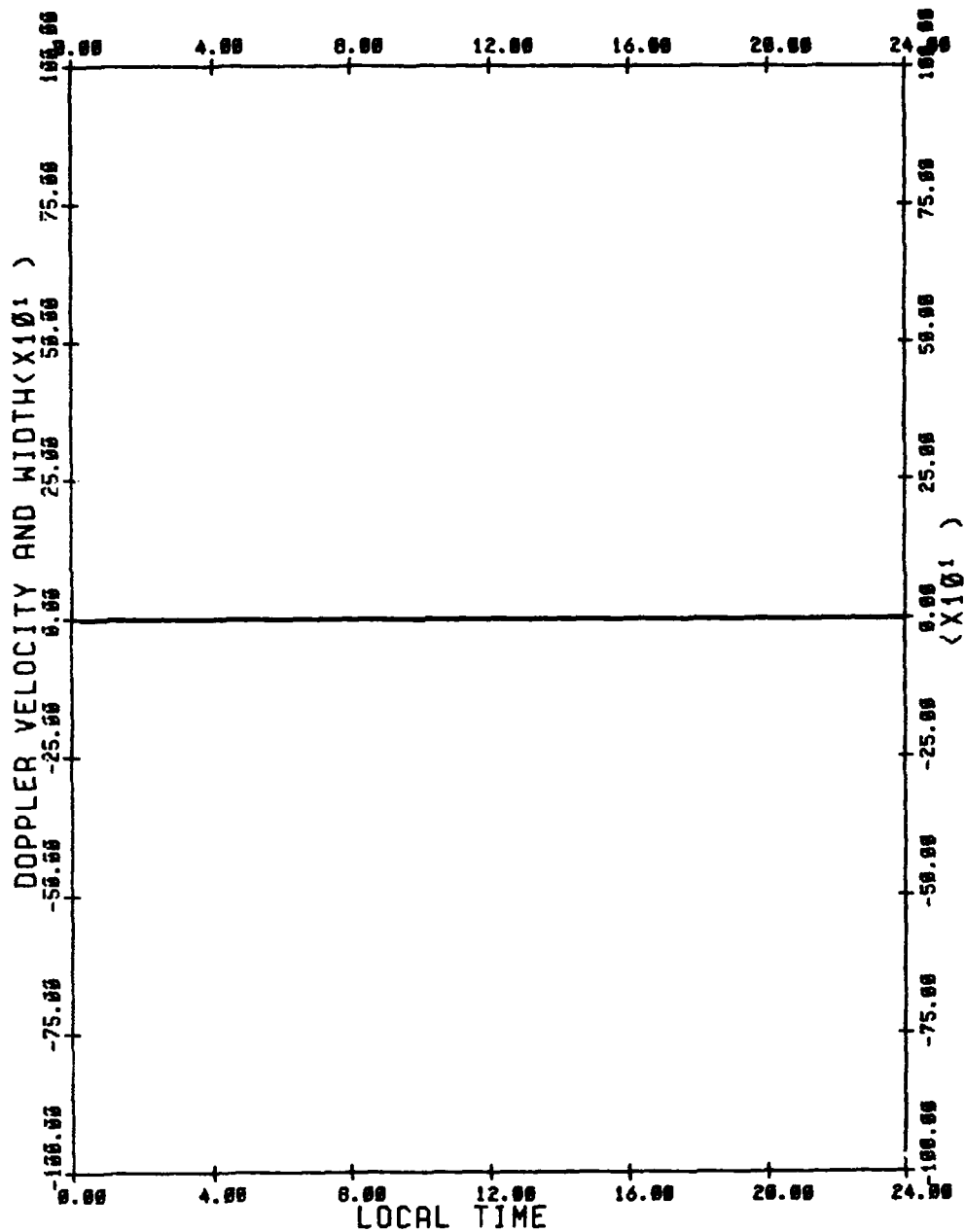
DOPPLER VELOCITY ———
 DOPPLER WIDTH ———
 CROSS POLAR CAP POTENTIAL DROP(V) = 50000
 E-FOLDING DISTANCE OF ARORAL E-FIELD(DEGREES) = 5
 LATITUDE OF POTENTIAL MAXIMUM(DEGREES) = 75
 OVAL OFFSET(DEGREES) = 5
 MEASUREMENT LATITUDE = 55
 VIEWING ANGLE = 30



DOPPLER VELOCITY _____
 DOPPLER WIDTH _____
 CROSS POLAR CAP POTENTIAL DROP(V) = 50000
 E-FOLDING DISTANCE OF ARDAL E-FIELD(DEGREES) = 5
 LATITUDE OF POTENTIAL MAXIMUM(DEGREES) = 75
 OVAL OFFSET(DEGREES) = 5
 MEASUREMENT LATITUDE = 55
 VIEWING ANGLE = 0



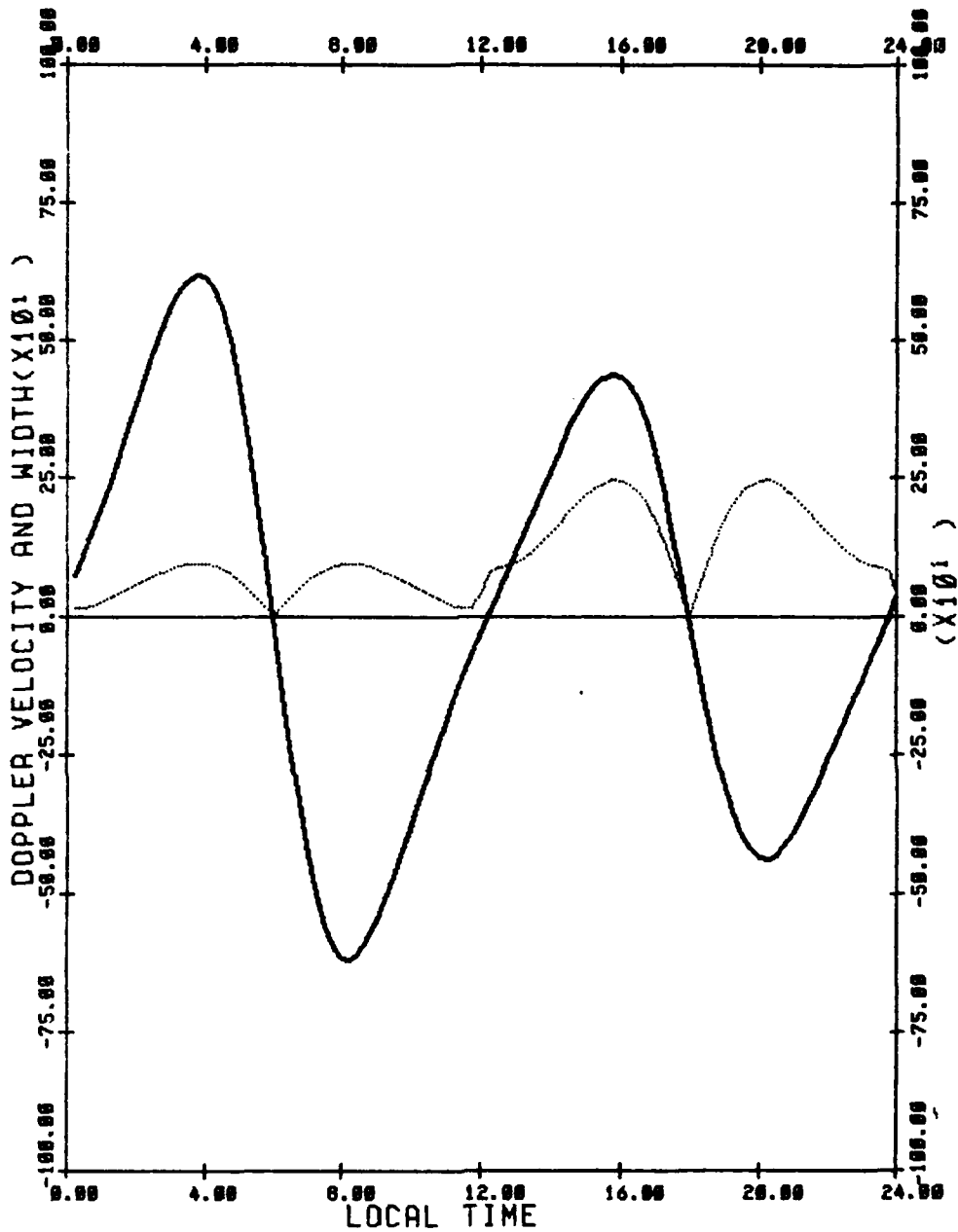
DOPPLER VELOCITY —————
 DOPPLER WIDTH —————
 CROSS POLAR CAP POTENTIAL DROP(V) = 50000
 E-FOLDING DISTANCE OF ARORAL E-FIELD(DEGREES) = 5
 LATITUDE OF POTENTIAL MAXIMUM(DEGREES) = 75
 OVAL OFFSET(DEGREES) = 5
 MEASUREMENT LATITUDE = 55
 VIEWING ANGLE = -30



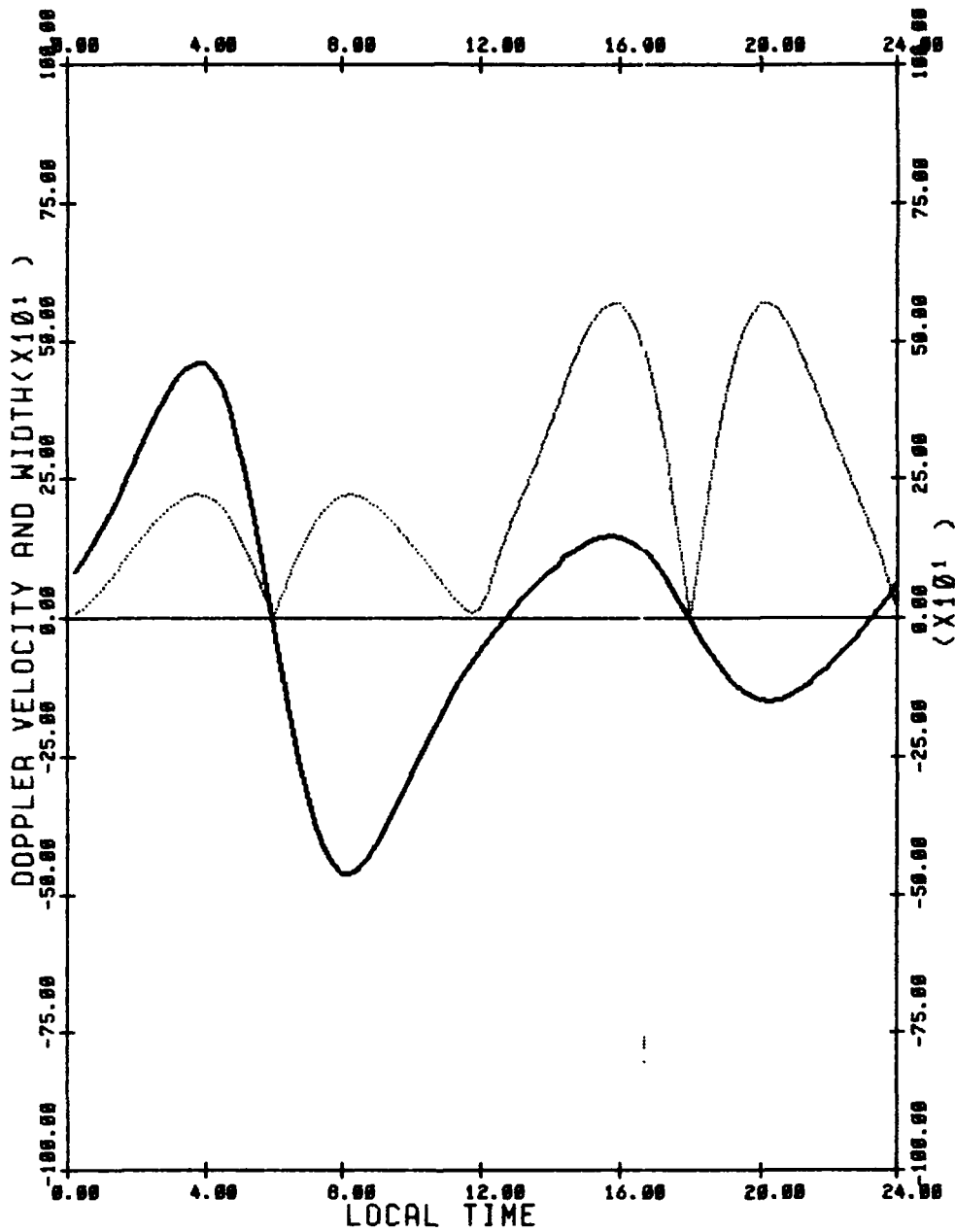
DOPPLER VELOCITY
 DOPPLER WIDTH
 CROSS POLAR CAP POTENTIAL DROP(V) = 50000
 E-FOLDING DISTANCE OF ARORAL E-FIELD(DEGREES) = 5
 LATITUDE OF POTENTIAL MAXIMUM(DEGREES) = 75
 OVAL OFFSET(DEGREES) = 5
 MEASUREMENT LATITUDE = 55
 VIEWING ANGLE = -60

APPENDIX B

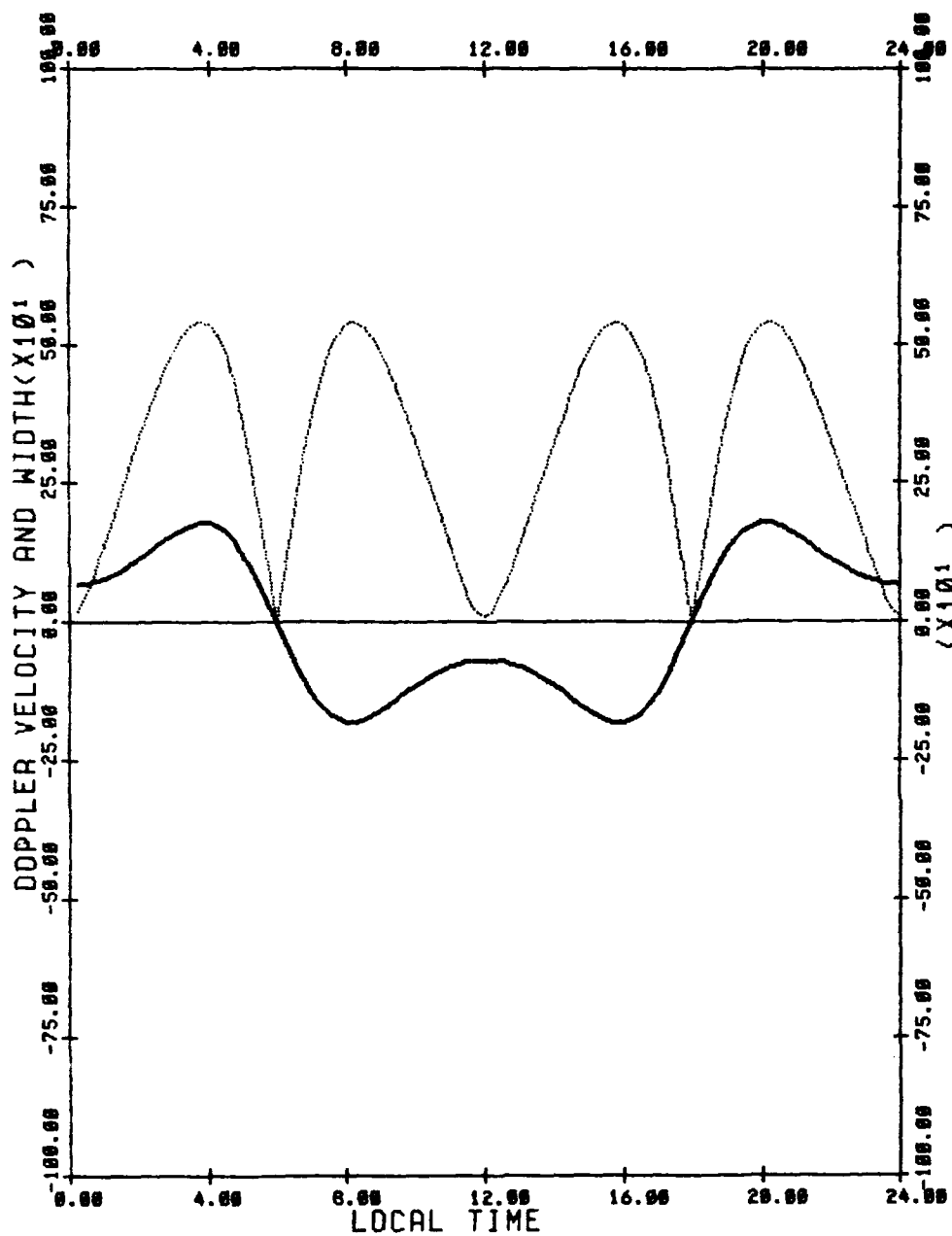
DOPPLER VELOCITY AND WIDTH PLOTS
FOR POTENTIAL DISTRIBUTION SHOWN IN FIGURE 4.6



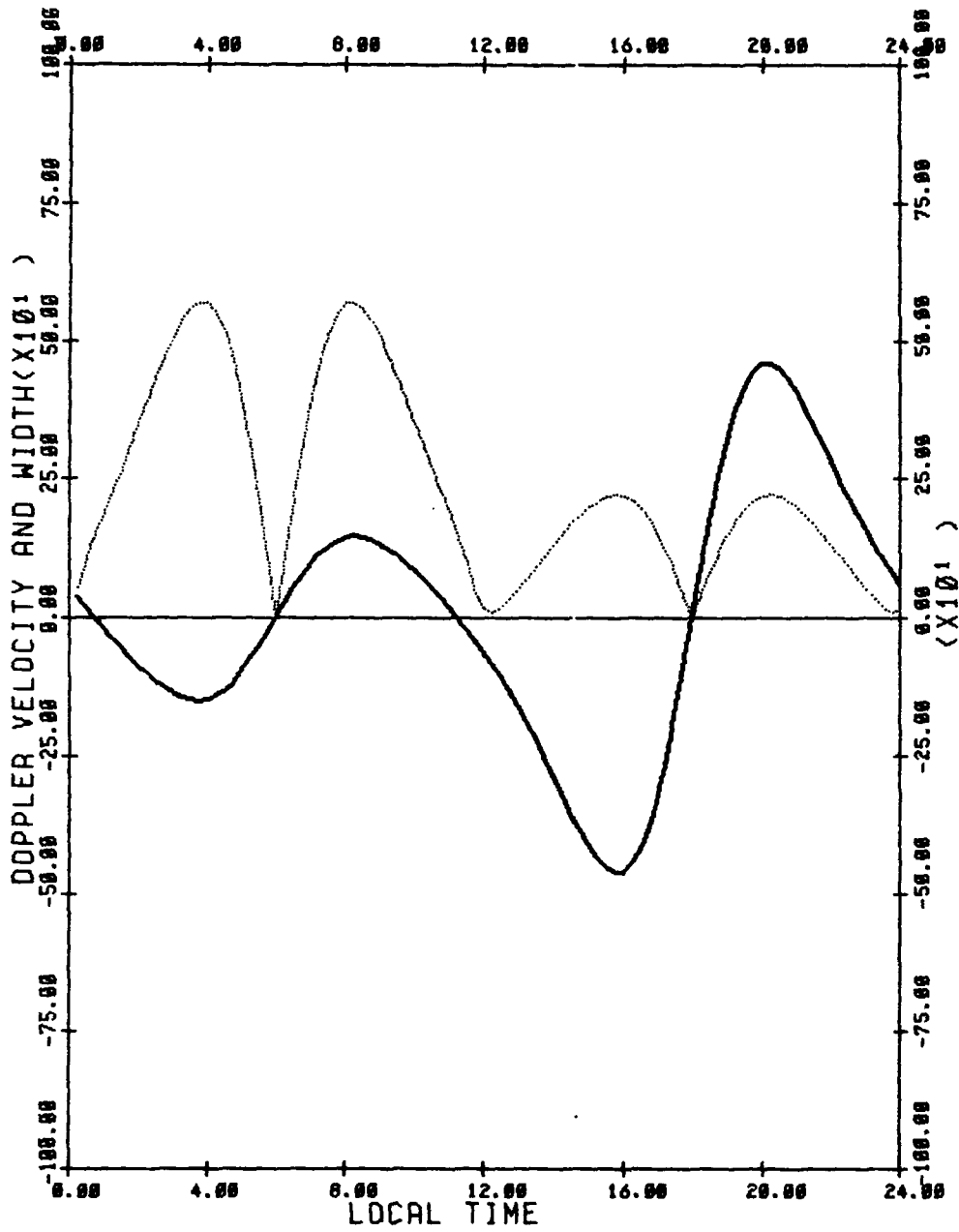
DOPPLER VELOCITY ———
 DOPPLER WIDTH - - - - -
 CROSS POLAR CAP POTENTIAL DROP(V) = 50000
 LATITUDINAL WIDTH OF E-FIELD STRIP(DEGREES) = 10
 LATITUDE OF POTENTIAL MAXIMUM(DEGREES) = 65
 OVAL OFFSET(DEGREES) = 5
 MEASUREMENT LATITUDE = 65
 VIEWING ANGLE = 60



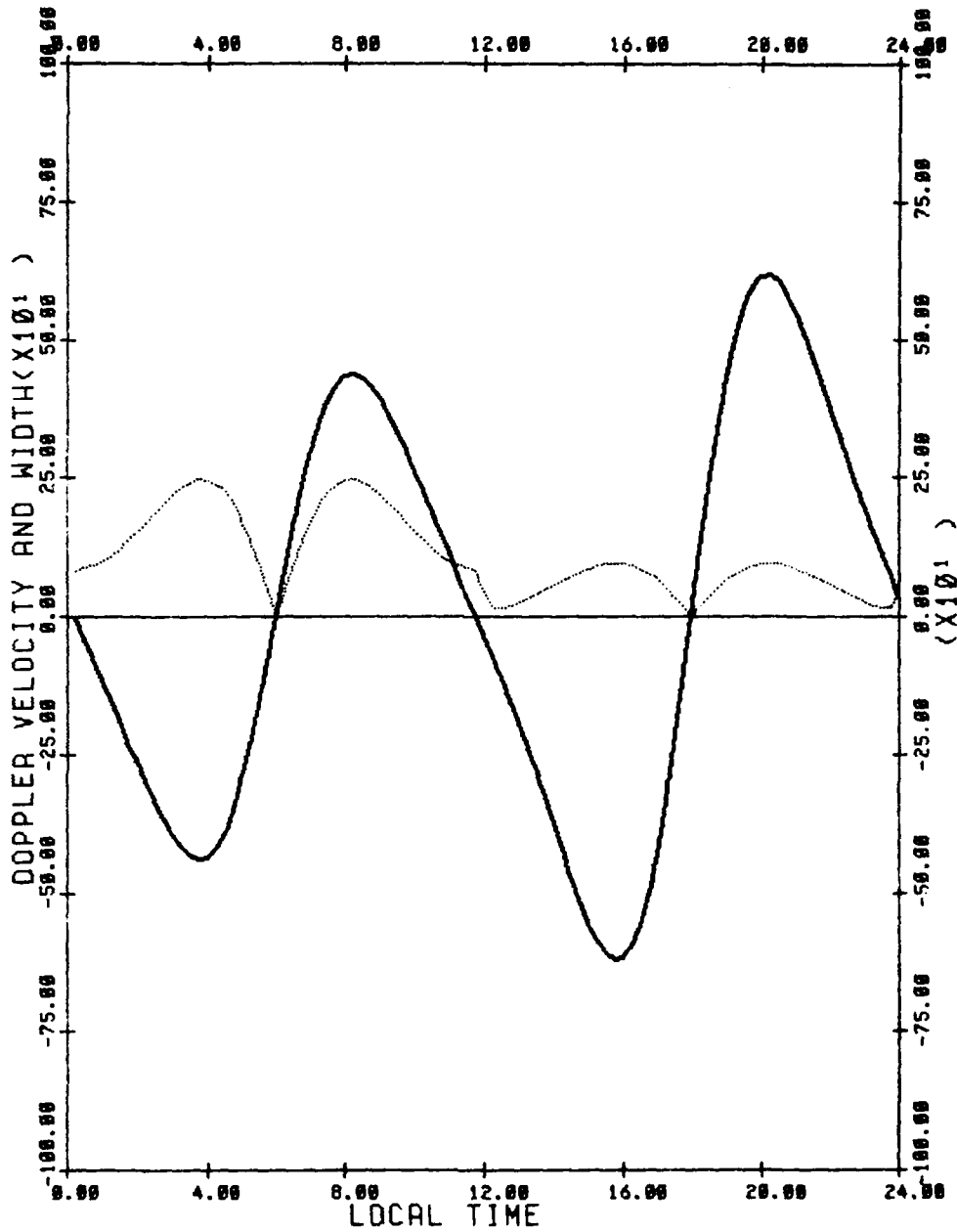
DOPPLER VELOCITY —————
 DOPPLER WIDTH
 CROSS POLAR CAP POTENTIAL DROP(V) = 50000
 LATITUDINAL WIDTH OF E-FIELD STRIP(DEGREES) = 10
 LATITUDE OF POTENTIAL MAXIMUM(DEGREES) = 65
 OVAL OFFSET(DEGREES) = 5
 MEASUREMENT LATITUDE = 65
 VIEWING ANGLE = 30



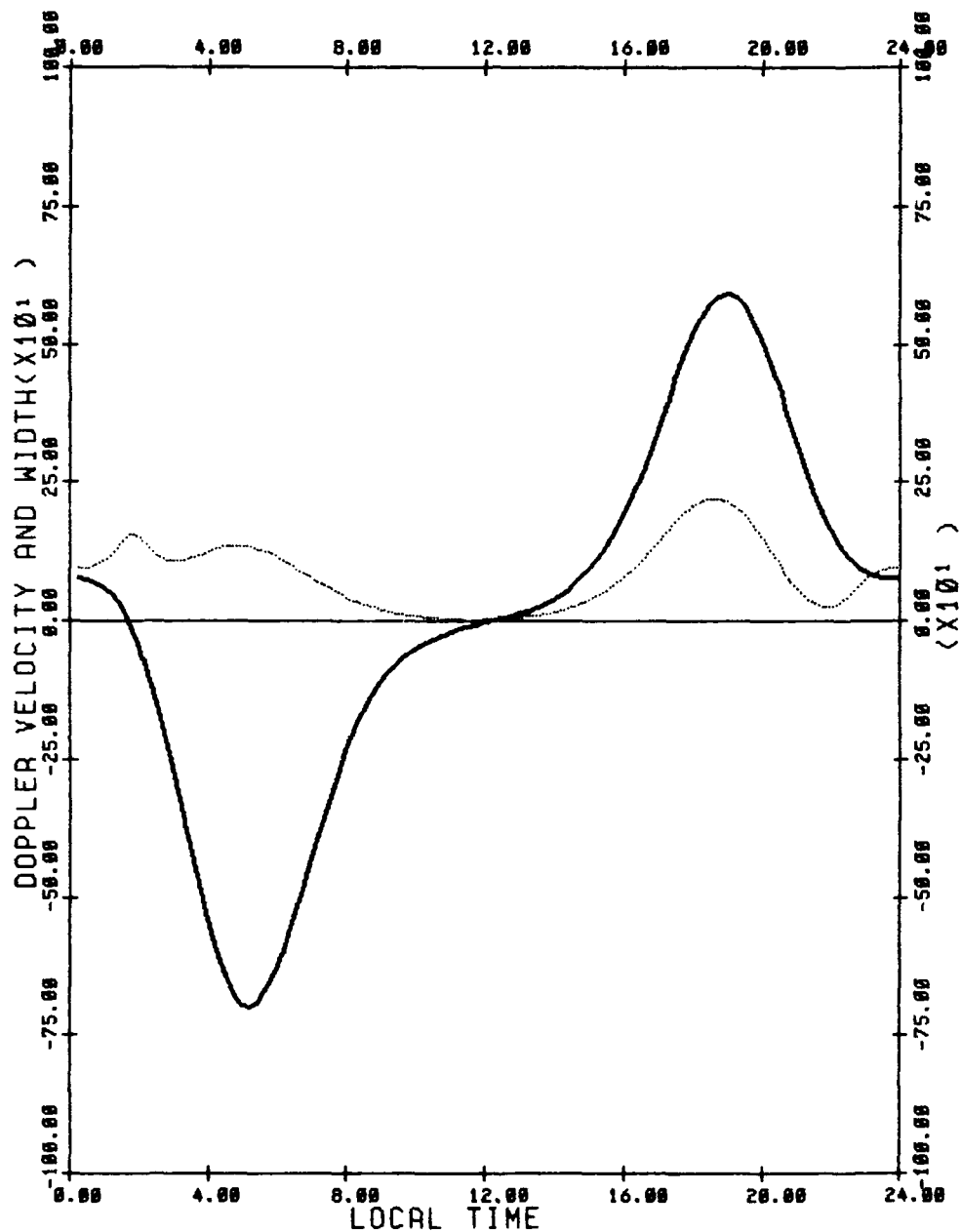
DOPPLER VELOCITY ———
 DOPPLER WIDTH - - - - -
 CROSS POLAR CAP POTENTIAL DROP(V) = 50000
 LATITUDINAL WIDTH OF E-FIELD STRIP(DEGREES) = 10
 LATITUDE OF POTENTIAL MAXIMUM(DEGREES) = 65
 OVAL OFFSET(DEGREES) = 5
 MEASUREMENT LATITUDE = 65
 VIEWING ANGLE = 0



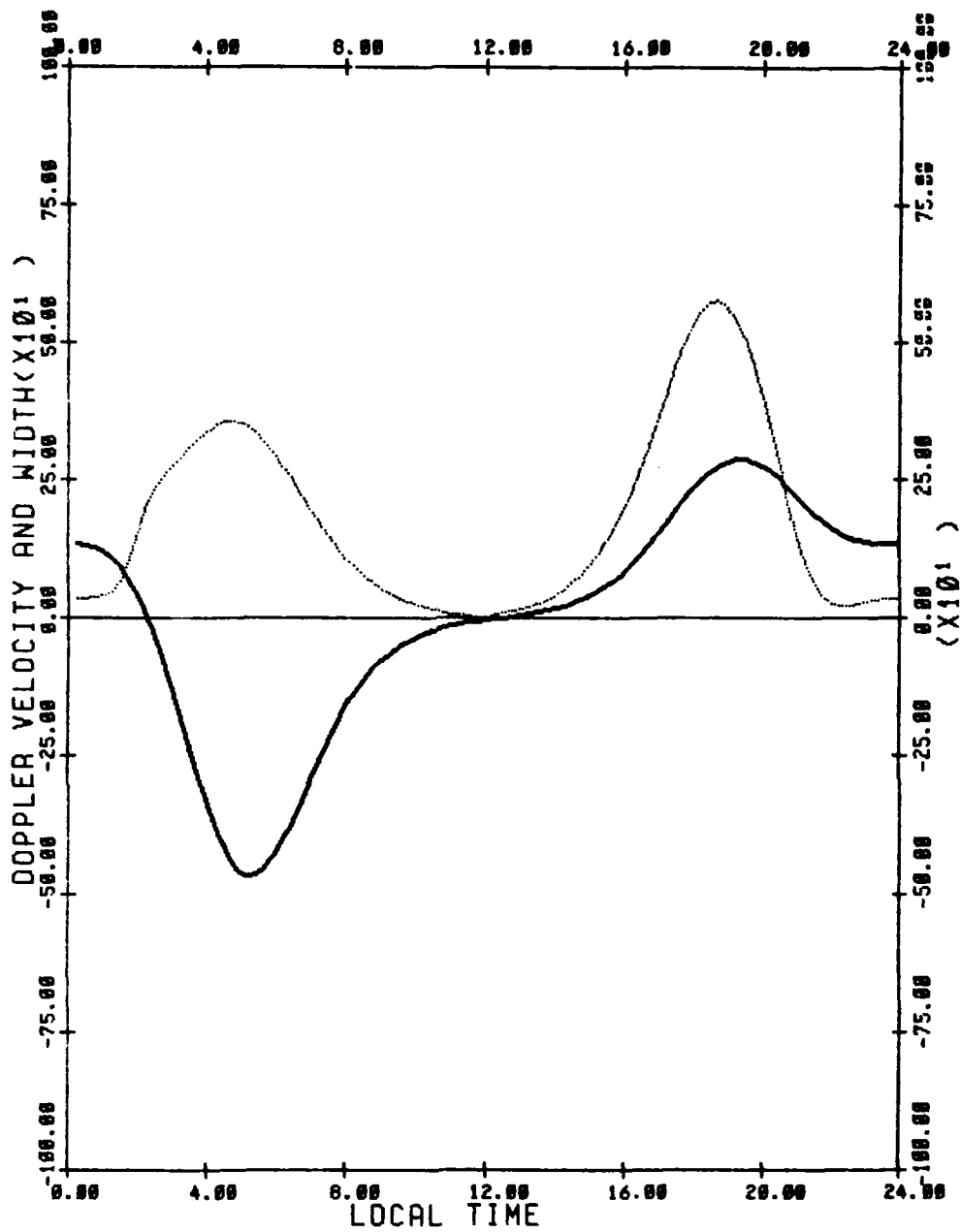
DOPPLER VELOCITY —————
 DOPPLER WIDTH - - - - -
 CROSS POLAR CAP POTENTIAL DROP(V) = 50000
 LATITUDINAL WIDTH OF E-FIELD STRIP(DEGREES) = 10
 LATITUDE OF POTENTIAL MAXIMUM(DEGREES) = 65
 OVAL OFFSET(DEGREES) = 5
 MEASUREMENT LATITUDE = 65
 VIEWING ANGLE = -30



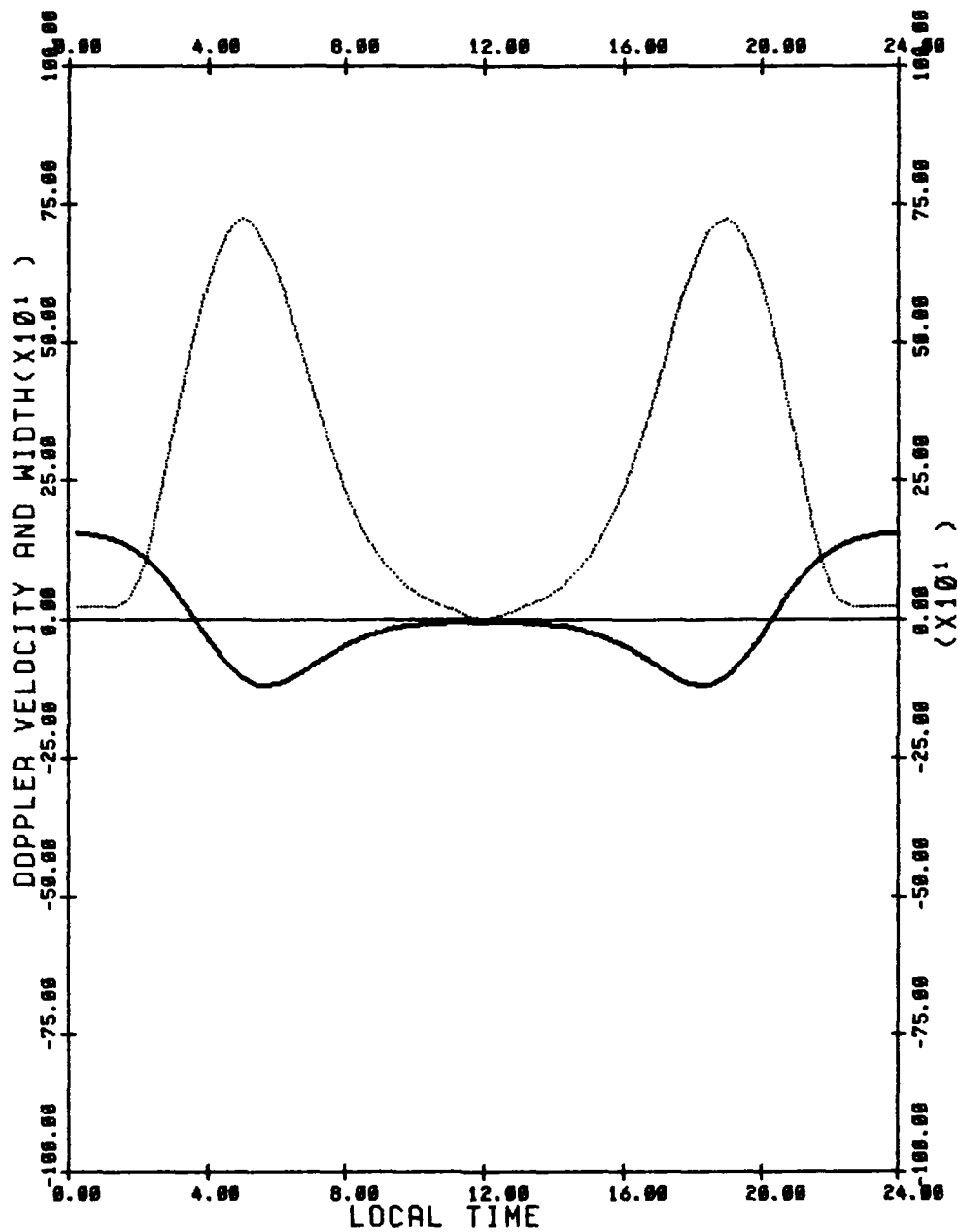
DOPPLER VELOCITY —————
 DOPPLER WIDTH
 CROSS POLAR CAP POTENTIAL DROP(V) = 50000
 LATITUDINAL WIDTH OF E-FIELD STRIP(DEGREES) = 10
 LATITUDE OF POTENTIAL MAXIMUM(DEGREES) = 65
 DVAL OFFSET(DEGREES) = 5
 MEASUREMENT LATITUDE = 65
 VIEWING ANGLE = -60



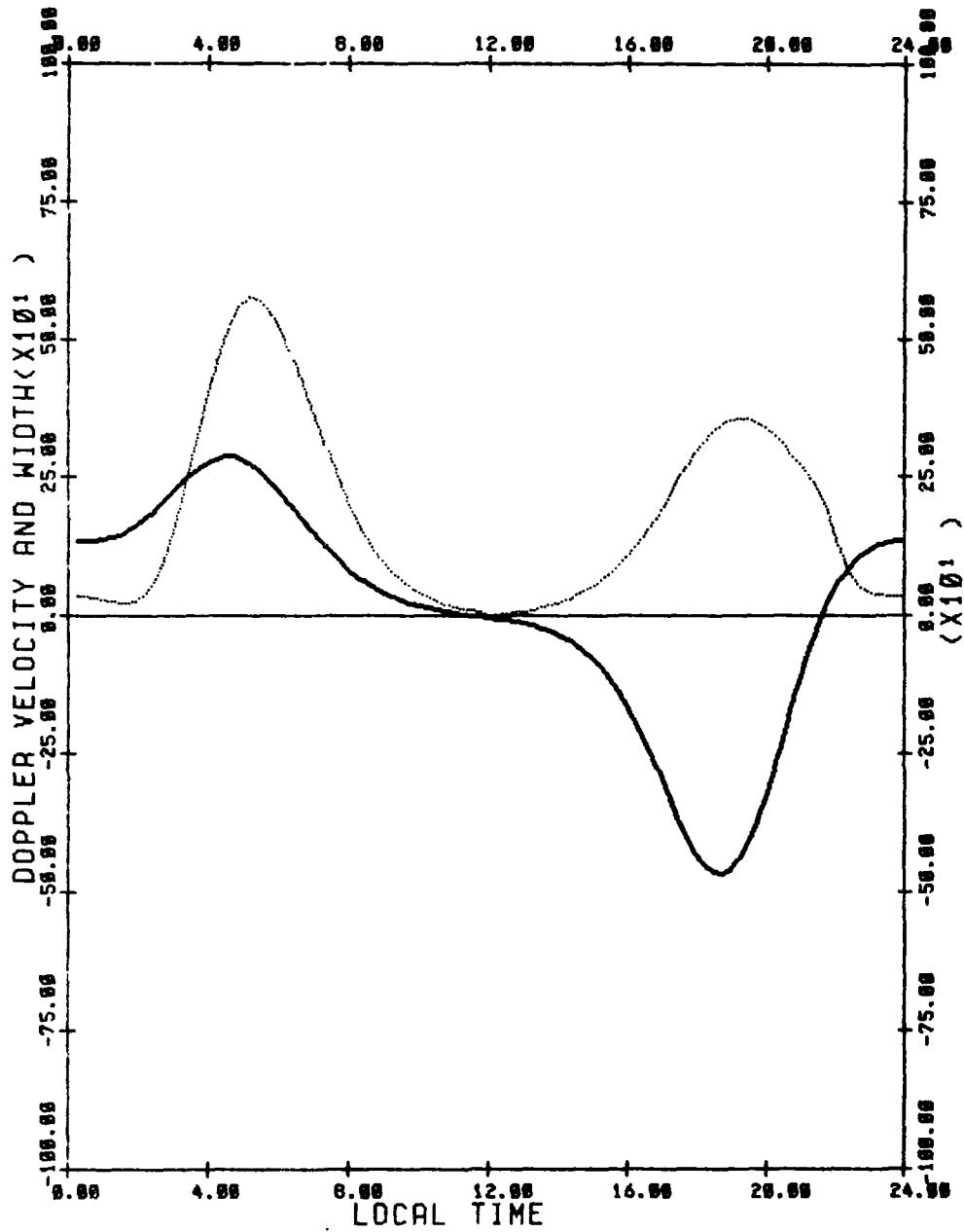
DOPPLER VELOCITY —————
 DOPPLER WIDTH - - - - -
 CROSS POLAR CAP POTENTIAL DROP(V) = 50000
 LATITUDINAL WIDTH OF E-FIELD STRIP(DEGREES) = 10
 LATITUDE OF POTENTIAL MAXIMUM(DEGREES) = 65
 OVAL OFFSET(DEGREES) = 5
 MEASUREMENT LATITUDE = 60
 VIEWING ANGLE = 60



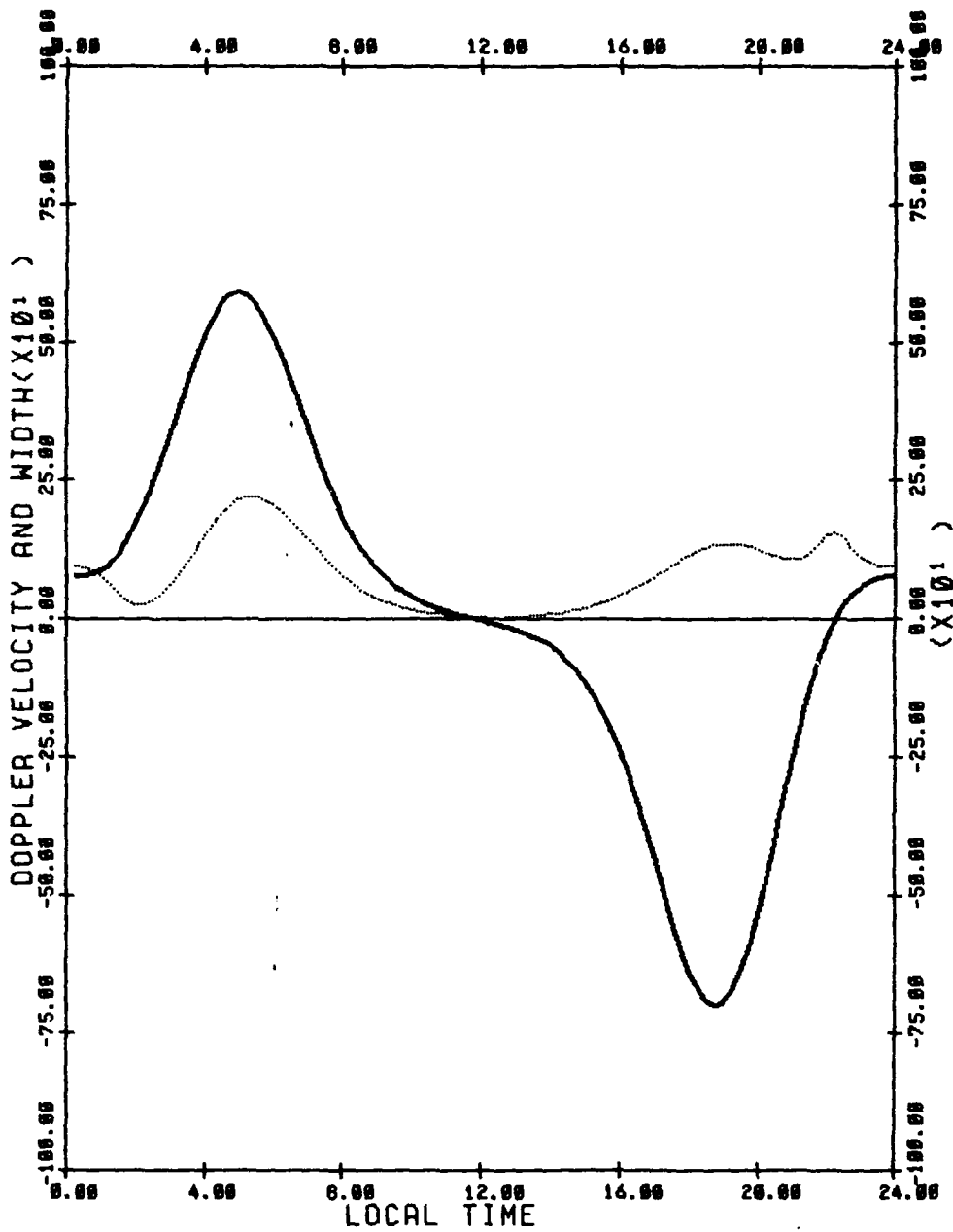
DOPPLER VELOCITY —————
 DOPPLER WIDTH - - - - -
 CROSS POLAR CAP POTENTIAL DROP(V) = 50000
 LATITUDINAL WIDTH OF E-FIELD STRIP(DEGREES) = 10
 LATITUDE OF POTENTIAL MAXIMUM(DEGREES) = 65
 OVAL OFFSET(DEGREES) = 5
 MEASUREMENT LATITUDE = 60
 VIEWING ANGLE = 30



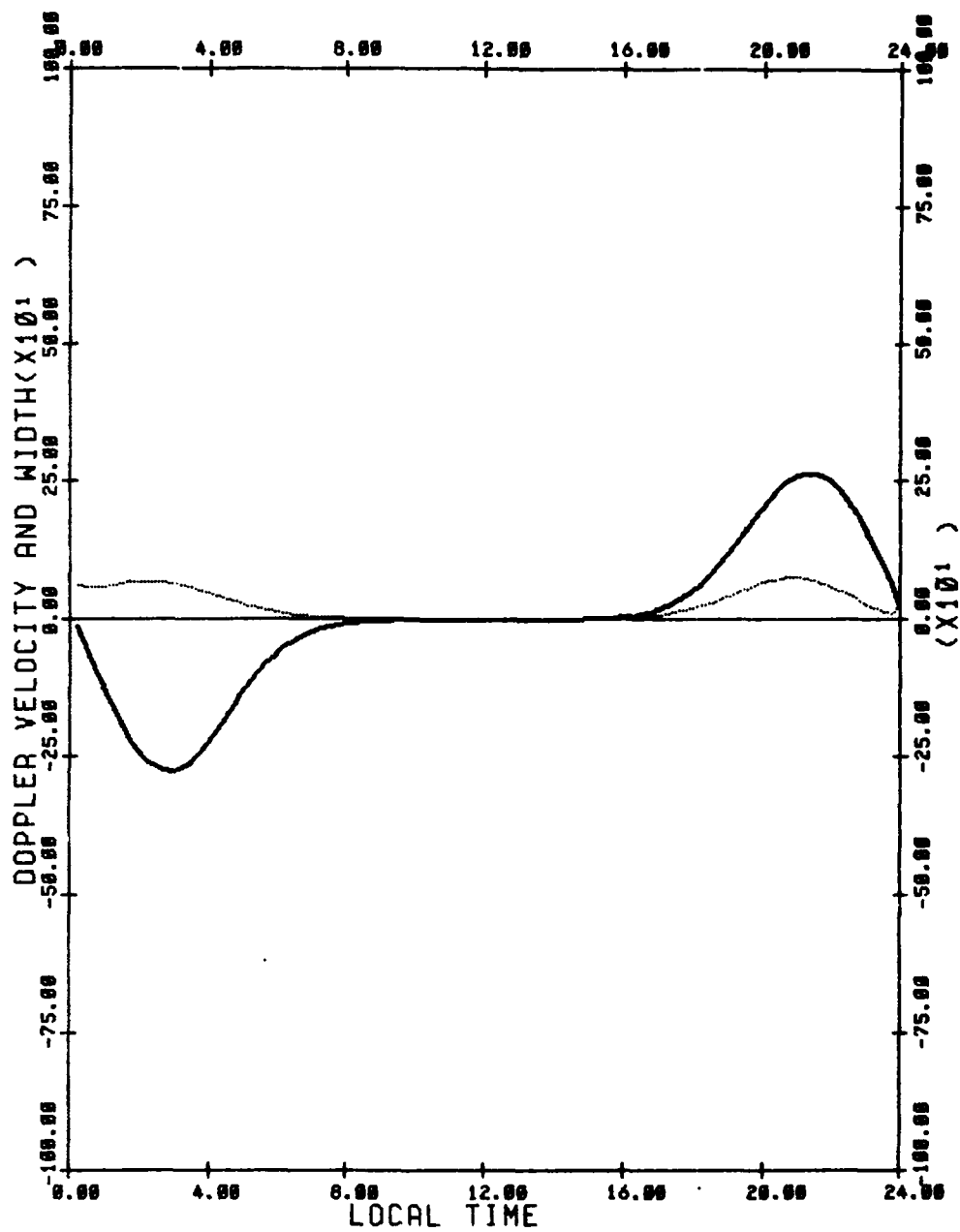
DOPPLER VELOCITY ———
 DOPPLER WIDTH - - - - -
 CROSS POLAR CAP POTENTIAL DROP(V) = 50000
 LATITUDINAL WIDTH OF E-FIELD STRIP(DEGREES) = 10
 LATITUDE OF POTENTIAL MAXIMUM(DEGREES) = 65
 OVAL OFFSET(DEGREES) = 5
 MEASUREMENT LATITUDE = 60
 VIEWING ANGLE = 0



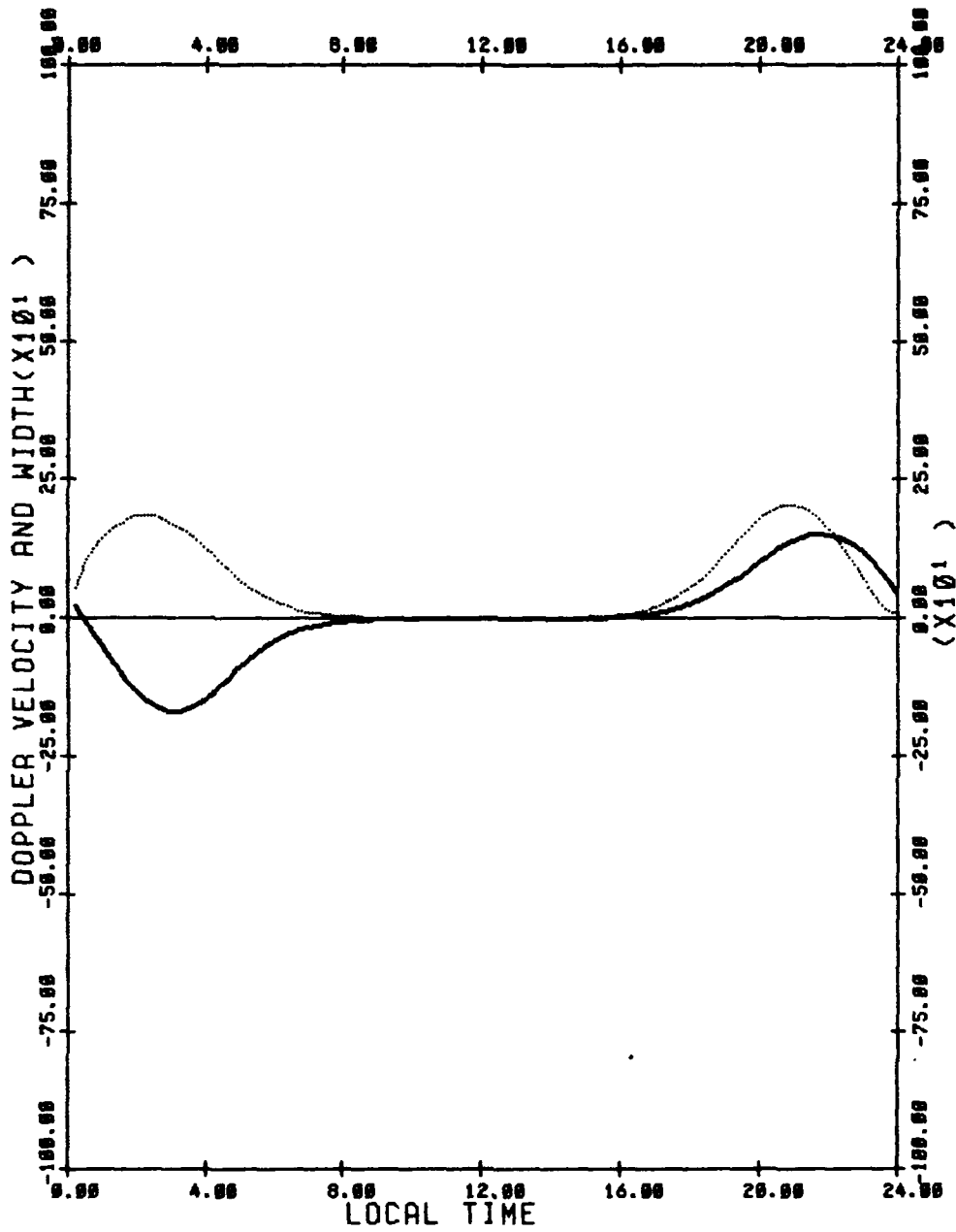
DOPPLER VELOCITY —————
 DOPPLER WIDTH - - - - -
 CROSS POLAR CAP POTENTIAL DROP(V) = 50000
 LATITUDINAL WIDTH OF E-FIELD STRIP(DEGREES) = 10
 LATITUDE OF POTENTIAL MAXIMUM(DEGREES) = 65
 OVAL OFFSET(DEGREES) = 5
 MEASUREMENT LATITUDE = 60
 VIEWING ANGLE = -30



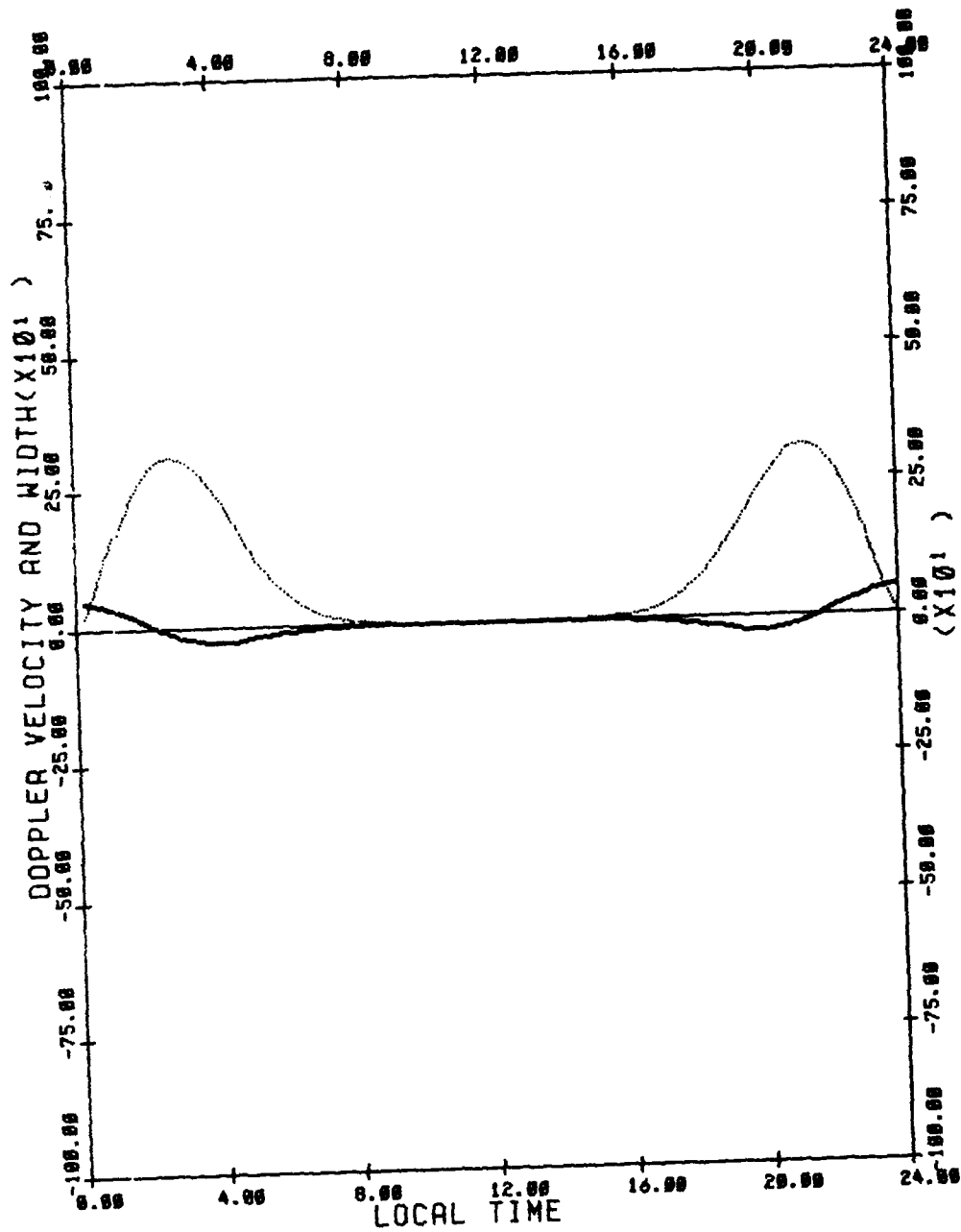
DOPPLER VELOCITY —————
 DOPPLER WIDTH - - - - -
 CROSS POLAR CAP POTENTIAL DROP(V) = 50000
 LATITUDINAL WIDTH OF E-FIELD STRIP(DEGREES) = 10
 LATITUDE OF POTENTIAL MAXIMUM(DEGREES) = 65
 OVAL OFFSET(DEGREES) = 5
 MEASUREMENT LATITUDE = 60
 VIEWING ANGLE = -60



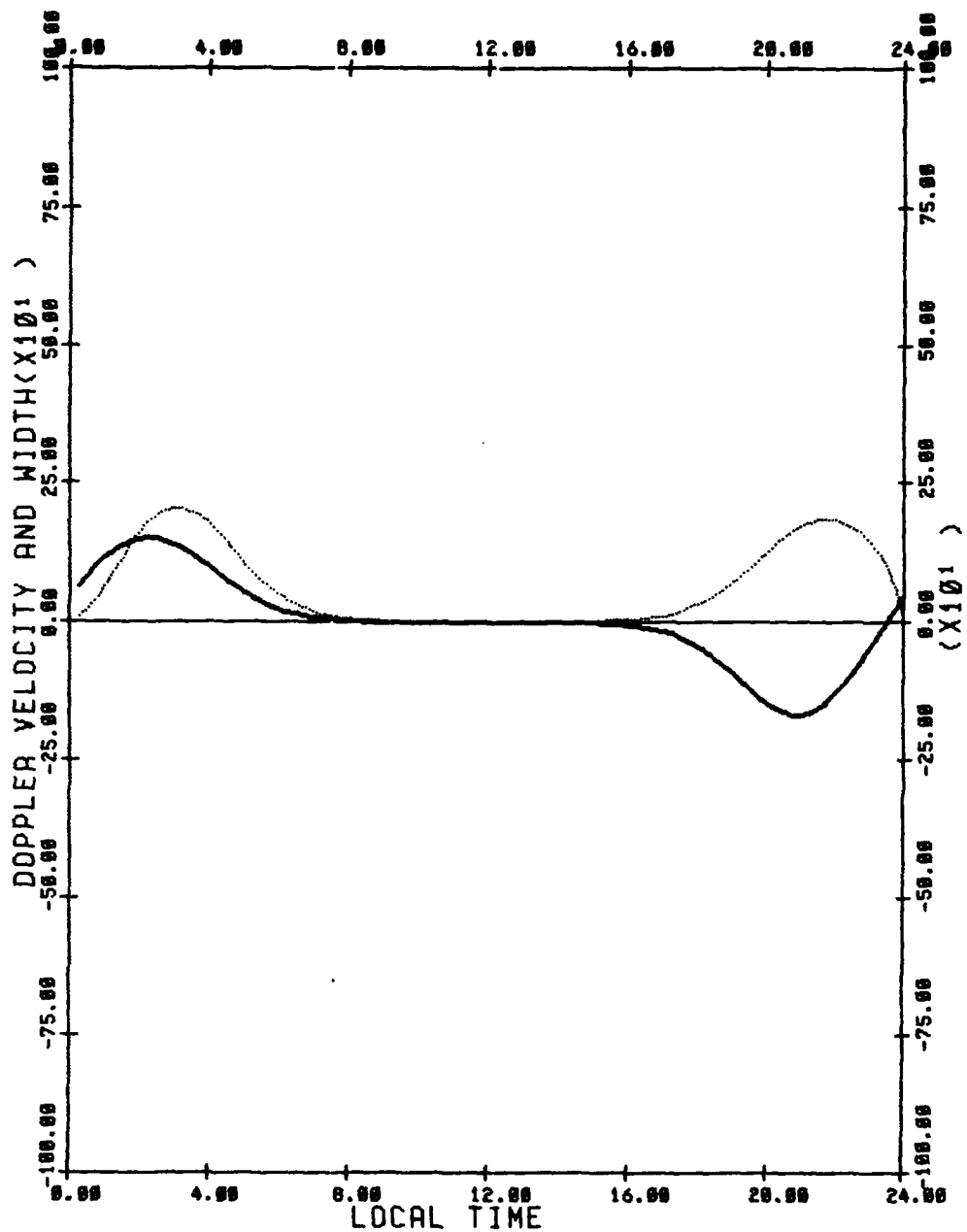
DOPPLER VELOCITY —————
 DOPPLER WIDTH - - - - -
 CROSS POLAR CAP POTENTIAL DROP(V) = 50000
 LATITUDINAL WIDTH OF E-FIELD STRIP(DEGREES) = 10
 LATITUDE OF POTENTIAL MAXIMUM(DEGREES) = 65
 OVAL OFFSET(DEGREES) = 5
 MEASUREMENT LATITUDE = 55
 VIEWING ANGLE = 60



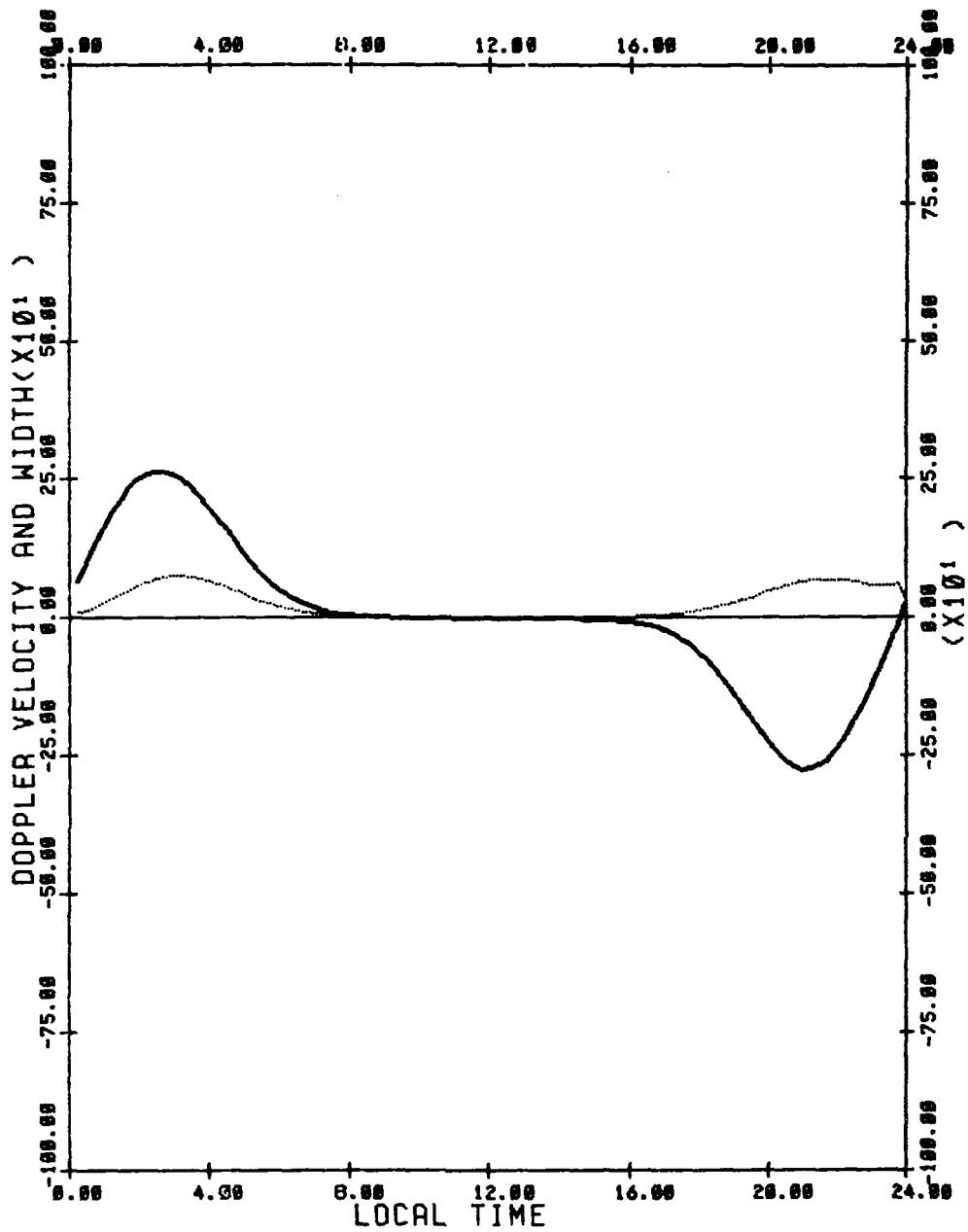
DOPPLER VELOCITY ———
 DOPPLER WIDTH - - - - -
 CROSS POLAR CAP POTENTIAL DROP(V) = 50000
 LATITUDINAL WIDTH OF E-FIELD STRIP(DEGREES) = 10
 LATITUDE OF POTENTIAL MAXIMUM(DEGREES) = 65
 OVAL OFFSET(DEGREES) = 5
 MEASUREMENT LATITUDE = 55
 VIEWING ANGLE = 30



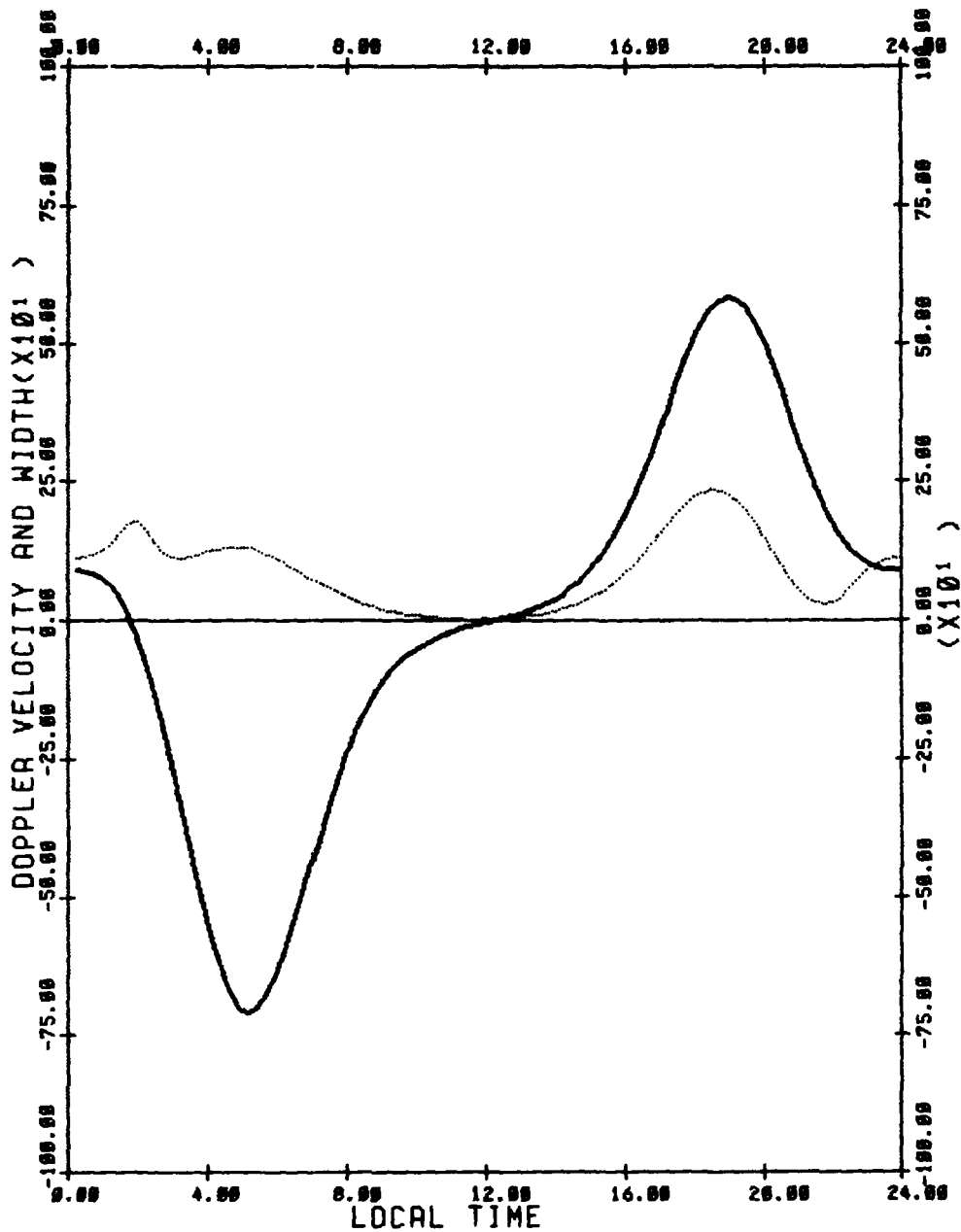
DOPPLER VELOCITY _____
 DOPPLER WIDTH _____
 CROSS POLAR CAP POTENTIAL DROP(V) = 50000
 LATITUDINAL WIDTH OF E-FIELD STRIP(DEGREES) = 10
 LATITUDE OF POTENTIAL MAXIMUM(DEGREES) = 65
 OVAL OFFSET(DEGREES) = 5
 MEASUREMENT LATITUDE = 55
 VIEWING ANGLE = 0



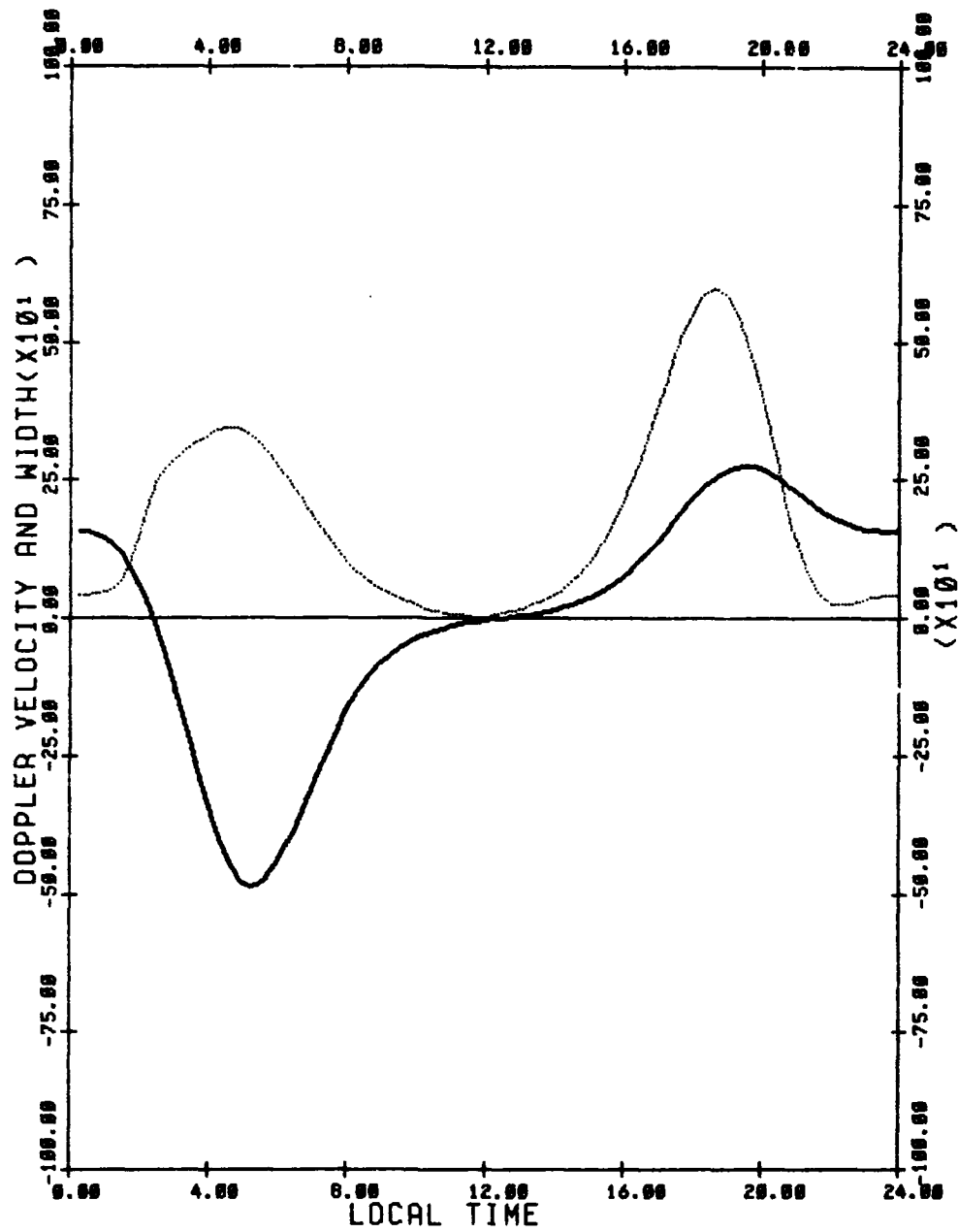
DOPPLER VELOCITY —————
 DOPPLER WIDTH - - - - -
 CROSS POLAR CAP POTENTIAL DROP(V) = 50000
 LATITUDINAL WIDTH OF E-FIELD STRIP(DEGREES) = 10
 LATITUDE OF POTENTIAL MAXIMUM(DEGREES) = 65
 OVAL OFFSET(DEGREES) = 5
 MEASUREMENT LATITUDE = 55
 VIEWING ANGLE = -30



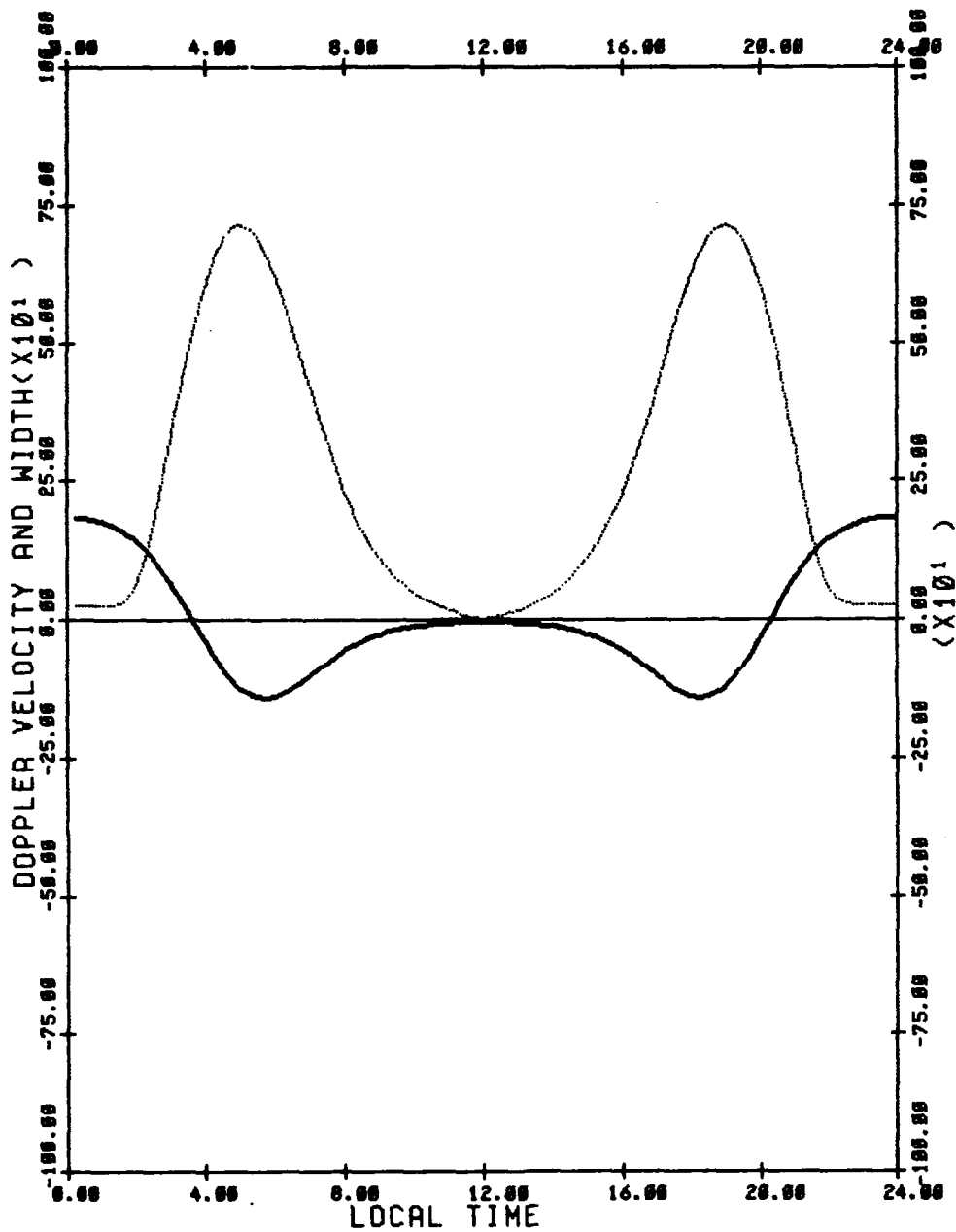
DOPPLER VELOCITY —————
 DOPPLER WIDTH - - - - -
 CROSS POLAR CAP POTENTIAL DROP(V) = 50000
 LATITUDINAL WIDTH OF E-FIELD STRIP(DEGREES) = 10
 LATITUDE OF POTENTIAL MAXIMUM(DEGREES) = 65
 OVAL OFFSET(DEGREES) = 5
 MEASUREMENT LATITUDE = 55
 VIEWING ANGLE = -60



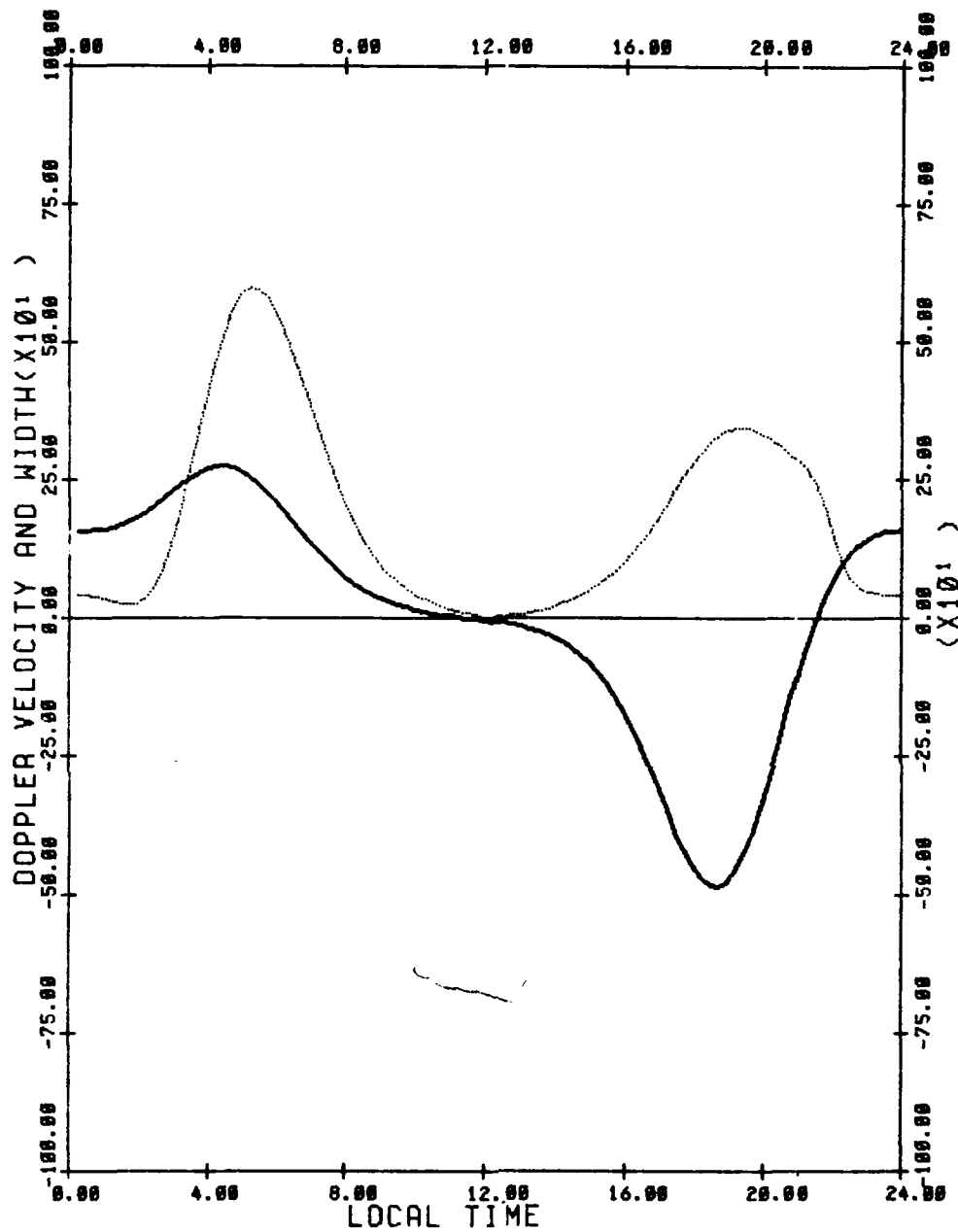
DOPPLER VELOCITY —————
 DOPPLER WIDTH - - - - -
 CROSS POLAR CAP POTENTIAL DROP(V) = 50000
 LATITUDINAL WIDTH OF E-FIELD STRIP(DEGREES) = 10
 LATITUDE OF POTENTIAL MAXIMUM(DEGREES) = 70
 DVAL OFFSET(DEGREES) = 5
 MEASUREMENT LATITUDE = 65
 VIEWING ANGLE = 60



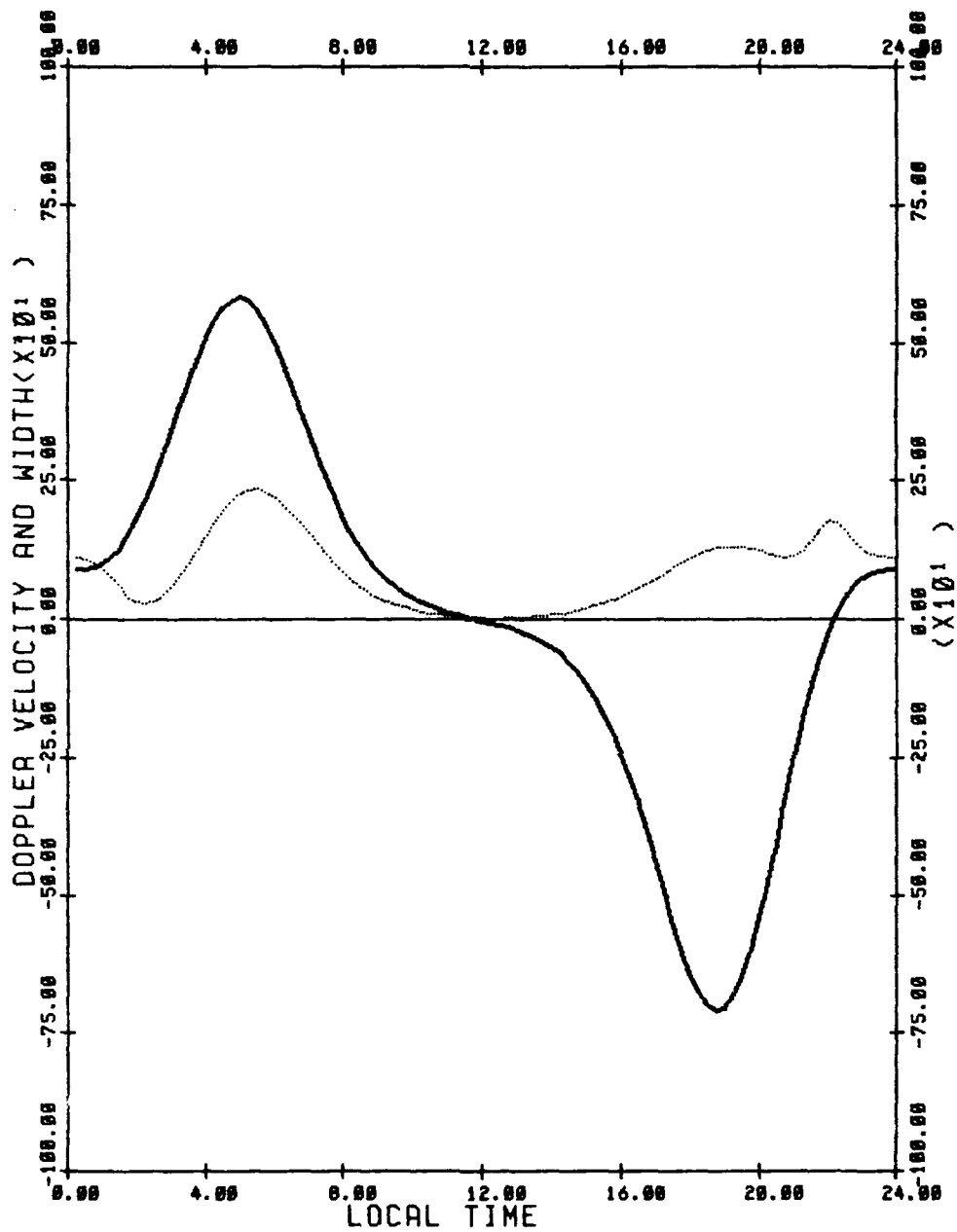
DOPPLER VELOCITY —————
 DOPPLER WIDTH - - - - -
 CROSS POLAR CAP POTENTIAL DROP(V) = 50000
 LATITUDINAL WIDTH OF E-FIELD STRIP(DEGREES) = 10
 LATITUDE OF POTENTIAL MAXIMUM(DEGREES) = 70
 DVAL OFFSET(DEGREES) = 5
 MEASUREMENT LATITUDE = 65
 VIEWING ANGLE = 30



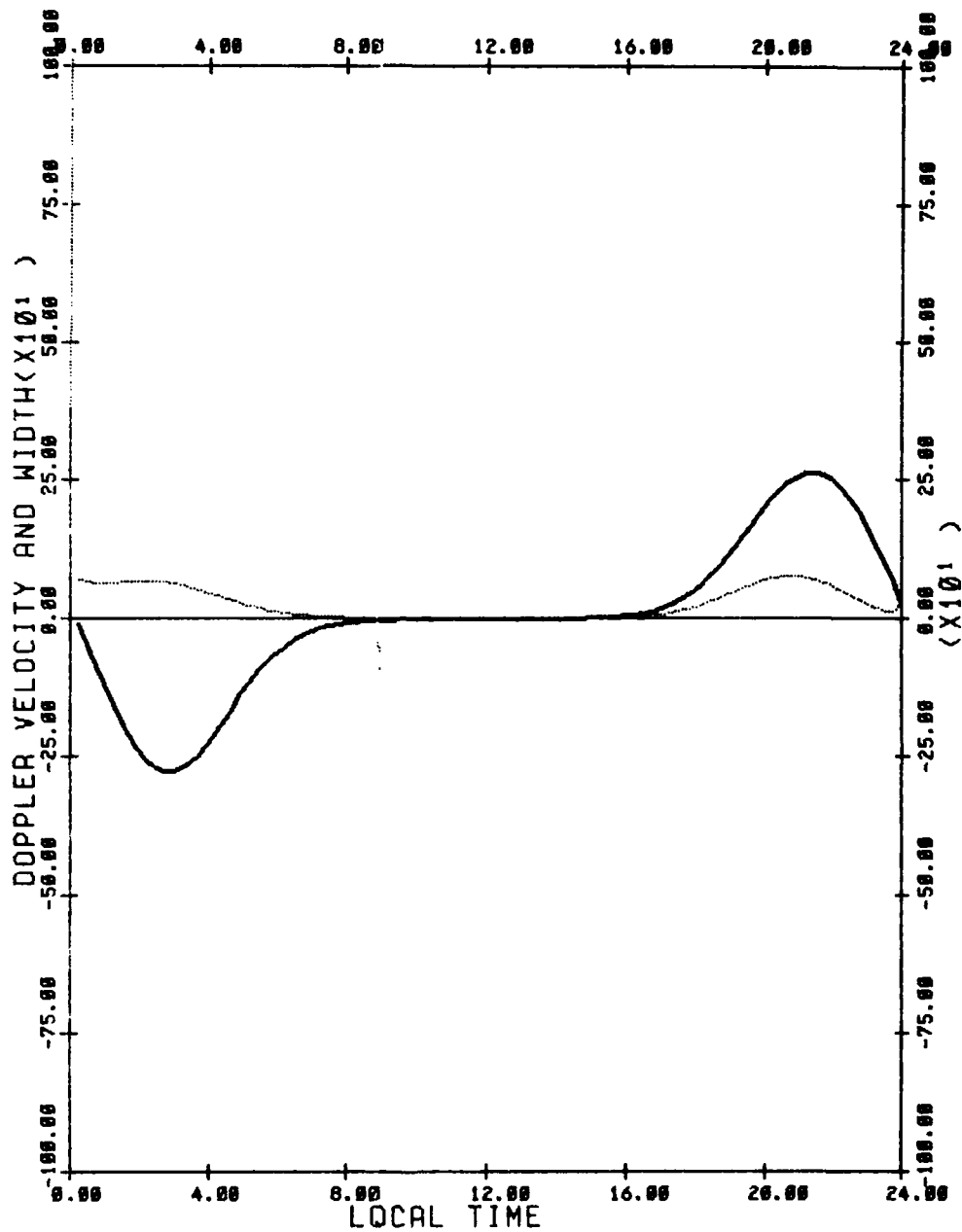
DOPPLER VELOCITY —————
 DOPPLER WIDTH - - - - -
 CROSS POLAR CAP POTENTIAL DROP(V) = 50000
 LATITUDINAL WIDTH OF E-FIELD STRIP(DEGREES) = 10
 LATITUDE OF POTENTIAL MAXIMUM(DEGREES) = 70
 OVAL OFFSET(DEGREES) = 5
 MEASUREMENT LATITUDE = 65
 VIEWING ANGLE = 0



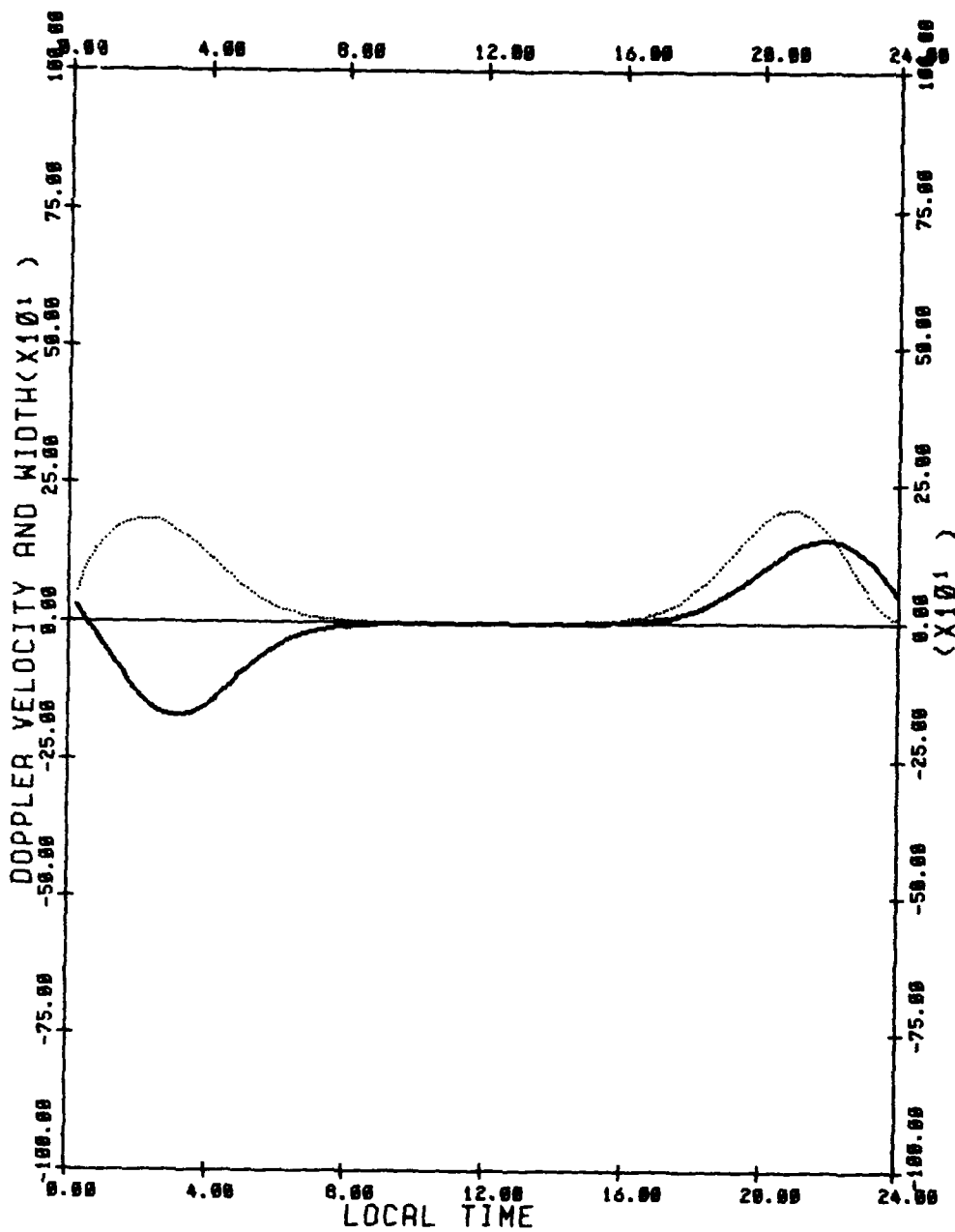
DOPPLER VELOCITY —————
 DOPPLER WIDTH - - - - -
 CROSS POLAR CAP POTENTIAL DROP(V) = 50000
 LATITUDINAL WIDTH OF E-FIELD STRIP(DEGREES) = 10
 LATITUDE OF POTENTIAL MAXIMUM(DEGREES) = 70
 OVAL OFFSET(DEGREES) = 5
 MEASUREMENT LATITUDE = 65
 VIEWING ANGLE = -30



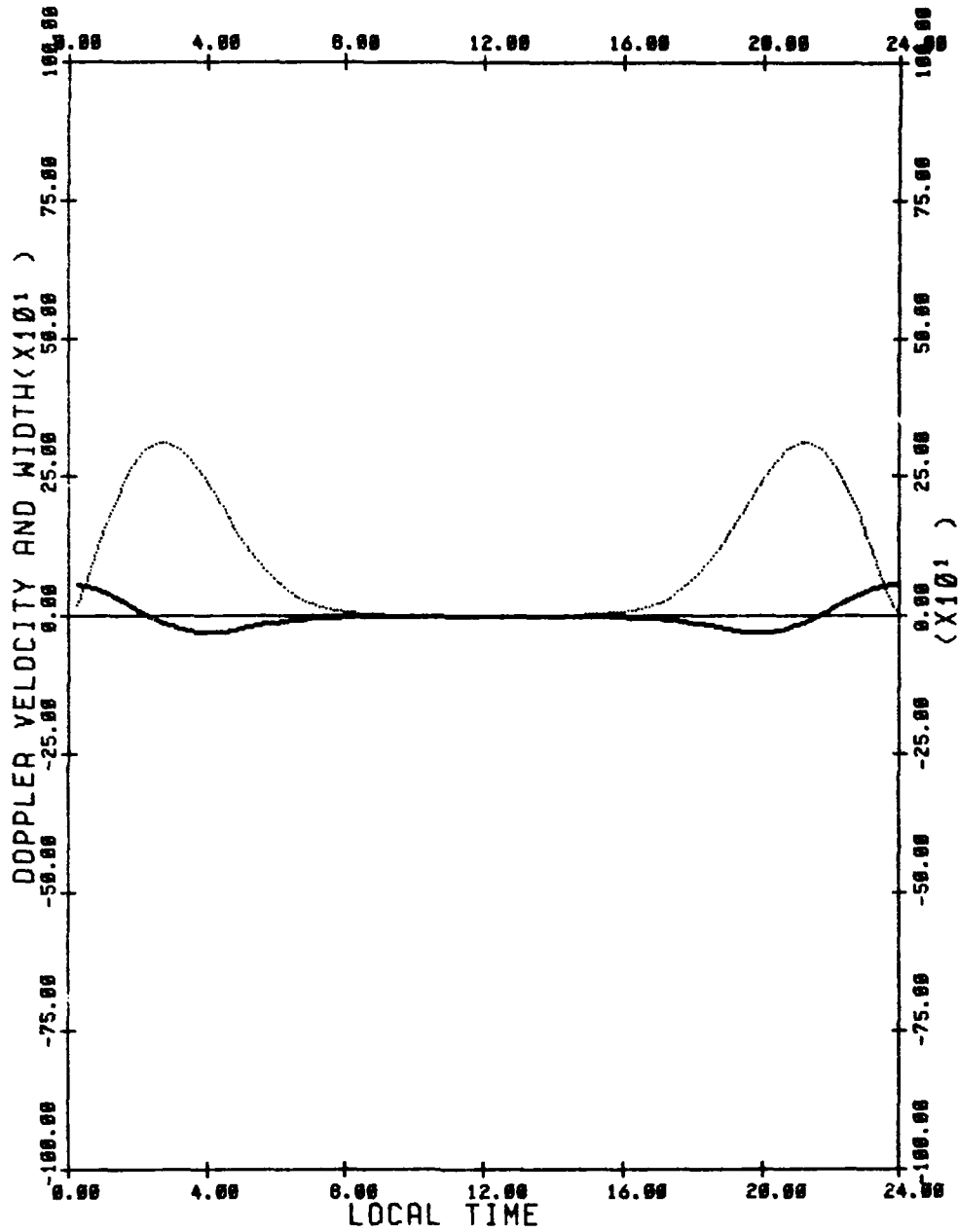
DOPPLER VELOCITY —————
 DOPPLER WIDTH - - - - -
 CROSS POLAR CAP POTENTIAL DROP(V) = 50000
 LATITUDINAL WIDTH OF E-FIELD STRIP(DEGREES) = 10
 LATITUDE OF POTENTIAL MAXIMUM(DEGREES) = 70
 OVAL OFFSET(DEGREES) = 5
 MEASUREMENT LATITUDE = 65
 VIEWING ANGLE = -60



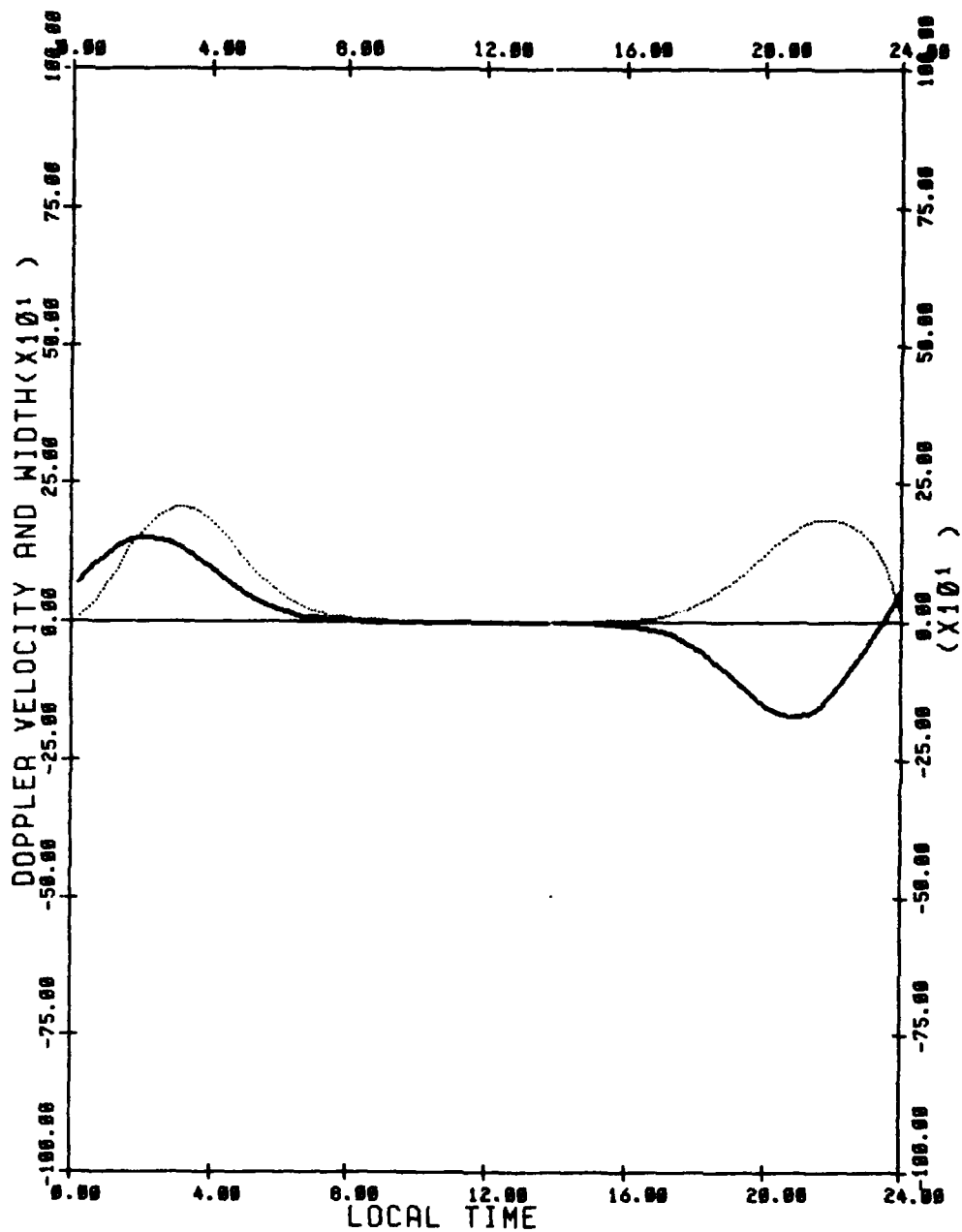
DOPPLER VELOCITY
 DOPPLER WIDTH
 CROSS POLAR CAP POTENTIAL DROP(V) = 50000
 LATITUDINAL WIDTH OF E-FIELD STRIP(DEGREES) = 10
 LATITUDE OF POTENTIAL MAXIMUM(DEGREES) = 70
 OVAL OFFSET(DEGREES) = 5
 MEASUREMENT LATITUDE = 60
 VIEWING ANGLE = 60



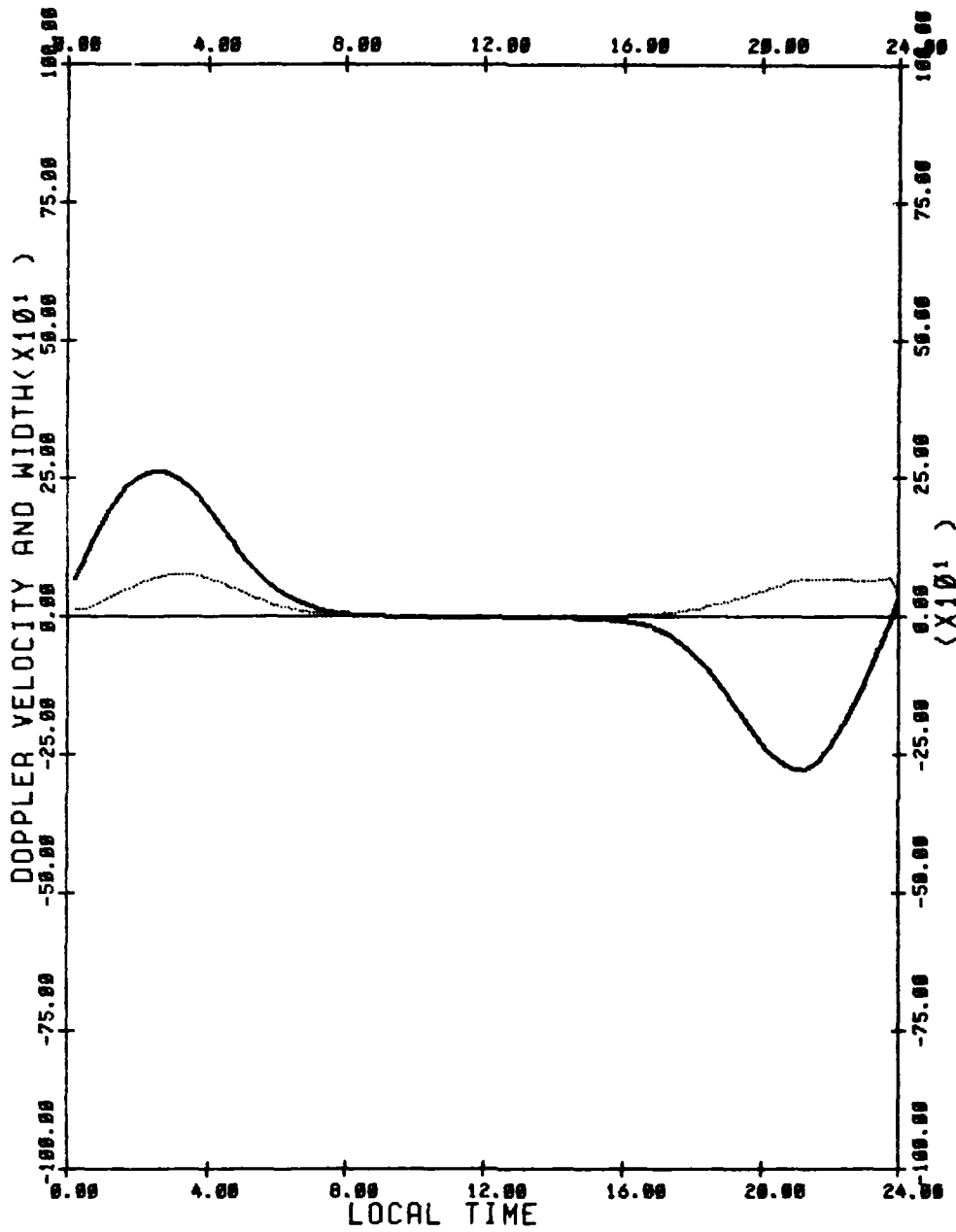
DOPPLER VELOCITY —————
 DOPPLER WIDTH - - - - -
 CROSS POLAR CAP POTENTIAL DROP(V) = 50000
 LATITUDINAL WIDTH OF E-FIELD STRIP(DEGREES) = 10
 LATITUDE OF POTENTIAL MAXIMUM(DEGREES) = 70
 DYAL OFFSET(DEGREES) = 5
 MEASUREMENT LATITUDE = 60
 VIEWING ANGLE = 30



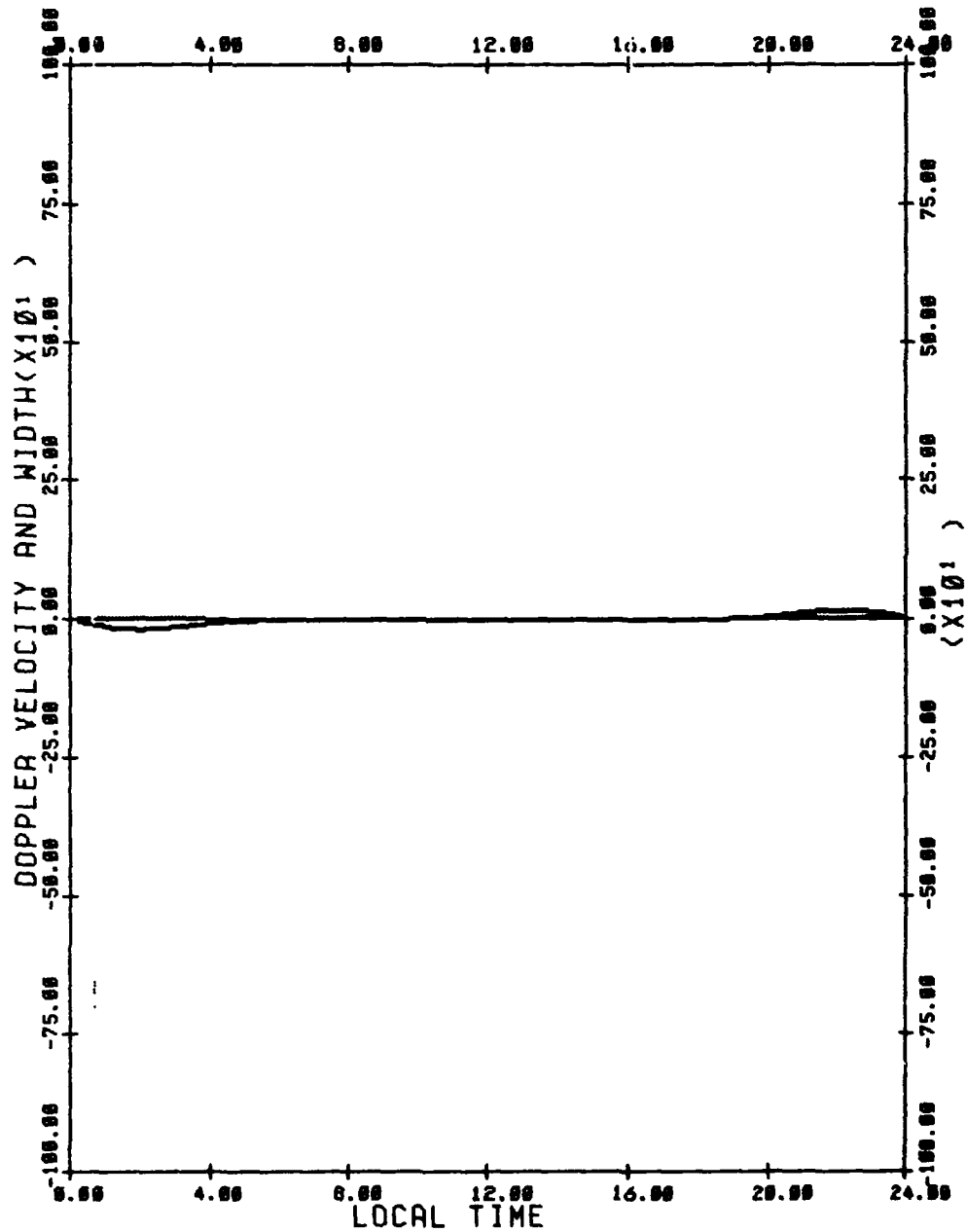
DOPPLER VELOCITY —————
 DOPPLER WIDTH - - - - -
 CROSS POLAR CAP POTENTIAL DROP(V) = 50000
 LATITUDINAL WIDTH OF E-FIELD STRIP(DEGREES) = 10
 LATITUDE OF POTENTIAL MAXIMUM(DEGREES) = 70
 OVAL OFFSET(DEGREES) = 5
 MEASUREMENT LATITUDE = 60
 VIEWING ANGLE = 0



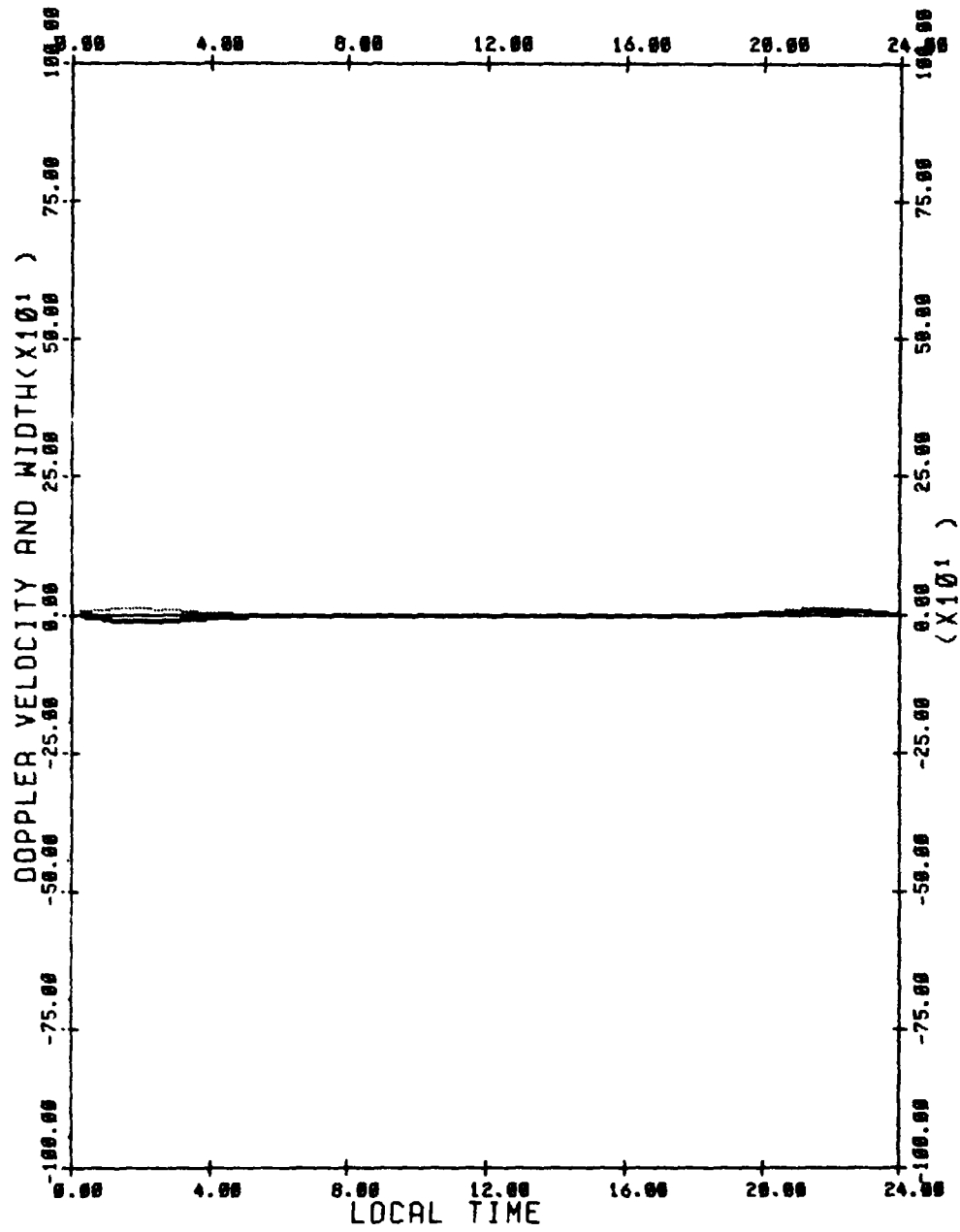
DOPPLER VELOCITY —————
 DOPPLER WIDTH - - - - -
 CROSS POLAR CAP POTENTIAL DROP(V) = 50000
 LATITUDINAL WIDTH OF E-FIELD STRIP(DEGREES) = 10
 LATITUDE OF POTENTIAL MAXIMUM(DEGREES) = 70
 OVAL OFFSET(DEGREES) = 5
 MEASUREMENT LATITUDE = 60
 VIEWING ANGLE = -30



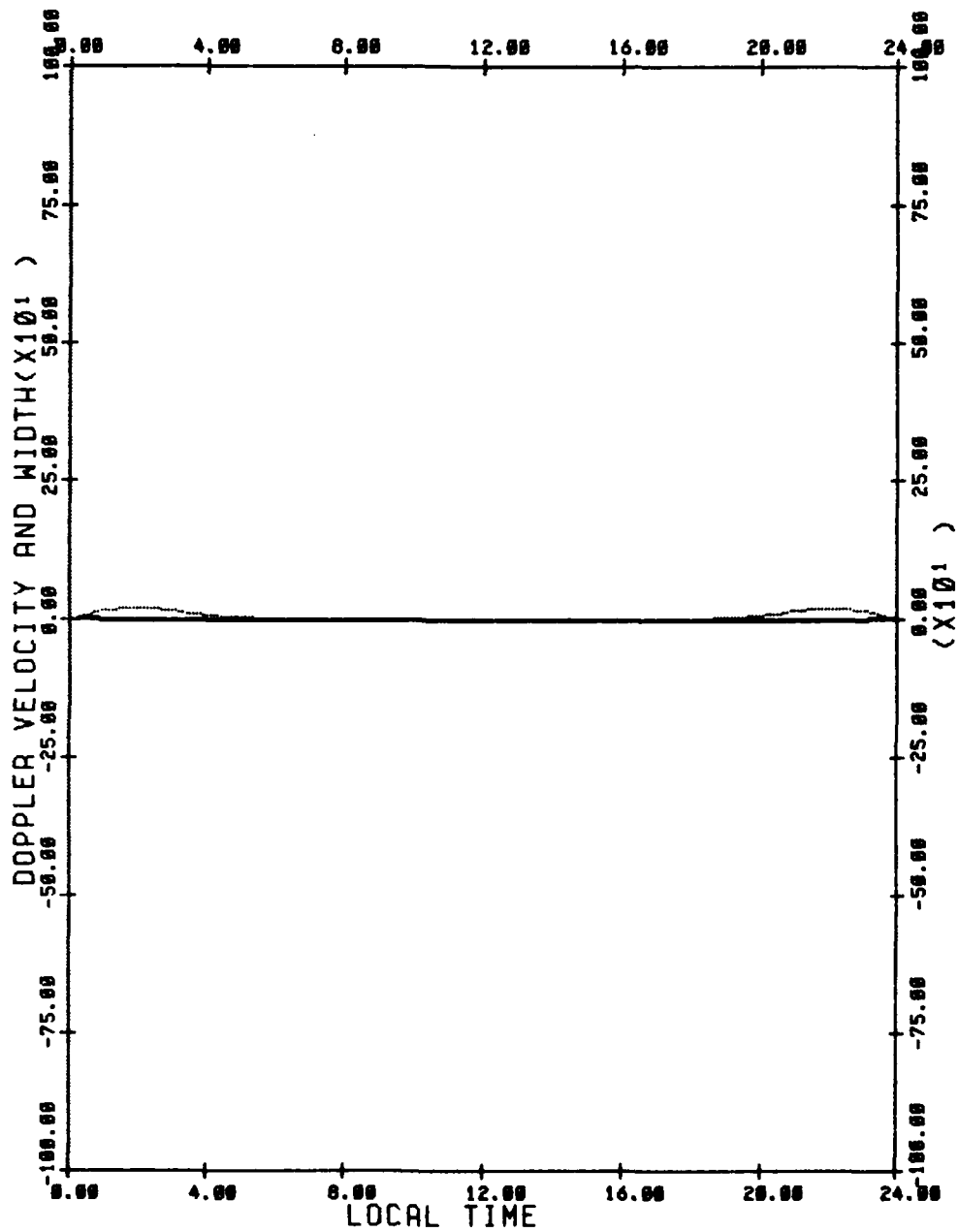
DOPPLER VELOCITY —————
 DOPPLER WIDTH - - - - -
 CROSS POLAR CAP POTENTIAL DROP(V) = 50000
 LATITUDINAL WIDTH OF E-FIELD STRIP(DEGREES) = 10
 LATITUDE OF POTENTIAL MAXIMUM(DEGREES) = 70
 OVAL OFFSET(DEGREES) = 5
 MEASUREMENT LATITUDE = 60
 VIEWING ANGLE = -60



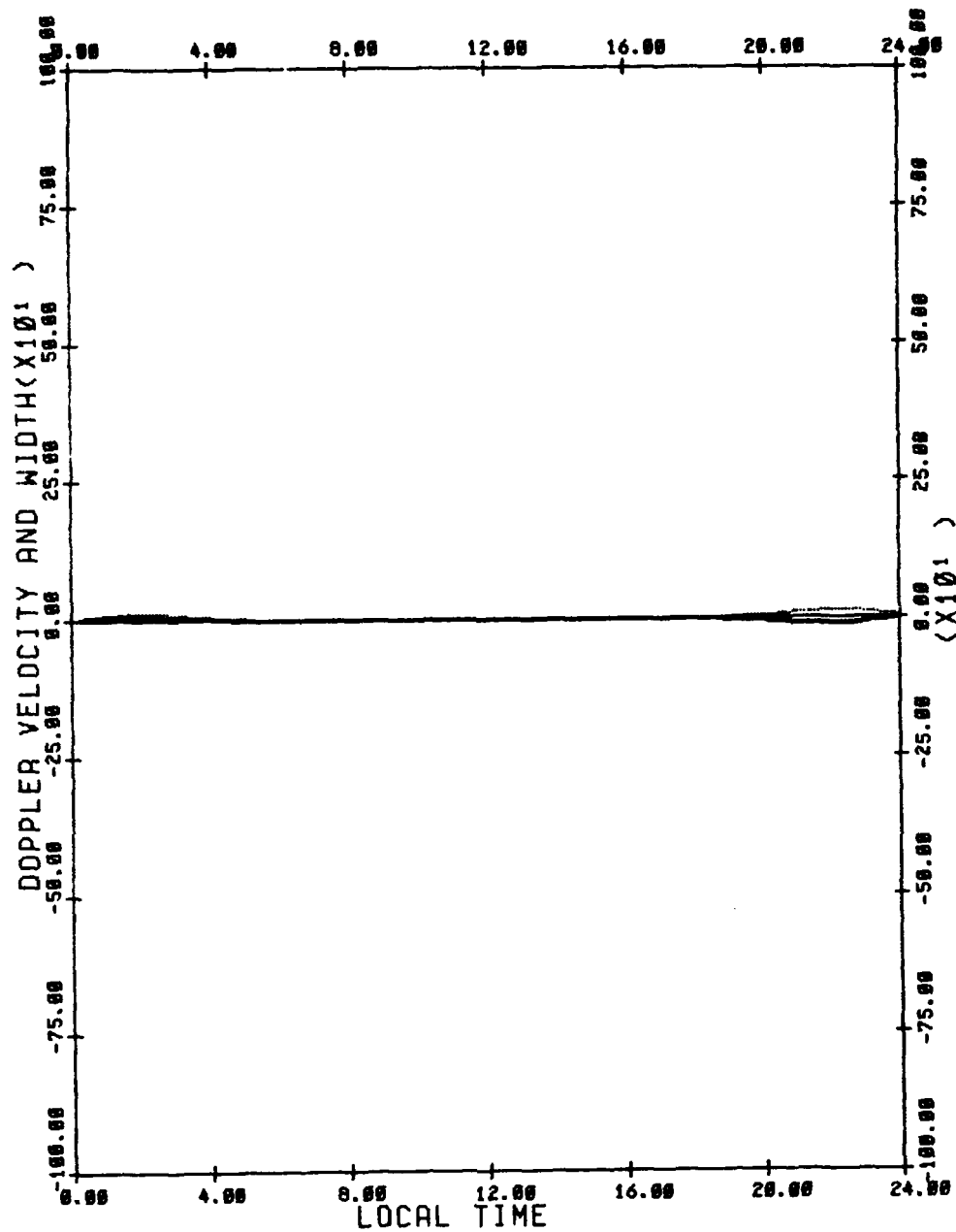
DOPPLER VELOCITY —————
 DOPPLER WIDTH —————
 CROSS POLAR CAP POTENTIAL DROP(V) = 50000
 LATITUDINAL WIDTH OF E-FIELD STRIP(DEGREES) = 10
 LATITUDE OF POTENTIAL MAXIMUM(DEGREES) = 70
 OVAL OFFSET(DEGREES) = 5
 MEASUREMENT LATITUDE = 55
 VIEWING ANGLE = 60



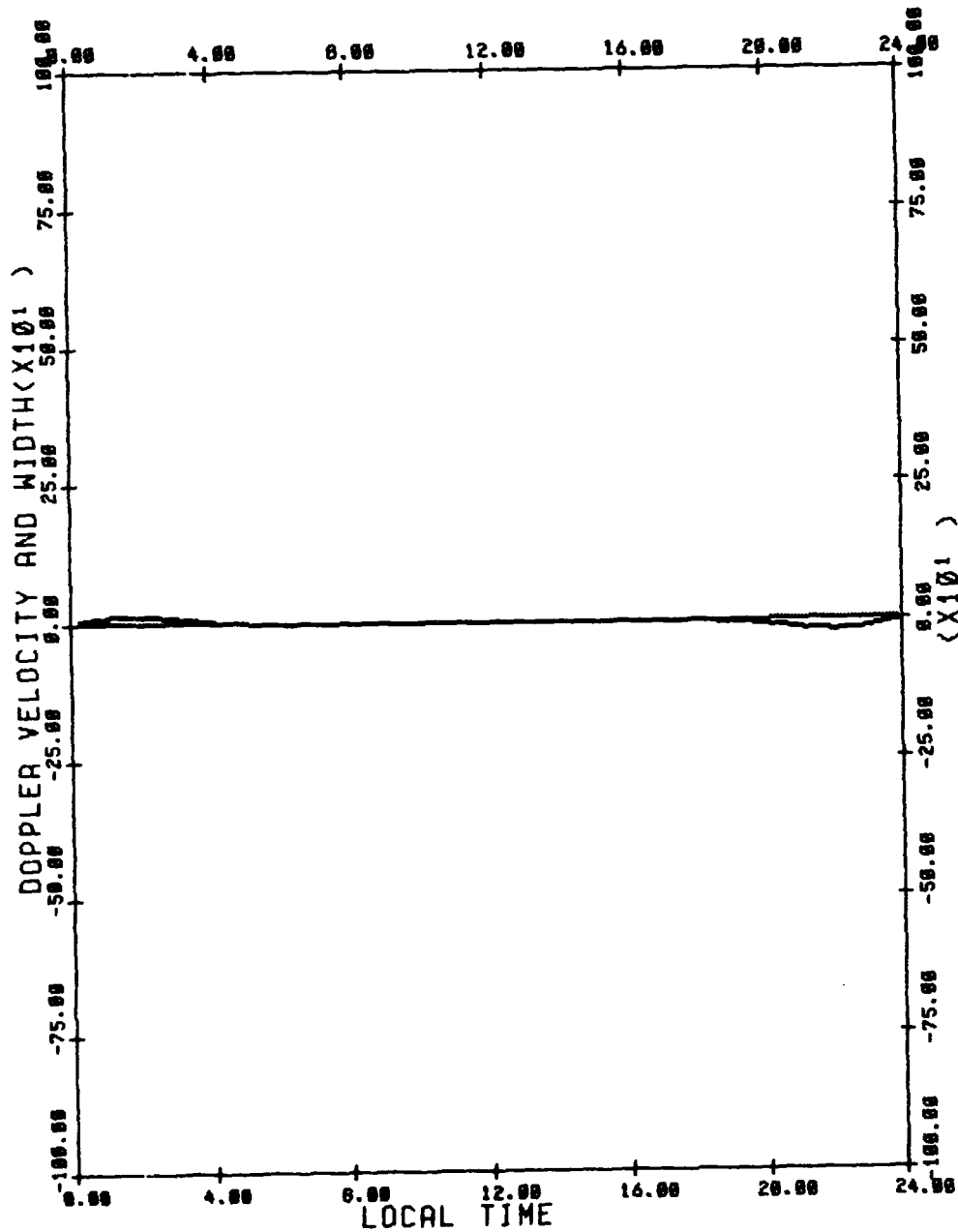
DOPPLER VELOCITY —————
 DOPPLER WIDTH - - - - -
 CROSS POLAR CAP POTENTIAL DROP(V) = 50000
 LATITUDINAL WIDTH OF E-FIELD STRIP(DEGREES) = 10
 LATITUDE OF POTENTIAL MAXIMUM(DEGREES) = 70
 OVAL OFFSET(DEGREES) = 5
 MEASUREMENT LATITUDE = 55
 VIEWING ANGLE = 30



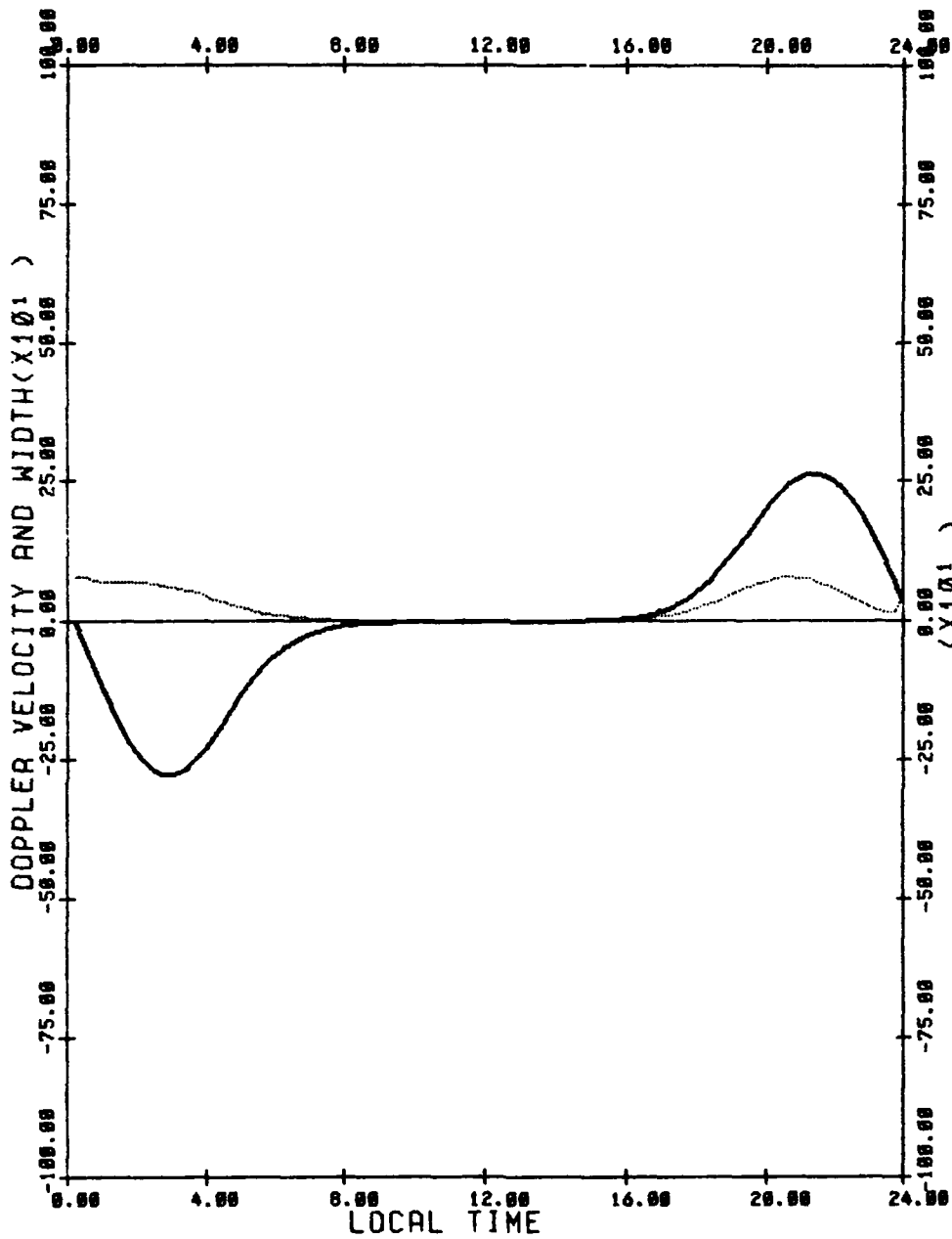
DOPPLER VELOCITY —————
 DOPPLER WIDTH
 CROSS POLAR CAP POTENTIAL DROP(V) = 50000
 LATITUDINAL WIDTH OF E-FIELD STRIP(DEGREES) = 10
 LATITUDE OF POTENTIAL MAXIMUM(DEGREES) = 70
 OVAL OFFSET(DEGREES) = 5
 MEASUREMENT LATITUDE = 55
 VIEWING ANGLE = 0



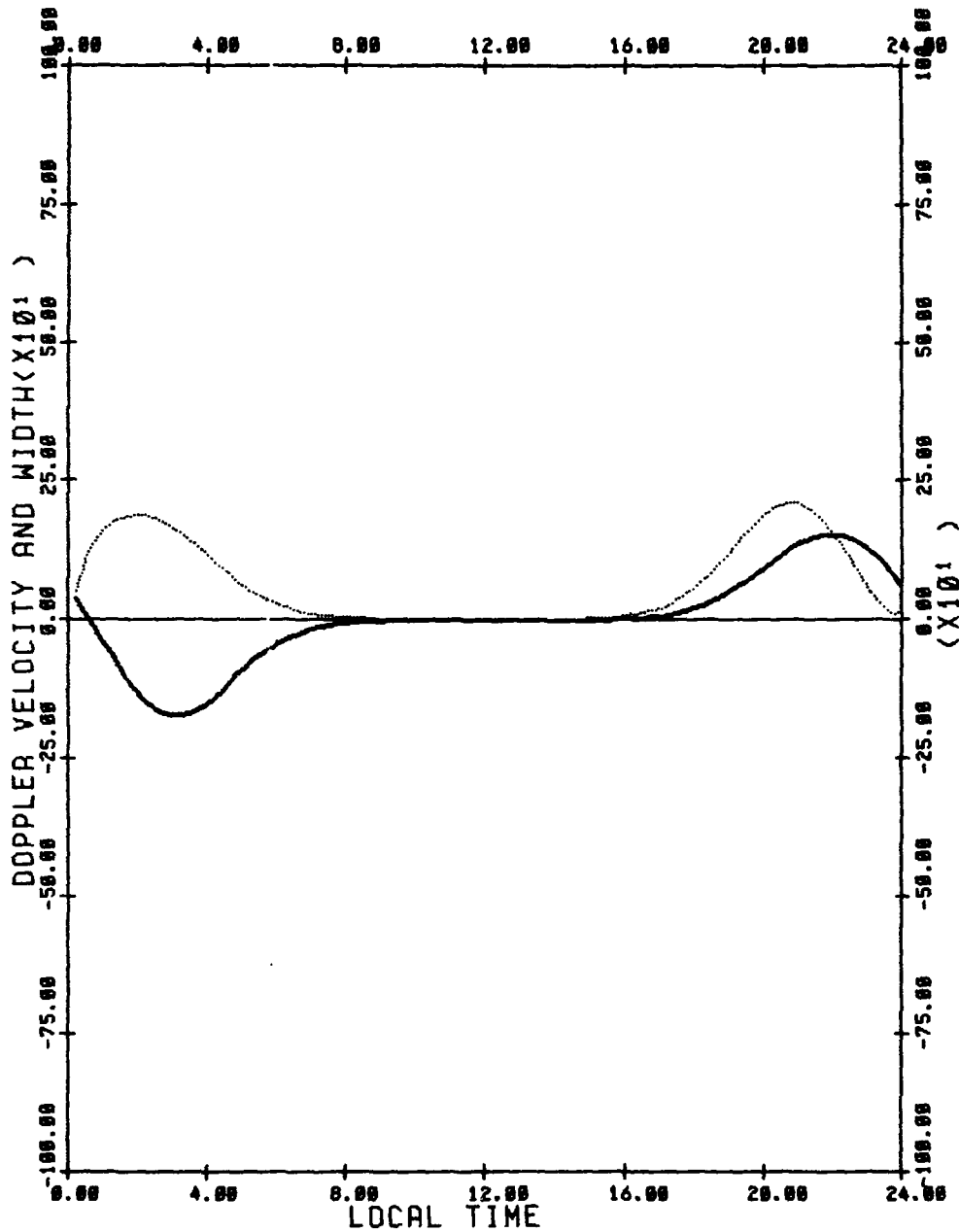
DOPPLER VELOCITY _____
 DOPPLER WIDTH _____
 CROSS POLAR CAP POTENTIAL DROP(V) = 50000
 LATITUDINAL WIDTH OF E-FIELD STRIP(DEGREES) = 10
 LATITUDE OF POTENTIAL MAXIMUM(DEGREES) = 70
 OVAL OFFSET(DEGREES) = 5
 MEASUREMENT LATITUDE = 55
 VIEWING ANGLE = -30



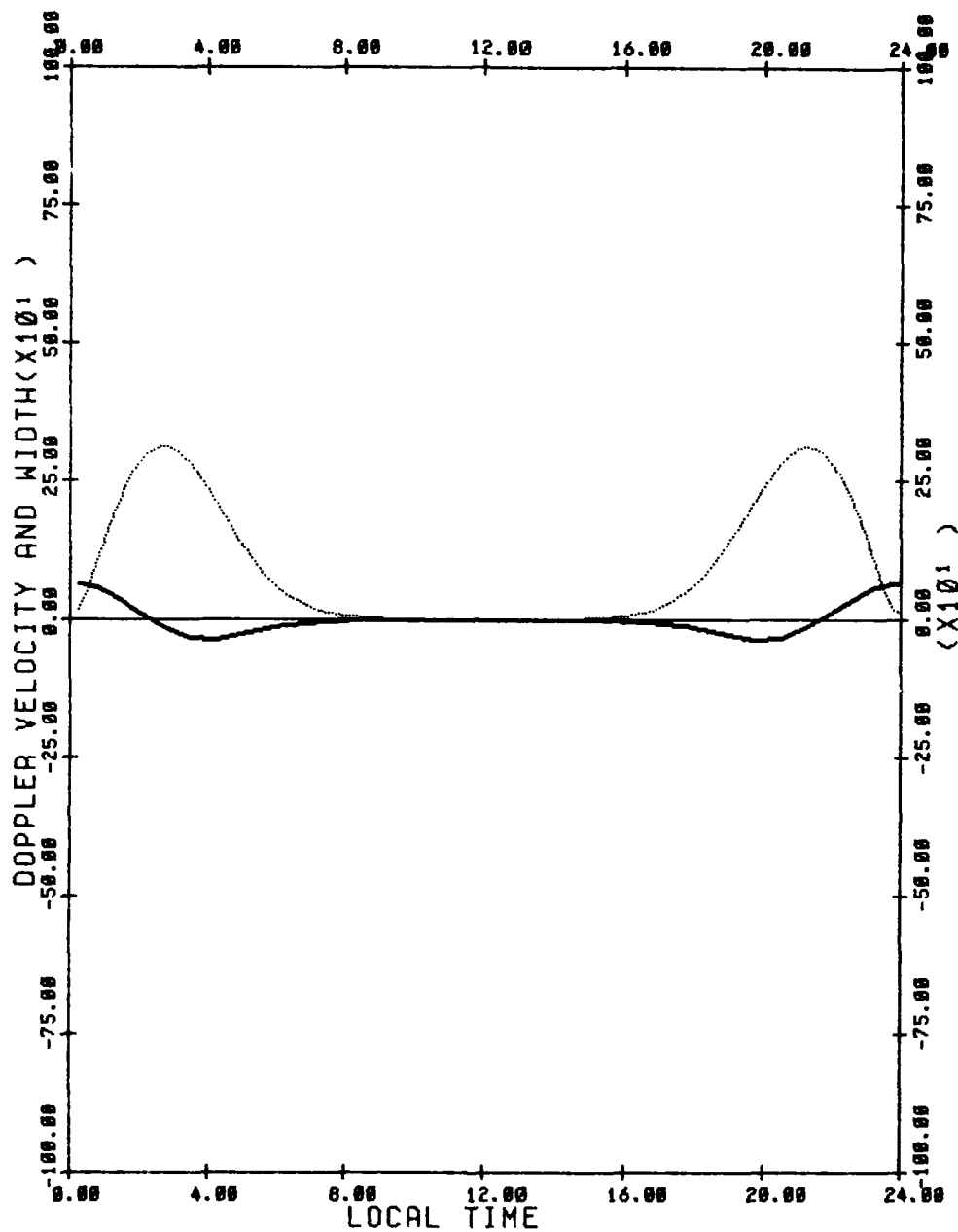
DOPPLER VELOCITY —————
 DOPPLER WIDTH - - - - -
 CROSS POLAR CAP POTENTIAL DROP(V) = 50000
 LATITUDINAL WIDTH OF E-FIELD STRIP(DEGREES) = 10
 LATITUDE OF POTENTIAL MAXIMUM(DEGREES) = 70
 OVAL OFFSET(DEGREES) = 5
 MEASUREMENT LATITUDE = 55
 VIEWING ANGLE = -60



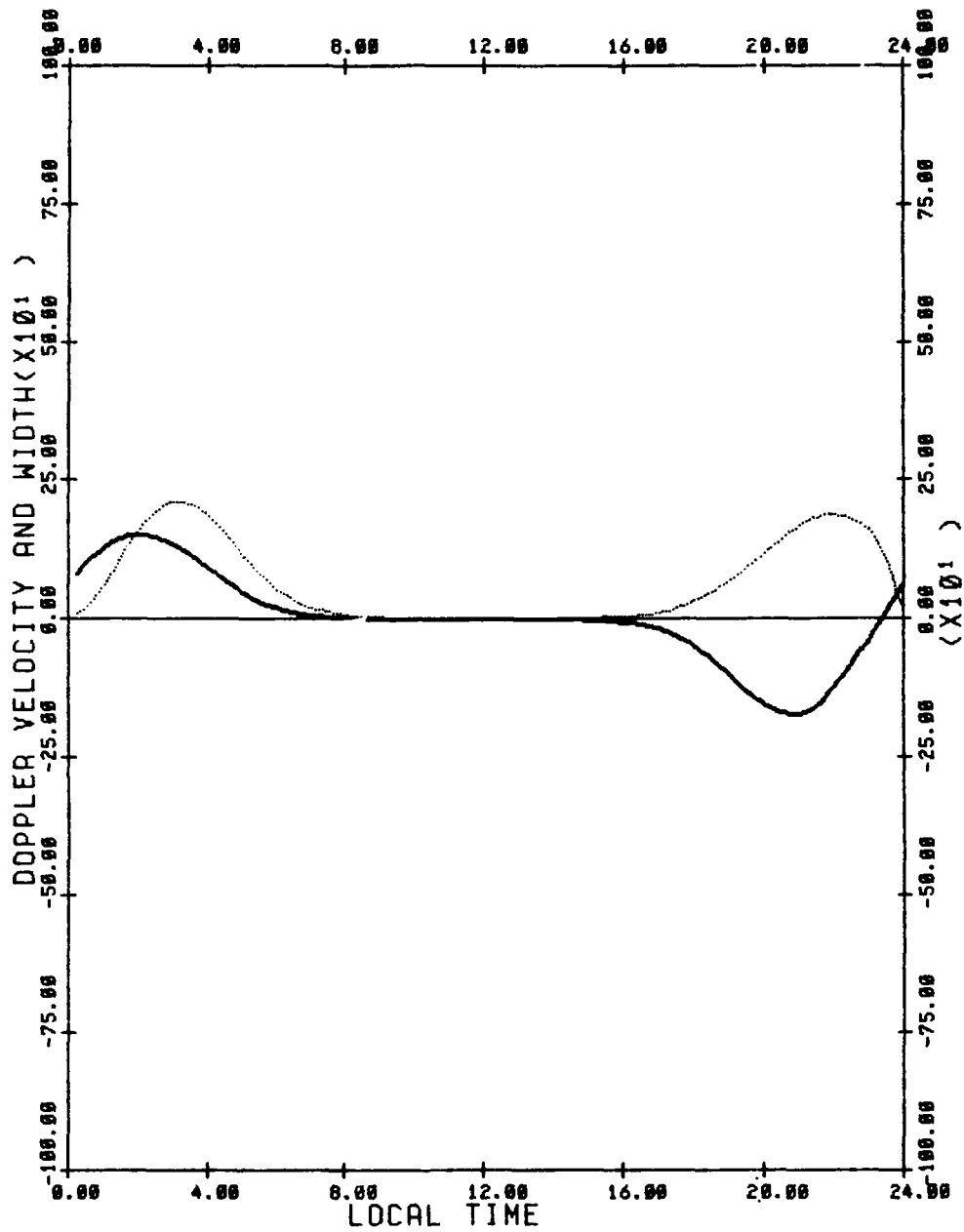
DOPPLER VELOCITY —————
 DOPPLER WIDTH - - - - -
 CROSS POLAR CAP POTENTIAL DROP(V) = 50000
 LATITUDINAL WIDTH OF E-FIELD STRIP(DEGREES) = 10
 LATITUDE OF POTENTIAL MAXIMUM(DEGREES) = 75
 OVAL OFFSET(DEGREES) = 5
 MEASUREMENT LATITUDE = 65
 VIEWING ANGLE = 60



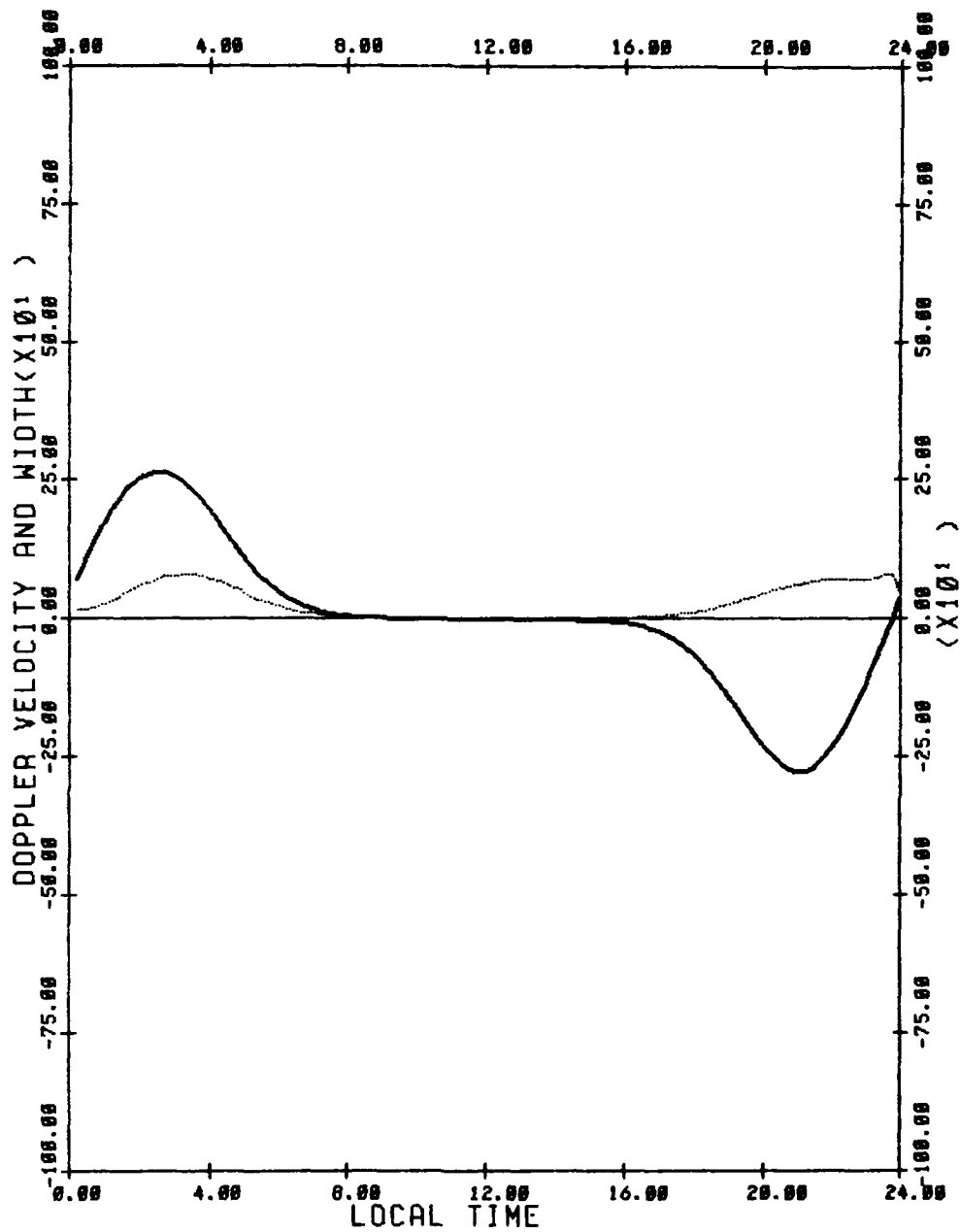
DOPPLER VELOCITY —————
 DOPPLER WIDTH - - - - -
 CROSS POLAR CAP POTENTIAL DROP(V) = 50000
 LATITUDINAL WIDTH OF E-FIELD STRIP(DEGREES) = 10
 LATITUDE OF POTENTIAL MAXIMUM(DEGREES) = 75
 OVAL OFFSET(DEGREES) = 5
 MEASUREMENT LATITUDE = 65
 VIEWING ANGLE = 30



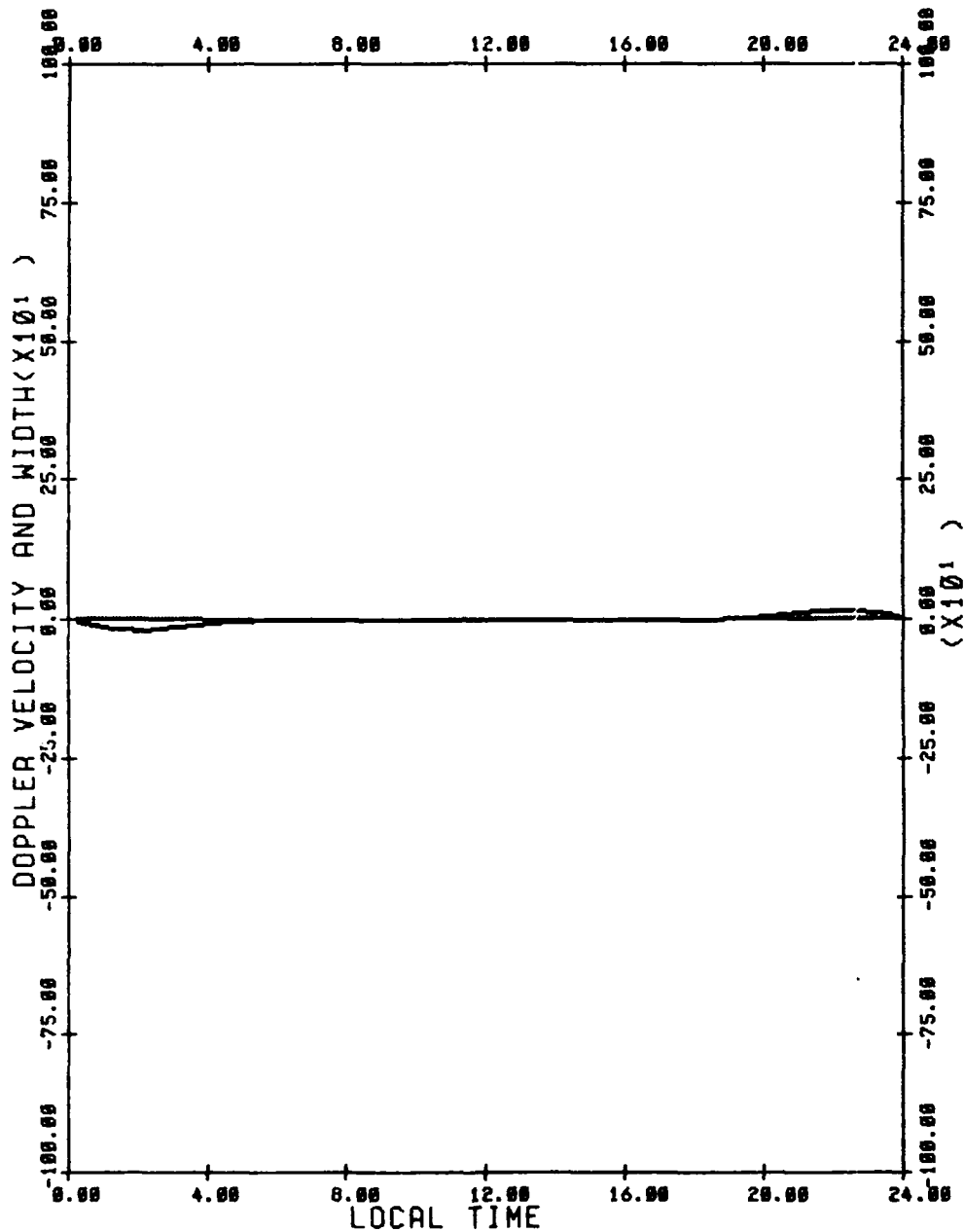
DOPPLER VELOCITY —————
 DOPPLER WIDTH
 CROSS POLAR CAP POTENTIAL DROP(V) = 50000
 LATITUDINAL WIDTH OF E-FIELD STRIP(DEGREES) = 10
 LATITUDE OF POTENTIAL MAXIMUM(DEGREES) = 75
 OVAL OFFSET(DEGREES) = 5
 MEASUREMENT LATITUDE = 65
 VIEWING ANGLE = 0



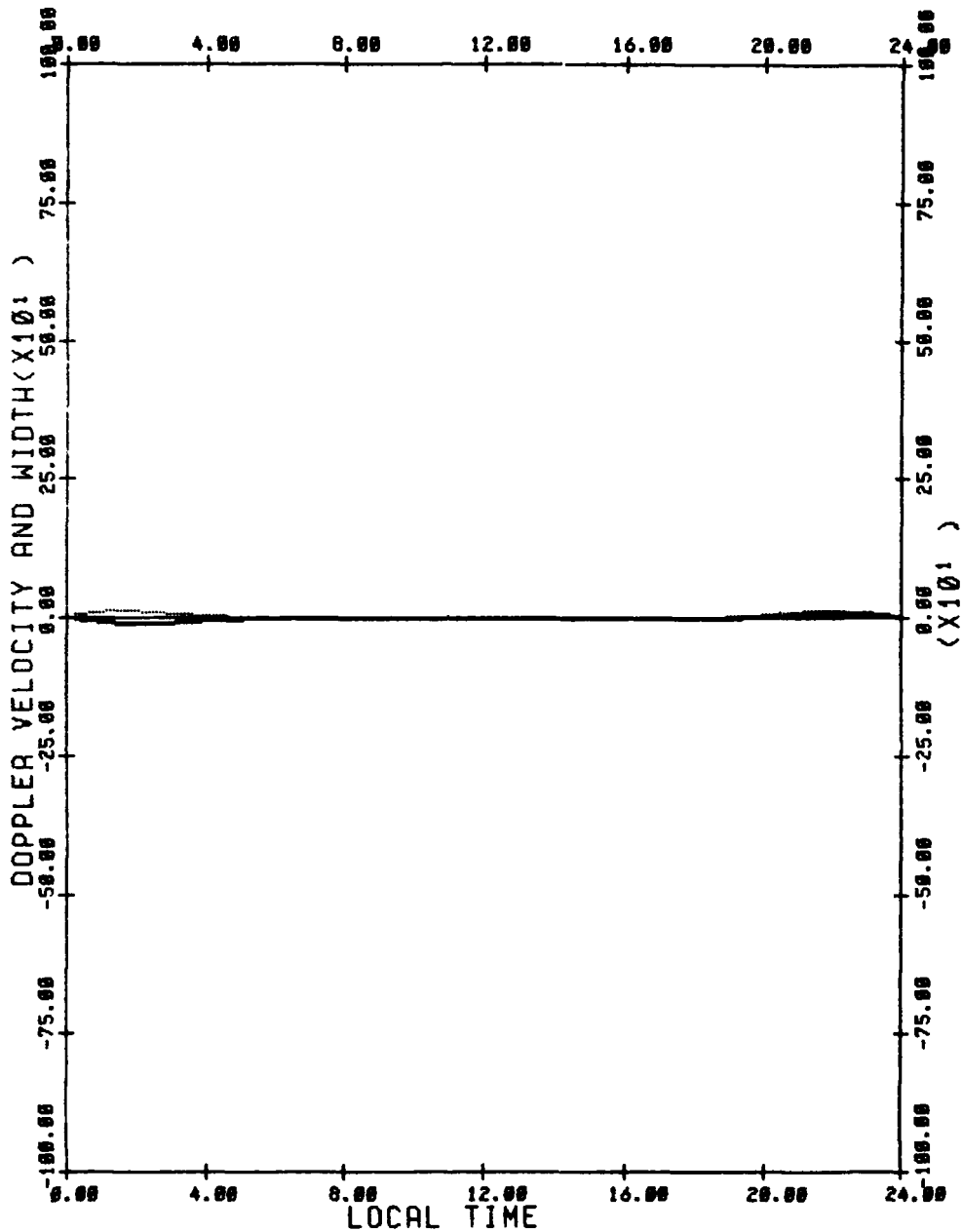
DOPPLER VELOCITY —————
 DOPPLER WIDTH
 CROSS POLAR CAP POTENTIAL DROP(V) = 50000
 LATITUDINAL WIDTH OF E-FIELD STRIP(DEGREES) = 10
 LATITUDE OF POTENTIAL MAXIMUM(DEGREES) = 75
 OVAL OFFSET(DEGREES) = 5
 MEASUREMENT LATITUDE = 65
 VIEWING ANGLE = -30



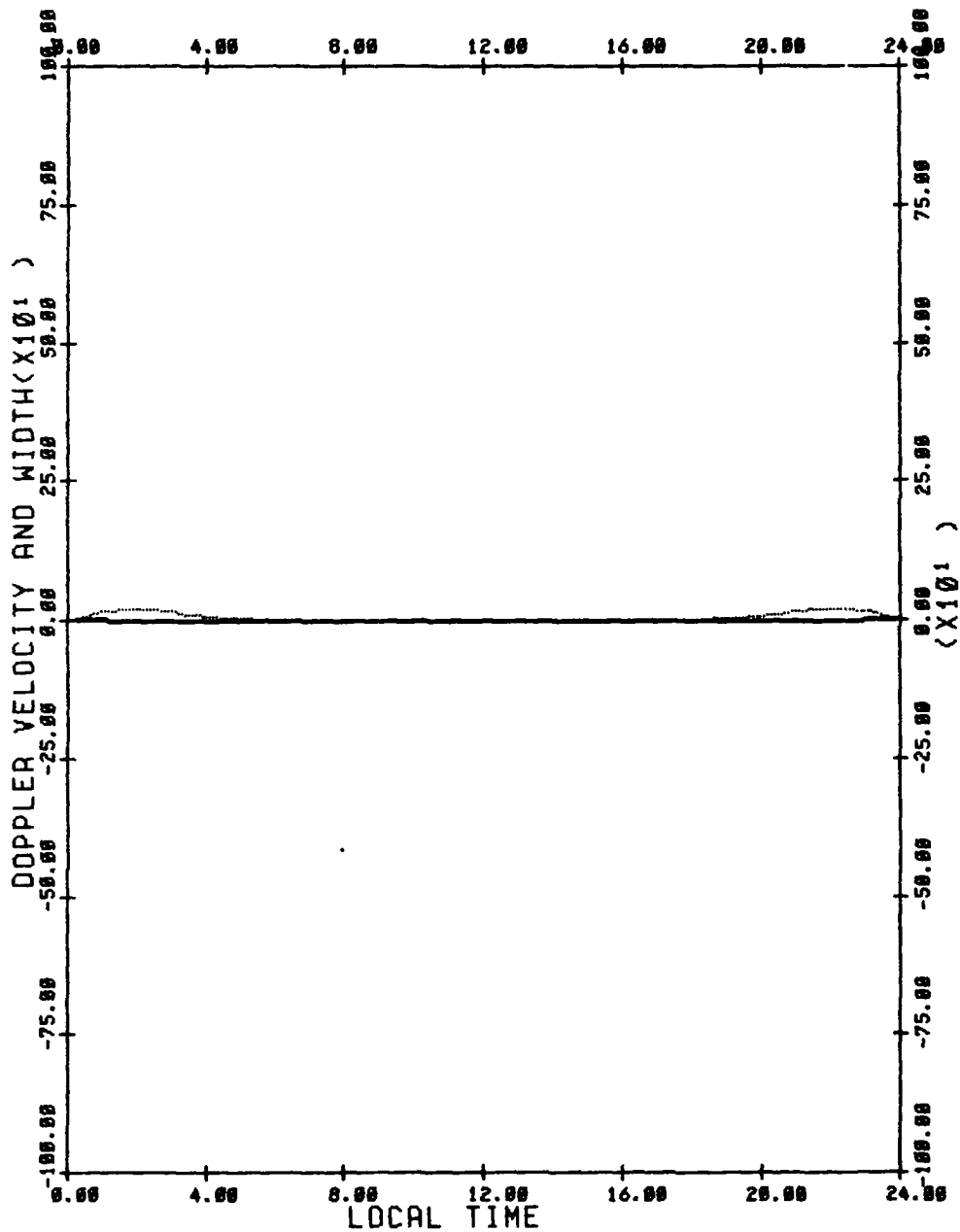
DOPPLER VELOCITY —————
 DOPPLER WIDTH -----
 CROSS POLAR CAP POTENTIAL DROP(V) = 50000
 LATITUDINAL WIDTH OF E-FIELD STRIP(DEGREES) = 10
 LATITUDE OF POTENTIAL MAXIMUM(DEGREES) = 75
 OVAL OFFSET(DEGREES) = 5
 MEASUREMENT LATITUDE = 65
 VIEWING ANGLE = -60



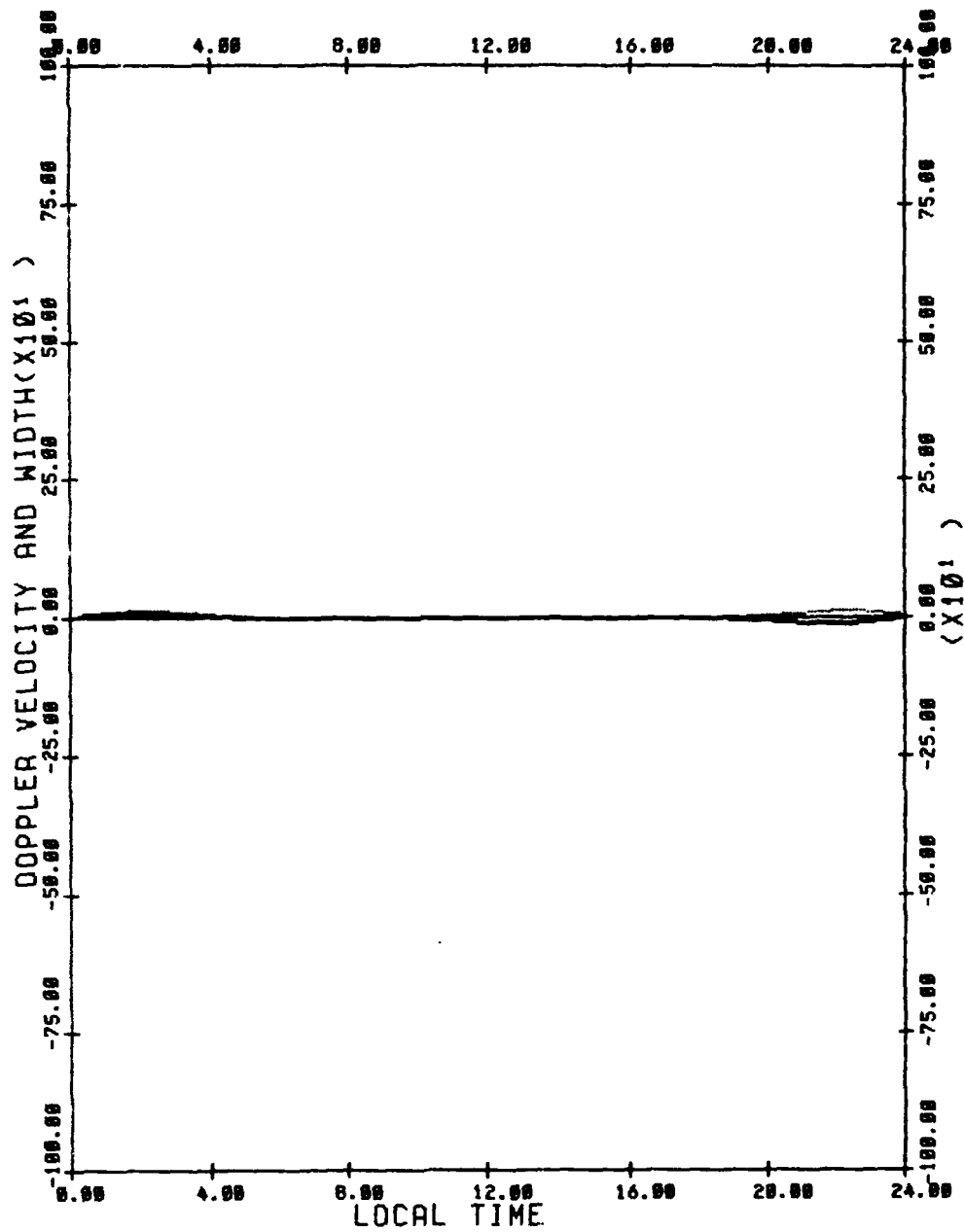
DOPPLER VELOCITY —————
 DOPPLER WIDTH - - - - -
 CROSS POLAR CAP POTENTIAL DROP(V) = 50000
 LATITUDINAL WIDTH OF E-FIELD STRIP(DEGREES) = 10
 LATITUDE OF POTENTIAL MAXIMUM(DEGREES) = 75
 OVAL OFFSET(DEGREES) = 5
 MEASUREMENT LATITUDE = 60
 VIEWING ANGLE = 60



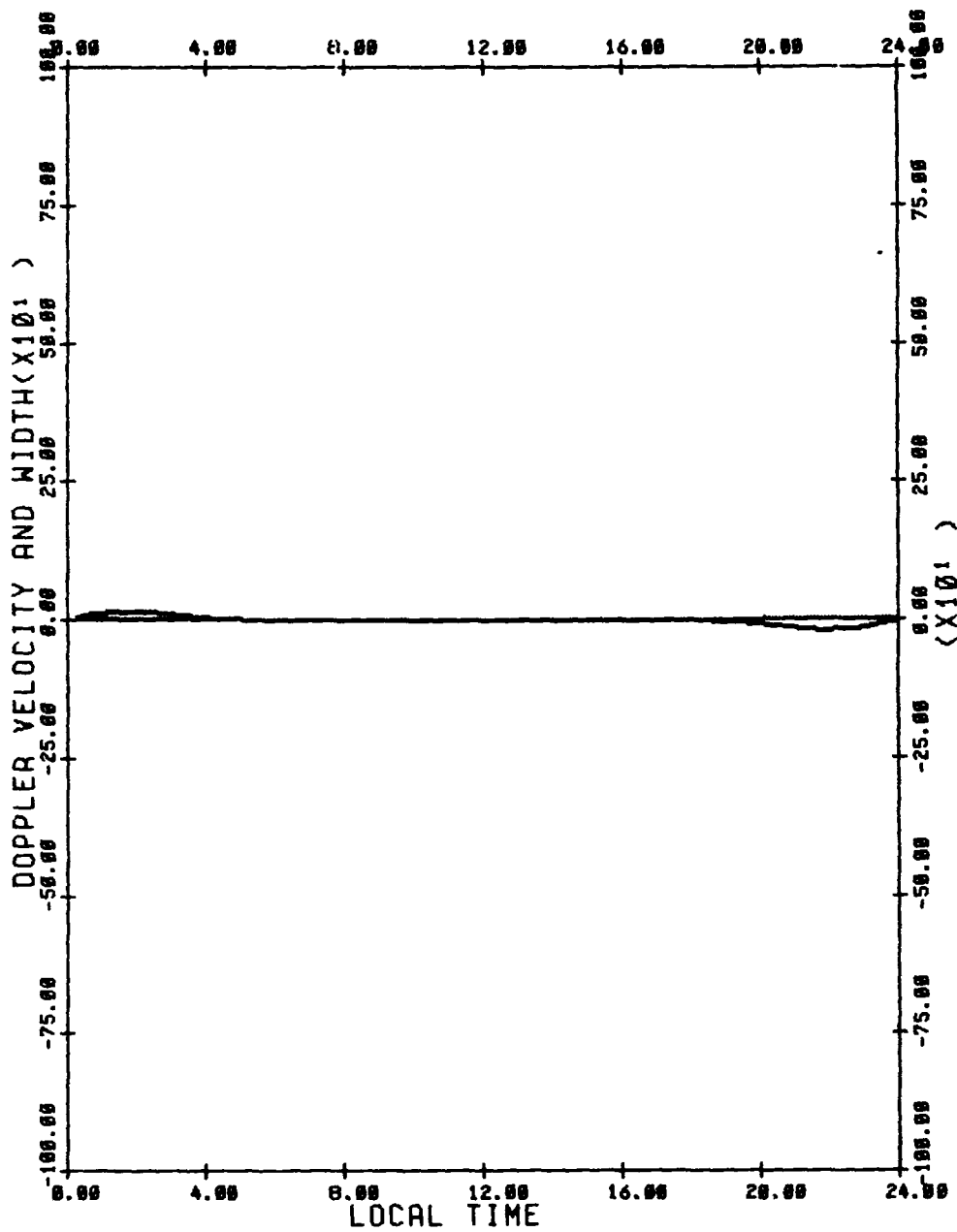
DOPPLER VELOCITY _____
 DOPPLER WIDTH _____
 CROSS POLAR CAP POTENTIAL DROP(V) = 50000
 LATITUDINAL WIDTH OF E-FIELD STRIP(DEGREES) = 10
 LATITUDE OF POTENTIAL MAXIMUM(DEGREES) = 75
 OVAL OFFSET(DEGREES) = 5
 MEASUREMENT LATITUDE = 60
 VIEWING ANGLE = 30



DOPPLER VELOCITY —————
 DOPPLER WIDTH - - - - -
 CROSS POLAR CAP POTENTIAL DROP(V) = 50000
 LATITUOINAL WIDTH OF E-FIELD STRIP(DEGREES) = 10
 LATITUDE OF POTENTIAL MAXIMUM(DEGREES) = 75
 OVAL OFFSET(DEGREES) = 5
 MEASUREMENT LATITUDE = 60
 VIEWING ANGLE = 0



DOPPLER VELOCITY
 DOPPLER WIDTH
 CROSS POLAR CAP POTENTIAL DROP(V) = 50000
 LATITUDINAL WIDTH OF E-FIELD STRIP(DEGREES) = 10
 LATITUDE OF POTENTIAL MAXIMUM(DEGREES) = 75
 OVAL OFFSET(DEGREES) = 5
 MEASUREMENT LATITUDE = 60
 VIEWING ANGLE = -30



DOPPLER VELOCITY —————
 DOPPLER WIDTH —————
 CROSS POLAR CAP POTENTIAL DROP(V) = 50000
 LATITUDINAL WIDTH OF E-FIELD STRIP(DEGREES) = 10
 LATITUDE OF POTENTIAL MAXIMUM(DEGREES) = 75
 OVAL OFFSET(DEGREES) = 5
 MEASUREMENT LATITUDE = 60
 VIEWING ANGLE = -60

MISSION
of
Rome Air Development Center

RADC plans and executes research, development, test and selected acquisition programs in support of Command, Control, Communications and Intelligence (C³I) activities. Technical and engineering support within areas of technical competence is provided to ESD Program Offices (POs) and other ESD elements. The principal technical mission areas are communications, electromagnetic guidance and control, surveillance of ground and aerospace objects, intelligence data collection and handling, information system technology, ionospheric propagation, solid state sciences, microwave physics and electronic reliability, maintainability and compatibility.

**DATA
FILM**